

The Interface Behavior in Two-Phase Flow; Impacts of Salinity and Wettability at Nano to Micro Scales

Lifei Yan

Environmental Hydrogeology Group
Utrecht University

The reading committee:

Prof. Azita Ahmadi, University of Bordeaux

Prof. Abbas Firoozabadi, Rice University, Reservoir Engineering Research Institute

Prof. M.T. van Genuchten, Federal University of Rio de Janeiro, Utrecht University

Prof. Shuyu Sun, King Abdullah University of Science and Technology (KAUST)

Prof. Hassan Mahani, Sharif University of Technology

The examination committee:

Prof. Abbas Firoozabadi, Rice University, Reservoir Engineering Research Institute

Prof. M.T. van Genuchten, Federal University of Rio de Janeiro, Utrecht University

Dr. Elizabeth May Braga Dully Pontedeiro, Federal University of Rio de Janeiro

Prof. Shuyu Sun, King Abdullah University of Science and Technology (KAUST)

Prof. Hassan Mahani, Sharif University of Technology

ISBN: 978-90-6266-635-5

NUR: 930

Copyright © 2022 Lifei Yan

Niets uit deze uitgave mag worden vermenigvuldigd en/of openbaar gemaakt door middel van druk, fotokopie of op welke andere wijze dan ook zonder voorafgaande schriftelijke toestemming van de uitgevers.

All rights reserved. No part of this publication may be reproduced in any form, by print or photo print, microfilm or any other means, without written permission by the publishers.

Printed in the Netherlands by Ipskamp

The Interface Behavior in Two-Phase Flow; Impacts of Salinity and Wettability at Nano to Micro Scales

两相流的界面性质: 盐度和润湿性在纳米到微米尺度上的影响

Het interfacegedrag in tweefasige stroom; Effecten van zoutgehalte en bevochtigbaarheid op nano- tot microscales
(met een samenvatting in het Nederlands)

Proefschrift

ter verkrijging van de graad van doctor aan de
Universiteit Utrecht
op gezag van de
rector magnificus, prof.dr. H.R.B.M. Kummeling,
ingevolge het besluit van het college voor promoties
in het openbaar te verdedigen op

woensdag 18 januari 2023 des middags te 12.15 uur

door

LIFEI YAN

geboren op 1 oktober 1987
te Hebei, China

Promotoren:

Prof. dr. R.J. Schotting

Prof. dr. S.M. Hassanizadeh

Copromotor:

Dr. A. Raoof

This dissertation was made possible with financial support from China Scholarship Council (CSC).

"Empty your mind, be formless. Shapeless, like water. If you put water into a cup, it becomes the cup. You put water into a bottle and it becomes the bottle. You put it in a teapot, it becomes the teapot. Now, water can flow or it can crash. Be water, my friend."

Bruce Lee

Contents

Chapter 1 Introduction	1
1.1 Suggested mechanisms of low-salinity effect	3
1.2 Fluid-solid interaction in LSWF	7
1.3 Fluid-fluid interaction in LSWF	8
1.4 Osmosis effects in LSWF	9
1.5 Emulsification effects in LSWF	12
1.6 Research objectives	16
1.7 Thesis outline	17
Chapter 2 Impact of water salinity differential on a crude oil droplet constrained in a capillary	25
2.1 Salinity effect on emulsification in crude oil	27
2.2 The hypothesis of water transport in oil phase	32
2.2.1 Formation of water-in-oil micro-emulsion	32
2.2.2 Water transport in oil phase	33
2.3 Experimental methods	35
2.3.1 Preparation of glass capillary and fluids property	35
2.3.2 Microscopy observation set-up	37
2.4 Results and discussion	41
2.4.1 Oil globule movement	41
2.4.2 Contact angle measurement	44
2.4.3 Pressure changes in a capillary	45
2.4.4 Future research	47
2.5 Conclusion	47
Chapter 3 Fundamental study of water transport through oil phase	51
3.1 Water transport in brine-oil-rock contacts	53
3.2 The theory of liquid membrane	55
3.2.1 Argument on osmosis theory	55
3.2.2 Water diffusion caused by concentration difference	57
3.2.3 Water transport caused by inverse micelle	59
3.2.4 Hypothesis on water transport in an n-alkane phase during LSWF	65
3.3 Research approach	69
3.4.1 Microfluidic experiments	69
3.4.2 Molecular dynamic model and simulation details	75
3.4.3 Interfacial behavior experiments	77
3.4 Result and discussion	82
3.4.1 Microfluidic experiments	82

3.4.2	Molecular scale water diffusion	102
3.4.3	Effect of salinity on spontaneous emulsification at the interface	106
3.4.4	Direct observation of spontaneous emulsification	112
3.5	Conclusion	118
<i>Chapter 4 A nano-scale numerical model of ion transport in a thin aqueous film</i>		125
4.1	Introduction	127
4.2	Theory of Electrical Double Layer	130
4.2.1	EDL theory	130
4.2.2	Electric field	131
4.2.3	Ion Transport	132
4.3	1D and 2D numerical modelling	132
4.3.1	2D model	133
4.3.2	1D model	135
4.3.3	Model Parameter values	137
4.4	Simulation results and discussion	138
4.4.1	Initial equilibrium condition for the 1D model	138
4.4.2	1D model verification under dynamic condition	139
4.4.3	1D Simulation results for a more realistic domain length	142
4.5	Conclusion	143
<i>Chapter 5 Wettability effect on pore-filling events for two-phase flow</i>		147
5.1	Introduction	149
5.2	Analytical solutions of two-phase flow in pore filling	152
5.2.1	Pressure distribution in a rectangular channel	152
5.2.2	Pressure change at diverging zone	157
5.3	Experimental set-up and micro-model wettability fabrication	158
5.3.1	Confocal scanning microscopy setup	158
5.3.2	Wettability control on PDMS	160
5.4	Direct numerical simulation of volume of fluid	164
5.4.1	Mass and momentum transport	164
5.4.2	Volume of Fluid (VOF) method	165
5.4.3	Pore geometry and boundary conditions	165
5.5	Experimental results and discussion	170
5.5.1	Description of displacement and validation of analytical solution	170
5.5.2	Water-air displacement	172
5.5.3	Water-fluorinert displacement	176
5.6	Simulation result	182
5.6.1	Comparison of the various boundary conditions	182
5.6.2	Wettability effect on meniscus behavior in pore filling	184

5.7	Future work	189
5.7.1	Further analysis of the dynamic contact angle	189
5.7.2	Wettability effect in a complex porous media	191
5.8	Conclusion	192
Chapter 6 Summary and Conclusion		199
	Summary and Conclusion	200
	Samenvatting en Conclusie	205
Appendix A		211
	Data and image processing in Chapter 1	211
Appendix B		212
	Data and image processing in Chapter 3	2112
B.1.	Images of experiment No.2 with n-heptane and 50 g/L LSW	212
B.2.	Images of experiment No.3 with n-heptane and no salinity differential	214
B.3.	Images of experiment No.5 with n-dodecane and 50 g/L LSW	214
B.4.	Images of experiment No.6 with n-dodecane and no salinity differential	215
B.5.	Images of experiment No.8 with n-heptane+1%SPAN80 and 50 g/L LSW	216
B.6.	Images of experiment No.11 with n-dodecane+1%SPAN80 and 50 g/L LSW	216
B.7.	Images of experiment No.12 with no salinity differential	217
B.8.	Imaging and data processing method	218
B.9.	Detailed non-bonded interactomic interaction parameters	221
B.10.	The dynamic number of diffusion water molecules across the oil phase in the three model systems during simulations	222
B.11.	The dynamic number of diffusion water molecules	222
B.12.	The modeling and calculation of interfacial tension	222
Acknowledgements		224
Curriculum Vitae		227
List of Publications		228

Chapter 1

Introduction

Two-phase flow in porous media is not only widespread in nature and daily life, but also broadly used in various industrial technologies, including textile technology, inkjet printing, fuel cell application, CO₂ sequestration, enhanced oil recovery and contaminate hydrology (Abidoye, Khudaida, & Das, 2015; Aslannejad et al., 2017; Morrow & Buckley, 2011; Wang, Basu, & Wang, 2008; Zhou & Blunt, 1997). To accurately calculate the flow velocity and phase interface positions over time, two classic tube models have been developed, parallel and serial (varying diameters within a tube) tube-bundle models (Bartley & Ruth, 1999; Scheidegger, 1954; Yuster, 1951). Although each model has its conceptional tube shape, both of them focus on the fluid displacement in capillaries, which inevitably involves capillary filling events. During drainage, in which a non-wetting fluid displaces a wetting fluid, the non-wetting fluid invades pore space showing a piston-like displacement under capillary-dominated flow (Hui & Blunt, 2000). The wetting fluid becomes trapped in the pore body or gives a snap-off process, which depends on the pore geometry and wettability (Singh et al., 2017). One critical question is therefore how to properly measure dynamics of pressure and velocity during pore-filling events with relevance to multiphase fluid flow. This is particularly important to inform reliable pore-scale computational models, i.e., pore network modelling and the direct simulation of tracking two-phase flow interfaces.

In oil and natural gas exploration, a better understanding of multiphase flow in porous media is a crucial aspect of improved oil and gas displacement efficiency. Low salinity water flooding (LSWF) is a tertiary method for improved oil recovery (EOR), which has substantially lower salinity (normally 1500 to 10,000 ppm salt concentration) than conventional sea water or formation water injected into a reservoir (Nande & Patwardhan, 2021). Within the process of LSWF, the contacts of solid-fluid-fluid are dynamically varying with water invasion, depending on factors, such as salt concentration, water/oil saturation, the chemical reaction between fluid and minerals, and oil redistribution. Compared with conventional high-salinity water flooding, LSWF can often improve oil recovery (not always) by about 5-38% based on the results from laboratory and field tests (Kokal & Al-Kaabi; Wood & Yuan, 2018). BP oil industry company ran a field test of single-well chemical tracer tests (SWCTT) using low-salinity water injection on Alaska North Slope. It turned out that residual oil saturation was substantially reduced and the corresponding oil recovery increased from 6 to 12% (McGuire, Chatham, Paskvan, Sommer, & Carini, 2005). Nevertheless, field

data validating increased oil recovery by low-Sal injection is still limited. Thyne and Gamage (2011) evaluated the potential for low-salinity waterflooding in the Minnelusa Formation in the Powder River Basin of Wyoming. They concluded that little or no incremental recovery from the low-salinity injection. Among the investigated 51 fields, 23 fields found no significant difference in the analysis of water breakthrough timing and water cut evolution between fields with low-salinity injection and mixed-water or saline injection.

1.1 Suggested mechanisms of low-salinity effect

Over the past 30 years, around 13 different responsible mechanisms have been proposed by researchers, including: (1) fine migration and mobilization (G. Tang & Morrow, 1997), (2) wettability alteration (Buckley, Liu, & Monsterleet, 1998), (3) reduced interfacial tension and increased pH effect (McGuire et al., 2005; Y. Zhang & Morrow, 2006) (4) multi-component ion exchange (MIE) (Lager, Webb, Black, Singleton, & Sorbie, 2008), (5) double layer expansion (DLE) (Ligthelm et al., 2009), (6) emulsification and micro-dispersion (Emadi & Sohrabi, 2013), (7) osmotic pressure (K Sandengen & Arntzen, 2013). The main mechanisms and their relationships are listed in Figure 1-1. Four main potential mechanisms and their drawbacks are briefly discussed below.

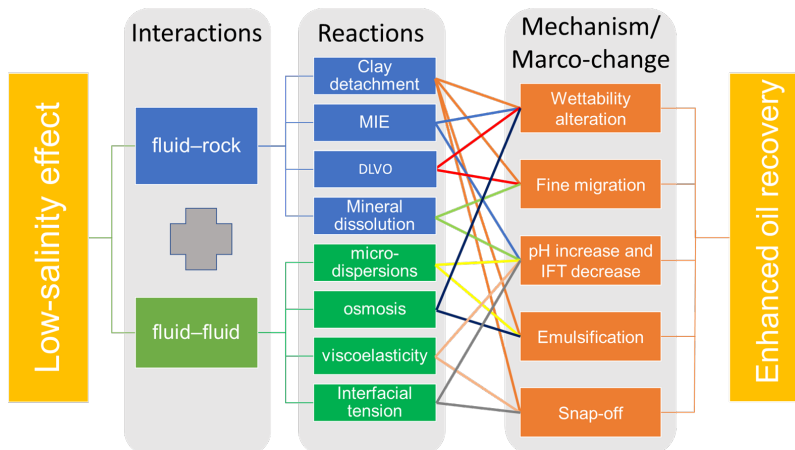


Figure 1-1: Suggested mechanisms for low-salinity effects and their relations.

- **Fine migration.** The systematic experimental work for low-salinity effects was done by G. Tang and Morrow (1997) (1999). They conducted a series of

core-flooding experiments and proposed that injecting low salinity water into clay-rich cores potentially mobilizes fine clay particles and partial stripping of mixed-wet fines from pore walls. Fine migration leads to a partial mobilization of residual oil which adheres to fine particles. Alhuraishawy, Bai, Wei, Geng, and Pu (2018) studied two key factors, salinity value and oil ageing time, by performing the experiments of imbibition, core flooding, and zeta potential and scanning electron microscopy (SEM). They also gave a similar conclusion that low water salinity injections induce mineral dissolution and sand migration which redistributes the flow pathways and increases oil displacement and sweep efficiency. Although several experimental observations have been used to support this mechanism, contradictory results have grown in number as well. Lager et al. (2008) reported numerous low-salinity core-flooding experiments with additional oil recovery but did not observe fine migration or significant permeability reductions both in reduced conditions and full reservoir conditions. Berg, Cense, Jansen, and Bakker (2010) described that changing the brine from high-salinity to low salinity caused the release of crude oil from a substrate covered with solidly attached clay particles in a flow cell, and no fines migration was directly observed, which provided direct experimental evidence of wettability modification by low salinity.

- **Wettability alteration.** Jadhunandan and Morrow (1995) found that the initial water saturation determines the rock wettability. Given a higher initial water saturation, the rock surface showed more water-wet. The LS effect may be related to wettability and makes the cores more water-wet and result in higher oil recovery. Sharma and Filoco (2000) proved that the core performed an improved oil recovery and the wettability changed from strongly water-wet close to intermediate wet, especially for the cores with lower ionic strength which were more water-wet. Vledder, Fonseca, Wells, Gonzalez, and Ligthelm (2010) acquired the field observations of wettability change in rock from oil-wet to water-wet in the Omar field in Syria after applying the LSW flooding and resulted in higher oil recovery. They collected the laboratory data from spontaneous imbibition experiments in cores and a single well Log-Inject-Log in an analogue field to support the observation. Although the wettability alteration is accepted as the main mechanism for explaining the low-salinity effect, it can be caused by multiple factors, such as DLE, MIE, mineral dissolution, etc. The reason still needs to be well understood.

- **Double layer expansion and MIE.** The Derjaguin-Landau-Verwey-Overbeek (DLVO) theory is used to correlate the electrokinetics of the rock surface to the thermodynamic interaction involved in the wettability alteration and the role of the thin liquid film (Tetteh, Brady, & Ghahfarokhi, 2020). The total disjoining pressure can be described by the sum of van der Waals forces (vdW), electrostatic or the electrical double layer (EDL) and structural forces. Ding and Rahman (2017) proposed the theory of oil adsorption on the carbonate substrate due to the opposite charge polarity on the rock-brine and oil-brine interfaces and the low-salinity effect on the force balance at the interfaces. Low ionic strength results in a reduced attractive force between the oil-brine-rock interfaces and leads to a bigger Debye length, which gives an expansion of the electrical double layer. The expansion increases the thickness of water film and alters rock wettability from oil-wet to water-wet (Alshakhs & Kovscek, 2016; Mahani, Keya, et al., 2015).

Multivalent ionic exchange is a mechanism of ion exchanges between the oil-brine and brine-rock interfaces, resulting in the desorption of crude oil from the rock surface (Strand, Høgenesen, & Austad, 2006). Lager et al. (2008) proposed the mechanism for sandstone based on cation exchange, ligand bonding and cation and water bridging. Low-salinity water flooding induces a stronger ligand bonding than cation bridging and cation exchange bonds. Therefore, carboxylic acids prefer to detach from the solid surface. Other researchers gave a similar mechanism for chalk formations and carbonate reservoirs (Fathi, Austad, & Strand, 2010; P. Zhang, Tweheyo, & Austad, 2007).

However, the MIE mechanism has been mostly studied using chalk or pure synthetic calcite (Karimi, Al-Maamari, Ayatollahi, & Mehranbod, 2016). Moreover, some contradictory works are showing no ion exchange reactions during LSWF. Tetteh, Veisi, Brady, and Barati Ghahfarokhi (2020) conducted core flooding experiments in tertiary mode using various salinity and composition brines. They measured the ionic composition of the effluent brine and pointed out that no ion exchange occurred in tertiary mode with/without using low salinity brines. The coexistence of DLE and MIE contribute to the wettability alteration in some extent, but which one affects the most is still uncertain. Additionally, both theories lack of the direct and solid evidence to

support the explanations, although some macro-observations show the water film generation and wettability alteration.

- **pH increase and IFT decrease.** McGuire et al. (2005) proposed that low salinity brine can lead to an increase pH and decrease IFT, resulting in a wettability alteration similar to the mechanism of alkaline flooding. Increased pH is due to the hydrogen ion exchange in water with adsorbed sodium ions. The increase imposes a significant change in zeta potential of rock and helps organic material desorption from the clay surfaces (Austad, 2013). Y. Zhang, Xie, and Morrow (2007) reported a slight rise in pH after LS brine injection. Decreased IFT is related to the salinity and the presence of natural surface-active agents in the crude oil forming water/oil or oil/water emulsions, which may improve the surface elasticity and hinders snap-off at the crude oil-brine interface (Garcia-Olvera & Alvarado, 2017). Mokhtari, Ayatollahi, and Fatemi (2019) noticed that IFT reached the lowest value after contacting brine with crude oil for 48 hours in a glass core and observed a reduction in effluent pH and EOR. However, the mechanisms between increased pH and decreased IFT do not have a corresponding relationship. J. J. Sheng (2014) reviewed the pH change before and after LS brine injection in literature and mentioned that some cases did not have pH change. He pointed out that the pH from actual tests was lower than the value to achieve emulsification and needs to be confirmed for the low-salinity water flooding.

During the low-salinity brine injection, the interactions among crude oil, brine and rock may be categorized into two major interactions: fluid-rock and fluid-fluid interactions. Because of the complicated system of brine/rock/crude oil, many mechanisms may be active and interacting. For instance, fine migration is related to the limited release of mixed-wet clay particles and mineral dissolution. As a result of mineral dissolution, LS solution gains a higher viscosity. According to the theory of multi-ion exchange, divalent cations (e.g. Ca^{2+} and Mg^{2+}) absorbed on the rock surface can be replaced by hydrogen ions as a result of a local pH increase (Austad, 2013), which amplifies the release of fines and the decrease in the permeability (Valdya & Fogler, 1992). Besides, the increase in pH leads to the reduction of oil-water interfacial tension and spontaneous water-oil emulsification (J. Sheng, 2010). Moreover, the saline water with lower ion strength enhances the electrostatic repulsion and double layer expansion, which also brings out the increase in the thickness of the water film between the oil and

rock surface. This process can alter the wettability towards water-wet and help to stabilize water-oil emulsion droplets (Khilar & Fogler, 1984; Nasralla & Nasr-El-Din, 2014). Therefore, in general, the low-salinity effect may not be explained by one single mechanism.

1.2 Fluid-solid interaction in LSWF

For fluid-solid interactions, Schmatz, Urai, Berg, and Ott (2015) acquired nano-scale imaging of oil-water-rock contact using cryogenic broad ion-beam polishing in combination with scanning electron microscopy. They observed that the non-wetting hydrocarbon phase is commonly separated from the rock by a thin brine film with local pinning at geometric and chemical heterogeneities. As a result of this situation, the injection of low-salinity water into a formation containing high-salinity water can cause the expansion of such thin brine films due to ionic diffusion (Joekar-Niasar & Mahani, 2016). Mahani, Berg, Ilic, Bartels, and Joekar-Niasar (2015) observed the detachment of crude oil droplets from the clay deposited glass substrate and described the kinetics of the low-salinity effect. Later on, they simulated the ionic transport using the coupled model of Nernst-Planck and Poisson equations and analyzed dynamics of pressure field evolution inside thin brine films under the effect of ionic strength gradient. Recently, Aseyednezhad, Yan, Hassanizadeh, and Raoof (2022) simulated the same system but using a novel 1-dimensional model. Bartels et al. (2016) conducted a series of microfluidic experiments with single sinusoidal channel micro-models functionalized with clay particles and captured the de-wetting process during a tertiary low-salinity injection. They considered the formation and expansion of a high-salinity water film along the solid substrate as a pore-scale mechanism for the low-salinity effect. Moreover, core-flooding experiments using micro-CT tomography have proved that pore structure, the forms of residual oil patterns (e.g., types of isolated, cluster, network, and film) and even surfactant adsorption have significant effect on enhanced oil recovery during low-salinity injection (Belhaj et al., 2021; R. Song et al., 2020; Wei et al., 2020).

1.3 Fluid-fluid interaction in LSWF

Some researchers highlighted that the effect of salinity on the water-oil interactions, i.e., osmosis, micro-emulsions, interfacial viscoelasticity, and use of non-ionic surfactant, have been overlooked in these studies (Kar, Cho, & Firoozabadi, 2022; Mahzari & Sohrabi, 2014; Kristian Sandengen, Kristoffersen, Melhuus, & Jøsang, 2016b; Wu & Firoozabadi, 2021). Salinity may influence local water-oil interfacial properties and pressure, which ultimately affect oil ganglion dynamics, droplets coalescence and oil phase connectivity. Rücker et al. (2015) imaged the dynamic transient process of mobile oil ganglion induced by water film swelling by using X-ray computed microtomography. They found that mass transfer in the oil phase was accompanied by the meniscus oscillation and coalescence processes. Ayirala, Al-Yousef, Li, and Xu (2018) experimentally investigated the microscopic-scale water ion interactions occurring at the crude-oil/brine interface under various salinity conditions. They noticed that the addition of salts could promote the transfer of surface-active components in the crude oil from the bulk phase into the interface. The sulfates-only brine showed the highest viscous and elastic moduli for the interfacial layers, meaning that addition of salt could significantly change the dynamic interface viscosities.

Often, small influences induced by salinity concentration gradient and water-oil emulsions are ignored during low-salinity water flooding experiments in favour of other involved processes (Aldousary & Kovscek, 2019; Riehm et al., 2017; W. Song & Kovscek, 2019). However, these processes can significantly change the rock wettability and oil movement in a period of days. Although some researchers (Malik, Wani, & Hashim, 2012; Sørbo, 2016; Speight, 2006) studied small changes in contact angle of water/oil under different salinities, the time scale of water-oil emulsion and the osmotic gradient is not clear. Obviously, the contact time scale in reservoirs is much larger than an experimental period. For instance, the experimental period for pore-scale displacement and core flooding experiments is several minutes to hours, which may not be sufficiently large to observe the formation of water-oil emulsion and dynamic changes of the contact line.

1.4 Osmosis effects in LSWF

The mechanisms for liquid-liquid interactions including osmosis, reduced interfacial tension and emulsification are overlooked in the efficiency of the oil recovery by mobilizing stagnant oil and changing the system wettability (Mahzari & Sohrabi, 2014). The number of publications every year related to the topics of osmosis and emulsification as low salinity effects is displayed in Figure 1-2. After 2010, the study of each topic has increased rapidly. Nevertheless, few researchers have taken both effects into account to explain enhanced oil recovery from low salinity.

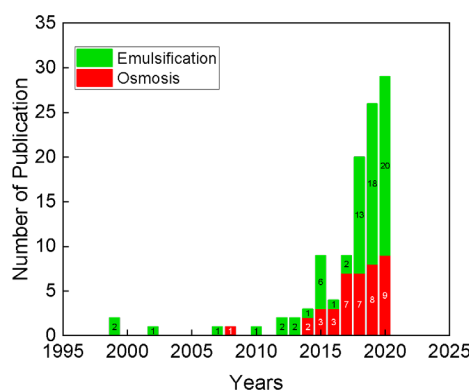


Figure 1-2: The number of publications from the 1990s to 2020 related to the low salinity effects of osmosis and emulsification.

Osmosis is a physical process as a result of salinity contrast, accompanying an osmotic water flux through a selectively permeable membrane. Hanshaw and Zen [23] discussed that osmotic pressure gradients can be responsible for anomalous high pressures in shale beds, which can lead to overthrust faulting of the shale. Young and Low [24] conducted a laboratory experiment using a clay compacted cell and demonstrated that the movement of solution through layers of clay is related to salt concentration difference and the corresponding hydraulic pressure. Marine and Fritz [25] proposed an osmotic model to explain anomalous hydraulic heads in the Dunbarton Triassic basin, with consideration of clay as a nonideal membrane that includes some solute components. Neuzil [26] pointed out that the magnitude of anomalous hydraulic heads depends primarily upon the solute concentration differences across the membrane, and the membrane properties such as porosity, permeability and rock surface charges. Fakcharoenphol,

Kurtoglu, Kazemi, Charoenwongsa, and Wu (2014) reported experimental and numerical modelling studies of osmotic pressure effect on oil recovery and conducted imbibition experiments using a laminated formation shale core to evaluate the potential of low-salinity waterflooding in Bakken. They proved that the chemical osmosis contributes to the withdrawal of crude oil from hydraulically stagnant pores that LSW cannot directly access. They compared the results from their mathematical model with the experimental data and indicated that osmotic pressure improves the counter-current flow of oil from both the water-wet and oil-wet segments of the core. Similarly, Takeda, et al. [28] performed chemical osmosis experiments with clay-bearing reservoir rocks and relevant simulations. Figure 1-3 shows the schematic of osmosis theory in a clay-rich porous media.

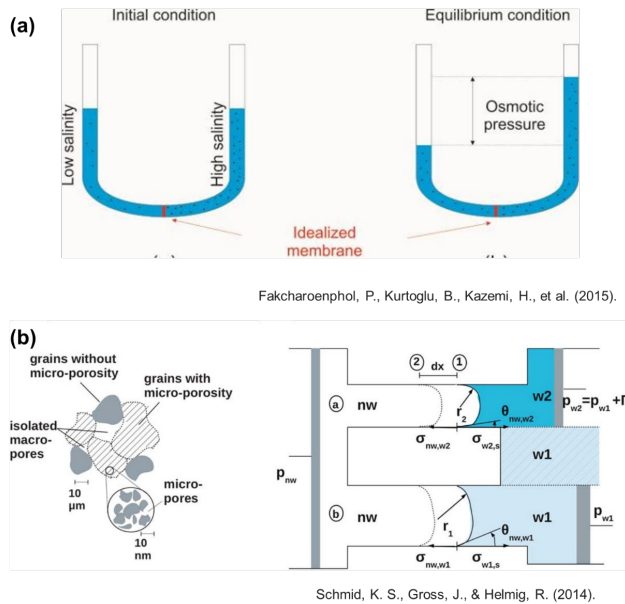


Figure 1-3: Schematic of osmosis theory. (a) shows an illustration of osmotic pressure from the initial condition and to equilibrium condition. Water molecules flow from low-salinity side of the clay idealized membrane to the high-salinity side to reach the salt concentration equilibrium. The difference of the hydraulic head is called osmotic pressure; (b) gives the illustrations of osmotic flow in the rocks containing dual-porosity, like shale and clay-rich rocks. Such rock comprises isolated macropores with the range of microns and microporous grains (slash-marked) with the range of nano-meters. The micropores act as geological membranes that persistently separate salinity contrasts in the wetting phase. The structure induces osmotic flow in the whole porous domain and consequent pressure difference.

Clay or micropores play as a semi-permeable membrane that allows water molecules to pass through, which consequently causes the pressure difference in the porous formation. Schmid, Gross, and Helmig (2014) extended the classical method of entry pressure for describing salinity-dependent capillary pressure and displacement events, as shown in Figure 1-3 (b). The micropores with two throat diameters are filled with a nonwetting (nw) phase and a wetting phase comprising two residual brines (w1 with low salinity and w2 with high salinity). Osmotic flow changes the capillary entry pressure and induces pore-invasion sequence, e.g., piston-like displacement and snap-off, depending on the local salt concentration. They have discussed the effect of osmosis on laboratory-scale quantities and concluded that the effect on multiphase flow in many cases is not distinguishable from a wetting change.

The mechanism of oil acting as a membrane for low-salinity water flooding is first proposed by K Sandengen and Arntzen (2013). They observed the movement of oil droplets under the influence of an osmotic gradient in a 1 mm diameter glass tube. Later on, they performed a capillary experiment to directly show the osmotic water transport through oil, Figure 1-4. Besides, quasi-2D microfluidic experiments for mimicking the tertiary mode of low-salinity water flooding were conducted as well (Kristian Sandengen, Kristoffersen, Melhuus, & Jøsang, 2016a). They noticed the expansion or contraction of the connate high-salinity water depending on the direction of imposed salinity gradient. Therefore, they concluded that the oil inside an oil-wet porous medium acts as a semipermeable membrane, which induces the relocation of residual oil and has the capability of yielding additional oil recovery.

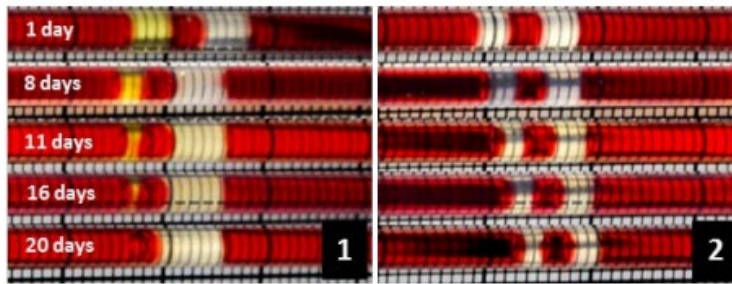


Figure 1-4: Images of osmosis transport through oil phase in oil-wet capillary tubes. Low-salinity water, high-salinity water and oil are shown in yellow, white and red, respectively. The right figure shows the baseline results containing high-salinity water only in capillary tube. Two tubes are monitored for 20 days. In the left figure, the yellow phase gradually shrinks as water is transported through the oil phase into the high-saline solution, while high-salinity water expands. However, the baseline result doesn't show the similar phenomenon. Slight shrinkage is caused by the water dissolution into crude oil.

Fredriksen, Rognmo, Sandengen, and Fernø (2017) investigated the osmosis effect on water transport through the oil phase (functioning as a semi-permeable membrane) from a low salinity solution towards a high salinity solution using capillary experiments, core-flooding experiments, and 2D micro-model experiments. They observed the trapped HSW water swelling in the long period of brine-oil contact under salinity contrasts and obvious oil remobilization during low-salinity water flooding. Crestel, Kvasničková, Santanach-Carreras, Bibette, and Bremond (2020) conducted microfluidic experiments in two systems, one with glass capillary and another with microfabricated cavities, for probing the oil motion on a solid substrate immersed in water. They observed the oil globule motion in confined systems and calculated the water flux induced by the theoretical osmotic pressure.

The results in literature indicated that osmosis could increase oil migration and had a positive effect on oil recovery during low salinity water flooding. In this paper we will consider the oil itself as a membrane for osmotic water transport.

1.5 Emulsification effects in LSWF

Regarding the micro-dispersion/emulsion process, Emadi and Sohrabi (2013) employed micro-models to observe interactions between crude oil and saline water. Spontaneous emulsification occurs when two immiscible liquids emulsify

without the aid of any external thermal or mechanical energy source until reaching a thermodynamically stable configuration with a minimum total system free energy (López-Montilla, Herrera-Morales, Pandey, & Shah, 2002). When the concentration of surfactants around the interface is beyond one critical concentration, also known as CMC (critical micelle concentration), the surfactant molecules can assemble the insoluble phase molecules and create the micelles in the soluble phase. In nature, some polar components, such as naphthenic acids, resins and asphaltenes, have the potential to act as active emulsifiers contributing to emulsion formation (Li et al., 2020). Water in oil (W/O) and oil in water (O/W) emulsions, even the water in oil in water (W/O/W) and the oil in water in oil emulsion (O/W/O) can be observed during the water flooding, however, the most familiar ones are the first two emulsions (Martínez-Palou et al., 2013). Surfactants are characterized by two functional groups, one hydrophilic and one hydrophobic. When water meets with crude oil, the surface-active components would adsorb onto the oil-water interface and each sides groups can find the greatest affinity to make the total free energy reaching minimum, which leads the spontaneous formation at nano- to pore-scale (Rodríguez-Hakim et al., 2020). A typical reverse micelle has a spherical shape with a size of $\sim 50\text{\AA}$ and is made of about 100 surfactant molecules (Goyal & Aswal, 2001). Numerous laboratory studies have provided the direct observation of emulsion generation when crude oil contacts with water in the process of water flooding. Figure 1-5 gives the observation spontaneous emulsification and the schematic of the process around water-oil interface. Wu and Firoozabadi (2021) imaged the spontaneous emulsification near the oil-aqueous phase interface and concluded that destabilization of water-in-oil emulsions in the bulk oil phase may improve the efficiency of oil displacement.

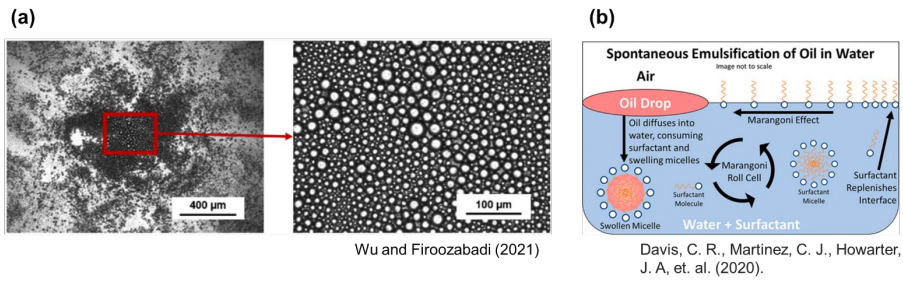


Figure 1-5: Spontaneous emulsification. (a), the micro-scale observation of spontaneous emulsification in the water-crude oil contact after 1 hour (Wu & Firoozabadi, 2021). The images were taken at the oil/deionized water interface at different magnifications after the oil is placed on the top of the aqueous phase. (b), a schematic of spontaneous emulsification at water-oil interface (Davis, Martinez, Howarter, & Erk, 2020). For water-soluble oils, once an oil droplet touches with emulsified-water, nanoscale emulsions formed spontaneously by diffusion of oil molecules into the aqueous surfactant solutions and subsequent swelling of surfactant micelles with oil. Marangoni flows were found to enhance spontaneity.

Emadi and Sohrabi (2013) observed that water micro-dispersions spontaneously formed at the water/oil interface within the crude oil phase during the low-salinity water flooding experiments in microfluidics, and the coalescence of micro-dispersion led to the swelling region of high salinity connate water that expelled residual oil from dead-end pores in the micromodel. They hypothesized that it could be considered as one mechanism for improved oil recovery. Du, Xu, Mejia, Zhu, and Balhoff (2019) reported a similar phenomenon in their microfluidic experiments and directly captured the dynamic process of water-in-oil emulsions formation that improved the oil sweep efficiency. Salehpour, Sakhaei, Salehinezhad, Mahani, and Riazi (2021) performed a series of static and dynamic micro-scale experiments to investigate the influence of fluid-fluid interactions on the fluid flow and oil recovery efficiency during low-salinity waterflooding. They directly captured the intensified spontaneous formation of W/O emulsions at the interface at a low flow rate. and the accompanying pressure fluctuation induced by emulsion division and rupture, see Figure 1-6 (a). They, therefore, believed that the emulsion formation leads to an additional contribution to enhanced oil recovery by LSWF.

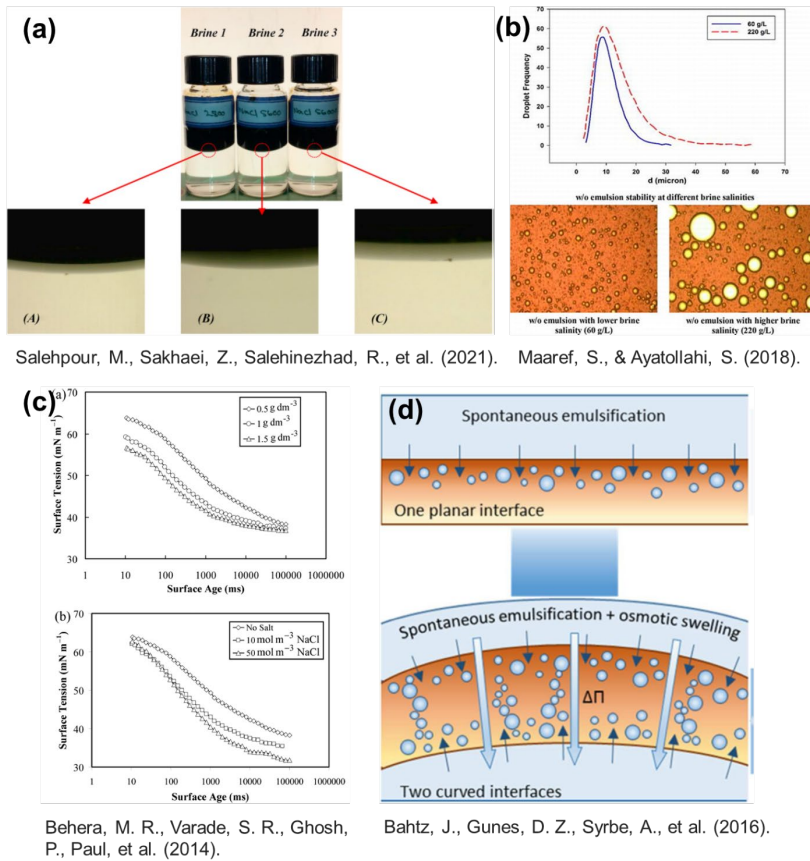


Figure 1-6: Salinity effect on the spontaneous emulsification. (a) shows direct observation of spontaneous emulsions at water-oil interface after crude oil contacting with various brines, 2800 ppm, 5600 ppm, and 56000 ppm salinity for 45 days (Salehpour et al., 2021); (b) shows two salt concentrations (60,000 ppm and 220,000 ppm) effect on the water-in-crude oil emulsion stability (Maaref & Ayatollahi, 2018); (c) shows the effects of surfactant and NaCl concentrations on the surface tension of water and oil (Behera, Varade, Ghosh, Paul, & Negi, 2014); (d) shows an osmotic imbalance between the two water phases of multiple water-in-oil-in-water (W1/O/W2) emulsions resulting in either emulsion swelling or shrinking due to water migration across the oil layer (Bahtz et al., 2016).

Some studies have shown the relationship between electrolyte concentration and emulsion size. Maaref and Ayatollahi (2018) prepared the samples of w/o emulsions with different sea water samples, which were synthesized to resemble Persian Gulf, Mediterranean, Red Sea, and North Sea water samples. They measured the emulsion size and gave log-normal function of emulsion droplet size distribution (Figure 1-6 c), which showed that the low-salinity condition had

more stable and uniform emulsions. Behera et al. (2014) studied the effects of surfactant, salt and oil concentrations on foaming in micellar solutions. They found that the initial foam volume generated in a blender test increased with increasing surfactant concentration but decreased with increasing salt concentration. Besides, the surface tension decreased with both of the increase in surfactant concentration and salt concentration, as shown in Figure 1-6 (c). Bahtz et al. (2016) pointed that controlled mass transport plays an important role for emulsion stability and transient emulsion thickening. They indicated two stages for water transport during spontaneous emulsification, see Figure 1-6 (d). In the first stage, the oil-phase structure was changed in a way that allows rapid, osmotically driven water transport in the second, osmotically dominated stage. These structural changes in the oil layer are strongly facilitated by the spontaneous formation of tiny water droplets in the oil phase, induced by the oil-soluble surfactant. Zabar, Nguyen, and Phan (2020) reported a similar phenomenon that increasing the concentration of NaCl from 0 to 5 M resulted in the spontaneous formation of smaller oil-in-water emulsions, while increasing the chain-length of the oil from C7 (n-heptane) to C16 (n-hexadecane) produced a decrease of 58.6 % in emulsion droplet diameter.

However, the descriptions of the dynamic emulsification and its quantitative effect on the water transport are not fully described yet. Even though the phenomenon of salt solution expansion may look like osmosis under a macroscale observation, whether the organic phase can be treated as a rigid membrane is still questionable and lacks solid evidence. How the water molecular behaves in the oil phase due to the salinity contrast is not quite clear. Thus, the quantitative analysis of the osmosis effect is still necessary to explain the phenomenon. Moreover, the descriptions of dynamic emulsification and its effect on water transport are not fully described yet.

1.6 Research objectives

In this study, the main aim is to investigate the fluid interface behavior under conditions of low ionic strength and attempt to get new insights into the mechanisms of the salinity differential effect and wettability alteration in low salinity water flooding. Three research directions have been studied: the impact of salinity contrast on oil remobilization from nano to micro-scale, the ion transport in thin aqueous film during wettability alteration, and the influence of

substrate wettability on the pore-filling event for two-phase flow. Overall, the main research questions will be focused on:

- (1) Can refined oil, under a salinity gradient condition, act as a semipermeable membrane without adding any surface-active components? And what is the main mechanism, osmosis theory or water solubility factors?*
- (2) With the presence of surfactants, what is the effect of emulsification on water transport in the oil phase? Can we gain fundamental insights into this aspect?*
- (3) In the process of aqueous film expansion on a rock surface, how do the electric potential and salt ion concentration profiles dynamically change? How to improve the existing model for a better understanding of electrochemical processes in electro-diffusion issues?*
- (4) Before and after LSWF, the wettability is altered and has the response to the multiphase displacement. What is a systematic and clear description of the wettability effect on the displacement in a single micro-channel and pore-filling?*

1.7 Thesis outline

These above-mentioned questions give rise to the different chapters of the thesis:

- In **Chapter 2**, 11 capillary tubes with an inner diameter of 800 μm are used to inject a sequence of low-salinity water, crude oil, and high-salinity water phases and to observe the evolution of the system. The monitoring was done for a period of 40 days. Two optical setups are used to dynamically capture the remobilization of oil globule and the 2D/3D contact interfaces. Moreover, microscopic pore pressures are directly measured at both low and high-salinity water phases containing the oil globule by two microscopic fiber-optic sensors. This chapter reaches insights on the potential mechanism of osmosis and proposes the hypothesis of emulsification and water diffusion through oil phase due to salinity contrast. It proves that the salinity differential can cause a micro-scale oil movement and pressure change inside fluids, which provides a further observation for the osmosis mechanism of LSWF.

- In **Chapter 3**, a series of microfluidic experiments are conducted using coated glass micro-chips for mimicking the low-salinity waterflooding process in an oil-wet rock formation. Contact between fluid phases included low-salinity water-alkane/high-salinity water in the porous micromodel, and the system was monitored for 70 hours. This chapter is a continuation of Chapter 2. Due to the complexity of crude oil used in the work of Chapter 2, it is difficult to quantify the individual effect of osmosis and emulsification on oil mobilization. Therefore, this chapter used pure alkanes and the alkanes with adding surfactants. The interfacial behavior influenced by the dynamic emulsification is also investigated at the nano to micro-scale. Moreover, to investigate the effect of salinity on water behavior in heptane, we conducted molecular dynamic (MD) simulations by considering three different concentrations in the high-salinity water region featuring our experiments. This chapter highlights the impact of salinity contrast on water region expansion and provides solid evidence of water transport through the oil phase.
- In **Chapter 4**, a 2D axisymmetric model is developed to investigate the ion transport within a film of water underlying an oil droplet, with negatively charged surfaces on its top and bottom boundaries. The film is initially filled with a high salinity electrolyte, and then it is exposed on lateral sides to a bulk fluid with lower salinity. In order to reduce the complexity and the computational effort, and averaged, one-dimensional, coupled Poisson-Nernst-Planck model is derived and developed to simulate electro-diffusion in the same system, which enhances the computational efficiency needed to simulate ion transport in charged media.
- In **Chapter 5**, the impact of substrate wettability is investigated in a polymer microfluidic experiment. The drainage and imbibition processes are performed with three displacement velocities for two-phase flow filling events in a single rectangular pore. The polymeric micro-model is designed with a depth of 100 μm and with one square pore body of 800 μm in width and length which is connected to 4,000 μm long inlet and outlet channels with a height of 150 μm . The models are rendered with three surface wettabilities of 60°, 95° and 120° static contact angle of a water droplet. This chapter investigates the interface behavior in a micro-

channel and a pore for all imbibition and drainage processes. Furthermore, a corresponding numerical simulation is conducted to predict the flow behavior and to track the two-phase interface.

- In **Chapter 6**, the main conclusions and recommendations for future work are presented.

References

- Abidoye, L. K., Khudaida, K. J., & Das, D. B. (2015). Geological carbon sequestration in the context of two-phase flow in porous media: a review. *Critical Reviews in Environmental Science and Technology*, 45(11), 1105-1147.
- Aldousary, S., & Kovscek, A. R. (2019). The diffusion of water through oil contributes to spontaneous emulsification during low salinity waterflooding. *Journal of Petroleum science and Engineering*, 179, 606-614.
- Alhuraishawy, A. K., Bai, B., Wei, M., Geng, J., & Pu, J. (2018). Mineral dissolution and fine migration effect on oil recovery factor by low-salinity water flooding in low-permeability sandstone reservoir. *Fuel*, 220, 898-907.
- Alshakhs, M. J., & Kovscek, A. R. (2016). Understanding the role of brine ionic composition on oil recovery by assessment of wettability from colloidal forces. *Advances in colloid and interface science*, 233, 126-138.
- Aseyednezhad, S., Yan, L., Hassanizadeh, S. M., & Raoof, A. (2022). An accurate reduced-dimension numerical model for evolution of electrical potential and ionic concentration distributions in a nano-scale thin aqueous film. *Advances in Water Resources*, 159, 104058.
- Aslannejad, H., Hassanizadeh, S., Raoof, A., de Winter, D., Tomozeiu, N., & Van Genuchten, M. T. (2017). Characterizing the hydraulic properties of paper coating layer using FIB-SEM tomography and 3D pore-scale modeling. *Chemical Engineering Science*, 160, 275-280.
- Austad, T. (2013). Water-based EOR in carbonates and sandstones: new chemical understanding of the EOR potential using “smart water”. In *Enhanced oil recovery Field case studies* (pp. 301-335): Elsevier.
- Ayirala, S. C., Al-Yousef, A. A., Li, Z., & Xu, Z. (2018). Water ion interactions at crude-oil/water interface and their implications for smart waterflooding in carbonates. *SPE Journal*, 23(05), 1817-1832.
- Bahtz, J., Gunes, D. Z., Syrbe, A., Mosca, N., Fischer, P., & Windhab, E. J. (2016). Quantification of spontaneous W/O emulsification and its impact on the swelling kinetics of multiple W/O/W emulsions. *Langmuir*, 32(23), 5787-5795.
- Bartels, W.-B., Mahani, H., Berg, S., Menezes, R., van der Hoeven, J., & Fadili, A. (2016). *Low salinity flooding (LSF) in sandstones at pore scale: micro-model development and investigation*. Paper presented at the SPE Annual Technical Conference and Exhibition.
- Bartley, J., & Ruth, D. (1999). Relative permeability analysis of tube bundle models. *Transport in Porous Media*, 36(2), 161-188.
- Behera, M. R., Varade, S. R., Ghosh, P., Paul, P., & Negi, A. S. (2014). Foaming in micellar solutions: Effects of surfactant, salt, and oil concentrations. *Industrial & Engineering Chemistry Research*, 53(48), 18497-18507.
- Belhaj, A. F., Elraies, K. A., Alnarabiji, M. S., Kareem, F. A. A., Shuhli, J. A., Mahmood, S. M., & Belhaj, H. (2021). Experimental investigation, binary modelling and artificial neural network prediction of surfactant adsorption for enhanced oil recovery application. *Chemical Engineering Journal*, 406, 127081.
- Berg, S., Cense, A., Jansen, E., & Bakker, K. (2010). Direct experimental evidence of wettability modification by low salinity. *Petrophysics-The SPWLA Journal of Formation Evaluation and Reservoir Description*, 51(05).
- Buckley, J., Liu, Y., & Monsterleet, S. (1998). Mechanisms of wetting alteration by crude oils. *SPE Journal*, 3(01), 54-61.
- Crestel, E., Kvasničková, A., Santanach-Carreras, E., Bibette, J., & Bremond, N. (2020). Motion of oil in water induced by osmosis in a confined system. *Physical Review Fluids*, 5(10), 104003.

- Davis, C. R., Martinez, C. J., Howarter, J. A., & Erk, K. A. (2020). Diffusion-Controlled Spontaneous Emulsification of Water-Soluble Oils via Micelle Swelling. *Langmuir*, 36(26), 7517-7527.
- Ding, H., & Rahman, S. (2017). Experimental and theoretical study of wettability alteration during low salinity water flooding-an state of the art review. *Colloids and Surfaces A: Physicochemical and Engineering Aspects*, 520, 622-639.
- Du, Y., Xu, K., Mejia, L., Zhu, P., & Balhoff, M. T. (2019). Microfluidic Investigation of Low-Salinity Effects During Oil Recovery: A No-Clay and Time-Dependent Mechanism. *SPE Journal*.
- Emadi, A., & Sohrabi, M. (2013). *Visual investigation of oil recovery by low salinity water injection: formation of water micro-dispersions and wettability alteration*. Paper presented at the SPE annual technical conference and exhibition.
- Fakcharoenphol, P., Kurtoglu, B., Kazemi, H., Charoenwongsa, S., & Wu, Y.-S. (2014). *The effect of osmotic pressure on improve oil recovery from fractured shale formations*. Paper presented at the SPE unconventional resources conference.
- Fathi, S. J., Austad, T., & Strand, S. (2010). "Smart water" as a wettability modifier in chalk: the effect of salinity and ionic composition. *Energy & fuels*, 24(4), 2514-2519.
- Fredriksen, S., Rognmo, A., Sandengen, K., & Fernø, M. (2017). Wettability effects on osmosis as an oil-mobilization mechanism during low-salinity waterflooding. *Petrophysics*, 58(01), 28-35.
- Garcia-Olvera, G., & Alvarado, V. (2017). Interfacial rheological insights of sulfate-enriched smart-water at low and high-salinity in carbonates. *Fuel*, 207, 402-412.
- Goyal, P., & Aswal, V. (2001). Micellar structure and inter-micelle interactions in micellar solutions: results of small angle neutron scattering studies. *CURRENT SCIENCE-BANGALORE*, 80(8), 972-979.
- Hui, M.-H., & Blunt, M. J. (2000). Effects of wettability on three-phase flow in porous media. *The Journal of Physical Chemistry B*, 104(16), 3833-3845.
- Jadhunandan, P., & Morrow, N. R. (1995). Effect of wettability on waterflood recovery for crude-oil/brine/rock systems. *SPE reservoir engineering*, 10(01), 40-46.
- Joekar-Niasar, V., & Mahani, H. (2016). Nonmonotonic pressure field induced by ionic diffusion in charged thin films. *Industrial & Engineering Chemistry Research*, 55(21), 6227-6235.
- Kar, T., Cho, H., & Firoozabadi, A. (2022). Assessment of low salinity waterflooding in carbonate cores: Interfacial viscoelasticity and tuning process efficiency by use of non-ionic surfactant. *Journal of colloid and interface science*, 607, 125-133.
- Karimi, M., Al-Maamari, R. S., Ayatollahi, S., & Mehranbod, N. (2016). Impact of sulfate ions on wettability alteration of oil-wet calcite in the absence and presence of cationic surfactant. *Energy & fuels*, 30(2), 819-829.
- Khilar, K. C., & Fogler, H. S. (1984). The existence of a critical salt concentration for particle release. *Journal of colloid and interface science*, 101(1), 214-224.
- Kokal, S., & Al-Kaabi, A. Enhanced oil recovery: challenges & opportunities.
- Lager, A., Webb, K. J., Black, C., Singleton, M., & Sorbie, K. S. (2008). Low salinity oil recovery-an experimental investigation I. *Petrophysics*, 49(01).
- Li, Z., Xu, D., Yuan, Y., Wu, H., Hou, J., Kang, W., & Bai, B. (2020). Advances of spontaneous emulsification and its important applications in enhanced oil recovery process. *Advances in colloid and interface science*, 277, 102119.
- Ligthelm, D. J., Gronsveld, J., Hofman, J., Brussee, N., Marcelis, F., & van der Linde, H. (2009). *Novel Waterflooding Strategy By Manipulation Of Injection Brine Composition*. Paper presented at the EUROPEC/EAGE conference and exhibition.
- López-Montilla, J. C., Herrera-Morales, P. E., Pandey, S., & Shah, D. O. (2002). Spontaneous emulsification: mechanisms, physicochemical aspects, modeling, and applications. *Journal of Dispersion Science and Technology*, 23(1-3), 219-268.

- Maaref, S., & Ayatollahi, S. (2018). The effect of brine salinity on water-in-oil emulsion stability through droplet size distribution analysis: A case study. *Journal of Dispersion Science and Technology*, 39(5), 721-733.
- Mahani, H., Berg, S., Ilıc, D., Bartels, W.-B., & Joekar-Niasar, V. (2015). Kinetics of low-salinity-flooding effect. *SPE Journal*, 20(01), 8-20.
- Mahani, H., Keya, A. L., Berg, S., Bartels, W.-B., Nasralla, R., & Rossen, W. R. (2015). Insights into the mechanism of wettability alteration by low-salinity flooding (LSF) in carbonates. *Energy & fuels*, 29(3), 1352-1367.
- Mahzari, P., & Sohrabi, M. (2014). *Crude oil/brine interactions and spontaneous formation of micro-dispersions in low salinity water injection*. Paper presented at the SPE improved oil recovery symposium.
- Malik, M. A., Wani, M. Y., & Hashim, M. A. (2012). Microemulsion method: A novel route to synthesize organic and inorganic nanomaterials: 1st Nano Update. *Arabian journal of Chemistry*, 5(4), 397-417.
- Martínez-Palou, R., Cerón-Camacho, R., Chávez, B., Vallejo, A. A., Villanueva-Negrete, D., Castellanos, J., . . . Aburto, J. (2013). Demulsification of heavy crude oil-in-water emulsions: A comparative study between microwave and thermal heating. *Fuel*, 113, 407-414.
- McGuire, P., Chatham, J., Paskvan, F., Sommer, D., & Carini, F. (2005). *Low salinity oil recovery: An exciting new EOR opportunity for Alaska's North Slope*. Paper presented at the SPE western regional meeting.
- Mokhtari, R., Ayatollahi, S., & Fatemi, M. (2019). Experimental investigation of the influence of fluid-fluid interactions on oil recovery during low salinity water flooding. *Journal of Petroleum science and Engineering*, 182, 106194.
- Morrow, N., & Buckley, J. (2011). Improved oil recovery by low-salinity waterflooding. *Journal of Petroleum Technology*, 63(05), 106-112.
- Nande, S. B., & Patwardhan, S. D. (2021). A review on low salinity waterflooding in carbonates: challenges and future perspective. *Journal of Petroleum Exploration and Production Technology*, 1-19.
- Nasralla, R. A., & Nasr-El-Din, H. A. (2014). Double-layer expansion: is it a primary mechanism of improved oil recovery by low-salinity waterflooding? *SPE Reservoir Evaluation & Engineering*, 17(01), 49-59.
- Riehm, D. A., Rokke, D. J., Paul, P. G., Lee, H. S., Vizanko, B. S., & McCormick, A. V. (2017). Dispersion of oil into water using lecithin-Tween 80 blends: The role of spontaneous emulsification. *Journal of colloid and interface science*, 487, 52-59.
- Rodríguez-Hakim, M., Anand, S., Tajuelo, J., Yao, Z., Kannan, A., & Fuller, G. G. (2020). Asphaltene-induced spontaneous emulsification: Effects of interfacial co-adsorption and viscoelasticity. *Journal of Rheology*, 64(4), 799-816.
- Rücker, M., Berg, S., Armstrong, R., Georgiadis, A., Ott, H., Schwing, A., . . . Leu, L. (2015). From connected pathway flow to ganglion dynamics. *Geophysical research letters*, 42(10), 3888-3894.
- Salehpour, M., Sakhaei, Z., Salehinezhad, R., Mahani, H., & Riazi, M. (2021). Contribution of water-in-oil emulsion formation and pressure fluctuations to low salinity waterflooding of asphaltic oils: A pore-scale perspective. *Journal of Petroleum science and Engineering*, 203, 108597.
- Sandengen, K., & Arntzen, O. (2013). *Osmosis during low salinity water flooding*. Paper presented at the IOR 2013-17th European Symposium on Improved Oil Recovery.
- Sandengen, K., Kristoffersen, A., Melhuus, K., & Jøsang, L. O. (2016a). Osmosis as mechanism for low-salinity enhanced oil recovery. *SPE Journal*, 21(04), 1227-1235.
- Sandengen, K., Kristoffersen, A., Melhuus, K., & Jøsang, L. O. (2016b). Osmosis as mechanism for low-salinity enhanced oil recovery. *SPE Journal*, 21(04), 1,227-221,235.
- Scheidegger, A. E. (1954). Statistical hydrodynamics in porous media. *Journal of Applied Physics*, 25(8), 994-1001.

- Schmatz, J., Urai, J. L., Berg, S., & Ott, H. (2015). Nanoscale imaging of pore - scale fluid - fluid - solid contacts in sandstone. *Geophysical research letters*, 42(7), 2189-2195.
- Schmid, K., Gross, J., & Helmig, R. (2014). Chemical osmosis in two - phase flow and salinity - dependent capillary pressures in rocks with microporosity. *Water Resources Research*, 50(2), 763-789.
- Sharma, M., & Filoco, P. (2000). Effect of brine salinity and crude-oil properties on oil recovery and residual saturations. *SPE Journal*, 5(03), 293-300.
- Sheng, J. (2010). *Modern chemical enhanced oil recovery: theory and practice*: Gulf Professional Publishing.
- Sheng, J. J. (2014). Critical review of low-salinity waterflooding. *Journal of Petroleum science and Engineering*, 120, 216-224.
- Singh, K., Menke, H., Andrew, M., Lin, Q., Rau, C., Blunt, M. J., & Bijeljic, B. (2017). Dynamics of snap-off and pore-filling events during two-phase fluid flow in permeable media. *Scientific reports*, 7(1), 1-13.
- Song, R., Peng, J., Sun, S., Wang, Y., Cui, M., & Liu, J. (2020). Visualized experiments on residual oil classification and its influencing factors in waterflooding using micro-computed tomography. *Journal of Energy Resources Technology*, 142(8), 083003.
- Song, W., & Kovscek, A. R. (2019). Spontaneous clay Pickering emulsification. *Colloids and Surfaces A: Physicochemical and Engineering Aspects*, 577, 158-166.
- Sørbo, I. G. (2016). *Polar Components in Crude Oils and Their Correlation to Physiochemical Properties*. The University of Bergen,
- Speight, J. G. (2006). *The chemistry and technology of petroleum*: CRC press.
- Strand, S., Høgenesen, E. J., & Austad, T. (2006). Wettability alteration of carbonates—Effects of potential determining ions (Ca²⁺ and SO₄²⁻) and temperature. *Colloids and Surfaces A: Physicochemical and Engineering Aspects*, 275(1-3), 1-10.
- Tang, G.-Q., & Morrow, N. R. (1999). Influence of brine composition and fines migration on crude oil/brine/rock interactions and oil recovery. *Journal of Petroleum science and Engineering*, 24(2-4), 99-111.
- Tang, G., & Morrow, N. R. (1997). Salinity, temperature, oil composition, and oil recovery by waterflooding. *SPE reservoir engineering*, 12(04), 269-276.
- Tetteh, J. T., Brady, P. V., & Ghahfarokhi, R. B. (2020). Review of low salinity waterflooding in carbonate rocks: mechanisms, investigation techniques, and future directions. *Advances in colloid and interface science*, 284, 102253.
- Tetteh, J. T., Veisi, M., Brady, P. V., & Barati Ghahfarokhi, R. (2020). Surface reactivity analysis of the crude oil–brine–limestone interface for a comprehensive understanding of the low-salinity waterflooding mechanism. *Energy & fuels*, 34(3), 2739-2756.
- Thyne, G., & Gamage, P. (2011). *Evaluation of the effect of low salinity waterflooding for 26 fields in Wyoming*. Paper presented at the SPE Annual Technical Conference and Exhibition.
- Valdya, R., & Fogler, H. (1992). Fines migration and formation damage: influence of pH and ion exchange. *SPE production engineering*, 7(04), 325-330.
- Vledder, P., Fonseca, J. C., Wells, T., Gonzalez, I., & Ligthelm, D. (2010). *Low salinity water flooding: proof of wettability alteration on a field wide scale*. Paper presented at the SPE Improved Oil Recovery Symposium.
- Wang, Y., Basu, S., & Wang, C.-Y. (2008). Modeling two-phase flow in PEM fuel cell channels. *Journal of Power Sources*, 179(2), 603-617.
- Wei, B., Zhang, X., Liu, J., Xu, X., Pu, W., & Bai, M. (2020). Adsorptive behaviors of supercritical CO₂ in tight porous media and triggered chemical reactions with rock minerals during CO₂-EOR and-sequestration. *Chemical Engineering Journal*, 381, 122577.
- Wood, D. A., & Yuan, B. (2018). Low-Salinity Water Flooding: From Novel to Mature Technology. In *Formation Damage During Improved Oil Recovery* (pp. 21-67): Elsevier.
- Wu, T., & Firoozabadi, A. (2021). Surfactant-Enhanced Spontaneous Emulsification Near the Crude Oil–Water Interface. *Langmuir*, 37(15), 4736-4743.

- Yuster, S. (1951). *Theoretical considerations of multiphase flow in idealized capillary systems*. Paper presented at the 3rd World Petroleum Congress.
- Zabar, M. K., Nguyen, C. V., & Phan, C. M. (2020). Quantifying the influence of salinity on spontaneous emulsification of hydrocarbons. *Colloids and Surfaces A: Physicochemical and Engineering Aspects*, 588, 124376.
- Zhang, P., Tveheyo, M. T., & Austad, T. (2007). Wettability alteration and improved oil recovery by spontaneous imbibition of seawater into chalk: Impact of the potential determining ions Ca^{2+} , Mg^{2+} , and SO_4^{2-} . *Colloids and Surfaces A: Physicochemical and Engineering Aspects*, 301(1-3), 199-208.
- Zhang, Y., & Morrow, N. R. (2006). *Comparison of secondary and tertiary recovery with change in injection brine composition for crude-oil/sandstone combinations*. Paper presented at the SPE/DOE symposium on improved oil recovery.
- Zhang, Y., Xie, X., & Morrow, N. R. (2007). *Waterflood performance by injection of brine with different salinity for reservoir cores*. Paper presented at the SPE annual technical conference and exhibition.
- Zhou, D., & Blunt, M. (1997). Effect of spreading coefficient on the distribution of light non-aqueous phase liquid in the subsurface. *Journal of Contaminant Hydrology*, 25(1-2), 1-19.

Chapter 2

Impact of water salinity differential on a crude oil droplet constrained in a capillary

Published as:

Yan, Lifei, Hamed Aslannejad, S. Majid Hassanizadeh, and Amir Raoof. "Impact of water salinity differential on a crude oil droplet constrained in a capillary: Pore-scale mechanisms." *Fuel* 274 (2020): 117798.

Abstract

Numerous experimental observations and field applications have confirmed that low-salinity water flooding is an effective technique for enhanced oil recovery. Given the complex physical and chemical processes, several controlling mechanisms have been proposed to explain the oil remobilization due to low-salinity effects. Osmosis and water-in-oil emulsification are among these mechanisms. However, our knowledge of these processes is limited, and their associated time scales are not well understood.

In this chapter, 11 capillary tubes with an inner diameter of 800 μm are used to inject a sequence of low-salinity water, crude oil, and high-salinity water phases and to observe the evolution of the system. The monitoring was done for a period of 40 days. We used two setups, based on imaging using a CMOS camera and a confocal laser scanning microscopy, to dynamically capture the remobilization of oil globule and the 2D/3D contact interfaces, respectively. Moreover, microscopic pore pressures were directly measured at both low and high-salinity water phases containing the oil globule by two microscopic fibre-optic sensors.

We observed that in the water-wet capillaries the oil globule moved a distance of about 524 μm . The contact angles at both low and high-salinity water interfaces with crude oil gradually decreased by 34.32° and 18.23° , respectively, during the first 15 days. We found that the pressure difference between high/low-salinity water phases reached a plateau with a maximum value of 1.65kPa during a period of 24 days. Further, we propose the hypothesis about emulsification and water diffusion through oil phase.

As mentioned in the Chapter 1, although several lab tests and field applications proved the potential and efficiency of LSWF, the underlying mechanisms are still very controversial. The saline water with lower ion strength enhances the electrostatic repulsion and double layer expansion, which also brings out the increase in the thickness of the water film between oil and rock surface. This process can alter the wettability towards water-wet and help to stabilize water-oil emulsion droplets (Khilar & Fogler, 1984; Nasralla & Nasr-El-Din, 2014). Therefore, in general, the low-salinity effect may not be explained by one single mechanism.

2.1 Salinity effect on emulsification in crude oil

To evaluate the contribution in this key aspect at the pore-scale, two aspects need attention: i) emulsion generation and water diffusion in an oil phase, and ii) the effect of water-oil emulsion and chemical osmotic gradient on the movement of the oil phase. In the following, we discuss these two aspects.

i) Emulsion generation and water diffusion in oil phase: in the application of low-salinity water flooding in a field, the water/oil emulsification and water micro-dispersion in oil are generally considered important contributors to boosting oil recovery ((Evdokimov, Fesan, Kronin, & Losev, 2016),(Riehm et al., 2017)). In the environment with low ion strength, due to double layer expansion, more emulsifiers such as surfactants and clay particles are formed causing oil release or its detachment from solid surfaces ((Song & Kovscek, 2019),(Aldousary & Kovscek, 2019)). When the crude oil is in contact with water, the polar components in the crude oil, such as naphthenic acids, resins and asphaltenes, are adsorbed at the phase interface which could bond with water molecules and produce water-in-oil emulsions ((Speight, 2014),(Sørbo, 2016)). The polar portion, OH-, attracts water molecules through hydrogen bonding to form a hydrophilic head (water-like) toward the aqueous phase. The non-polar portion is a hydrophobic tail (oil-like) orientating toward oil phase ((Malik, Wani, & Hashim, 2012)). Consequently, a water-in-oil reverse micelle is formed (Figure 2-1). A typical reverse micelle has a spherical shape with a size of $\sim 50\text{\AA}$ and is made of about 100 surfactant molecules ((Goyal & Aswal, 2001)).

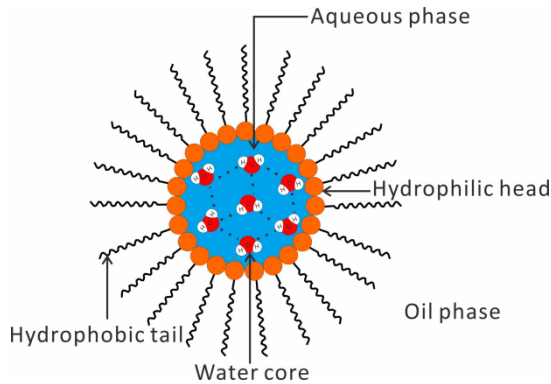


Figure 2-1: Schematic diagram of a water-in-oil reverse micelle. The natural surfactant in crude oil typically has hydrophilic groups (i.e., its head, shown by orange color) and hydrophobic groups (i.e., its tail, shown black color), meaning it contains both a water-soluble and oil-soluble component. In nonpolar phase, upon the introduction of water, the hydrophobic groups are attached to the water molecules by a hydrogen-oxygen bond to reduce the free energy of the system. When the water concentration increases in the system, the surfactant molecules start to aggregate into nanoscopic water-in-oil reverse micelles so that the polar heads encapsulate the water core while the hydrophobic tails extend into the nonpolar phase.

Miller (1988) discussed the water-in-oil spontaneous emulsification by diffusion in a ternary system consisting of water, a hydrocarbon, and a surfactant (Miller, 1988). Diffusion could lead to emulsification resulting in a region of local supersaturation for reaching an equilibrium state when aqueous and oleic phases with a surfactant are brought into contact with each other. Emadi and Sohrabi (2013), using magnified images, observed that water micro-droplets formed in the crude oil phase close to the interface (Emadi & Sohrabi, 2013). They hypothesized that micro-dispersion of water, due to low-salinity water injection, was responsible for oil recovery. Evidence in the literature shows that low-salinity water can accelerate the formation of water-in-oil emulsion and can increase the water content of the oil ((Mazara & Sohrabi, 2014), (Rostami, Mehraban, Sharifi, Dejam, & Ayatollahi, 2019)). Aldousary and Kovscek (2019) described that water hydrated ions can dissolve within the crude oil to reach the equilibrium condition (Aldousary & Kovscek, 2019). The solubility limit not only depends on crude oil type but also on brine salinity. As time passes, progressively more reverse micelles generate nearby interfaces to drive spontaneous emulsification ((Evdokimov et al., 2016), (Umar, Saaid, Sulaimon, & Pilus, 2018)).

Mokhtari and Ayatollahi (2019) determined that salinity can significantly affect the physical properties of oil phase around the water-oil interface (e.g., its pH, viscosity and density). In their experiments, they found a large number of emulsions after water and crude oil were in contact for a period of 45 days ((Mokhtari & Ayatollahi, 2019)). For the contact with lower salinity water (10 times diluted seawater), the dissolution of naphthenic acid in water and the formation of water-in-oil emulsion both increased, which caused a decrease of aqueous phase conductivity and pH by 22% and 6%, respectively. Meanwhile, microscopy imaging showed that water content in oil phase was 3.950 g/L, which was higher by 1.97% compared to its value for oil in contact with undiluted seawater. Additionally, the interface showed a rag-shaped form due to the emulsion formation and asphaltene agglomerates, and a nearby increase in crude oil density.

To better explain the relationship between water content and brine salinity, we have plotted the relationship between brine salinity and water content in oil in Figure 2-2, based on data from three studies listed in Table 2-1.

Table 2-1: The property of different salinity brine and water content extracted from three works

Brine type	Salinity (ppm)	Ion strength	Water content (wt%)	Data source
Formation water	189,682	3.674	1.32	2019-Mokhtari and Ayatollahi(Mokhtari & Ayatollahi, 2019)
Sea water	41,659	0.832	1.97	
2X diluted sea water	20,833	0.416	0.66	
10X diluted sea water	4,162	0.0832	3.95	
Synthetic brine (NaCl and CaCl ₂)	2,000	-	7.34	2014-Mahzari and Sohrabi(Mahzari, Sohrabi, Cooke, & Carnegie, 2018)
Deionized water	0	0	6.92	2019-Aldousary and Kovscek(Aldousary & Kovscek, 2019)

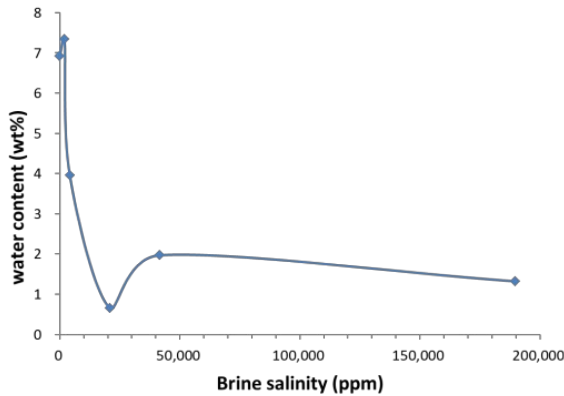


Figure 2-2: The relationship between brine salinity and water content in oil. The graph is generated based on the data in Table 2-1.

As shown in Figure 2-2, in general, water-content in oil decreases with the increase of salinity, however, may have a non-monotonic behaviour. Up to a salinity of about 6,600 ppm, the water content decreases sharply from 7.34% to 0.66% with the increase of salinity. As the salinity increases up to about 40,000 ppm, water content increases to about 2% and then remains almost constant with a slight decrease. It is indeed known that, in a low-salinity water environment, when the salinity is less than a threshold value, there is higher water content in oil phase ((Chakravarty, Fosbøl, & Thomsen, 2015), (Mokhtari & Ayatollahi, 2019)).

Alternatively, the interfacial tension (IFT) gradually increases with the increase of salinity ((Wei et al., 2017), (Hua et al., 2016), (Ayirala, Al-Yousef, Li, & Xu, 2018), (Binks & Horozov, 2006), (Mokhtari & Ayatollahi, 2019)). Rostami (2019) performed micro-model experiments and found the oil-water interface with two times diluted formation water had the largest number of asphaltene particles, and the interfacial tension was lowest compared to the results with higher water salinities (Rostami et al., 2019). When slightly increasing water salinity, e.g., adding a small amount of salt to pure water, the ions tend to interact with the polar components, and this causes IFT to decrease and reach a minimum value at a given threshold salt concentration. At higher salt concentrations, more ions accumulate at the oil-water interface and the polar compounds in the oil phase become less ionized with a lower tendency to move into the oil-water interface, remaining the system with a high interfacial tension.

ii) The effect of water-oil emulsion and chemical osmotic gradient on the movement of the oil phase: considering a single pore occupied by a sequence of LSW, crude oil, and HSW, the water content within the oil phase near the LSW-oil interface is higher than, on the other side, near the HSW-oil because of emulsion formation (Aldousary & Kovscek, 2019). The crude oil coming from the formation has reached the equilibrium with formation brine over extensive time and contains salt dissolved in the form of dispersed small water droplets (Du, Xu, Mejia, Zhu, & Balhoff, 2019). The crude oil may even contain crystalline salt formed by pressure and temperature changes during production (Yang et al., 2019). To explain the osmosis effect on oil remobilization, some researchers ((Wen & Papadopoulos, 2001), (Sandengen, Kristoffersen, Melhuus, & Jøsang, 2016), (S. B. Fredriksen, Rognmo, & Fernø, 2018)) suggest water transfer in oil from LSW to HSW contacts due to diffusion of water molecules and water-in-oil reverse micelle driven by the osmotic pressure generated by salinity difference of crude oil and LSW/HSW. However, some studies ((Emadi & Sohrabi, 2013), (Mahzari & Sohrabi, 2014)) hypothesized that the micro-dispersion of water into oil and its coalescence can cause swelling of high-salinity water side, which leads to an increase in the pressure of HSW side. The generated pressure can remobilize the trapped oil globule. Therefore, the implication of water diffusion/dispersions in oil phase is still not clear and the origin of pressure changes in the LSW-oil-HSW system are not well understood.

In order to explore the effect of water salinity, three questions should be addressed: i) how does the osmotic pressure affect oil remobilization in an LSW/Crude oil/HSW system? ii) What is the mechanism for the generation of osmotic pressure and what is its magnitude? iii) how do the contact angles of LSW and HSW interfaces change due to oil remobilization over longer time periods?

In this study, to answer these questions, we prepared a number of sealed capillaries containing an LSW/Crude oil/HSW arrangement, which is similar to the situation shown in Figure 2-3. Thus, we injected LSW, crude oil, and HSW in series into a capillary and monitored it for an extended period. We used a CCD camera, a confocal microscope, and pressure sensors to continuously monitor the oil globule movement, changes in contact angles of LSW/HSW interfaces, and pressure in LSW/HSW phases, respectively.

2.2 The hypothesis of water transport in oil phase

2.2.1 Formation of water-in-oil micro-emulsion

Studies have shown that different salt concentrations lead to different water contents in oil phase, due to the formation of water-in-oil micro-droplets, when water and crude oil are brought to contact with each other ((Mahzari & Sohrabi, 2014), (Aldousary & Kovscek, 2019)). This process is a function of the water salinity. Figure 2-3 illustrates the link between the formation of water-in-oil emulsion and salinity. There are two situations in the illustrations (Figure 2-3 a and b): one with the contacts of deionized water (DIW)/crude oil/HSW, and the other with the contacts of LSW/crude oil/HSW. In the case of the contact between DIW and crude oil, the situation is shown on the left side of Figure 2-3a. As soon as oil meets deionized water, water molecules enter the oil phase and surface-active compounds (surfactants) near the oil-water interface start to combine with water molecules within oil and get rearrangement of their distribution in response to the present electrostatic attractions. The hydrophilic head is attracted toward a water molecule and the non-polar portion points toward oil molecules (Goyal & Aswal, 2001). The surfactants occupy surface sites, allowing more water to pass through the interface which may form water-in-oil emulsions nearby. The second situation is shown in Figure 2-3b. For water having the threshold salt concentration (the lowest IFT), in the left part of Figure 2-3b, some water molecules combine with ions, such as Na^+ , Cl^- , Ca^{2+} , SO_4^{2-} , to form an aqueous solution, which dominates the interface polarization effect. The ionic strength of LSW results in an increase in the adsorption of polar compounds at the interface. The accumulation of them leads to the lower interfacial tension. Meanwhile, the absorbed polar compounds start to take more surface sites instead of formed water-in-oil emulsions. Some generated reverse micelles may detach from interface and pass through the oil phase ((Emadi & Sohrabi, 2013), (Chávez-Miyauchi, Firoozabadi, & Fuller, 2016)). Afterwards, the interface becomes a relatively complex system, including water-oil emulsions, water-encapsulated ions-oil emulsions, and dispersed anions and cations. For a high-salinity environment, shown in the right part of Figure 2-3 a and b, the Debye length is much smaller, and this reduces the adhesion of polar components to the interface. Moreover, ions accumulate at the oil-brine interface and decrease the charge screening. Therefore, less oil-water emulsification occurs, and the interfacial

tension increases comparing to the low-salinity ambient (Chakravarty et al., 2015).

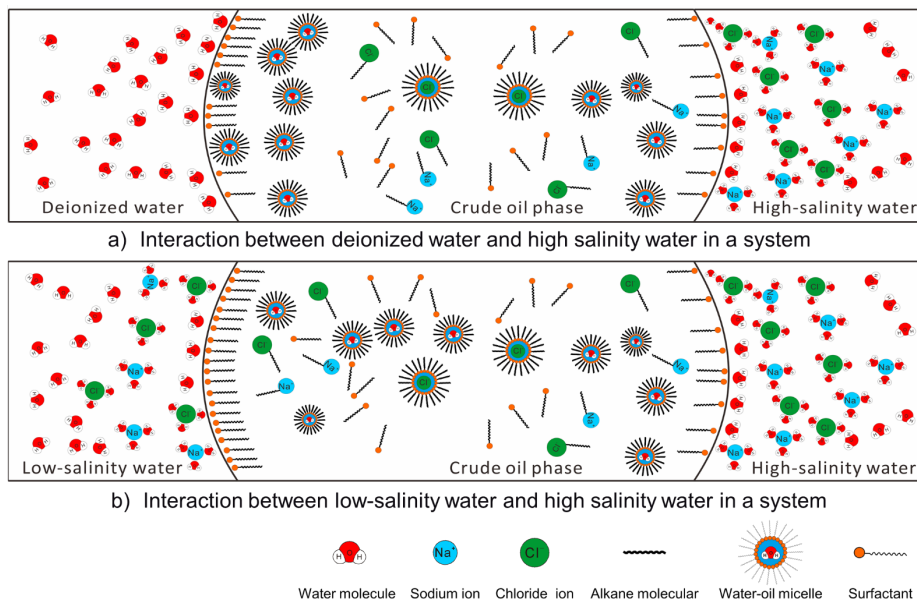


Figure 2-3: The schematic diagram of interactions between crude oil and deionized water, low-salinity water, and high-salinity water phases. The crude oil phase is considered to have been in equilibrium with brine. Salt ions form complexes with positively and negatively charged organic compounds in oil. Water not only diffuses molecularly in oil but also exists as reverse micelles. When deionized water (shown in the left part of Figure 2-3a) is brought into contact with equilibrated crude oil, the surfactants attract water molecules and aggregate them into reverse micelles, reducing the surface tension. With the increase in water concentration in oil, the formation of reverse micelles gets accelerated. In the case of LSW environment (the left part of Figure 2-3b), the salt ions cause the polarization of the interface, which can adsorb more polar compounds on the oil-water interface. The accumulation of polar compounds makes some reverse micelles away from interface. In the case of HSW environment, in the right part of plots 3a and 3b, the surface free energy increases due to the shorter Debye length. It results in the reduction of reverse micelle formation and makes surfactant stable around the interface.

2.2.2 Water transport in oil phase

After the generation of water-oil emulsions, due to the difference in salinity between LSW and crude oil, that is equilibrated with formation water, reverse micelles, as well as water molecules, can diffuse through the oil phase by osmotic

pressure. The diffusion of water molecules can be described by Fick's equation ((Davies & Wiggill, 1960)):

$$\frac{\partial c}{\partial t} = D \frac{\partial^2 c}{\partial x^2} \quad [2.1]$$

where c is the concentration in the oil phase, t is time, D is the diffusion coefficient of ion in oil, and x is the distance in the direction of diffusion. Aldousary and Kovsky (2019) pointed out that the diffusion coefficient of water molecules in oil is two orders of magnitude higher than that of hydrated ions. It means that the diffusion of hydrated ions in crude oil may be negligible.

The diffusion coefficient can be approximated by the Stokes-Einstein equation (Cheng et al., 2007).

$$D = \frac{k_B T}{6\pi\eta r} \quad [2.2]$$

where η is the dynamic viscosity, k_B is Boltzmann's constant, T is the absolute temperature, and r is the radius of the reverse micelle.

The diffusion time scale is $t_d = L^2/D$, where L is the oil phase thickness. For example, in our study, the dynamic viscosity of crude oil is 6.55×10^{-3} Pa·s, the radius is 50 Å, and the length of oil phase is 1cm. As mentioned above so, the diffusion coefficient of a water reverse micelle would be around 6.56×10^{-11} m²/s and the estimated time for it to pass through oil phase is about 18 days.

Since the crude oil contains salty water initially dispersed in crude oil, we hypothesize that the chemical osmosis could occur when the crude oil is brought into contact with pure water or low-salinity water. If we assume the oil as an ideal semi-permeable membrane, which only allows water molecules to pass through, the osmotic pressure can be described by Marine and Fritz (1981) with the derivation of the van 't Hoff formula.

$$\Pi = \frac{RT}{V} \ln \left(\frac{a_1}{a_2} \right) \quad [2.3]$$

where Π is osmotic pressure, R is gas constant, V is the partial molar volume of solvent, a_1 and a_2 are an activity of water in low-salinity water and high-salinity water, respectively. Currently, the osmotic pressure for saline water in oil semi-

membrane is not known so it is difficult to calculate an accurate value of osmotic pressure.

2.3 Experimental methods

2.3.1 Preparation of glass capillary and fluids property

We used 11 capillaries with an inner diameter of $800 \pm 3 \mu\text{m}$ and length of $100 \pm 0.20 \text{ mm}$ made of borosilicate glass 3.3 (Hirschmann Laborgeräte GmbH & Co.). These capillaries were classified into two groups based on the capillary inner surface properties: water-wet (with a water contact angle $< 90^\circ$) and oil-wet (with a water contact angle $> 90^\circ$). The water-wet capillaries include No.1a-No.3b as well as No.6a and 6b, which have the original wettability of the glass (i.e., water wet). The oil-wet ones include No.4, No.5a and No.5b treated by salinization using trichloro- (1H,1H,2H,2H-perfluorooctyl) silane.

All capillaries were cleaned several times using deionized water and ethanol ($\geq 96\%$ (v/v) purchased from VWR International). After cleaning and air drying, three liquids were consecutively injected by a syringe pump (Harvard Apparatus 1 Pico Plus Elite Programmable Syringe Pump) into capillaries in the order of i) low-salinity water, ii) crude oil, and iii) high-salinity water. The low-salinity water was a 10,000 ppm NaCl solution obtained by dissolving sodium chloride powder (purchased from Sigma-Aldrich) in deionized water. High-salinity water was a 100,000 ppm NaCl solution. The properties of crude oil are listed in Table 2-2.

Table 2-2: Properties of the crude oil, including saturated, Aromatic, Resin and Asphaltene (SARA) components, density, and viscosity at 20°C .

Content	wt%
Saturates	45.4
Aromatics	42.19
Resin	12.28
Asphaltenes	0.13
Residual	0.99
Total Acid Number (TAN)	0.77 mg KOH/g
Density (g/cm^3)	0.9
Viscosity ($\text{mPa}\cdot\text{s}$)	6.55

The capillaries were divided into 6 sets based on the sequence of fluid injections (determining the contact of glass capillary with different phases during the short injection period) and surface wettability (being water-wet or oil-wet). Each set had 2 capillaries as replicates (except experiment No.4 because the replicate capillary for No.4 was broken during the experiment). The injection flow rate was $2\mu\text{L}/\text{min}$ controlled by a syringe pump. The injection direction for each capillary is shown in Figure 2-4 by blue color arrows. Capillaries No.1a and No.1b were filled with half crude oil and half saline water as benchmark samples. Capillaries No.2a to No.3b were all filled with a sequence of LSW/Crude oil/HSW, however, as shown by blue arrows, filled from opposite ends of the capillary to consider the effect of possible wettability changes induced by injection sequence. No.4 to No.5b were filled in a similar order but capillaries were oil-wet. No.6a was firstly injected with a little amount of crude oil and then with LSW/Crude oil/HSW, which was also used to explore possible wettability effects due to the injection phase. To get insight into the behaviour of the system and collect complementary information, capillary No.6b was the reference capillary with LSW-crude oil-LSW (i.e., same water salinities on both sides of the oil phase). After preparation, the capillaries were sealed with Norland Optical Adhesive 81 (NOA81), which was cured by ultraviolet light into a hard polymer. Finally, the capillaries were fixed on a holding frame and placed on a board and monitored by a camera for 40 days at 21°C . During the observation period, we carefully transported the plate with capillaries from the camera set-up to the confocal set-up for taking 2D and 3D images of fluid interfaces in a time interval of two days.

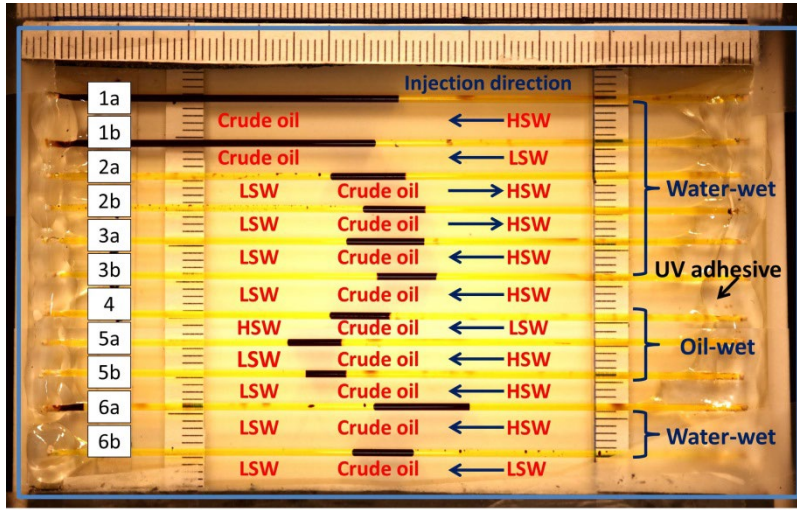


Figure 2-4: The picture of six sets of capillaries with different processing situations. Each set has two capillaries as replicates (except No.4). The experiment number for each capillary is given on the left side of the figure. Types and injection directions of fluids (crude oil in black, brine in yellow) are marked with dark blue color and arrows, respectively, under each capillary. The capillary inner surface wettability is provided on the right side of the figure. The top 6 and bottom 2 capillaries have the same water-wet wettability as borosilicate glass. No.4 to No.5b were treated with silane to become hydrophobic. We sealed all capillary ends using transparent UV adhesive (black arrow) and fixed them on a frame (blue rectangular).

2.3.2 Microscopy observation set-up

CMOS camera set-up

In order to capture the oil globule movement, we used a Canon 5D camera with EF 180 mm f/3.5L Macro USM lens shown in Figure 2-5. The set-up consisted of a CMOS camera, a vertical board, an LED light source, and a laptop. All capillaries were put on a board in front of the LED light. We set the camera to take one photo per hour.

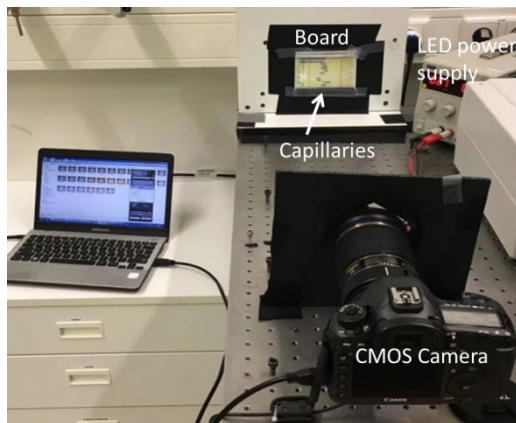


Figure 2-5: A picture of CMOS camera set-up. The CMOS camera is connected to a laptop to set the imaging frequency and data acquisition. During the experiments, the setup was covered with a black box to avoid the effect of room light.

Confocal microscope set-up

In order to visualize the oil-water interfaces inside the capillary tubes, a confocal laser scanning microscope was used (Nikon A1+ Eclipse Ti inverted microscope with A1R confocal module). Confocal scanning microscopy uses imaging modality for optical sectioning of a capillary, which enables imaging of thin and small sections at high resolution. We used fluorescence confocal laser scanning microscope mode (CLSM) for 2D and 3D imaging reconstruction of water-oil interfaces. Specific fluorescent probes provided temporal and spatial colocalization of substances of interest.

High and low-salinity waters were dyed with fluorescein sodium salt (Sigma-Aldrich), which was used as a tracer for fluorescence recovery. The water part was visualized in green using a laser wavelength of 405 nm. The oil part in a capillary was seen in black. Optimization of imaging parameters yielded a distinction between water and oil resulting in a clear visualization of their interfaces. Images were captured using a 20x microscope objective and the view domain was $0.6 \times 0.6 \text{ mm}^2$. In order to capture the entire interface of water and oil (in an X-Y plane), a bigger view domain would have been necessary. Since the inner diameter of the capillary tube is $800 \text{ }\mu\text{m}$, two images covering the entire diameter of the tube were taken and assembled into one image. To shorten the imaging time and limitation of the light to transfer large distances through the oil phase, given the cross-sectional symmetry of the capillary tube, a half capillary

cross-section was imaged. A range of 2D optical sectioning was continuously conducted from the bottom to the middle of capillaries with multiple steps in the Z direction. After 2D image acquisition and combination, the 3D-image reconstruction of water was performed near the LSW-oil and HSW-oil interface, as shown in Figure 2-6 (a-b). Additionally, we scanned the whole fluid contacts in the tube (7 mm long) to verify whether there was a water film during fluid injections. The image, Figure 2-6 (c), shows that the water has discontinuous adsorptions on the wall in the crude oil section, which is difficult to provide a pathway for water penetration in oil.

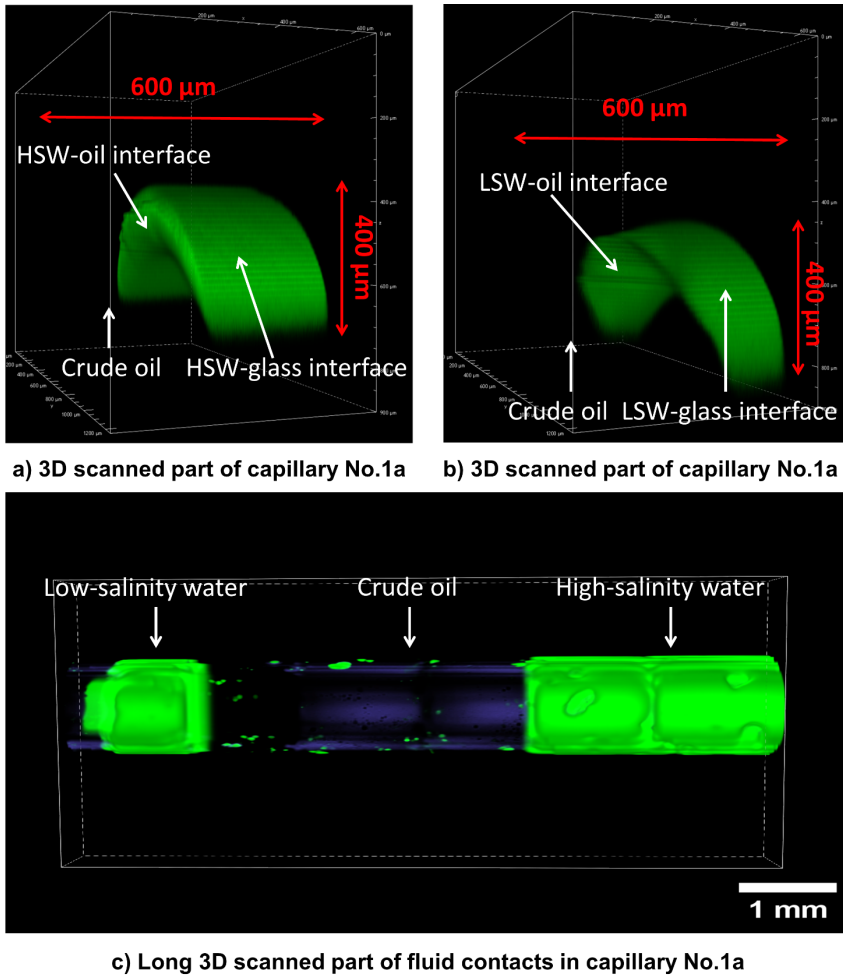


Figure 2-6: Scanned parts of capillary No.1a and No.1b around the interfaces. Scan area was 600 μm \times 400 μm \times 800 μm . The glass edge is shown in red lines. Oil phase is on the left

part of scan area but is not shown under laser scanning. Water phase is on the right part of the scan area in green. The interface between oil and water is the cavity as shown with white arrows. The top curved part is the interface between brine and glass tubes. Only half of the interfaces are scanned. Due to the penetration limitation of laser, closer to the middle of the tube less light could penetrate and interface is, therefore, less visible. However, the interfaces in the half of the tube could be imaged accurately.

As shown in Figure 2-6, dyed water and crude oil were shown in green and black colors, respectively. During the experiment period, the interfaces were imaged using confocal laser microscopy. Any change in interfaces was monitored. We took 2D and 3D images of all water-oil interfaces every two to three days, so the dynamic changes in contact angle and contact line could be monitored with 2D scanning slices and 3D reconstruction.

Pressure monitoring set-up

To observe the pressure changes in the capillaries, two fibre-optic micro-transducers were planted in LSW and HSW ends of a capillary, as shown in Figure 2-7. The pressure sensor has a cylindrical cavity with a diameter of $260\mu\text{m}$ at the front, connecting with a sensor module through a $\Phi 160\mu\text{m}$ optic fibre. The measurement ranges from 40 Pa up to 40 kPa with a resolution of 40 Pa. The accuracy is 0.6% of the full range. The details of pressure sensors and monitoring set-up can be found in the literature (Karadimitriou, Hassanizadeh, Joekar - Niasar, & Kleingeld, 2014) and (Zarikos, Hassanizadeh, van Oosterhout, & van Oordt, 2018). With this set-up, the pressures of LSW and HSW could be recorded every 8 minutes for 40 days.

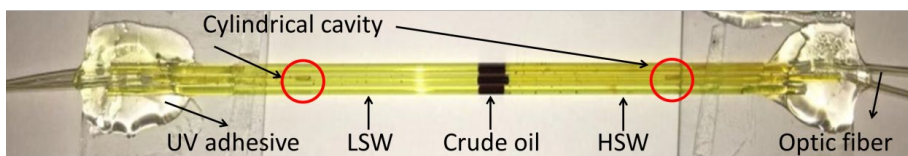


Figure 2-7: Two fiber optic micro-transducers are used as pressure sensors in the capillary. Three capillaries were prepared with LSW, crude oil, and HSW using the same method as in Section 2.3.1. Two pressure sensors were plugged into LSW and HSW separately. The positions of transducer heads are shown by red circles.

Our experimental observations and data analysis made it possible to study three main issues. methods, oil globule movement, contact angle changes, and pressure changes in the capillaries.

2.4 Results and discussion

2.4.1 Oil globule movement

In order to quantify the oil phase movement, we processed the camera images using ImageJ software. The main steps of image processing are shown in Appendix A material: cropping oil parts of images, making binary images, subtracting the oil areas with a wand tool, and then measuring the length difference of the front and end of oil globules from the beginning to the end of the experiment.

The amount and direction of displacement of oil globules within 40 days are shown in Figure 2-8. The positive value shows oil movement toward the LSW side, while the negative value is for the reverse direction. In capillary No.1a and No.1b with half-crude oil and half HSW or LSW, respectively, the oil phase moved towards the aqueous phase because of the emulsification of water into oil (Du et al., 2019; Emadi & Sohrabi, 2013). The measurement error is $\pm 20\mu\text{m}$.

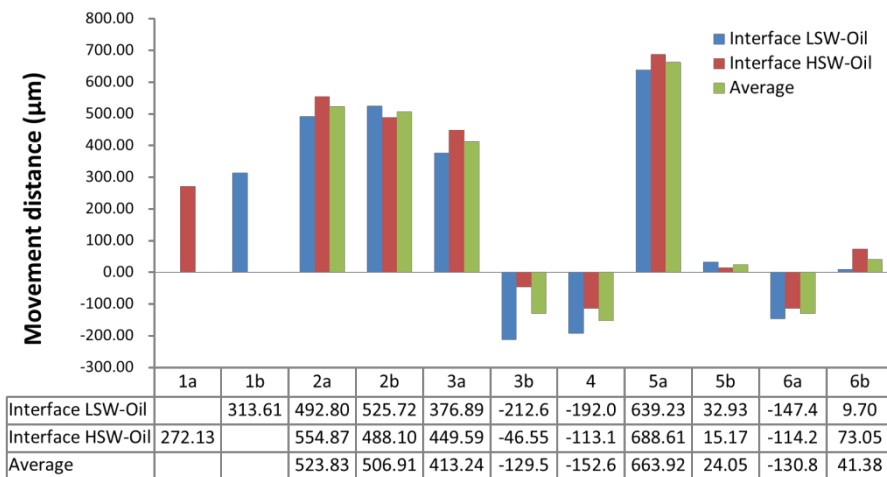


Figure 2-8: The movement of oil globule. The positive values indicate that the oil globule moved from the side with HSW to the side with LSW. The negative value means oil moved in the opposite direction. The values for capillary No.1a and 1 b mean that the interface between oil and brine moved toward the water side. The movement of oil globule is shown using three numbers in blue, red, and green, respectively showing the amount of movement based on the LSW-oil meniscus, HSW-oil meniscus, and average value.

Figure 2-8 showed oil displacement for nine capillaries (based on experimental conditions shown as No.2a to No.6b). We can see that the oil globules in water-wet capillaries, No.2a to No.3a, as well as in oil-wet capillary, No.5a, moved from the HSW side towards the LSW side. The maximum oil phase movements were around 524 μm and 664 μm in water-wet capillaries and oil-wet capillaries, respectively. However, the oil globules showed an opposite movement of oil globule in capillaries No.3b, No.4 and No.6a. For the capillaries No.3b and No.4, we observed that the menisci between oil globule and LSW/HSW became highly irregular. These irregular menisci occurred at the beginning of experiment when three fluids were injected into one capillary and were not gradually generated during the experimental period. This is because, due to different viscosities of oil and water, during the injection phase obtaining a perfect water-oil meniscus for all capillaries was difficult. Such interface irregularities are reported in the literature which also made uncertainty for pressure distribution over the menisci compared to interfaces with clear and regular shapes (Long & Zhang, 2018; Suh, Kang, Jang, Kim, & Yun, 2018). For capillary No.6a, we injected a small volume of crude oil prior to the injection of LSW. Although the possible wettability effects, due to the injection phase can be decreased with this method, meanwhile crude oil could change wettability by leaving behind a thin film of oil along the capillary (Agrawal, Xu, Darugar, & Khabashesku, 2018). Such oil films can affect the displacement of the oil globule (Unsal & Moulet-Vargas, 2013). The reference capillary No.6b had LSW on both sides of the oil phase contained the same salinity, where no significant movement of oil phase was observed. The nine capillary experiments show that oil globule displacement is mostly affected by the difference in salinity of water on the two sides of the oil.

Based on the obtained images, we measured the average displacement as well as the speed of movement for the oil-water meniscus over time (Figure 2-9 a-b). In order to fully present meniscus movement over 40 days, we considered averaging the movement of contact point among water, oil and glass, and the movement of oil-LSW and oil-HSW menisci for each oil globule. Using this data, the speed of meniscus movement was also calculated, which indicated the presence of 3 stages: i) interface curvature change, ii) significant movement of oil phase, and iii) slow movement of oil phase. The first stage includes changes in interface curvature mainly controlled by the wettability of the solid surface and the time needed for the meniscus to reach equilibrium. For example, in the water-wet

capillaries, the meniscus curvature increased compared to those in the oil-wet capillaries while no large bulk-phase movements were observed in this stage. The contact angle with the low-salinity water dramatically decreased within the first 10 days. The second stage occurred 11-22 days after the start of experiments. In this stage, most of capillaries had obvious meniscus movements (averaged values $>100 \mu\text{m}$), where the oil globules started to move. The time scale for this stage is comparable with the time scale for water diffusion through the oil phase (described in Section 2.2) which has been reported by other studies as well (Aldousary & Kovsky, 2019). The magnitude of meniscus movement in this period mainly presents the bulk oil movement rather than the change of interface curvatures. During this stage, which includes a transfer of water from the LSW side towards the HSW side, the pressure in HSW side started to increase so that the pressure difference between LSW and HSW sides slowly reached to a maximum value (Emadi & Sohrabi, 2013; S. B. Fredriksen et al., 2018). Next, during the third stage, the oil phase showed movement with lower speed, compared to the second stage, as the pressure differences between the two ends started to diminish. Therefore, stage three includes the gradual decrease of the established pressure difference over time which is discussed in Section 2.4.3.

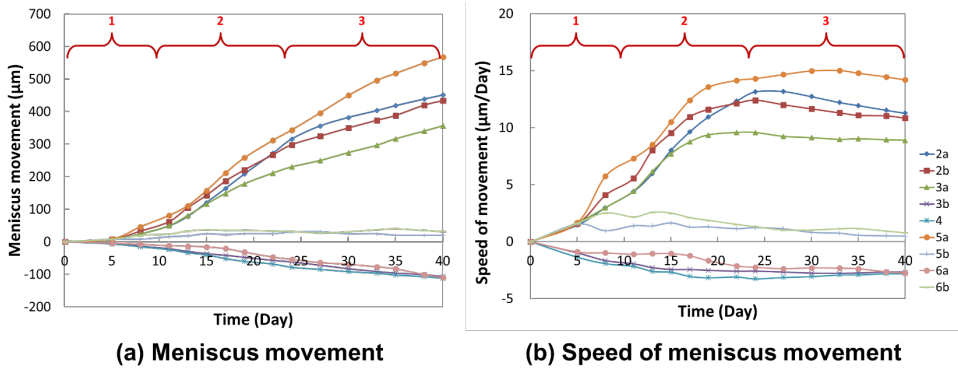


Figure 2-9: The movement of meniscus over time (a) and its associated speed (b) belonging to capillaries No.2a to No.6b for a period of 40 days. There are 16 average values of meniscus movement for each capillary (i.e., we selected one image per 2-3 days). The measurement was obtained after processing the images using the ImageJ software. In (a), the positive values indicate a movement of oil globule from the side with HSW to the side with LSW. The negative values indicate oil movement in the opposite direction. In (b), the speed of movement was calculated as $\frac{dx}{dt}$, where dx was the movement difference between two measurement points, and dt was the associated elapsed time.

2.4.2 Contact angle measurement

Contact angles of brine-oil-glass in all capillaries were captured and measured using a confocal microscope. Taking capillary No.2a as an example, the changes in contact angle of LSW-oil and HSW-oil interfaces are shown in Figure 2-10. The measurement error is $\pm 1^\circ$.

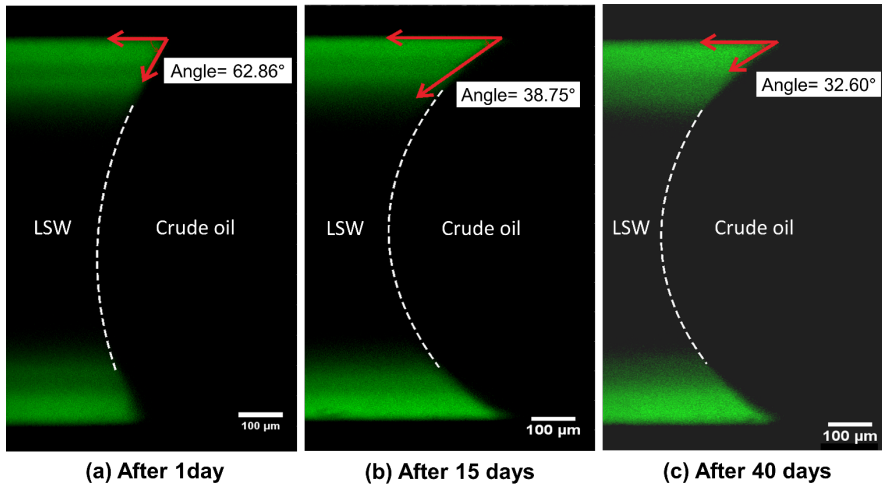


Figure 2-10: 2D-images of contact angle changes of LSW side in the capillary No.2a. The contact angles after 1 day, 15 days, and 40 days are measured and shown in plots (a), (b), and (c), respectively. As discussed in Section 2.2, the confocal microscope scanned the half of capillary. The scanning area includes several different layers in depth. We have chosen the layer that is closest to the middle of the capillary for capturing the most precise contact angle. In this case, due to the penetration limitation of laser, middle part of interfaces was missed for observation. The white color lines in pictures illustrate the missing part of the interfaces. The green parts represent the LSW phase (shown in the left part with white lines). The right section of white lines indicates the crude oil phase.

The figures show that the contact angle at the LSW side significantly decreased by 24.11° after 15 days and had a reduction at 5.39° afterwards. This behaviour occurs during the first stage of the meniscus movement shown in Figure 2-9. In order to show the dynamic change of contact angles, Figure 2-11 shows measurements for five capillaries (including capillaries No.2a, 3a, 4, 5a and 6b). Figure 2-11 shows the change of contact angles at both LSW and HSW sides for each capillary during a period of 40 days.

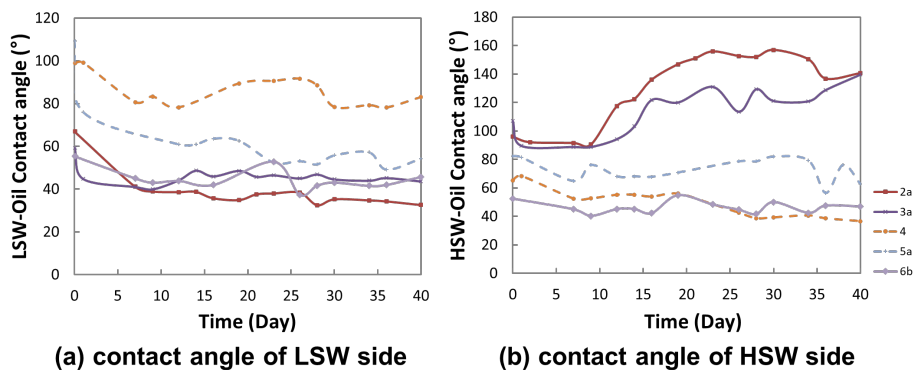


Figure 2-11: Change of contact angles in LSW sides (shown on the left plot) and HSW sides (shown on the right plot). There are 16 points for each curve. Solid curves present the water-wet capillaries. Dashed ones are for the oil-wet capillaries.

In Figure 2-11, all curves in the first 10 days sharply dropped, meaning that both LSW and HSW can increase water wettability of the glass surface. The alteration generally takes 10-14 days based on the trend of contact angle changes. The contact angle on the LSW side has the most reduction with the maximum value of about 34° in capillary No.2a showing a 16% change of the contact angle. The changes in contact angles on HSW side are around 18° providing a 50 g/L change. After about 14 days, the changes on LSW side show slow reduction, but those on HSW side become larger or stops changing. These behaviours can be caused by the oil movement as at the HSW side the interface passes a region which was previously in contact with oil (i.e., the original location of oil phase) and became slightly oil-wet (e.g., graphs 2a and 3a in the right plot of Figure 2-11 showing the contact angle of HSW side sharply increased by even up to around 60°). Moreover, from Figure 2-11 (a), we can conclude that the water-wet capillaries have larger contact angle changes compared to the oil-wet capillaries. In the first 14 days, the water-wet capillaries had an average reduction of about 17° , while the oil-wet capillaries had an average reduction of only 4° .

2.4.3 Pressure changes in a capillary

Using the pore-scale pressure monitoring set-up, the pressure changes were continuously monitored in LSW and HSW phases in capillary No.2a using two micro pressure sensors. The sensors were set to an initial value of zero and set to record a value every eight minutes. Results of pressure difference with two values

per day are shown in Figure 2-12 together with the measured LSW-side contact angle.

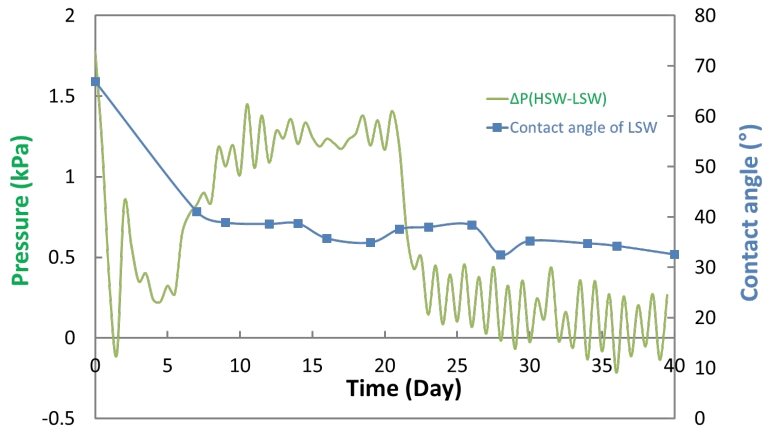


Figure 2-12: Graphs of monitored pressure difference in HSW and LSW phase in capillary No.2a. The green curve shows the pressure difference. The fluctuations in the curve may come from the atmospheric pressure variation around sensors because of slight fluctuations in room temperature. The contact angle of LSW in capillary No.2a is also shown as a black curve for comparison with the tendency of pressure.

According to the measurements of meniscus movement, we can explain the pressure difference according to the three stages (marked with numbers in the top section of Figure 2-12) as i) gradual increase of pressure difference, ii) pressure difference reaches a plateau, and iii) decay of pressure difference. In stage one, the curvature changes of LSW-oil and HSW-oil menisci induce growth of pressure in LSW and HSW phases. During the 6th to 12th day, pressure difference gradually reached a plateau with the maximum value of 1,650 Pa, which was caused by the processes of dissolution and emulsion formation of water into oil phase (Miller, 1988). The LSW-side lost more water than the HSW-side so the pressure drop on LSW-side was larger which can explain the movement of oil globules in the capillary No.1a and No.1b. Both oil phases invaded into brine phase (S. Fredriksen, Rognmo, Sandengen, & Fernø, 2017; Zheng & Yapa, 2002). In stage two, a relative stable pressure difference is established between HSW and LSW sides with a value of around 1,400 Pa. As observed by other studies (S. Fredriksen et al., 2017), water diffusion due to osmotic pressure between LSW and crude oil as well as between HSW and crude oil causes the transfer of water along the capillary. The period of forming a plateau, from the

12th to the 22nd day, agrees with the second stage of meniscus movement. The meniscus in this stage had significant movement and some of them showed a faster movement than those in the third stage. In the third stage, from 23rd to the 40th day, the pressure difference decays to get back almost to a zero value. This can be due to reaching equilibrium between salt concentrations on LSW and HSW sides after water diffusion from LSW side to HSW side. Based on Figure 2-12, within the first 10 days, the contact angle dramatically decreased. Afterwards, the contact angle maintained a value of around 38° for about 14 days. From the 24th day onwards, the contact angle slowly dropped about 6° , which is overall consistent with the result from pressure change measurements.

2.4.4 Future research

This study introduced methods and results for monitoring oil globule movement and measuring pressure change in a capillary. We observed the movement of oil globules and contact angle changes using a CMOS camera set-up and a confocal microscope, respectively. Besides, the pressures in LSW and HSW phases for a long-time period (40 days) were detected.

Based on our measurements and mechanisms reported in the literature, we could explain the dynamic of the system using spontaneous emulsification and osmosis processes. The relative theories have been expressed by many researchers (Aldousary & Kovscek, 2019; Emadi & Sohrabi, 2013; S. Fredriksen et al., 2017; Miller, 1988). Yet, the very complex and coupled chemical and physical interactions between brine and crude oil require future works to fully characterize the system. Future research are needed to i) observe and characterise the emulsification process especially adjacent to water-oil interfaces, and ii) obtain more data on pressure changes in the LSW/Crude oil/HSW system. A dynamic measurement and characterization of the chemical evolution of different phases of the system would be ideal to confirm the presence of proposed mechanisms, which is, however, very challenging due to the small volumes of fluid phases used in capillary experiments.

2.5 Conclusion

- 1) Oil globules can be remobilized by water diffusion in crude oil. The oil movement was observed and measured.

- 2) Based on the contact angle measurement of low/high-salinity water, we can confirm that LSW and HSW both have the potential of making the surface more water-wet, but LSW can make hydrophilic surface more water-wet than the hydrophobic surface.
- 3) Pressure change of water with low and high salinity is monitored and its tendency is consistent with the change of contact angle and oil movement. Besides, the pressure measurement also provides proof of the water diffusion and osmosis effect.
- 4) We proposed three stages for the changes in contact angle and pressure. Correspondingly, we give the potential explanations for the changes in the three stages.

Reference

- Agrawal, D., Xu, K., Darugar, Q., & Khabashesku, V. (2018). *Enhanced Oil Recovery by Nanoparticle-Induced Crude Oil Swelling: Pore-Scale Experiments and Understanding*. Paper presented at the SPE Asia Pacific Oil and Gas Conference and Exhibition.
- Aldousary, S., & Kovscek, A. R. (2019). The diffusion of water through oil contributes to spontaneous emulsification during low salinity waterflooding. *Journal of Petroleum science and Engineering*, 179, 606-614.
- Ayirala, S. C., Al-Yousef, A. A., Li, Z., & Xu, Z. (2018). Water Ion Interactions at Crude-Oil/Water Interface and Their Implications for Smart Waterflooding in Carbonates. *SPE Journal*.
- Binks, B. P., & Horozov, T. S. (2006). *Colloidal particles at liquid interfaces*: Cambridge University Press.
- Chakravarty, K. H., Fosbøl, P. L., & Thomsen, K. (2015). *Brine crude oil interactions at the Oil-Water Interface*. Paper presented at the SPE Asia Pacific Enhanced Oil Recovery Conference.
- Chávez-Miyauchi, T. s. E., Firoozabadi, A., & Fuller, G. G. (2016). Nonmonotonic elasticity of the crude oil-brine interface in relation to improved oil recovery. *Langmuir*, 32(9), 2192-2198.
- Cheng, J., Chen, J.-F., Zhao, M., Luo, Q., Wen, L.-X., & Papadopoulos, K. D. (2007). Transport of ions through the oil phase of W1/O/W2 double emulsions. *Journal of colloid and interface science*, 305(1), 175-182.
- Davies, J., & Wiggill, J. (1960). Diffusion across the oil/water interface. *Proceedings of the Royal Society of London. Series A. Mathematical and Physical Sciences*, 255(1281), 277-291.
- Du, Y., Xu, K., Mejia, L., Zhu, P., & Balhoff, M. T. (2019). Microfluidic Investigation of Low-Salinity Effects During Oil Recovery: A No-Clay and Time-Dependent Mechanism. *SPE Journal*.
- Emadi, A., & Sohrabi, M. (2013). *Visual investigation of oil recovery by low salinity water injection: formation of water micro-dispersions and wettability alteration*. Paper presented at the SPE annual technical conference and exhibition.
- Evdokimov, I. N., Fesan, A. A., Kronin, A. M., & Losev, A. P. (2016). Common Features of "Rag" Layers in Water-in-Crude Oil Emulsions with Different Stability. Possible Presence of Spontaneous Emulsification. *Journal of Dispersion Science and Technology*, 37(11), 1535-1543.
- Fredriksen, S., Rognmo, A., Sandengen, K., & Fernø, M. (2017). Wettability effects on osmosis as an oil-mobilization mechanism during low-salinity waterflooding. *Petrophysics*, 58(01), 28-35.
- Fredriksen, S. B., Rognmo, A. U., & Fernø, M. A. (2018). Pore-scale mechanisms during low salinity waterflooding: Oil mobilization by diffusion and osmosis. *Journal of Petroleum science and Engineering*, 163, 650-660.
- Goyal, P., & Aswal, V. (2001). Micellar structure and inter-micelle interactions in micellar solutions: results of small angle neutron scattering studies. *CURRENT SCIENCE-BANGALORE*, 80(8), 972-979.
- Hua, Z., Li, M., Ni, X., Wang, H., Yang, Z., & Lin, M. (2016). Effect of injection brine composition on wettability and oil recovery in sandstone reservoirs. *Fuel*, 182, 687-695.
- Karadimitriou, N., Hassanizadeh, S., Joekear - Niasar, V., & Kleingeld, P. (2014). Micromodel study of two - phase flow under transient conditions: Quantifying effects of specific interfacial area. *Water Resources Research*, 50(10), 8125-8140.
- Khilar, K. C., & Fogler, H. S. (1984). The existence of a critical salt concentration for particle release. *Journal of colloid and interface science*, 101(1), 214-224.
- Long, L., & Zhang, B. (2018). The distribution of fluids in irregular capillary tubes: a new capillary model based on the single-corner capillary. *Journal of Petroleum Exploration and Production Technology*, 8(2), 341-350.

- Mahzari, P., & Sohrabi, M. (2014). *Crude oil/brine interactions and spontaneous formation of micro-dispersions in low salinity water injection*. Paper presented at the SPE improved oil recovery symposium.
- Mahzari, P., Sohrabi, M., Cooke, A. J., & Carnegie, A. (2018). Direct pore-scale visualization of interactions between different crude oils and low salinity brine. *Journal of Petroleum science and Engineering*, 166, 73-84.
- Malik, M. A., Wani, M. Y., & Hashim, M. A. (2012). Microemulsion method: A novel route to synthesize organic and inorganic nanomaterials: 1st Nano Update. *Arabian journal of Chemistry*, 5(4), 397-417.
- Marine, I. W., & Fritz, S. J. (1981). Osmotic model to explain anomalous hydraulic heads. *Water Resources Research*, 17(1), 73-82.
- Miller, C. A. (1988). Spontaneous emulsification produced by diffusion—a review. *Colloids and Surfaces*, 29(1), 89-102.
- Mokhtari, R., & Ayatollahi, S. (2019). Dissociation of polar oil components in low salinity water and its impact on crude oil–brine interfacial interactions and physical properties. *Petroleum Science*, 16(2), 328-343.
- Nasralla, R. A., & Nasr-El-Din, H. A. (2014). Double-layer expansion: is it a primary mechanism of improved oil recovery by low-salinity waterflooding? *SPE Reservoir Evaluation & Engineering*, 17(01), 49-59.
- Riehm, D. A., Rokke, D. J., Paul, P. G., Lee, H. S., Vizanko, B. S., & McCormick, A. V. (2017). Dispersion of oil into water using lecithin-Tween 80 blends: The role of spontaneous emulsification. *Journal of colloid and interface science*, 487, 52-59.
- Rostami, P., Mehraban, M. F., Sharifi, M., Dejam, M., & Ayatollahi, S. (2019). Effect of water salinity on oil/brine interfacial behaviour during low salinity waterflooding: A mechanistic study. *Petroleum*.
- Sandengen, K., Kristoffersen, A., Melhuus, K., & Jøsang, L. O. (2016). Osmosis as mechanism for low-salinity enhanced oil recovery. *SPE Journal*, 21(04), 1,227-221,235.
- Song, W., & Kovscek, A. R. (2019). Spontaneous clay Pickering emulsification. *Colloids and Surfaces A: Physicochemical and Engineering Aspects*, 577, 158-166.
- Sørbo, I. G. (2016). *Polar Components in Crude Oils and Their Correlation to Physiochemical Properties*. The University of Bergen.
- Speight, J. G. (2014). *The chemistry and technology of petroleum*: CRC press.
- Suh, H., Kang, D., Jang, J., Kim, K., & Yun, T. (2018). *Capillary pressure at irregularly shaped pore throat*. Paper presented at the Proc. of the 7th International Conference on Unsaturated Soils.
- Umar, A. A., Saaid, I. B. M., Sulaimon, A. A., & Pilus, R. B. M. (2018). A review of petroleum emulsions and recent progress on water-in-crude oil emulsions stabilized by natural surfactants and solids. *Journal of Petroleum science and Engineering*, 165, 673-690.
- Unsal, E., & Moulet-Vargas, E. (2013). *Impact of wetting film flow in pore scale displacement*. Paper presented at the SCA.
- Wei, B., Wu, R., Lu, L., Ning, X., Xu, X., Wood, C., & Yang, Y. (2017). Influence of Individual Ions on Oil/Brine/Rock Interfacial Interactions and Oil–Water Flow Behaviors in Porous Media. *Energy & Fuels*, 31(11), 12035-12045.
- Wen, L., & Papadopoulos, K. D. (2001). Effects of osmotic pressure on water transport in W1/O/W2 emulsions. *Journal of colloid and interface science*, 235(2), 398-404.
- Yang, L., Zhang, X., Zhou, T., Lu, X., Zhang, C., & Zhang, K. (2019). The effects of ion diffusion on imbibition oil recovery in salt-rich shale oil reservoirs. *Journal of Geophysics and Engineering*, 16(3), 525-540. doi:10.1093/jge/gxz025
- Zarikos, I., Hassanizadeh, S., van Oosterhout, L., & van Oordt, W. (2018). Manufacturing a micro-model with integrated fibre optic pressure sensors. *Transport in Porous Media*, 122(1), 221-234.
- Zheng, L., & Yapa, P. D. (2002). Modeling gas dissolution in deepwater oil/gas spills. *Journal of Marine Systems*, 31(4), 299-309.

Chapter 3

Fundamental study of water transport through oil phase

Published as:

Yan, L., Chang, Y., Hassanizadeh, S. M., Xiao, S., Raoof, A., Berg, C. F., & He, J. (2022). A quantitative study of salinity effect on water diffusion in n-alkane phases: From pore-scale experiments to molecular dynamic simulation. *Fuel*, 324, 124716.

In preparation: Direct evidence of salinity differential effect on water transport in oil: pore-scale mechanisms

Abstract

The study in the previous chapter indicates the influence of salinity differential on the constrained oil between brines. However, the complexity of crude oil introduces difficulty in quantitatively evaluating the effect of salinity and how the constrained oil performs in a porous media is still not well understood. To gain insights into the process of water transport through an oil phase, we have conducted a series of microfluidic experiments. The solid surface in the micromodels has been rendered oil-wet. Sequential fluid injections with high-salinity water (HSW), pure or surfactant-added synthetic oils and low-salinity water (LSW) are performed to obtain a fluid distribution where oil is sandwiched between disconnected HSW water and connected LSW. Such fluid distribution is assumed relevant in natural reservoirs. A $2,797.16 \times 2,238.39 \mu\text{m}^2$ area is continuously observed over 70 hours under a high-resolution microscope. We observe that the salinity contrast over oil films can cause water transport through the oil and lead to swelling of the trapped high-salinity water, resulting in the movement of oil phases along the solid grains. Dodecane displays higher water transport than heptane. We compare salinity contrasts of 1.7-170 g/L and 50-170 g/L. The higher salinity contrast induces higher water transport for both heptane and dodecane. The lower salinity contrast of 50-170 g/L salinity contrast gives less water flux, even reaching zero after a prolonged time. With the addition of a surfactant (Span 80) in alkanes, we observe spontaneous emulsification at the LSW-oil interface, while no apparent micro-emulsions were found at the HSW-oil interface. We notice an almost 100 times increase in water transport for both n-heptane and n-dodecane due to the addition of the surfactant, which reveals that the water-in-oil micro-emulsions enhance water transport through the oil phase. The introduction of emulsification weakens the influence of salinity on the transport of water molecules in the oil phases. Based on our observations, two scenarios for explaining water transport through the oil phase are proposed: water diffusion due to chemical potential and water transport via reverse micelle or micro-emulsions movement. The relative influence of these two transport mechanisms is dependent on the rate of generation of emulsions at the LSW-oil interface, which we observe to be significantly altered by surfactants in the oil phase.

In the previous chapter, we attempt to explain the movement of oil globules using the combined theory of emulsification and osmosis, where the water is transported through the oil phase via reverse micelle. The results have consistent with theoretical calculations. However, to achieve the phenomenon, two factors are crucial (at least on the face of it): surface-active components (or called surfactant) and water concentration difference. This induces the following questions: what happens in the pure oil phases without the presence of surfactant? If the oil remobilization still occurs, how to explain it? How to improve the proposed hypothesis? To answer the questions, we need to separately review the nature of osmosis and emulsification. Although some works, e.g., Sandengen, Kristoffersen, Melhuus, and Jøsang (2016), have shown the swelling phenomenon of individual water droplets in a pure oil phase by osmotic-like flow, it is difficult to attribute this behavior to osmosis without further research. In this chapter, we will attempt to discuss the nature of water diffusion through oil phase. Then, a systematic study of water transport through oil phase is performed by giving molecular dynamic simulation and the solid evidence of salinity effect on oil redistribution in microfluidic experiments. Furthermore, the impact of salinity on water-oil interfacial behavior are investigated by applying dynamic light scattering equipment and interfacial tension measurement.

3.1 Water transport in brine-oil-rock contacts

In the theory of osmosis, the chemical potential difference between two sides of a semi-membrane drives a net passage of water to the side being more saline, whereas the dissolved ions are excluded in such transport. Osmotic flow ceases when the aqueous activities of the two solutions on both sides of the membrane are the same, i.e., when the two water regions have reached the same salinity. In the analysis of oil displacement, some researchers believe that crude oil can be treated as a semi-permeable liquid membrane. Du, Xu, Mejia, Zhu, and Balhoff (2019) captured the dynamic behavior of trapped oil dewetting and swelling during water flooding in micromodels with a single dead-end pore and observed the generation of micro-emulsions inside the swelling oil phase. They explained the phenomenon of oil swelling and micro-emulsions with a theory of water diffusion through crude oil low-salinity water towards high-salinity water.

From the mentioned literature, there are two primary explanations for oil motion due to a salinity contrast: water diffusion through water films (formed between

oil phase and pore walls) resulting in film expansion along water-wet rock surfaces (Figure 3-1 a) and water transport through oil phases (Figure 3-1 b). Note that here we do not consider the chemical reactions between fluids and minerals and the roughness in real rocks. The former mechanism (i.e., water diffusion into HSW film) comes about when the thin HSW film is directly exposed to an LSW environment. In other words, the solid substrate needs to be water-wet and the HSW area should not be blocked by the oil phase. In nature, HSW is commonly original at the residual state in a green oil reservoir. In this situation, the second mechanism (i.e., water diffusion through oil phase) becomes sensible for explaining the HSW expansion. Consequently, the research questions could be whether the oil phase can be treated as a membrane and what causes the water diffusion through the squeezed oil phase.

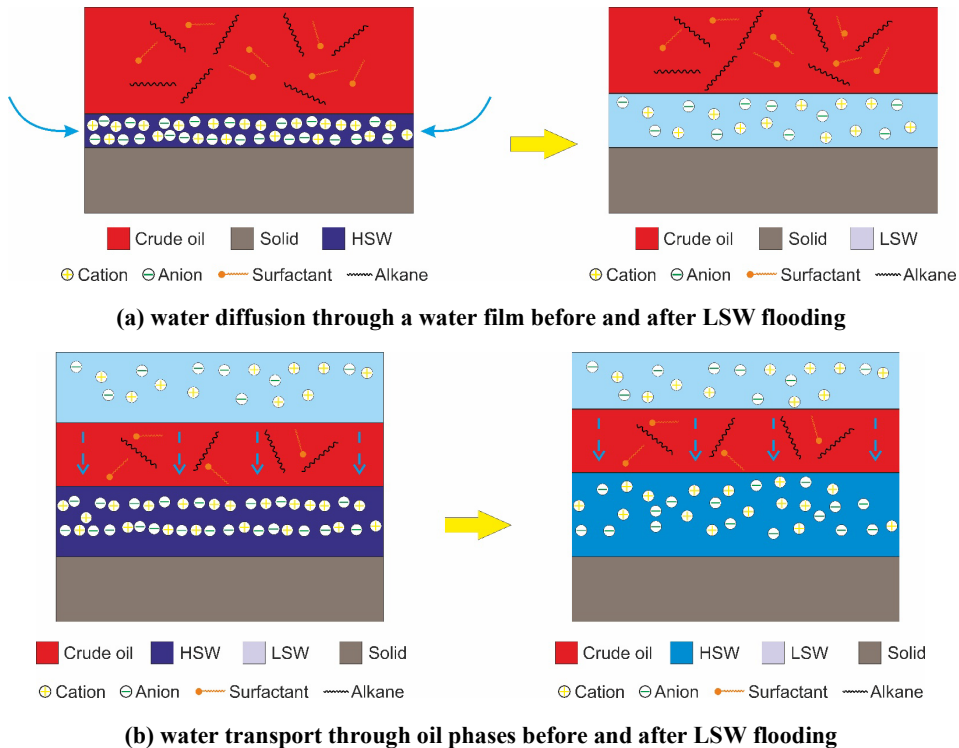


Figure 3-1: Schematic diagrams of oil motion caused by water diffusion through a water film and oil phase, respectively. (a) shows the expansion of the confined HSW layer between the oil and the solid surface. The blue arrows indicate the water transport into the HSW layer. The ion concentration is correspondingly reduced. (b) shows the expansion of the HSW layer blocked by the oil phase. The dashed arrows give the direction of water

transport. The ion concentration becomes less due to the increase in water molecules. The HSW regions in both pictures have expanded due to tertiary LSW flooding and have lower ion concentrations. As a result, the confined oil regions become remobilized.

From a molecular-scale perspective, molecular simulations (MD) have been employed in recent decades to study the salinity effect on the oil-water interface behavior. Such simulations are proven to be an effective tool for capturing molecular movements and further elucidating the underlying mechanisms for the transport of small molecules across a membrane, and thereby the continuum-scale transport process (MacElroy & Boyle, 1999). Marrink and Berendsen (1994) performed molecular dynamics simulations on a phospholipid/water system and obtained insight into the water transport through a lipid membrane. By computing the free energy and diffusion rate profiles of water molecules across the bilayer, they determined the water permeation rate and proposed a combined solubility-diffusion model by taking the inhomogeneity of the membrane into account for describing the theoretical permeation process. Zhao, Yao, Ramiseti, Hammond, and Wen (2018) investigated the salinity effect on the water/n-decane interface by simulating six cases with different NaCl concentrations from 0 to 1.0 M. In their work, the simulation case with 0.2 moles NaCl yielded the minimum interfacial tension value and the maximum contact angle of a decane droplet on a water surface, which showed an optimal salinity to reach a minimum interfacial tension (IFT) value. Zhang et al. (2019) discussed the diffusion behavior of microscopic particles and their distribution at fluorobenzene-water and pentanol-water interfaces at a molecular scale. They observed that more water molecules entered the pentanol region with an increase in the NaCl concentration, leading to a rougher and thicker interface. Moreover, the diffusion coefficient of water molecules became lower when electrolyte ions were added to the brine. Although the effects of salinity on wettability and interfacial phenomena have been studied in depth, the oil displacement caused by water transport through hydrocarbon liquids has not been directly observed nor investigated yet via MD simulations.

3.2 The theory of water transport in liquid membrane

3.2.1 Argument on osmosis theory

In most literature, the two processes of conventional osmosis and water diffusion in the oil phase are often mixed. Classically, the membrane considered in

osmosis, e.g., biological, synthetic, or polymeric membrane, is normally insoluble to the aqueous phase. Non-aqueous membranes have been studied in numerous experiments since the 1960s. Lakshminarayanaiah and White (1969) conducted experiments on water flow through solid polymeric and nonaqueous liquid membranes and found that the process of water transport through a rigid membrane physically differs from that through a liquid membrane. In the case of solid membranes, e.g., a hollow fiber polyamide membrane (Sanahuja-Embuena et al., 2021), water flow is driven by the osmotic force from pure water to the saline water compartment and the pathway depends on the porous membrane properties, such as pore radius, permeability, and surface electrical behavior. In the case of organic liquid membranes, water diffusion is described as the motion of a species by means of kinetic jumps into neighboring vacancies, where the water pathway cannot be defined because of the kinetic motion of all molecules. Even though the phenomenon of salt solution expansion may look like osmosis under a macroscale observation, the organic phase cannot be treated as a rigid membrane.

On the other hand, the hydrocarbon layer thickness in organic liquids and salinity in aqueous solutions play an important role in the water solubility in hydrocarbon liquids (Wenhui Li, Nan, You, & Jin, 2021), especially in crude oil containing natural surfactants. Schatzberg (1965) investigated the diffusion coefficient of water in four types of hydrocarbon liquids and concluded that the solubility of water decreased with increasing molecular weight in saturated hydrocarbons. Heidman, Tsonopoulos, Brady, and Wilson (1985) found that the solubility of water in hydrocarbons is at least two orders of magnitude higher than the solubility of hydrocarbons in water, which depended on the polarizability and van der Waals interactions between the hydrocarbon and water. According to the Hildebrand solubility formula (Schatzberg, 1963) salt significantly affects water activity and the solubility in hydrocarbon liquids. Presumably, higher salt concentration decreases water activity and solubility.

For low-salinity flooding of a hydrocarbon reservoir, salinity in an aqueous solution would influence the water solubility and water concentration in the crude oil phase during the tertiary low-salinity water flooding. Aldousary and Kovscek (2019) reported measurements of water content in crude oil after exposing it to different salinity brines for several days. The results showed that the crude oil gained the highest water concentration when contacted with deionized water, and

the concentration was about 25 times less when contacted with formation water that had an ionic strength of approximately 150,000 mg/L. Mokhtari and Ayatollahi (2019) reached a similar conclusion by directly observing the dynamic change of water droplets at the crude oil/water interface with different brine samples over 45 days. Although various organic compounds, e.g., aromatics, asphaltic, etc., in crude oil might influence the movement of water molecules in oil to some extent, the salt concentration in the aqueous phase undoubtedly is a determining factor for the water solubility in oil.

3.2.2 Water diffusion caused by concentration difference

Water has a certain solubility in the alkane phase, but the salinity effect on solubility is not clear yet, especially for special brine and alkane. In the system of LSW/alkane/HSW, the interface of LSW/alkane hence contains more water content than that of HSW/alkane. As mentioned in the Introduction, the ionic strength can strongly impact the water concentration in the crude oil phase (Aldousary & Kovscek, 2019; Mokhtari & Ayatollahi, 2019). The relationship is not linear, meaning that there is an optimal salt concentration leading to the lowest water content. The exact relationship of water solubility in n-alkane versus salinity is barely studied in the literature, which causes a challenge to calculate the accurate water mass flux in an alkane. To quantify the water volumetric flux and mass flux, a series of microfluidic experiments have been conducted. In Section 3.4, by measuring the area change of trapped HSW in our experiments, we estimate a relationship between salinity and water volumetric flux.

The mass flux of water dissolved in oil, J_w (mole of water per unit area per time) is given by Fick's first law, $J_w = -D_w \nabla c_w$, where D_w is the diffusion coefficient of water in oil and c_w is the molar concentration of water. For cases where the solute molecule is smaller than the solvent, the diffusion coefficient can be approximately calculated by the modified Stokes-Einstein equation, $D_w = \frac{k_B T}{6\pi\eta^{0.78}r}$, where k_B is Boltzmann's constant ($m^2 \cdot kg \cdot s^{-2} \cdot K^{-1}$), T is the absolute temperature (K), η is the shear viscosity of the solvent ($kg \cdot m^{-1} \cdot s^{-2}$) and r is the radius of the solute (m) (Hynes, Kapral, & Weinberg, 1979; Su, Duncan, Momaya, Jutila, & Needham, 2010). Under stationary conditions, the flux of water through the alkane phase in the direction of the concentration gradient can be approximated as

$$J_{w,x} = -D_w \frac{\partial c_w}{\partial x} = D_w \frac{c_w^{LSW} - c_w^{HSW}}{\Delta x} \quad [3.1]$$

where c_{LSW} and c_{HSW} are the water concentrations in the oil at the LSW-alkane and HSW-alkane interfaces, respectively, and Δx is the distance between these two interfaces.

Linking to the expression of chemical potential, the equality of the chemical potentials of water at each interface at equilibrium gives

$$\mu_w^{LSW} = \mu_w^0 + RT \ln a_w^{LSW} \quad [3.2]$$

$$\mu_w^{HSW} = \mu_w^0 + RT \ln a_w^{HSW} \quad [3.3]$$

where μ_w^0 is the chemical potential of pure water, a_w^{LSW} and a_w^{HSW} are the water activities of low- and high-salinity brine. In an isothermal system, the difference of chemical potential of water across the oil membrane is,

$$\Delta \mu_w = \mu_w^{HSW} - \mu_w^{LSW} = RT \ln \frac{a_w^{HSW}}{a_w^{LSW}} \quad [3.4]$$

The relationship between concentration and chemical potential can be expressed as

$$\frac{d\mu}{dx} = \frac{RT}{c(x)} \frac{dc(x)}{dx} \quad [3.5]$$

where R is gas constant, T is the absolute temperature, and $c(x)$ is the water concentration at x . Combing the equations 3.1, 3.4 and 3.5, the linear flux relations for the case that water concentration depends on one coordinate x can be written as

$$J_{w,x} = -D_w \frac{c(x)}{dx} \ln \frac{a_w^{HSW}}{a_w^{LSW}} \quad [3.6]$$

Furthermore, if concern the driving force comes from the difference in chemical potential outside of water around the oil membrane, meaning there is an osmotic flow in the oil phase. Therefore, the chemical potential of water can be also rewritten as:

$$\Delta\mu_o^* = \mu_o^{*,HSW} - \mu_o^{*,LSW} = \bar{V}(\Delta P - \Delta\Pi) \quad [3.7]$$

where $\Delta\mu_o^{*,HSW}$ and $\Delta\mu_o^{*,LSW}$ are the chemical potentials of water at the two sides of oil phase, ΔP is the hydrostatic pressure difference across the membrane, V is the partial molar volume of solvent, and Π is the theoretical osmotic pressure existing across the membrane. The theoretical osmotic pressure is a function of the difference of activities of water in the two solutions (a_o^{HSW} and a_o^{LSW}) across the membrane:

$$\Delta\Pi = \frac{RT}{V} \ln \frac{a_o^{HSW}}{a_o^{LSW}} \quad [3.8]$$

Therefore, the osmotic flux across the oil membrane can be expressed as,

$$J_{o,x} = -D_w \frac{c(x)}{dx} \frac{\bar{V}}{RT} \Delta\Pi \quad [3.9]$$

The open question is, whether the water diffusion through oil phase is due to the water solubility difference inside oil phase, or the chemical potential of water across the oil phase. In our theory, we believe the answer is the solubility difference, as the water phases at two sides of oil phase do not directly touch each other and osmotic flow can not be initialized. Crestel, Kvasničková, Santanach-Carreras, Bibette, and Bremond (2020) have shown a similar theoretical description for water diffusion in oil, where calculated water flux with the water solubility in oil equilibrated with the concentrated solution.

3.2.3 Water transport caused by inverse micelle

Regarding the scenario with emulsion transport in the oil phase, we must consider the water flux induced by the movement of inverse micellar. Within the process of reserve micelle formation, some salt ions are wrapped by a water shell inside the micelles as hydrates (Pays, Giermanska-Kahn, Pouligny, Bibette, & Leal-Calderon, 2002). Although salt ions could be possibly transported through the organic phases, the amount of entrapped ions is much smaller than that of the water shell surrounding the ions since the majority content in the reverse micelles is water (Cheng et al., 2007). Therefore, in our work, we do not assume the ion transport through the phase.

Wen and Papadopoulos (2000) used capillary video-microscopy to capture the water transport between two aqueous phases and through an intervening oil phase under osmotic pressure, Figure 3-2. They observed that tiny emulsion droplets spontaneously formed at the water-oil interface and then detached and moved into the oil phase, within 30-minute contact of water and surfactant-added oil. However, involving the high salinity aqueous drops (≥ 5 M NaCl), they didn't observe spontaneous emulsification in the Span-containing n-hexadecane. They also proposed the mechanism of water permeation through oil via reverse micelle and hydrated surfactant, Figure 3-2 (b). Water can be transported across the oil layer by being incorporated in reverse micelles, but the theoretical description is not well clear yet. Water can be transported via hydrated surfactant as well. The hydrophilic portion of the surfactant hydrates on the interface of low-salinity brine and oil. The hydrated molecules diffuse to the interface between the oil and the high-salinity phase and then get dehydrated there. While no direct evidence has been presented in support of these mechanisms, at the same time differences in their contributions to water transport rates have not been determined. In this section, we attempt to derive a transport law for micelles that describes the effect of electrostatic interactions among the micelles as well as the hydrodynamic drag they experience.

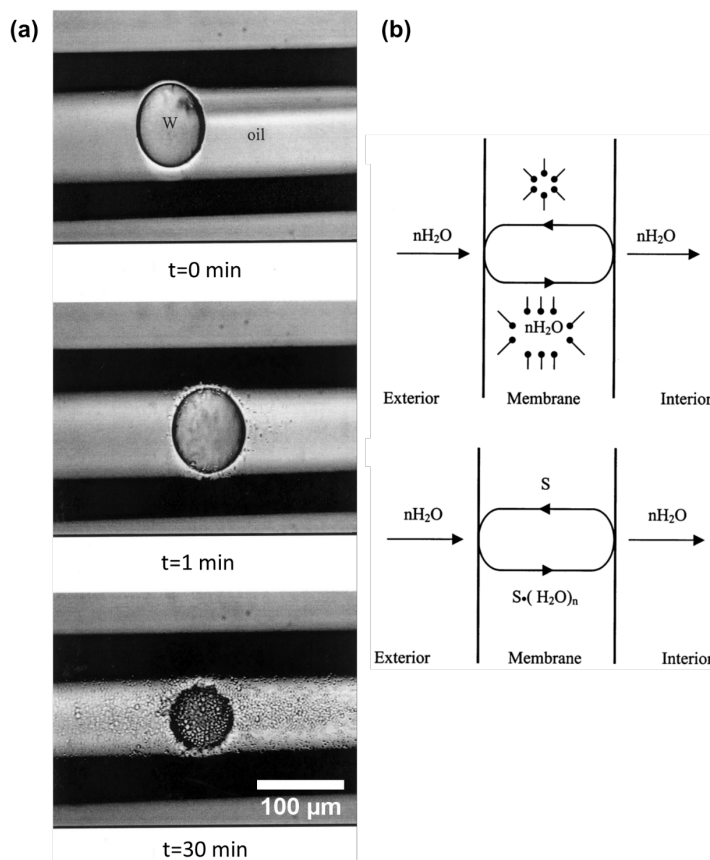


Figure 3-2: Spontaneous emulsification in W/O system and the relevant potential mechanisms (Wen & Papadopoulos, 2000). (a) shows the images of the processes of water-oil spontaneous emulsification during 30 minutes of contact. A droplet of pure water (w) was placed in the micro-capillary tube that was filled with n-hexadecane containing 0.1 M Span 80 (o). (b) illustrates the water transport through oil phase via micelles and hydrated surfactants.

Now, we consider the spatial diffusion of micelle due to the effect of electrostatic interactions and derive a transport law for micelles. This law is identical in form to Fick's law, but with a diffusion coefficient $D_m \sim C_m$ where C_m is the micelle concentration. Figure 3-3 describes a situation where two micelles penetrate each other's double layers and give rise to electrostatic repulsion. This layer of charges, sometimes called the diffuse electric double layer has a thickness r_0 which is known as the Debye length. Typically, r_0 is 1-5 nm. Once these electric forces

are mobilized, the micelles will start to move according to their hydrodynamic mobility.

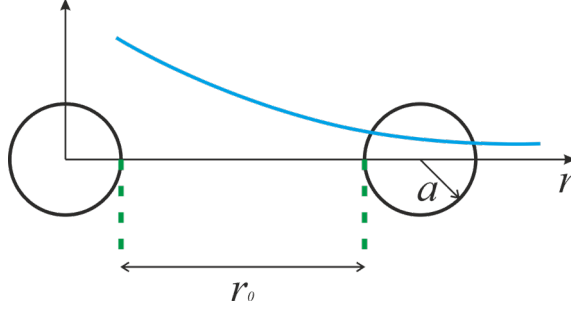


Figure 3-3: The mobile charge distribution around one of two micelles of radius a and a center separation r . The diffuse electric double layer has a thickness of r_0 .

First, we shall assume that two micelles at a separation r subject each other to an electric force

$$\mathbf{f} = \frac{q^2 \mathbf{u}_r}{4\pi\epsilon_0 r^2} e^{-\frac{r-2a}{r_0}} \quad [3.10]$$

where q is their charge, ϵ_0 the electric vacuum permittivity, a the micelle radius, r_0 is the Debye length with a typical range of 1-5 nm, and \mathbf{u}_r the unit vector in the r -direction. The thickness of the electric double layer in the liquid is $r - 2a$. The exponential function is introduced only to provide a cut-off to the interaction range.

Now, the total force on a given micelle is given by all its neighbours, which we will represent by a number of the concentration field $C_m(\mathbf{r})$, the number of particles per volume. This is a mean-field approximation that yields the force

$$\mathbf{F} = \int dV C_m(\mathbf{r}) \mathbf{f} \quad [3.11]$$

If $C(\mathbf{r})$ is constant, this expression will integrate to 0 for symmetry reasons. So, we write

$$C_m(\mathbf{r}) = C_0 + \mathbf{r} \cdot \nabla C_m \quad [3.12]$$

Introducing spherical coordinates and aligning the z axis with ∇C_m , we can write the force as

$$\mathbf{F} = \int dV \mathbf{r} \cdot \nabla C_m \mathbf{f} \quad [3.13]$$

which is non-zero only in the z-direction. Since $(\mathbf{u}_r)_z = \cos \theta$, we get the total force

$$\mathbf{F} = \int dV \mathbf{r} \cdot \nabla C_m \cos \theta f(r) = 2\pi \int_0^\pi d\theta \sin \theta \cos^2 \theta \int_{2a}^\infty dr r^3 f(r) |C_m| = \frac{q^2 r_0^2}{3\epsilon_0} \nabla C_m \quad [3.14]$$

Neglecting inertia this force must be balanced by the hydrodynamic drag, so that the micelle flux J_m (number of micelles per unit area per time) may be written

$$J_m = C_m \mu_m \mathbf{F} \quad [3.15]$$

where μ_m is the mobility of a micelle. Inserting the above expression \mathbf{F} allows us to write the flux in the form of Fick's law, as

$$J_m = -D_m \nabla C_m \quad [3.16]$$

with the diffusivity

$$D_m = \mu_m \frac{q^2 r_0^2}{3\epsilon_0} C_m \quad [3.17]$$

Now, the mobility may be approximated by the Stokes formula

$$\mu_m = \frac{1}{6\pi\eta a} \quad [3.18]$$

where η is the viscosity of the surrounding oil.

We can now compare the magnitude of D_m to that of the molecular diffusion constant $D_w = k_B T \mu_w$ of water in oil. The ratio of two diffusion constants is

$$\frac{D_w}{D_m} = (C_m r_0^3) \frac{\delta}{a} \frac{q^2}{k_B T 3\epsilon_0 r_0} \quad [3.19]$$

where $N_D = C r_0^3$ is the number of neighboring micelles within the Debye length, δ/a is the ratio of molecular- to micelle size, and the last factor is the ratio of the micelle electrostatic energy to the thermal energy. Taking $q = ze$, $r_0 = 3$ nm and T to the room temperature, the ratio can be written

$$\frac{q^2}{k_B T 3 \epsilon_0 r_0} \approx 100 z^2 \quad [3.20]$$

In order to have $D_e \gg D_m$, the charge number should have the relationship

$$z \gg \sqrt{\frac{a}{100 \delta}} N_D \quad [3.21]$$

with a condition that will be fulfilled for moderate z -values and $N_D \sim 1$. Therefore, the electrostatic driving of micelles may cause a water transport that could easily exceed that of molecular diffusion.

By considering water transport via micelle diffusion in alkanes, the flux of water $J_w^{micelle}$ (mole of micelles per unit area per time) can be expressed as

$$J_w^{micelle} = J_m = -\frac{q^2 r_0^2}{18 \pi \eta \epsilon_0 a} \frac{C_m}{N_A} \nabla C_m \quad [3.22]$$

where N_A is the Avogadro constant.

Therefore, the total flux of water in the x direction with the combination of water diffusion (equation 3.6) and micelle diffusion (equation 3.20) in alkanes can be given as

$$\begin{aligned} J_{total} &= J_w^{diffusion} + J_w^{micelle} \\ &= -\frac{D_w^{diffusion}}{dx} c(x) \ln \frac{a_w^{HSW}}{a_w^{LSW}} - D_m \frac{dC_m}{dx} \end{aligned} \quad [3.23]$$

where dx is the thickness of the alkane phase.

By considering the expansion of high-salinity water, the relevant concentrations of salt, soluble water, and micelles are dynamically changing with the increase in water volume. In absence of any chemical reactions, the water transport under dynamic conditions can be derived from Fick's first law and the mass conservation as follow,

$$\frac{\partial c_w}{\partial t} = \frac{\partial}{\partial x^2} \left[D_w^{diffusion} c(x) \ln \frac{a_w^{HSW}}{a_w^{LSW}} \right] + \frac{\partial}{\partial x^2} (\partial D_m C_m(t)) \quad [3.24]$$

3.2.4 Hypothesis on water transport in an n-alkane phase during LSWF

During the process of low-salinity water flooding, the contact of water-rock occurs significant changes shown in Figure 3-4 and described as follows. Before water injection into oil reservoirs, connate water (high-salinity brine) and crude oil take place in the pore spaces in the formation. With the invasion of low-salinity water, most crude oil is displaced, and few connate water is trapped by crude oil and solid rocks. With long-term liquid contacts, the trapped connate water gradually grows through the two scenarios as depicted in the Introduction section: water transport through oil phase and water diffusion through a water film. Accordingly, the oil phase moves due to the water expansion. Here we consider the situation of water transport through oil phase only.

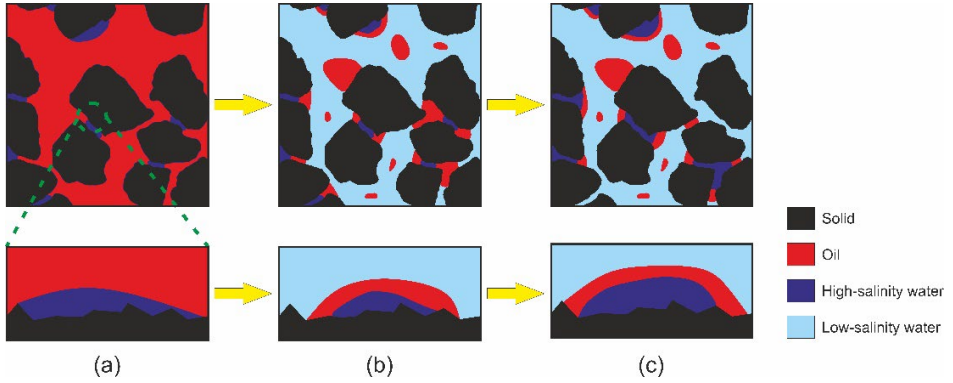


Figure 3-4. 2D Schematics of changes in brine-oil-solid contact during a low-salinity water displacement. (a), the initial state of connate water and crude oil in a porous domain; (b) shows the state after low-salinity water flooding; (c) shows the state after a long-term contact among LSW, oil and HSW.

Given the complex components in crude oil, we propose two processes of water transport through oil phase for explaining the pore-scale experiments: water diffusion for pure alkanes and water transport via reverse micelles and emulsions for surfactant presence, illustrated in

. Although the illustration has been proposed in Chapter 2, section 2.2, the following explanation is more suitable for the realistic situation, e.g., considering

the rock-fluid-fluid contacts in a pore and classifying the situations into two specific scenarios.

In the first scenario without considering surfactant effort (

a), the HSW-oil interface and LSW-oil interface contain different water concentrations inside the oil resulting from the salinity effect on water solubility. Schatzberg (1963) and Heidman et al. (1985) both proposed that high salinity has the potential to cause less water diffusion into oil, while low salinity causes a higher value. The interface of LSW-oil hence contains more water content than that of HSW-oil. Due to the chemical potential, water molecule diffuses from the LSW-oil interface towards the HSW-oil side. This hypothesis can be supported by a molecular dynamic simulation to describe the trajectory of water molecule movement inside heptane phases. In the second scenario (

b), the surfactant molecules gather on the water-oil interface for reaching the greatest affinity to minimize the energy. The surfactant molecules accumulate at water-oil interfaces with different concentrations that depend on the salinity concentrations of brine water on two sides of oil. When the concentration of surfactants around the interface is above the critical micelles concentration (CMC), micelles or reverse micelles (depending on the type of surfactant, either oil-soluble or water-soluble) will generate by diffused water molecules and dissociative polar components and eventually form microemulsion droplets in dispersed phases. In this work, we only discuss the case of reverse micelles, meaning that water is acting as the core of a reverse micelle. As the concentration of emulsion increases, the nucleated emulsion droplets may remain as a group and coalesce into larger droplets based on the balance between Gibbs free energy and entropic limitations (Miller, 1988). However, the size of these reverse micelles is highly dependent on the brine salinity, oil and surfactant properties (Binks & Clint, 2002). The increasing ionic strength may cause more asphaltene and resin molecules to adsorb at the interface, which leads to more compact and rigid films. The salt concentration influences the concentration of spontaneously formed reverse micelles. Higher ionic strength gives lower concentration and slows down the swelling of the reverse micelle. The repulsion between the charged micelles induces micelle movement and gradually leaves away from the water-oil interface. The reverse micelles contain water cores and contribute to water transport through the organic phases. Meanwhile, emulsification at the interface can reduce the surface tension and change the interfacial viscoelasticity,

which possibly reduces the viscosity force to the movement of HSW-oil contact line and help the HSW region expansion We attempt to prove this hypothesis through the following experimental and numerical approaches.

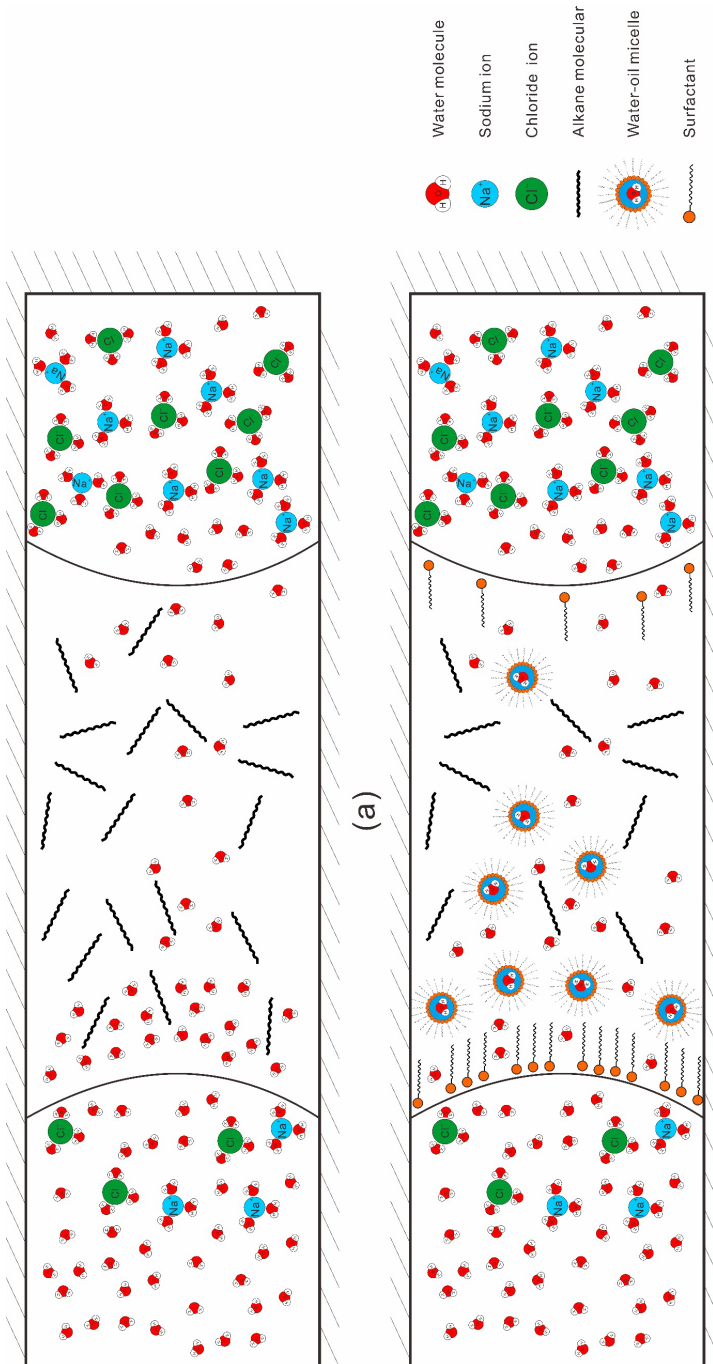


Figure 3-5. Schematics of water transport through oil phase under salinity difference. (a) is one scenario of water diffusion induced by the chemical potential; (b) is another scenario of water transport induced by both chemical potential and micelle transport.

3.3 Research approach

3.4.1 Microfluidic experiments

In this work, to quantitatively evaluate the process of water diffusion through an n-alkane phase and its contribution to the remobilization of constrained oil, we conducted a series of experiments in glass microfluidic devices with complex pore structures, mimicking the conditions at the tertiary low-salinity waterflooding process in oil reservoirs. Crude oils are customarily characterized by the type of hydrocarbon compound that is most prevalent in them: alkanes, naphthenes, and aromatics. The composition of crude oil varies depending on the geological reservoir and source. Alberta Sweet Mix Blend oil was identified to contain 281 compounds, where the n-alkane distribution shows that n-C8 to n-C17 were present in a higher concentration than other n-alkanes (Z. Wang, Fingas, & Li, 1994). Our previous work (L. Yan, Aslannejad, Hassanizadeh, & Raoof, 2020) showed that the salinity contrast could affect the constrained crude oil movement. However, due to the complex components of crude oil, it is difficult to give a quantitative analysis and to properly distinguish the contributions of each compound to the experimental results. Therefore, we consider choosing two normal alkanes with different carbon chain lengths to present the experiments and reflect the phenomenon of water transport through oil.

The transparent micromodel provides an ideal environment to visualize dyed fluids and their behaviors in the porous medium. Before the experiments, the micromodels were treated to become hydrophobic in order to gain an oil-wet solid and prevent the formation of thin water films on the pore walls. We have conducted a series of microfluidic experiments with three different salinity contrasts and four synthetic oils to ascertain those two aspects in a relatively realistic pore-scale system. We sequentially inject high-salinity brine, oil and low-salinity brine into the micro-chip and expect to establish a sandwich-like contact of HSW-oil-LSW, like the distribution in Figure 3-6, where the oil phase was confined between LSW and HSW. Without external flow and pressure disruption, a $2,797.16 \times 2,238.39 \mu\text{m}^2$ area is continuously observed over 70 hours under a high-resolution microscope. Through the experiments, we are able to monitor the oil movement induced by expansion in the trapped HSW area and distinguish the

difference in the addition of surfactant in oil phases. Furthermore, the evaluation of salinity contrasts is described by giving an analytical method.



Figure 3-6: Illustration of fluid contacts in microfluidics.

Microchip information and wettability fabrication

To obtain the direct pore-scale visualization of fluid behavior, we build an optic setup using an Olympus SZX7 Zoom Stereo Microscope with a magnification range from 8x to 56x connecting to a 9-megapixel UC90 digital camera with a high resolution of $\sim 0.83 \mu\text{m}/\text{pixel}$. The micro-chip holder is placed on the manually driven stage on the microscope platform. A dual-drive system syringe pump, Harvard Apparatus Pump 33 DDS, is used for fluids injection into the microchip for mimicking the waterflooding process in an oil reservoir. The quasi-2D microchip is provided by Micronit Technologies B.V., the Netherlands. The microchip (Figure 3-7 b) has a top-view domain of 10 mm (width) \times 20mm (length), with a permeability of 2.5 Darcy and a porosity of 57%. Note that the porosity and permeability are expected not to affect water transport through oil phase in the pore space of micro-chips. It is made of borosilicate glass and designed with random grain structures (black areas in the figure) to represent the rock shape in one slice of sandstone core. The anisotropic acid etching method is applied to achieve the pore spaces with a uniform depth of $20 \mu\text{m}$.

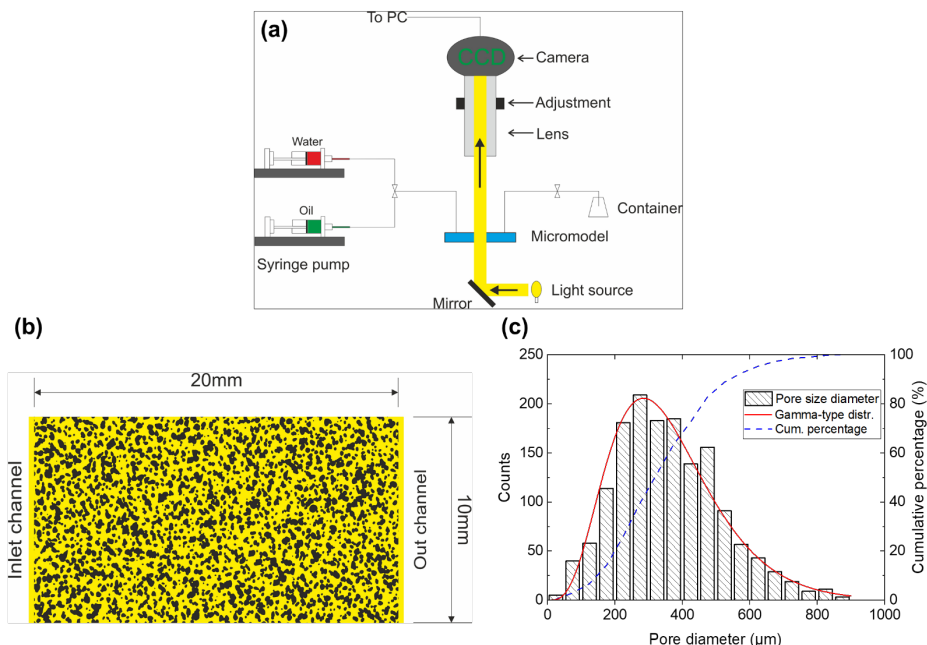


Figure 3-7: Images of microscope setup and microchip design. (a) shows a schematic picture of observation setup; (b) gives a bird's view of the microchip. Black areas are the grain structures, and yellow areas are the pore space and inlet/outlet channels; (c) shows the pore diameters distribution and the gamma-type fitted curve.

To avoid the generation of water film along the grains, we fabricate the microchips from naturally water-wet to oil-wet, by using a siliconizing fluid, 1,7-Dichloro-1,1,3,3,5,5,7,7-Octamethyltetrasiloxane. The siliconizing fluid is diluted with heptane to make a 1% v/v solution. Afterwards, we sequentially inject the diluted solution, heptane and methanol, into a dry and clean microfluidic chip with an injection rate of 50 $\mu\text{L}/\text{min}$ for 5 minutes each. When finishing the injections, we put the micro-chip in the oven at 80°C and dry it for 24 hours.

To avoid the formation of water-thin films on the pore walls, we rendered the wettability of micro-chips from naturally water-wet to oil-wet. A siliconizing fluid, 1,7-Dichloro-1,1,3,3,5,5,7,7-Octamethyltetrasiloxane, was used for this purpose. The procedure, similar to the procedure used in Arab, Kantzas, Torsæter, Akarri, and Bryant (2021), is briefly explained below.

- Dilute the siliconizing fluid in heptane to make a 1% v/v solution.

- Sequentially inject the solution, heptane, and methanol into a dry and clean microfluidic chip with an injection rate of 50 $\mu\text{L}/\text{min}$ for 5 minutes each.
- Dry the chip in the oven at 80°C for 24 hours.

After treatment, the micro-chip renders strongly oil-wet. The contact angles of water, dodecane and dodecane+Span 80 droplets in the air are $\approx 97^\circ$, $\approx 17^\circ$ and $\approx 10^\circ$, respectively, as shown in Figure 3-8.

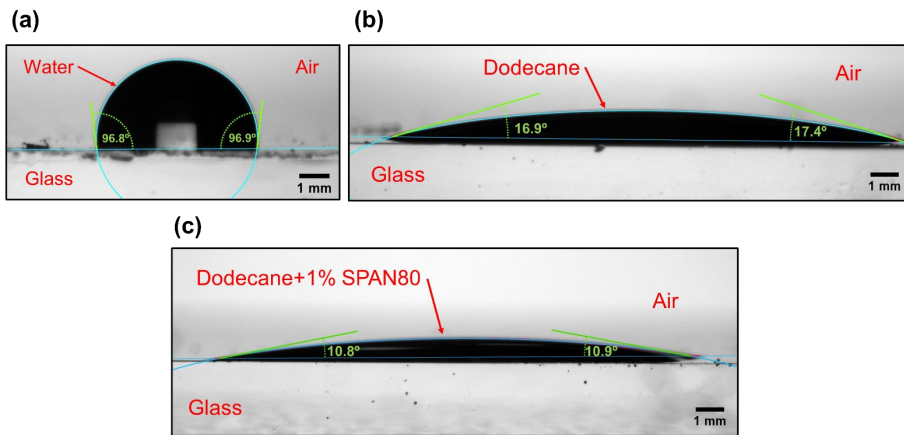


Figure 3-8: Pictures of contact angle on the modified glass microchips. (a), water contact angle in air; (b), dodecane contact angle in air; (c) dodecane+1% Span 80 contact angle in the air.

Therefore, we assumed that there were no thin water films along the grain surfaces and no water flux through corners. Moreover, our previous work (L. Yan et al., 2020) in glass-based capillaries also has demonstrated that there was no continuous fluorescent water film generated along the solid surface during the fabrication procedures, either with hydrophilic capillaries or hydrophobic capillaries.

Fluid preparation and Injection procedures

We prepared three types of brine and four types of alkanes: 1.7 g/L LSW, 50 g/L LSW, 200 g/L HSW, pure dodecane, dodecane + 1% or 2% Span 80, pure heptane, and heptane + 1% Span 80. All chemicals were purchased from Sigma Aldrich. High-salinity water was synthetically made by mixing deionized water and different amounts of four pure salts to produce a ≈ 170 g/L solution: NaCl,

Na_2SO_4 , $\text{MgCl}_2 \cdot 6\text{H}_2\text{O}$, and $\text{CaCl}_2 \cdot 2\text{H}_2\text{O}$. Then, we diluted the HSW either 100 times or four times to obtain two salinity brines of 1.7 g/L LSW and 50 g/L LSW, respectively. The composition of high-salinity brine is listed in Table 3-1. N-heptane (C_7H_{16}) and n-dodecane ($\text{C}_{12}\text{H}_{26}$) are selected as the oil phases for verifying the effect of carbon chain lengths and equilibrated with high salinity water for 24 hours. To investigate the emulsification effect, we added hydrocarbon-soluble Span 80 to both dodecane and heptane for creating the water-in-oil micro-emulsions in the oil phase. The concentration of 1% w/w Span 80 ($\approx 1.75 \times 10^{-2}$ mol/L) has far exceeded 1,000 times the critical micelle concentration for heptane (1.8×10^{-5} mol/L) and dodecane (1.9×10^{-5} mol/L) (Peltonen, Hirvonen, & Yliruusi, 2001).

Table 3-1: Chemical composition of high-salinity brines at ambient conditions

Ion	Compound added	Mol. Weight (g/mole)	HSW Concentrations (mg/L)
Na^+	NaCl	58.44	50374
Ca^{2+}	$\text{CaCl}_2 \cdot 2\text{H}_2\text{O}$	146.8	10983
Mg^{2+}	$\text{MgCl}_2 \cdot 6\text{H}_2\text{O}$	203.1	1586
SO_4^{2-}	Na_2SO_4	142.04	234
Cl^-			109181
TDS*			172358

*-Total dissolved solids

To clearly distinguish the three phases under the camera, we dyed the low-salinity brine and oil with two different dyeing chemicals, methylene blue, and Sudan red, respectively. Methylene blue makes low-salinity brine appear blue under the microscope, while Sudan red tints oil brown. No dye is added to the 170 g/L high salinity brine, which remained transparent. Note that only a few amounts of dyes can achieve the staining effect and do not influence the fluid properties. Thereafter, we always filter the dyed solution to remove undissolved dye particles and prevent pore clogging.

For generating the LSW-oil-HSW system inside a microchip, we first vacuum all the air in a wettability-modified and then saturate it with high-salinity water considered as resident water. Subsequently, the oil phase, i.e., heptane or dodecane, is injected at a rate of 100 $\mu\text{L}/\text{min}$ to displace HSW out of the microchip. Due to the relatively high injection rate, most HSW can be displaced

by the injected oil, and the rest of HSW remains in the microchip. Next, LSW is injected at a rate of 5 $\mu\text{L}/\text{min}$ (about 0.4 ft/day) to flush out most of the oil. The injection is stopped when the LSW breakthrough occurs. We wait 30 minutes for allowing fluid distribution inside the microchip to become stable. Finally, the inlet and outlet valves are shut down to avoid external interference. These injection procedures provide multiple sandwich-like clusters of LSW-alkane-HSW in the irregular-shaped pores. With the addition of Span 80, the surface tension of the water-oil significantly decreases and varies with time. To approximately calculate the capillary number, we assume the surface tensions for the oily phases (heptane, dodecane, heptane+Span 80, and dodecane+Span 80) have a wide range of 1~50 N/m (Benmekhbi, Simon, & Sjöblom, 2014). Therefore, the capillary number has the range of $3 \times 10^{-8} \sim 1.4 \times 10^{-6}$ and the tertiary fluid displacement in the porous media is dominated by capillary force. Overall, two types of experiments are carried out: with and without adding Span 80 to an alkane. All types of experiments are listed in Table 3-2. Additionally, four baseline experiments are performed without a salinity contrast, where the resident water and flooding water both have a salinity of 1.7 g/L. Each experiment is repeated twice to check the reproducibility. To acquire the change of water-oil interfaces, the observed domain containing at least one LSW-oil-HSW cluster is continuously monitored for at least 70 hours at room temperature.

Table 3-2: List of experiments conducted in micro-chips

Exp. No	Series	Alkane type	Resident water	Flooding solution	Info.
1	Without surfactant	n-heptane	HSW (170 g/L)	LSW (1.7 g/L)	reference
2			HSW (170 g/L)	LSW (50 g/L)	
3			LSW (1.7 g/L)	LSW (1.7 g/L)	
4		n-dodecane	HSW (170 g/L)	LSW (1.7 g/L)	
5			HSW (170 g/L)	LSW (50 g/L)	
6			LSW (1.7 g/L)	LSW (1.7 g/L)	
7	With surfactant	n-heptane+1% Span 80	HSW (170 g/L)	LSW (1.7 g/L)	reference
8			HSW (170 g/L)	LSW (50 g/L)	
9			LSW (1.7 g/L)	LSW (1.7 g/L)	
10		n-dodecane+1% Span 80	HSW (170 g/L)	LSW (1.7 g/L)	
11			HSW (170 g/L)	LSW (50 g/L)	
12			LSW (1.7 g/L)	LSW (1.7 g/L)	

By continuously monitoring the areas of interest for 70 hours, we captured the movement of alkane/water interfaces and changes in the HSW regions. With the aid of the relevant image processing and measurement, we estimated the process of water diffusion and its contribution to the HSW swelling. Furthermore, we carried out molecular dynamic (MD) simulations with three different brines to better understand the molecular mechanisms of water diffusion in the n-heptane phase due to the salinity difference. As the molecular level resolution (corresponding to nanoseconds and angstrom scales) is significantly higher than those in pore-scale experiments, MD simulations allowed us to observe the behavior of water molecules across the heptane phase at various positions that are difficult to be directly observed and analysed in pore-scale experiments.

3.4.2 Molecular dynamic model and simulation details

In order to explore the water salinity effect on water transport across an oil film and the resulting alkane remobilization at a pore-scale, a simulation system consisting of the major ingredients used in experiments was designed. The dimension of the system is shown in Figure 3-9. All MD simulations were carried out using the LAMMPS package (Plimpton, 1995). The visualization and analysis were implemented by the OVITO software (Stukowski, 2009). Specifically, pure water (PW) and saline water (SW) were set on the two sides of a layer of oil phase (pure heptane). The system was assigned periodic boundary conditions. However, in order to guarantee the differences in salinity at two sides of the oil phase, graphene layers were used as separators on the z-direction at both ends of the simulation box, like many previous studies (Wen Li et al., 2016; P. Wang et al., 2017; Y. Yan, Wang, Li, Loh, & Zhang, 2017). The graphene layers would not affect the interactions of water molecules with the oil phase due to the cut-off distance. The oil phase had a thickness of 36 Å covering the whole cross-sectional area of the simulation box ($102 \times 51 \text{ Å}^2$). The density of the oil phase was calibrated to match experimental measurements (Aminabhavi, Patil, Aralaguppi, & Phayde, 1996; Patterson & Morris, 1994). In total, the system contained 705 heptane molecules and 16374 water molecules (half on each side). The Na^+ and Cl^- ion concentration in one of the water layers was chosen so as to correspond with the experiments in this work, namely with the concentration of 0 g/L, 50 g/L, and 170 g/L. Thus, three types of systems with ion concentration differences between two water-solution layers of 0 g/L-0 g/L, 0 g/L-50 g/L, and 0 g/L-170 g/L were modeled.

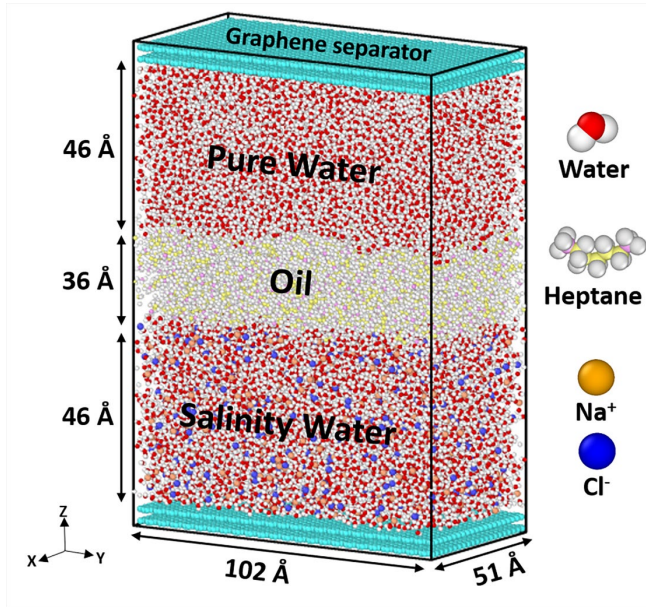


Figure 3-9: Simulation system and the structures of the molecular components.

The Optimized Potentials for Liquid Simulations All-Atom (OPLS-AA) force field was applied for heptane molecules (Jorgensen, Maxwell, & Tirado-Rives, 1996), and the simple point charge (SPC) model was used to describe water molecules (Berendsen, Grigera, & Straatsma, 1987). Na^+ and Cl^- ions were modeled using the Leonard-Jones parameters derived by Aluru et al. (Joung & Cheatham III, 2008). Leonard-Jones potential (LJ 12-6) and the Coulomb potential were employed to describe the non-bonded interaction and the electrostatic interaction, respectively, as defined by Eq. (5) below:

$$V_{\text{non-bonded}} = 4\epsilon_{ij} \left[\left(\frac{\sigma_{ij}}{r_{ij}} \right)^{12} - \left(\frac{\sigma_{ij}}{r_{ij}} \right)^6 \right] + \frac{q_i q_j}{4\pi\epsilon_0 r_{ij}} \quad [3.25]$$

where ϵ_{ij} and σ_{ij} denote the energy well depth and van der Waals radius, and q_i were the atomic charge of atom i . Arithmetic mixing rule was adopted to calculate LJ potentials between species i and j . The cut-off distance was 12 Å. For long-range electrostatic interactions, the particle-particle particle-mesh (PPPM) method was chosen (Hockney & Eastwood, 2021). The force field parameters for all atoms were given in Table SI-1 in the supporting materials.

For all simulations, the graphene separators were position fixed as the solid wall. The rest of the system was first energy-minimized using the steepest descent method and subsequently subjected to equilibration under the NVT ensemble. The time step used in the simulation was 1 fs. The temperature of the system was fixed to 340 K using the Nosé–Hoover thermostat with a damping coefficient of 100 fs (Nosé, 1984). The equilibration time of the system was 1 ns. Five independent simulations were carried out for each system, each with a simulation length of 46 ns. The trajectory of the simulation was collected every 10000 fs during the simulation for the analysis of water diffusion and mass transport in the system.

3.4.3 Interfacial behavior experiments

Dynamic Light scattering set-up

Dynamic Light Scattering (DLS) was used to measure the micelles size of emulsions. Dynamic light scattering is a technique that determining the size distribution profile of small particles in suspension or polymers in solution [38]. The Zetasizer Nano measures particle size across the range 0.3 nm to 10 μm . The system is highly sensitive to the presence of low levels of aggregates or larger particles because light scattering intensity correlates with particle size to the power six. We used Zetasizer Nano ZS90, which was purchased from Malvern Panalytical. The picture of the equipment, sample chamber and light scanning methods for Zetasizer are shown in Figure 3-10. A monochromatic light source, usually a laser, shot through a polarizer and into the sample. The scattered light then goes through a second polarizer, where it is collected by a photomultiplier with the resulting image projected onto a screen. Small particles in a suspension/dispersion are subject to Brownian motion. The rate of Brownian motion can be directly determined from the scattered light pattern created by the moving particles. Analysis of these short-term intensity fluctuations yields the speed of the Brownian motion, which is used to calculate the particle size with the Stokes-Einstein relationship.

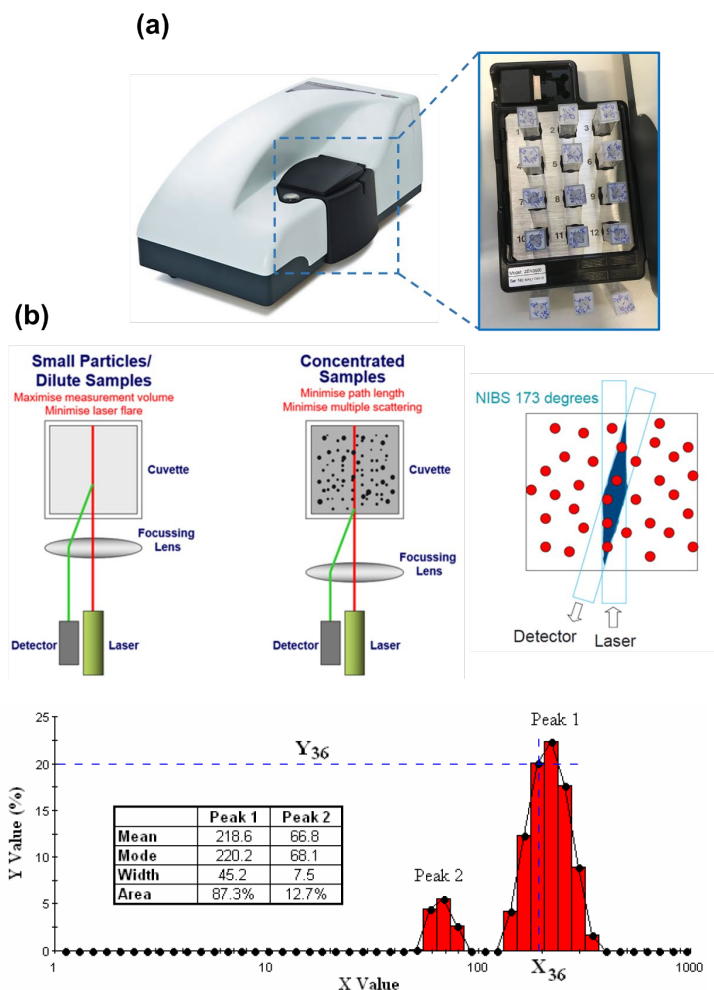


Figure 3-10: Pictures of DLS system. (a), photos of Zetasizer Nano ZS90 and a sample holder; (b), schematic showing the key components of a DLS system – laser, detector, focussing lens and cuvette (which holds the sample) – in a NIBS configuration. The acquired result from ZetaSizer is also explained.

The application of the Backscatter detection is by a patented technology called NIBS (Non-Invasive Back-Scatter). This detects scattered light at a large angle relative to the incident beam (173° in the case of the Zetasizer Nano) which not only increases sensitivity but also extends the range of concentration over which accurate size data can be collected by reducing multiple scattering. Multiple scattering is when the scattered light interacts with more than one particle before

detection. Within the Zetasizer Nano, NIBS technology also includes high-quality movable optics that automatically optimises the focus position of the lens to reduce multiple scattering, improve the signal to noise and thereby increase accuracy for all samples. The overall result is accurate, relevant particle size data across a concentration range running from 0.1 ppm to 40 g/L w/v, enabling measurement of the widest range of formulations without any need for dilution.

What main result we can expect from Zetasizer experiment is the peak statistics, which allow users to gain the values of the mean, mode, width, and area calculated according to standard statistical procedures, shown in the above figure. For peaks that coalesce, the peak extent is defined to be the saddle point, and the statistics are then computed over this modified peak extent. Peak statistics are calculated using the expressions given as, $\%Area = \sum_i Y_i$ and $Mean = \sum \frac{S(i)I(i)}{Area}$, where Area is defined as the area under each peak, relative to the total area of the distribution, Mean is defined as the average value of the peak, weighted by the Y axis parameter; Y_i is the Y axis value of the i th X axis class/bin and X_i is the X axis value in the center of the X axis class/bin.

Sample preparation

Sample Clean and square cuvettes made of scratch-free glass or optically translucent disposable plastic (3×3 mm, 5×5 mm or 10×10 mm) are used. Plastic cuvettes with inbuilt electrodes capable of DLS measurement is also available. The sample should be clean, homogeneous and transparent without any precipitation. The minimal volume of sample required varies with the model (12 μ L for Zetasizer). However, at least 1–2 ml of sample should be prepared in order to obtain good quality data. To study the emulsion properties generated by spontaneous emulsification, we first placed the salinity brine at the bottom of a cuvette and then gently covered the brine with a layer of oil on the top, Figure 3-11 (a). The emulsion generation zone height is a little lower than the laser height to detect the emulsion size change versus time.

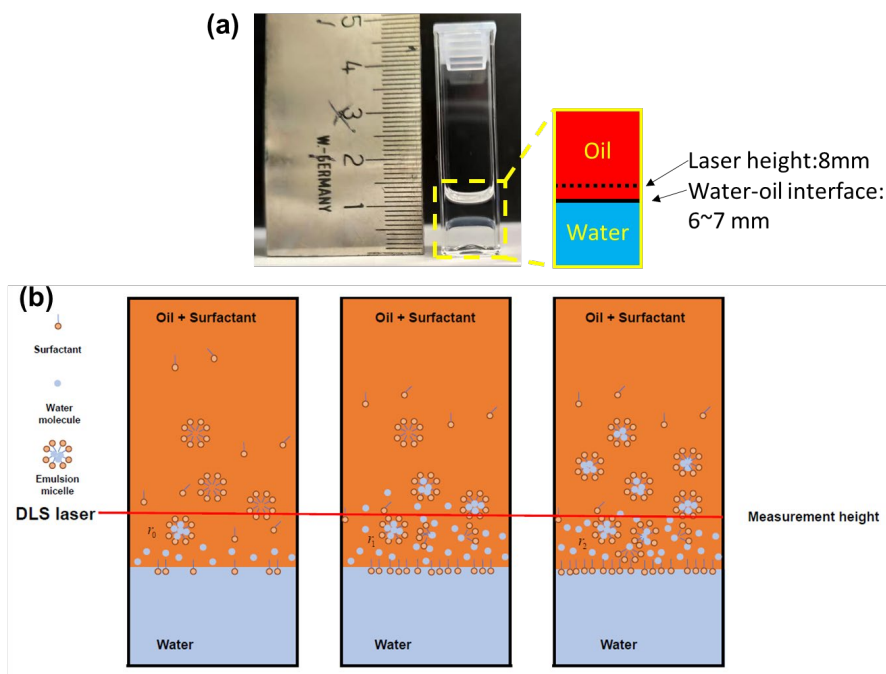


Figure 3-11: Photo of one sample and a proposed governing mechanism for the spontaneous emulsification. (a), picture of one sample, where oil is placed on the top and brine at the bottom of the cuvette; (b), a diagram of the emulsification process during 24-hour monitoring. The water-in-oil emulsions first spontaneously form at the water-oil interface and then diffuse into the oil phase (illustration is modified based on the reference Davis, Martinez, Howarter, and Erk (2020)).

When the alkane phase covers the surface of the aqueous phase, spontaneous emulsification occurs (Figure 3-11 b). Diffusion is the dominating mechanism and is responsible for spontaneous emulsification of these systems. Additionally, these convective flows are driven in part by the diffusion of oil into the aqueous phase as well as the electrostatic interactions among reverse micelles. At the beginning of water-oil contact, oil molecules begin to diffuse through the water. In the mediate period (generally minutes to hours depending on the alkane type and surfactant concentration), the oil molecules reach the fixed measurement location, enter surfactant micelles in that vicinity, and swelling is detected. Afterwards, the water-in-oil micelles at the measurement location grow gradually with time. The initial micelle size is smaller than the micelle size after swelling with oil. Note that this mechanism is proposed for the case of oil-soluble

surfactants and requires the presence of surfactant micelles (i.e., the surfactant concentration must be above the CMC).

To compare the effects to the observation in the microfluidic experiments, we use the same brine as in the microfluidic experiments i.e., 0, 1.7 g/L, 17 g/L, 50 g/L and 170 g/L. The samples are listed in Table 3-3: List of samples and measurement information.

Table 3-3: List of samples and measurement information

Aqueous solutions	Oil type	Surfactant	Measurement interval time
DIW	heptane		
1.7 g/L			
17 g/L	—————	1% Span 80	Every 0.5 hours within 1 day
50 g/L			
170 g/L	dodecane		

Note: Oil solution is prepared by mixing 1% wt Span 80 and stirred overnight.

Pendant drop experiment set-up

Pendant drop tensiometry offers a solution to determine surface and interfacial tension and observe the droplet behavior in many colloidal systems. An experimental investigation of spontaneous emulsification is proposed with a brine drop pendant in a dodecane environment with adding surfactant. The experimental apparatus consists of a camera, a dispensing system, and a light source. The drop shape analyzer is KRUSS DSA100E. The schematic of the apparatus is shown in Figure 3-12.

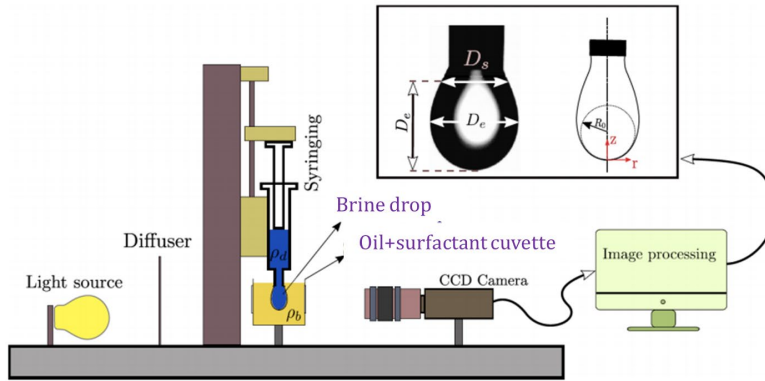


Figure 3-12: Sketch of the pendant drop experimental apparatus (Ahmadikhamsi, Golfier, Oltean, Lefèvre, & Bahrani, 2020)

In each experiment, a syringing pump is used for injecting the fluid until the desired drop size ($\approx 9 \mu\text{L}$). A brine drop is generated in the open cuvette that is prefilled with surfactant-added oil phase. The whole process is recorded for over 5 hours using a CCD camera (DMK 23U618, Monochrome, up to 120 images/s, The Imaging Source, Bremen, Germany) connected to a PC. The oil here is dodecane + 1% Span 80. Similar to the experiment of dynamic light scattering, we prepare four synthetic brines (0, 1.7, 17, and 50 g/L) to form a pendant drop. Meanwhile, the surface tension of water-dodecane+Span 80 can be also measured. The interfacial tension is then calculated from the Bond number as follows:

$$B_o = \frac{\Delta\rho g R_0^2}{\gamma} \quad [3.26]$$

where the density difference is $\Delta\rho = \rho_b - \rho_d$, ρ_b and ρ_d are the bulk (oil) and drop (brine) densities, respectively. R_0 is the drop dimension, γ is the interfacial tension, and g is the gravitational acceleration.

3.4 Result and discussion

3.4.1 Microfluidic experiments

3.4.1.1 Observation of water diffusion in pure alkanes

Given massive images and results, we mainly present the detailed results for experiments No.1 and 4 in this section, while other results are shown in Appendix B. The monitoring domain has an area of $2,797.16 \mu\text{m} \times 2,238.39 \mu\text{m}$ (width \times height). Over 70 hours of observation, we select the regions with stable clusters of LSW-Oil-HSW and develop the image and data processing method described in Appendix B. Therefore, a quantitative analysis can be given for the expansion rate of HSW areas, water volumetric flux and the dimensionless flux in oil phases.

Experiments with *n*-heptane

In this experiment, the observed domain is shown in Figure 3-13.

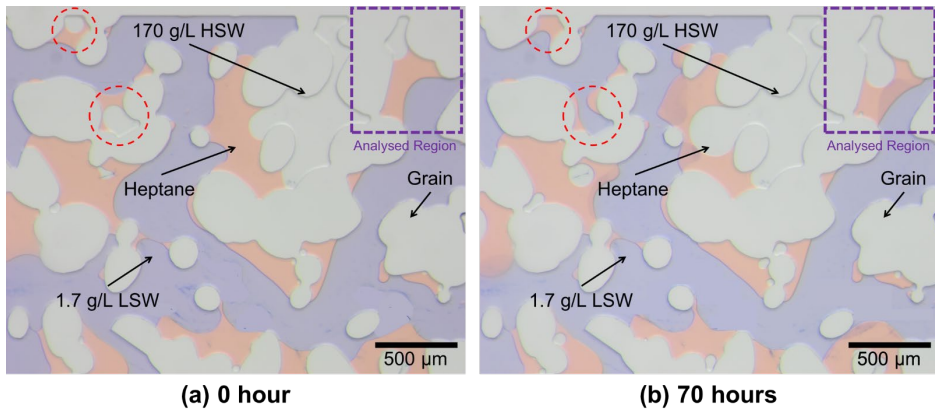


Figure 3-13: Images of the observed domain in experiment No.1 at 0 hour and 70 hours, where the oil phase is pure *n*-heptane.

There is no emulsification observed in the whole monitoring process. In the figure, blue areas represent the bulk phase of 1.7 g/L LSW in the micro-chip. Light brown areas are the heptane phase which is confined among low-salinity water, grain and resident high-salinity water. The colorless regions along grains are the trapped 200 g/L HSW. The color of HSW and the grains are identical, but we can easily filter out the areas of the grain by using the micromodel mask in image analysis. The blue-dashed square delineates the zone selected with clear isolated LSW-heptane-HSW systems for showing the HSW expansion and further discussion. We notice all HSW areas have significant swelling and the curvature of the HSW-heptane interface gradually increased, which induces the constrained oil motion. Correspondingly, the distance between the HSW-heptane interface and LSW-heptane interface decreases. One interesting phenomenon is the sudden burst of expanded HSW bubbles when the two interfaces touch each

other, shown in the red dashed circles. Through bubble-bursting, HSW eventually merges into the bulk phase and the surrounding oil phase is therefore relocated and absorbed along the solid grains.

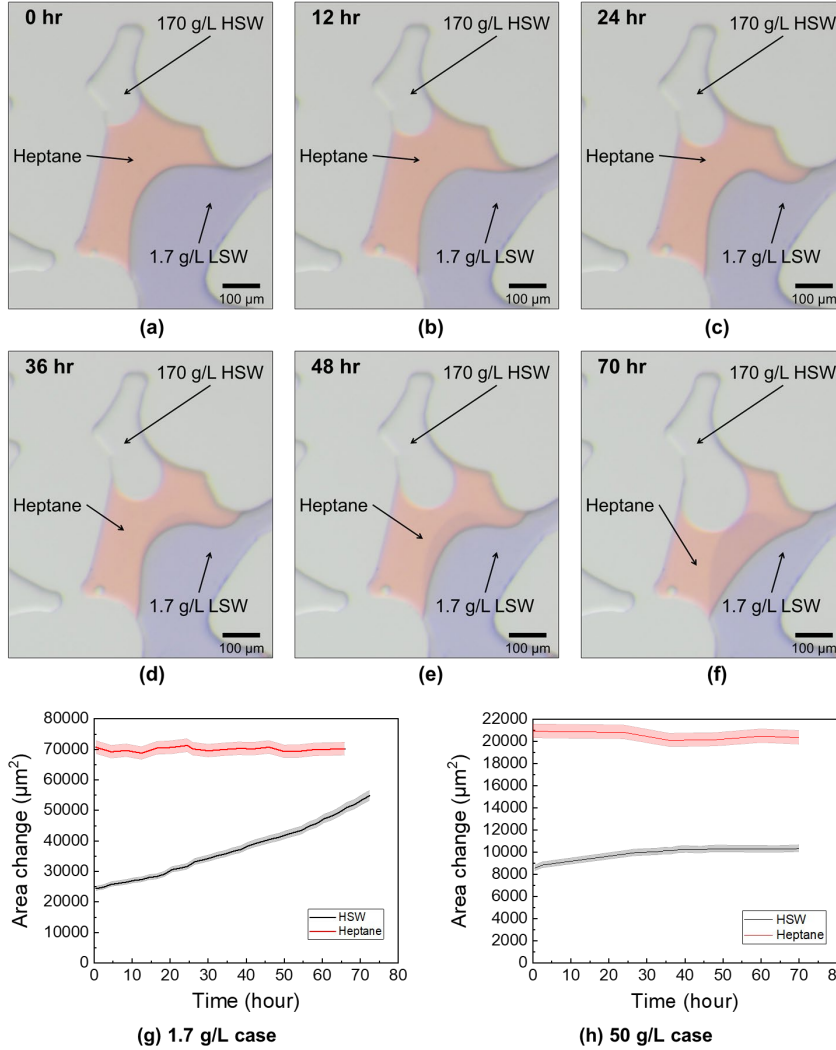


Figure 3-14: Images of the isolated LSW-heptane-HSW cluster in the analyzed region at six different times from 0 to 70 hours, (a-f). The bluish area presents 1.7 g/L LSW as the bulk phase. Heptane is shown in brown, and 170 g/L HSW is confined by heptane and solid surfaces. (g-h) gives the area changes of heptane and HSW for 1.7 g/L case and 50 g/L case for 70 hours, respectively. Measurement error is 3% and indicated in the shadow band.

Figure 3-14: (a-f) indicates the change in HSW area of the analyzed region during 70 hours of monitoring. We observe the curvature of the HSW water-alkane interface gradually increases, indicating there is a change in local capillary pressure between the HSW and the oil. The distance between the HSW and LSW interfaces therein decreases as well during the observation period. By measuring the area of HSW and the oil area (shown in Figure 3-14g), the HSW area in the analyzed region grew by 119.4%, while the heptane area is nearly unchanged. With the strong oil-wet microchip, we do not observe the thin water films of LSW along the grains. Therefore, the increase in the HSW area is attributed to water molecules passing through the heptane region. The fluid pressure inside HSW area increases caused by water flux through oil phase, which induces the menisci deformation and displaces the oil out of the throat. The images of the observed domain for the case of 50-170 g/L salinity contrast are shown in the figure B-1 of Appendix B. HSW area with lower salinity contrast has a slight swelling, reaching a plateau after about 30 hours, and eventually increases by 20.7% after 70 hours (Figure 3-14h), while the oil region area is still relatively constant. It is clear that the expansion in the HSW area is much less than with a higher salinity contrast.

In baseline experiment No.3, where connate and injected water has equal salinity of 1.7 g/L, water and heptane areas keep the equilibrium state during the observation period, indicating that a low-ionic environment without a salinity contrast does not cause any water transport through oil and no oil motion. The images are presented in Appendix B.

Experiments with n-dodecane

In order to investigate the influence of hydrocarbon length on water diffusion, we choose n-dodecane as another alkane solution and conduct experiments No.4-No.6. Figure 3-15 gives the images of the observed domain in experiment No.4 at 0 hour and 70 hours of observation. One region is analyzed to study changes in HSW and oil clusters in detail; see the blue-dashed square in Figure 3-15. Similar to the experiment with heptane, all trapped HSW areas get significantly expanded. The phenomenon of HSW bubble burst is also recorded and the surrounding oil is relocated.

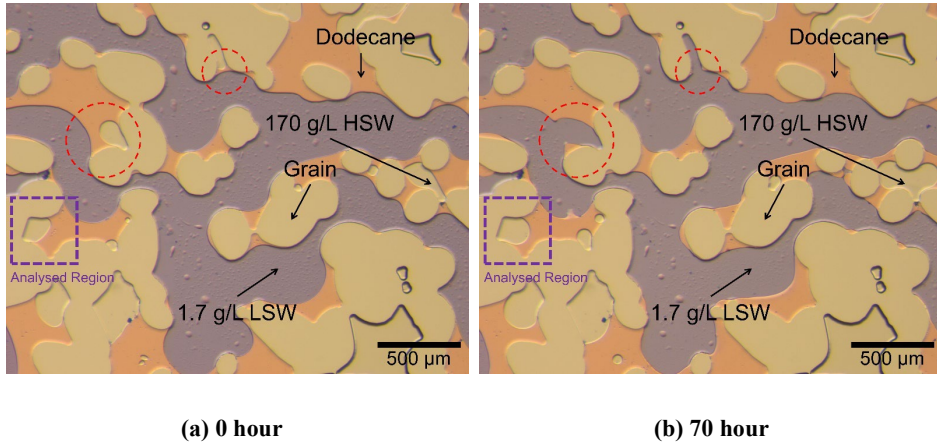
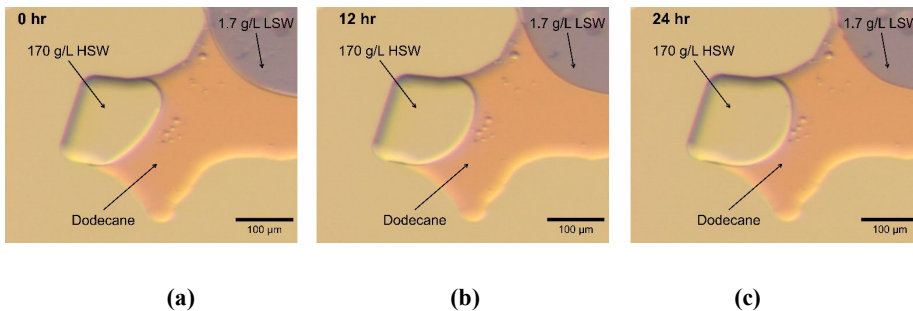


Figure 3-15: Images of the observed domain in experiment No.4 at 0 hour and 70 hours, where the oil phase is pure n-dodecane.

The zoomed-in images of the analyzed region are shown in Figure 3-16. From the images, the interface of HSW-dodecane becomes stretched, and the distance between HSW and LSW gradually decreases. Based on the area measurements, see Figure 3-16g, the HSW area grows by 41.2% after 70 hours, while oil areas do not have an obvious change. The area continues to expand after even 70 hours. For the case of 50 g/L LSW, all images are shown in Appendix B. HSW area finally expands by 82.7%. A similar trend is presented in the plotted curve of area change compared to the trend in heptane experiment. After about 30 hours, the HSW maintain a certain area, which means that the water diffusion in oil phase gets equilibrium. Note that the numbers of expansion can not be comparable for different areas and different experiments, because each analyzed region has an individual initial area of HSW, interface length of water-oil, and the thickness of oil phase. However, we can derive a dimensionless form for water flux and each region becomes to be comparable. The derivation of the dimensionless form is given in Section 3.



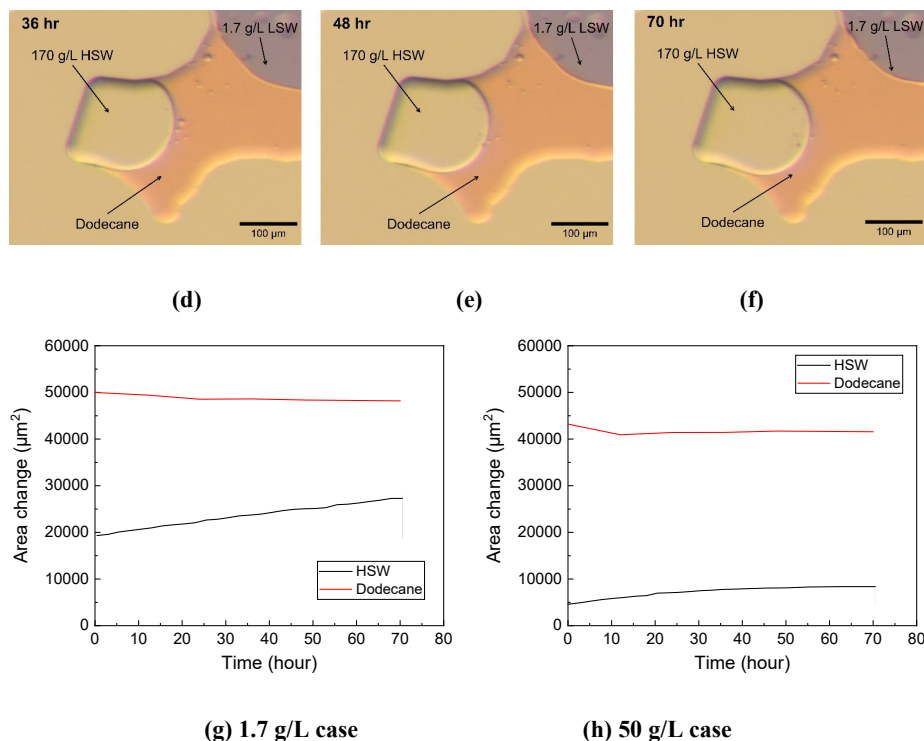


Figure 3-16: Images of the isolated LSW-dodecane-HSW cluster in the analysed region at six different times from 0 to 70 hours, (a-f). The bluish area presents 1.7 g/L LSW as the bulk phase. Dodecane is shown in brown, and 170 g/L HSW is confined by dodecane and solid surfaces. (g-h) gives the area changes of dodecane and HSW for 1.7 g/L case and 50 g/L case during 70 hours, respectively. Measurement error is indicated in the shadow band.

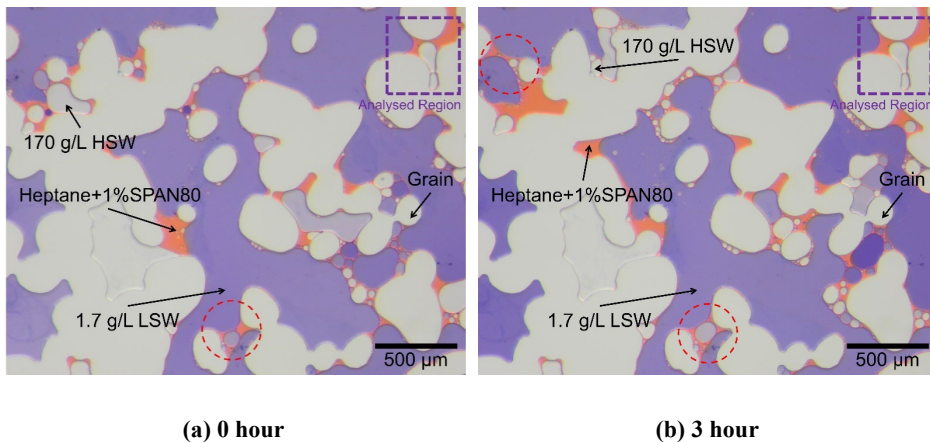
A reference experiment is conducted to verify no effect of low salinity on the water diffusion in alkane phases. The images of one LSW/dodecane/LSW system are presented in Appendix B. No obvious change in trapped LSW areas is found. It proves that a low-salinity environment has no effect on oil remobilization for both types of alkanes.

3.4.1.2 Observation of water transport in Span 80-added oil

To investigate the surfactant effect on water transport, we perform eight experiments by adding 1% or 2% Span 80 in pure heptane and pure dodecane and give two reference experiments with no salinity contrast for both alkanes. Results of experiments No.7 and 10 are mainly presented in the following two sub-sections. Other images and results can be found in Appendix B.

Experiments with n-heptane+ Span 80

Figure 3-17 presents the oil and water distributions in the observed domain for experiment No.7 at 0 and 70 hours of monitoring. In the figures, the oil phase (orange) is heptane with added 1% Span 80, and flooding water (purple) is 1.7 g/L LSW. The region for analysis is marked with a blue-dashed square. Unlike in experiments with alkanes, the microemulsions generate during water injection, although the injection rate is relatively low (5 $\mu\text{L}/\text{min}$). Within the first several hours of observation, the interfacial tension of the water-oil decreases dramatically. For example, the interfacial tension of water-decane drops from 30 N/m to 10 N/m after about 1-hour contact with a concentration of 0.01 wt% Span 80 (Benmekhbi et al., 2014). Besides, the presence of surfactant affects the emulsion stability, interface viscoelasticity and fluid coalescence (Ayirala, Al-Yousef, Li, & Xu, 2018). Therefore, compared to the cases without adding a surfactant, more emulsions form during the observation and the oil phase is preferable to be displaced along the grain. We also capture the dynamic change of oil collar shape and coalescence between grains, shown with the red dashed circles. At 3 hours of observation (upper circle in Figure 3-17b), one oil collar generates due to the oil relocation and film expansion surrounding the two grains. The collar thickness gradually grows with the oil invasion and displacement from out of the observed domain. The below circle shows similar changes for 70 hours. Another interesting phenomenon is that most water-in-oil emulsions do not burst even touching the HSW-oil interface, although they are continuously swelling.



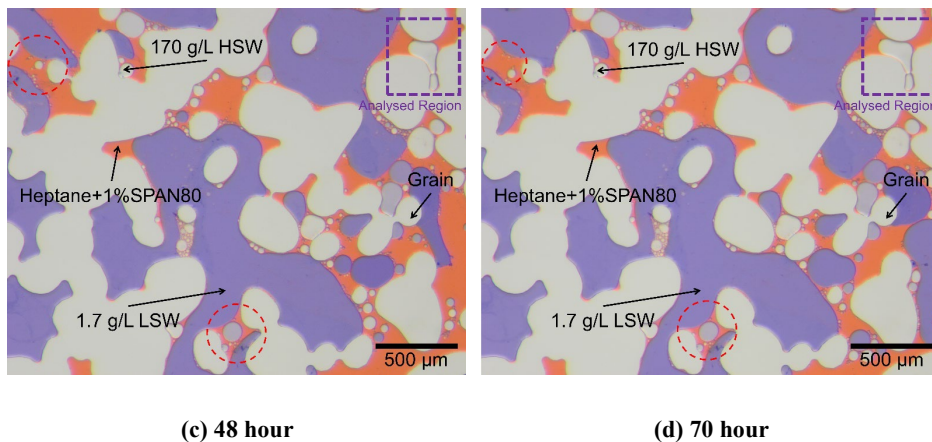
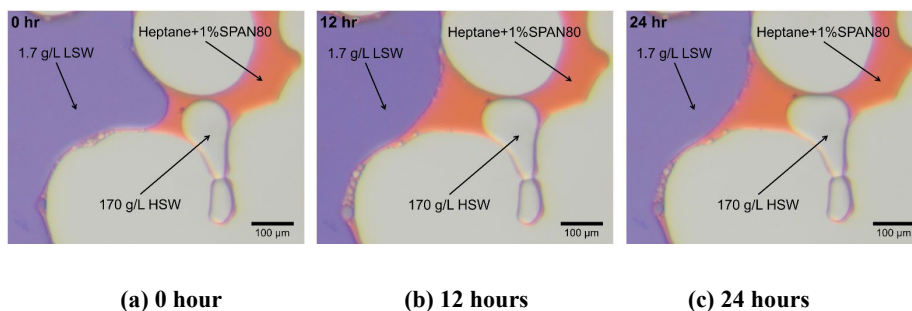
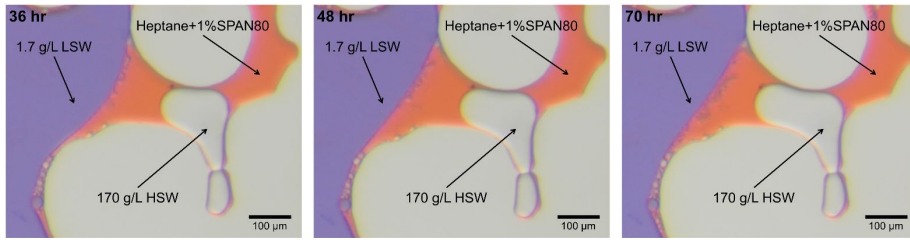


Figure 3-17: Images of the observed domain in experiment No.7 at 0, 3, 48 and 70 hours, where the oil phase is heptane+1% Span 80.

The varying emulsion and oil film introduce difficulties to find a stable system of LSW-oil-HSW for image and data analysis. Changes in the analysed region, in this case, are shown in Figure 3-18(a-f). HSW area swells significantly and deforms at the throat. Although the thickness of constrained oil film increases due to the unstable film flow, the distance between LSW-oil interface and HSW-oil interface is decreasing. Unlike the experiment with pure heptane, the thin oil film along the grains contains multiple micro-emulsions and dynamically varies its film thickness as the accumulation and swelling of emulsions. Notably, within the monitoring period, LSW-oil interface generates countless nano- to micro-scale emulsions and the front of aggregated emulsion gradually invades into the oil phase, whereas the HSW-oil interface does not show the capturable emulsions by the camera.

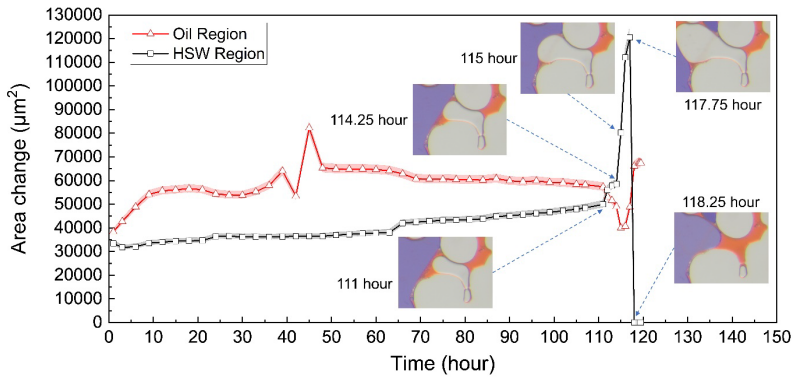




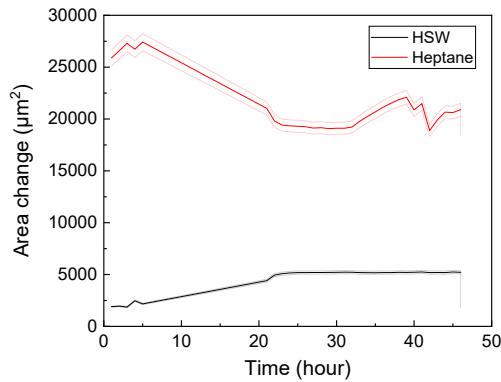
(d) 36 hours

(e) 48 hours

(f) 70 hours



(g) 1.7 g/L case



(h) 50 g/L case

Figure 3-18: Images of the isolated LSW-heptane+1%Span 80-HSW cluster in the analysed region at six different times from 0 to 70 hours, (a-f). The bluish area presents 1.7 g/L LSW as the bulk phase. Heptane is shown in brown, and 170 g/L HSW is confined by heptane and solid surfaces. (g) gives the area changes of oil and HSW for 1.7 g/L case during 70 hours.

Measurement error is indicated in the shadow band. Five representative images for the

sudden steps of the curves are added and pointed with the dashed blue arrows. (h) shows the results for the case with 50-170 g/L salinity contrast.

Figure 3-18g presents the oil and HSW area changes. The oil area shows unstable fluctuations, especially for the sudden decrease and increase in the analyzed domain after about 45 hours of observation. At 70 hours, the analyzed HSW region swells by 28.24% and has a relatively stable increase before 111 hours. The diagram also shows two stages of rapid growth in HSW area when the HSW-oil interface becomes closer to the LSW-oil interface. From 111 to 114.25 hours of observation, the front of HSW-oil interface gradually moves out of the throat until touching the LSW-oil interface and the length is elongated due to the divergence of pore throat. Afterwards, the HSW area dramatically expands and deforms within 3.5 hours before the bubble burst, which is induced by the fast water molecular diffusion from LSW to HSW. The high viscoelastic phenomenon is not observed in the experiments with pure alkanes. Finally, the HSW bubble cannot maintain the large deformation and mixes with LSW. The images for the No.8 experiment with 50 g/L LSW are shown in Appendix B. From the measurements, the HSW area in the analyzed region has an expansion of 174.51% after 46 hours. The plotted curve gives an obvious flat stage of HSW growth after around 23 hours, which has a similar tendency in No.4 experiment. The fluctuation of oil area comes from the unstable oil film along grains. One notable phenomenon is that the generated oil films are much thinner ($\sim 2\text{ }\mu\text{m}$ thickness and $400\text{ }\mu\text{m}$ length between two grains in the 46-hour image) than the ones in the experiments with pure n-heptane, displaying the high elasticity of the oil-water interfaces with the presence of surfactant. Besides, the LSW bulk phase is cut into parts by the thin oil films and there are no capturable emulsions generated around both LSW-oil and HSW-oil interfaces.

Experiments with n-dodecane+ Span 80

To study the effect of carbon chain length of oil, we conduct experiments with surfactant-added n-dodecane. Below we present four moments of the changes in the experiment No.10, shown in Figure 3-19. The analyzed region is marked with a blue dashed square. Most oil phases are stable and displaced in and out of the observed domain through film flow along the grains. The expansion in collar oil films is captured as well, shown in the left-hand red dashed circle. The other two circles indicate the good malleability of oil film due to the presence of Span 80, even if the expanded HSW almost directly contacts the LSW-oil interface for 70

hours without burst. Unlike in experiment No.7, oil phases do not contain multiple micro-emulsions close to each other and have less displacement in the observation period.

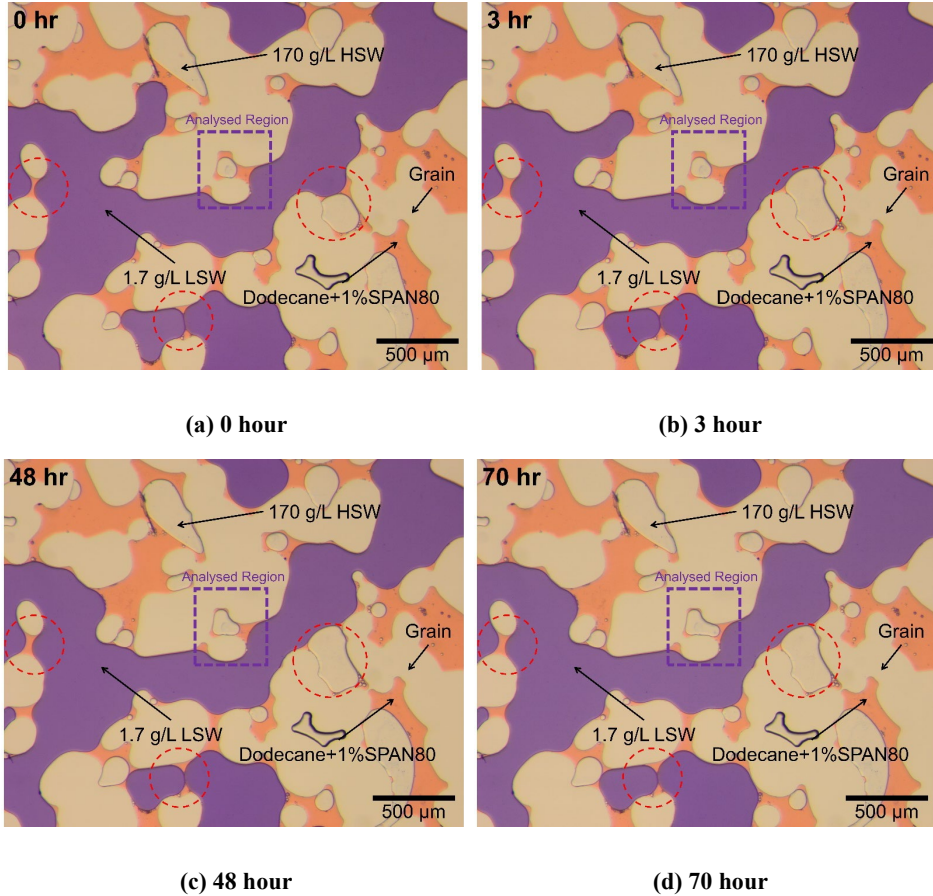
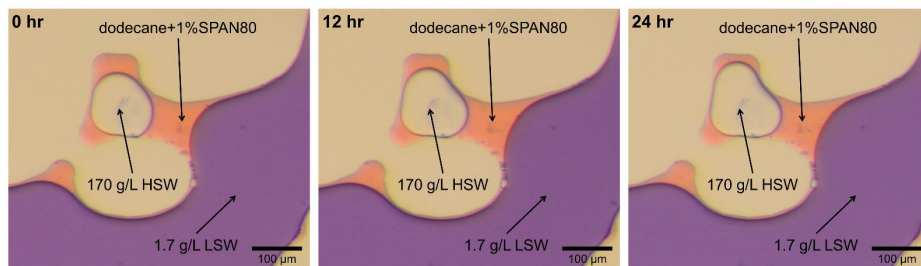


Figure 3-19: Images of the observed domain in experiment No.7 at 0, 3, 48 and 70 hours, where the oil phase is dodecane+1% Span 80.

Zoom-in images of the analyzed region are displayed in Figure 3-20. Within the first 70 hours, the HSW increases by 71.9% and gradually squeezes oil out of the pore space, therefore, the thickness of oil between HSW-oil and LSW-oil interfaces becomes narrow. The oil area continuously decreases because of the displacement. Around 74.5 hours, the two interfaces contact each other and the HSW area suddenly increases by 89.77% in 2.5 hours, as shown in Figure 3-20f. The front of HSW bubble rapidly jumps out the throat. After 77 hours, the HSW stops growing and yields the pressure balance between the HSW bubble and oil-

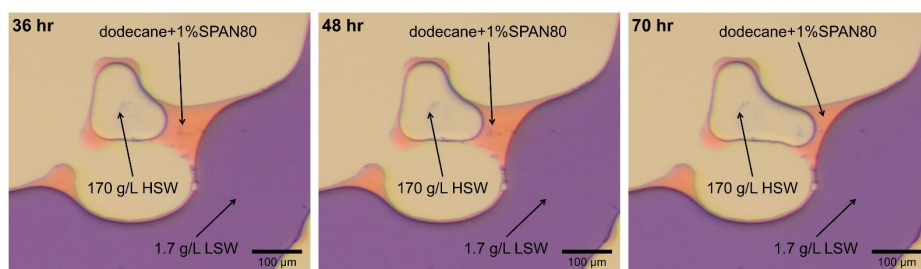
LSW surface tension. Another notable point is that fewer nano- to micro-emulsions are found around the LSW-oil interface inside oil phases than in the experiments with heptane. The generated emulsions, e.g., the black dots and colorless HSW-in-oil bubbles below pictures, remain the position and shape and have no significant swelling and aggregation.



(a) 0 hour

(b) 12 hours

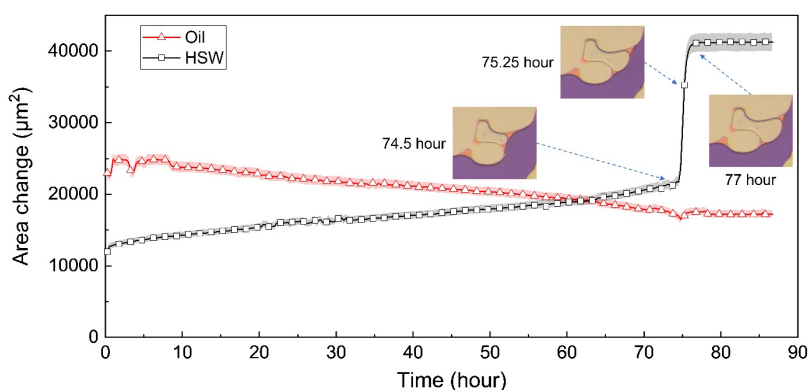
(c) 24 hours



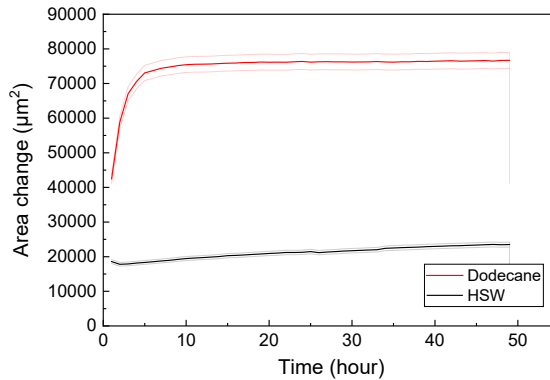
(d) 36 hours

(e) 48 hours

(f) 70 hours



(g) 1.7 g/L case



(h) 50 g/L case

Figure 3-20: Images of the isolated LSW-dodecane+1% Span 80-HSW cluster in the analysed region at six different times from 0 to 70 hours, (a-f). The bluish area presents 1.7 g/L LSW as the bulk phase. Dodecane is shown in brown, and 170 g/L HSW is confined by dodecane and solid surfaces. (g) gives the area changes of oil and HSW for 1.7 g/L case during 70 hours. Measurement error is indicated in the shadow band. Five representative images for the sudden steps of the curves are added and pointed with the dashed blue arrows. (h) shows the results for the case with 50-170 g/L salinity contrast.

Experiment No.11 with a salinity contrast of 50-170 g/L is shown in Appendix B. The measurements for oil and HSW areas are plotted in Figure 3-20h. The analyzed HSW area steadily swells by 26.4% in 48 hours and reaches a plateau around 34 hours, while the oil phase maintains a stable value after the sudden invasion of LSW due to the changeful locations of water-oil interfaces. In addition, a baseline experiment No.12 with no salinity contrast is also conducted for eliminating the effect of low ionic strength on the water-oil interfacial behavior. From the images in Appendix B, there is no expansion of connate LSW water and no displacement of constrained oil, which indicates that the salinity contrast gives crucial contributions to the emulsification and oil mobilization in the systems of HSW-oil-LSW.

3.4.1.3 Calculation of water flux into the alkane phase

From the images of an LSW-alkane-HSW cluster in the microchips, we can obtain direct information on the width of the alkane phase, the contact areas of LSW-alkane and HSW-alkane, and volume changes of HSW and LSW. However, it is indirect to gain a relationship between the water mass flux through the oil to the change of volume of HSW under various boundary conditions. To

obtain comparable results in water flux in different experiments, we need a method for normalizing the water diffusion flux for different phase geometries. Based on the theoretical method described in Section 3.2.2, we can have a derivation for the specific cases in the experiments. The schematic geometry of an LSW-alkane-HSW system is shown in Figure 3-21.

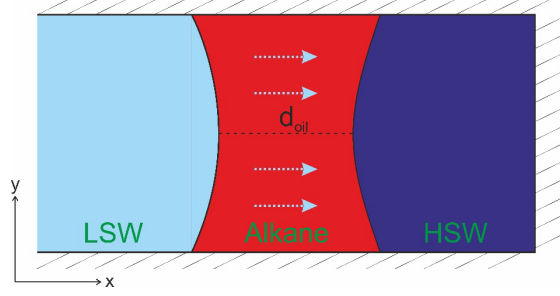


Figure 3-21: Schematic representation of an LSW-alkane-HSW system. The direction of water mass flux diffusing through one alkane phase is shown by light blue arrows.

As the confined oil commonly has irregular geometry, we consider the water diffusion only in the direction of the minimum thickness of oil, denoted by d_{oil} , and use this distance as the length of water transport through the oil from the LSW to the HSW. We assume that the water transport through the oil phase occurs over an average cross-sectional area $A_{ave}^c = hL_{ave}$, where h is the height of the pores in the micro-fluidics chip and L_{ave} is the average lengths of HSW-oil and LSW-oil interfaces. Thus, the water mass flux through an oil meniscus can be also approximated as:

$$\int_{A_{ave}^c} J_w dA \approx \bar{J}_w hL_{ave} = D_w \frac{c_{LSW} - c_{HSW}}{d_{oil}} hL_{ave} \quad [3.27]$$

Next, consider the rate of volume increase in the HSW region, Q_w . This can be written as:

$$Q_w = \frac{dV_{HSW}}{dt} = h \frac{dA_{HSW}}{dt} \quad [3.28]$$

where A_{HSW} is the observed planar area of HSW. The right-hand side of Eq. (3.27) is equal to the right of Eq. (3.28) multiplied by water density, ρ_w :

$$D_w \frac{c_{LSW} - c_{HSW}}{d_{oil}} L_{ave} = \rho_w \frac{dA_{HSW}}{dt} \quad [3.29]$$

Using Eq. (3.29), the water mass flux in two oils with different salinity conditions, $D_w(c_{LSW} - c_{HSW})/d_{oil}$, can be evaluated. From the literature (Su et al., 2010), the diffusion coefficients of water in heptane and dodecane are $7.4 \pm 0.75 \times 10^{-9} \text{ m}^2/\text{s}$ and $3.0 \pm 0.27 \times 10^{-9} \text{ m}^2/\text{s}$. The typical size of a water-Span 80-oil reverse micelle is 5 nm (Kopanichuk, Vedenchuk, Koneva, & Vanin, 2018). The self-diffusion coefficient of a single reverse micelle can be calculated by using the Stokes-Einstein equation,

$$D = \frac{k_B T}{6\pi\eta r} \quad [3.30]$$

where η is the dynamic viscosity, k_B is Boltzmann's constant, T is the absolute temperature, and r is the radius of the reverse micelle. Therefore, the diffusion coefficients of a reverse micelle for heptane and dodecane are $1.2 \times 10^{-10} \text{ m}^2/\text{s}$ and $3.2 \times 10^{-11} \text{ m}^2/\text{s}$. Additionally, the concentration difference between the LSW-alkane interface and HSW-alkane interface, $(c_{LSW} - c_{HSW})$, can be estimated.

To compare the water volumetric flux for different cases, we define reference parameters as: $t_{ref} = \frac{d_{oil}A_0}{D_w L_{ave}}$, and $Q_{ref} = hA_0/t_{ref}$, where A_0 is the initial area of HSW. The corresponding dimensionless forms can be given as, $A^* = A_{HSW}/A_0$, $t^* = t/t_{ref}$, and $Q^* = \frac{Q_w}{Q_{ref}} = \frac{d_{oil}}{D_w L_{ave}} \frac{dA_{HSW}}{dt}$. In the next sections, we discuss the salinity and Span 80 effect on water transport in alkanes by giving the function of dimensionless volumetric flux versus dimensionless time and the changes in water concentration over time.

3.4.1.4 Effects of salinity, carbon length and SPAN 80 on the water transport in oil

Figure 3-22 presents the plots of dimensionless water volumetric flux versus time for the absence and presence of Span 80 in alkanes. To compare the water flux, we calculate and list the average values of water fluxes and water concentration for all kinds of oil in Table 3-4. Within pure heptane, the average values of dimensionless water flux are 3.13×10^{-6} and 4.02×10^{-7} for the salinity contrasts of

1.7-170 g/L and 50-170 g/L, respectively, while the values for dodecane are 6.43×10^{-6} and 1.19×10^{-6} .

Table 3-4: Average values of water flux and concentration difference in oil phase

Exp. No	Series	Alkane type	Salinity contrast (LSW-HSW)	Dimensionless water flux ($\times 10^{-6}$ [-])	Water concentration difference ($\times 10^{-3}$ g/L)
1	Without SPAN 80	n-heptane	1.7 g/L-170 g/L	3.13	3.47
2			50 g/L-170 g/L	0.40	0.43
3		n-dodecane	1.7 g/L-170 g/L	6.43	6.45
4			50 g/L-170 g/L	1.19	2.23
5	With Span 80	n-heptane+ Span 80	1.7 g/L-170 g/L	70.66	162.68
6			50 g/L-170 g/L	34.70	378.54
7		n-dodecane+ Span 80	1.7 g/L-170 g/L	101.20	507.61
8			50 g/L-170 g/L	395.75	427.53

In both cases of pure heptane and dodecane, Figure 3-22a, a higher salinity contrast contributes to a higher water flux. The water fluxes have a non-linear change over time, where occur a dramatic drop in $t^* < 100$ then gradually flattens and remains stable, especially for the cases with 50-170 salinity contrast reaching zero water flux around $t^* > 200$. Moreover, the results show that dodecane with a longer carbon length performs a higher water flux than heptane for both salinity contrasts. Correspondingly, the concentration difference between the HSW-oil interface and LSW-oil interface has a similar trend with water flux during the experimental period, shown in Figure 3-22b. The concentration difference change proves that salinity plays a critical role in the water solubility and diffusion in oil. With the presence of Span 80, shown in Figure 3-22c, four volumetric water fluxes get almost 100 times boosted and have higher initial values than those in pure alkanes phases. In $0 < t^* < 4$, the fluxes decrease significantly and reach relatively stable states. The average values of water concentration difference for Span 80-added experiments have about 47 to 876 times larger than those for pure experiments. Interestingly, the curves do not display remarkable distinction for heptane and dodecane and no clear influence by the two salinity contrasts, which

indicates that the addition of Span 80 plays a dominating role in the water transport and eliminates the effect of carbon length to some extent.

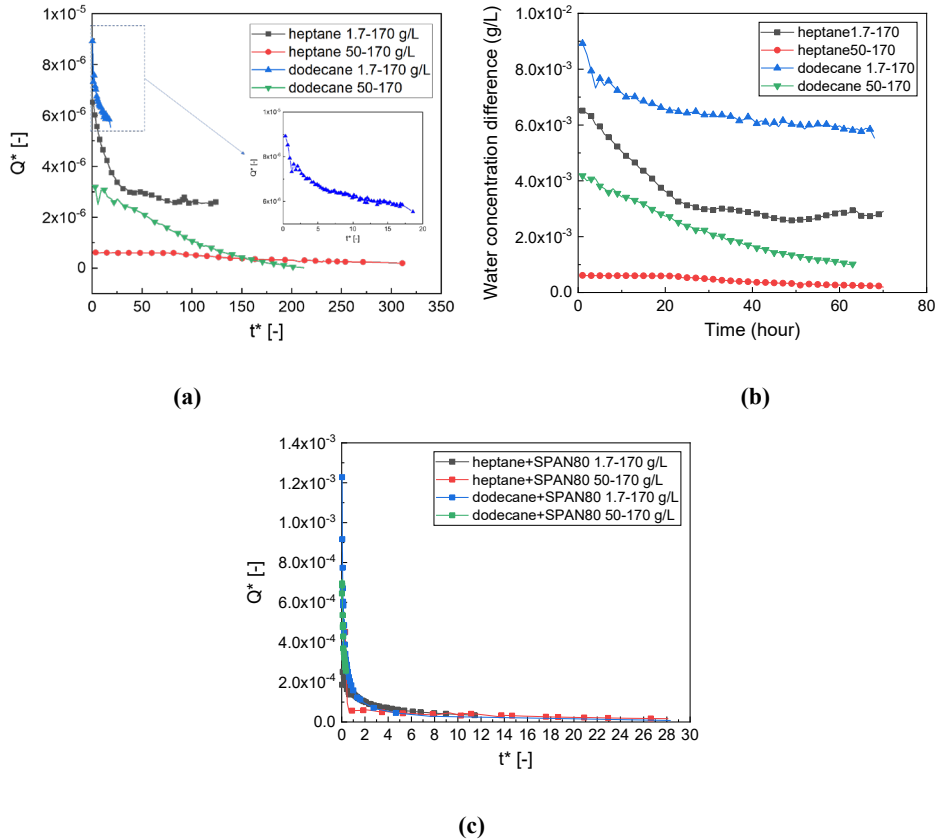


Figure 3-22: Relationships between dimensionless water volumetric flux and time. (a) give the comparison between the absence and presence of Span 80 in two pure alkanes. (b) gives the effect of Span 80 on the water fluxes. (c) gives the change of water concentration difference between the two brine-oil interfaces.

3.4.1.5 Pore-scale visualization of spontaneous emulsification

Spontaneous emulsification may occur when water and oil are in direct contact. The size of inverse micellar depends on both brine salinity and surfactant concentration. Santana-Solano, Quezada, Ozuna-Chacón, and Arauz-Lara (2012) performed some experiments to directly observe the spontaneous emulsification at the water-oil interface and proved that the inverse micellar swell with the increase of surfactant concentration. Therefore, to capture the emulsification process, we increase the Span 80 concentration in dodecane and experiment with

the salinity contrast of 1.7-170 g/L. Figure 3-23(a-c) shows the direct observation of the emulsification process at the LSW-oil interfaces over the monitoring period. As high salinity generally inhibits the formation of emulsification, only the LSW-oil interface has visible emulsions and dynamic aggregation. With the aggregation and growth of emulsions, the LSW-oil interface becomes coarse, and the emulsion saturation zone has expansion. For other experiments with 1% Span 80 or 50-170 g/L brines, the emulsion is existed either as black dots or cannot be captured by the camera. Given that the single water-in-dodecane+Span 80 emulsion has a size of 250 nm (Guha, Anand, & Varanasi, 2017), the change in numbers of emulsions can be calculated with the measurement of saturation zone area, shown in Figure 3-23d. The emulsions number displays a linear increase, and the fitted line is also plotted in the figure.

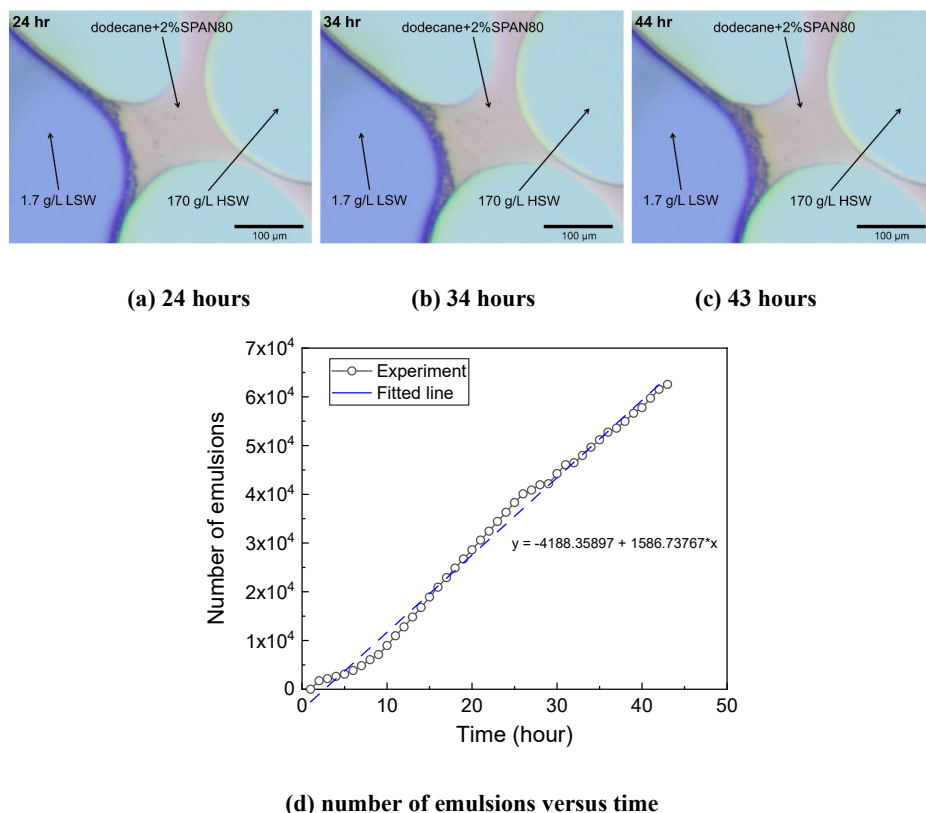
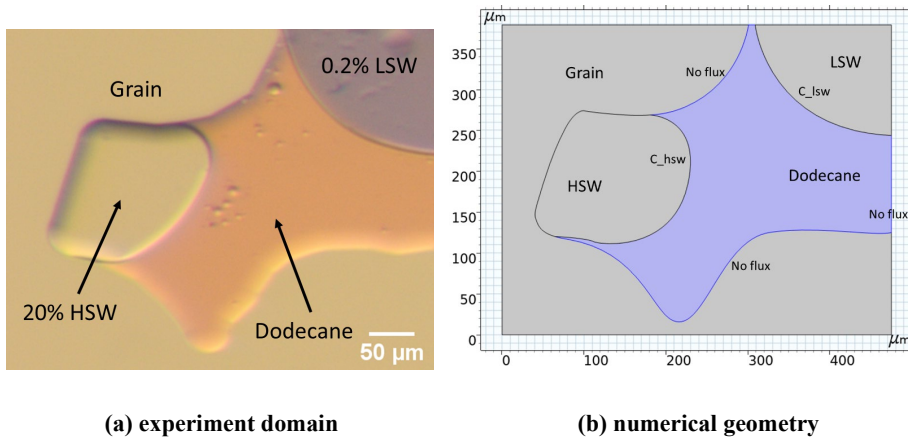


Figure 3-23: Images of spontaneous emulsification in the experiment with dodecane+2% Span 80. (a-c) show the accumulation of water-in-oil emulsions at the LSW-oil interface at 24 hours, 34 hours, and 43 hours of observation. (d) a plot of the number of emulsions in the emulsion saturation zone

3.4.1.6 Numerical validation of water diffusion due to water concentration difference

The numerical simulation allows us to have the relationship between the HSW expansion and water concentration of the HSW-oil interface. To accurately analyze this relationship, a modeling of water diffusion in oil is performed in COMSOL Multiphysics 5.4. We verify the results from microfluidic experiment for No. 4 involving pure n-dodecane and evaluate the concentration difference at two brine-oil interfaces. The experimental region and modelling geometry are shown in Figure 3-24.



(a) experiment domain **(b) numerical geometry**
Figure 3-24: Images of experimental and numerical domains. (a) shows the observation domain in the No.4 microfluidic experiment; (b) illustrates the modeling domain and boundary conditions.

The blue-highlighted region is our computational domain for water transport through pure dodecane. From the literature (Schatzberg, 1963), we know that the water concentration in dodecane for 1.7 g/L low-salinity brine is 65 mg/L. As the lack of water solubility at the HSW-oil contact line, we can apply 9 gradually reduced values of the water concentration with 3.61, 3.6, 3, 2.5, 2, 1.5, 1, 0.5, 0 mol/m³. Other boundaries are given as no flux. The simulation time is 30 hours.

By measuring the HSW area, the HSW region increased 3305.81 μm^2 with about 17.9% larger than the initial area, Figure 3-25. According to the calculation method mentioned in Section 3.4.1.3, the approximate water concentration at the HSW-oil interface is 48.5 mg/L with giving the oil thickness Δx as 150 μm , which is much lower than water concentration at the LSW-oil interface.

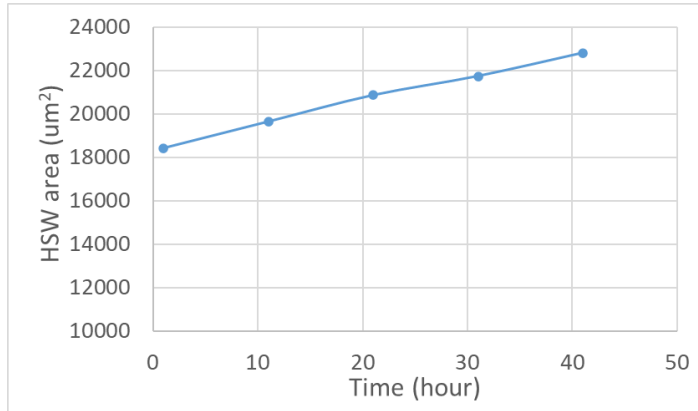


Figure 3-25: HSW area change during 42 hours in the case of No.4 microfluidic experiment.

In the case of water concentration 2 mol/m^3 , the concentration distributions (mol/m^3) in the domain at $t=0 \text{ h}$ and 30 h are also obtained as below.

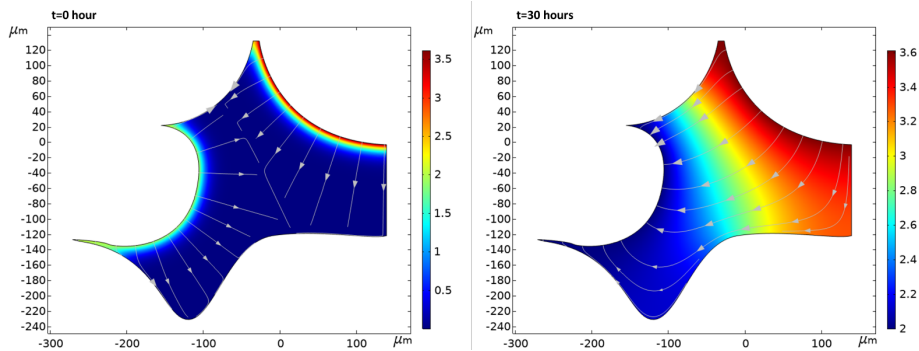


Figure 3-26: water concentration distribution in the domain at 0 and 30 hours. The streamlines of water flux in shown with arrows.

The increased area change of HSW after 30 hours has a function of water concentration at the HSW-oil contact line as plotted in Figure 3-27.

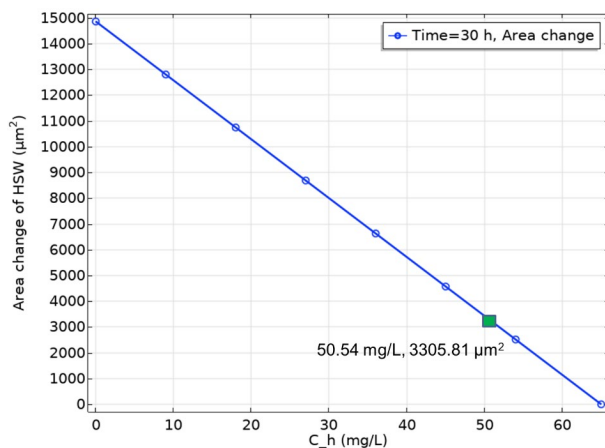


Figure 3-27: Relationship between HSW area and water concentration at HSW-oil interface. The blue line is the linear function of the relationship. The green square remark is the HSW area and the corresponding water concentration estimated from the theoretical method.

From the picture, we can easily find out that the increased area of HSW would reach $3305.81 \mu\text{m}^2$ after 30 hours if the water concentration is 50.54 mg/L at the HSW-oil interface, which is close to the theoretical value (48.5 mg/L). The simulation results demonstrate that the expansion in the trapped HSW area potentially comes from the difference in water concentration between two brine-oil interfaces.

3.4.2 Molecular scale water diffusion

Diffusion of water molecules across the oil phase was captured by molecular dynamic (MD) simulations. Results corroborate experimental observations. As seen from the diffusing trajectory, shown in Figure 3-28a, a fraction of water molecules from the pure water (PW) phase can migrate through the oil phase into the saline water (SW) phase. Movement of a water molecule across the oil phase was a random and rare event in the simulations. Typically, a water molecule sampled the PW phase for a significantly long simulation time, and by chance swiftly diffused through the oil layer into the SW phase (Figure 3-28a). For obtaining a quantitative net inflow of water molecules, the changes in the number of water molecules in and out of the SW phase were monitored in the simulations. As shown in Figure 3-28b, the net inflow of water molecules were significantly different among the three model systems that were already introduced in Section

3.3.2. For the system with two pure water phases (0 g/L-0 g/L), no obvious net inflow was observed between the two PW phases, meaning there was no obvious statistical directionality in water migration across the oil phase. For a higher salinity in the SW phases of 50 g/L and 170 g/L NaCl, a net inflow of water molecules toward the PW phase was identified, with the threshold increasing the ion concentration in the SW phase (Figure 3-28b). During the whole simulation, no ion was monitored diffused through the oil phase. Such results strongly suggested a correlation between water diffusion preferences and the ion concentration differences in the system and provided atomic-scale validation to the findings in the microfluidic experiments. It should be noted here that the oil phase used in the simulation system was orders of magnitude thinner than in experiments to reveal water diffusion in the oil phase in a feasible simulation time. Water diffusion through the oil phase in experiments should require a much longer time in reality.

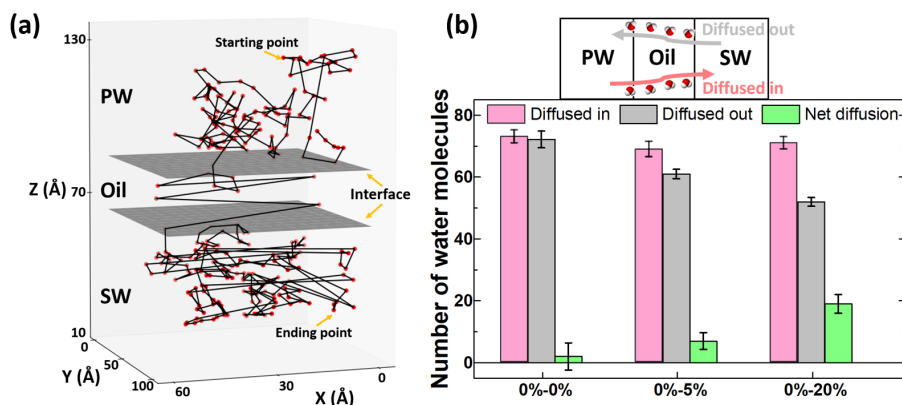


Figure 3-28: Water diffusion across the oil phase and net diffusion in the systems. (a) A typical migration trajectory of a water molecule across the oil phase (the abrupt steps of trajectory in the oil phase resulted from the periodic boundary condition of the simulation box.). (b) Comparison of net diffusion of water molecules into the SW phase in the three model systems.

Water molecules diffused through the oil phase in the system need to cross two interfaces. The nature of the oil-water interface played a key role in the net inflow of water migration. The average equilibrium densities of different components along the z-direction of the system in the early stage of the simulations were characterized to investigate the structure of the interface. As the density profiles

of the systems plotted in Figure 3-29a and in Appendix B show, the density values of both pure water and heptane agree well with experimental values (around 1.0 g/cm³ and 0.68 g/cm³, respectively). With the addition of ions, the water density in the SW was slightly lower than the PW phase (Figure 3-29a), due to the effects of volume exclusion and structural coordination of ions on the nearby water molecules as observed in other studies (Badizad, Koleini, Hartkamp, Ayatollahi, & Ghazanfari, 2020; Koleini, Mehraban, & Ayatollahi, 2018). Here, both sodium and chloride ions might undergo hydration reactions and surrounding shells of water molecules were obviously formed, as snapshots shown in Figure 3-29a. Furthermore, each system contained two well-defined interfaces between oil and the two water solutions, due to the immiscibility of the water and oil molecules. The average of interfacial thickness and interfacial tension of each interface was determined by the ion concentration, as seen from results given in Figure 3-29b. The interfacial thickness was calculated here using the 90–90 criterion (Xu et al., 2013), namely the distance between two lines, where the local density is equal to 90 g/L of the respective bulk value (the blue region highlighted in Figure 3-29b). The interfacial tension, γ , was calculated from the following equation (Chang et al., 2021) :

$$\gamma = \frac{1}{2} L_z [p_{zz} - \frac{1}{2} (p_{xx} + p_{yy})] \quad [3.31]$$

where L_z is the length of the simulation domain in the z -direction; p_{xx} , p_{yy} , p_{zz} are the stress tensor components in the x , y , and z directions, respectively. More detailed information on the calculation is given in Appendix B. The calculated interfacial tension for the heptane/water interface is around 49.8 mN/m, which agreed well with the experimental value of 50.1 mN/m (Kumar, 2012). The results indicated that higher salinity led to higher interfacial tension, and at the same time lower interfacial thickness. The dependence of both interfacial tension and thickness was in line with observations in previous studies (Paul & Chandra, 2004; Underwood & Greenwell, 2018; Zhao et al., 2018). Such dependence can be attributed to the strong electrostatic force induced by ions in the solution, where water molecules strongly bound to the ions and restrained the tendency of migration to the interface. Therefore, higher salinity led to a lower miscibility of SW and heptane. Lower salinity contrast also resulted in a reduction of probability of water diffusion through the interface into the oil phase, which drove the net inflow of water molecules from PW into SW (Figure 3-28b).

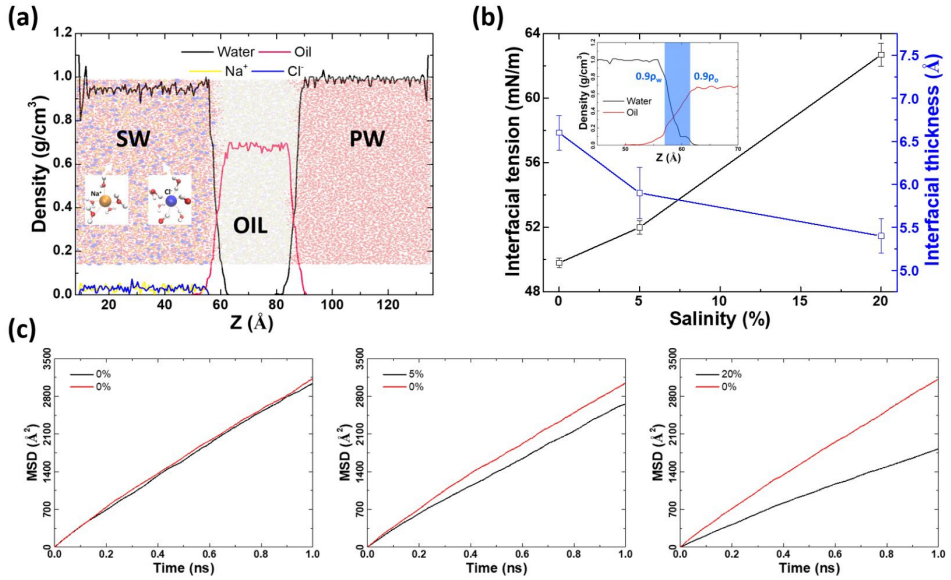


Figure 3-29: Molecular scale water dynamics. (a) Density profiles of the major components in the 0 g/L-oil-170 g/L system. (b) Profiles of interfacial tension and thickness in the 0 g/L-oil-170 g/L system. (c) The representative change of mean square displacement (MSD) of water molecules with time in three different water solution phases.

The salinity also significantly affected water diffusion. Water diffusion can be quantitatively characterized by water molecular mean square displacement (MSD) in the three systems with various salinity, which are shown in Figure 3-29c. The water molecular diffusion coefficient (D) was evaluated using the following equation:

$$D = \frac{1}{6} \lim_{t \rightarrow \infty} \frac{dMSD}{dt} \quad [3.32]$$

The diffusion coefficient of water molecules in PW (pure water) phase in all systems was found to be around $5.16 \pm 0.39 \mu\text{m}^2/\text{ms}$, matching well with values by experiments and other simulations ($5\text{-}5.5 \mu\text{m}^2/\text{ms}$) (Easteal, Price, & Woolf, 1989; Tsimpanogiannis et al., 2019). With the increasing salinity, the diffusion coefficient decreased significantly, yielding values of ± 0.28 and $2.98 \pm 0.27 \mu\text{m}^2/\text{ms}$ for systems with 50 g/L and 170 g/L salinity, respectively. Higher salinity resulted in slower water diffusion. Such results were expected, as the attraction of ions to water molecules and the formation of hydrated ions, on the one hand, hindered the diffusion of water molecules and, on the other hand, decreased the

number of free molecules in the system. The result was also consistent with the analysis of changes in the interface structure. Therefore, the existence of a hydrated ion structure not only affects the migration of water molecules but also weakens their solubility in oil at the oil-water interface. This effect resulted in a lower solubility of water in oil on the SW side, which drives the phenomenon of directional net flow of water towards the high salinity water (as described in Figure 3-28b).

3.4.3 Effect of salinity on spontaneous emulsification at the interface

In our light scattering experiments, we measured the spontaneous emulsion droplet size with the same fluids as the one used in the microfluidic experiments. The size change of emulsion droplets and the emulsion accumulation may affect the water transportation behavior (Aldousary & Kovsky, 2019). Figure 3-30 shows images of the spontaneous emulsification process for 1.7 g/L brines with Span 80 added dodecane for 24 hours. In the beginning, the water-oil interface presents a clear boundary in transparent color. No obvious emulsion can be visually observed. After three hours, some white turbidity appeared on the oil-water interface, where the concentration of reverse micelles are gradually increasing. At around 5 hours, we can see that a thicker whitish layer of emulsion appeared at the upper oil-water interface. Based on the proposed mechanism in Section 3.3.3, the white area is comprised of large numbers of emulsions and their aggregation due to the reverse micelle diffusion into the oil phase. After around 7 hours the color and shape of the emulsion layer became stable. However, the size of these emulsion droplets can be different with the salinity because of hydrated ions concentration in the oil phase. Heptane samples have the similar phenomena, but the emulsion generation period and diffusion behavior are slightly different, see the below discussion. Therefore, we performed 10 sets of DLS experiments to study the salinity effect on spontaneous emulsion generation.

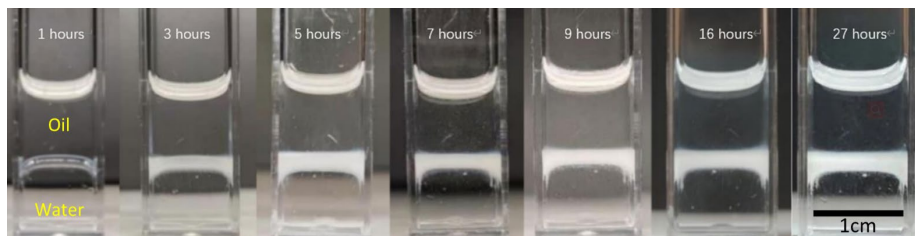


Figure 3-30: Emulsification for dodecane+1% SPAN 80 contacting with 1.7 g/L brines during 27 hours. Emulsions accumulate above the brine-oil interface after 3 hours and generate a thicker layer subsequently.

Correspondingly, we plot the change in the size distribution of microemulsions during 24 hours for the case of 1.7 g/L LSW with dodecane+1%Span80, see Figure 3-31. The measurements give a clear change tendency and support the corresponding phenomenon in Figure 3-30. The size distribution includes three peak regions: 1-10 nm, 10-1,000 nm, and 1,000-10,000 nm. Thus, there are up to three peaks. In the beginning, few emulsions are detected because of the initial contact between water and oil. As time goes on until 5 hours, middle-size emulsions (10-1000 nm) gradually generate and take the most proportion at the brine-oil interface. Some small-size and large-size emulsions are detected as well, but the intensity keeps low values ($\sim 4.2\%$ for 2 nm diameter emulsions at 5 hours). After 5 hours, more small-size emulsions form but large-size ones disappear. Furthermore, we plot the normalized proportions of intensity for three peaks. The small-size and middle-size emulsions dominate the interface area. The middle-size intensity keeps increasing until about 15 hours and then has almost the same value as the small-size intensity. At 24 hours, two sizes own 52.9% and 47.1% of intensity, respectively. The dynamic change of mean size for small-size and middle-size peaks is shown in the figure as well. Peak size (or distribution size) is calculated with a mean size and a width for each separate size peak of the distribution. The curves dedicate that small-size and middle-size emulsions maintain relatively stable distributions (mean values with 2.1 and 90.2 nm for two peaks), while both have a slight increase after about 15 hours, especially for the middle-size emulsions. It means the emulsions have swelling due to reverse micelles diffusion.

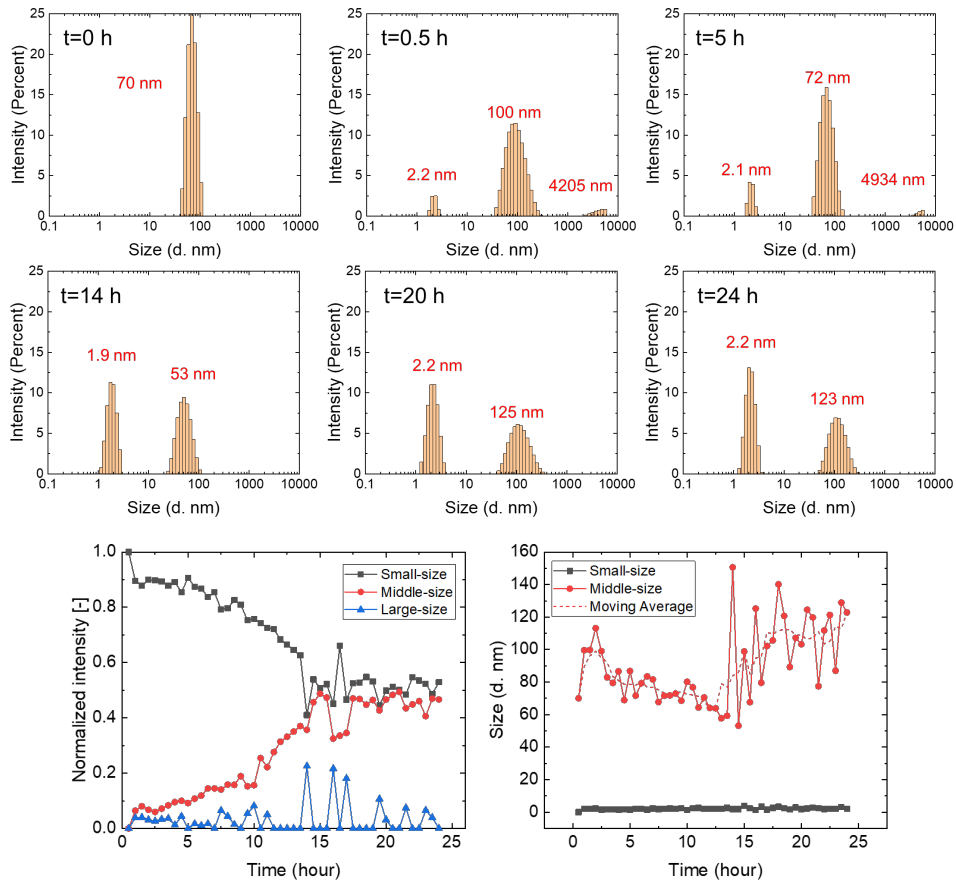


Figure 3-31: The change in the size distribution of emulsions at the interface of 1.7g/L brine and dodecane + 1% Span 80 during 24 hours. The images contain the measurements at 6 moments. The mean size for every size peak is marked in the figures. Future, the normalized intensity for three peaks is plotted. The dynamic change of small-size and middle-size emulsions are measured.

To directly figure out the salinity and oil effects on the size distribution, we also investigate and plot the measurements of emulsion size for the five salinities: 0, 1.7, 17, 50 and 170 g/L. Figure 3-32 gives a straightforward phenomenon of emulsion position at brine-oil interfaces due to the salinity. In general, both oil present less visible emulsions with an increase in salinity, especially for the cases of 50 and 170 g/L. In the case of dodecane, 1.7 g/L salinity causes a most uniform dispersion of emulsions in the oil phase.

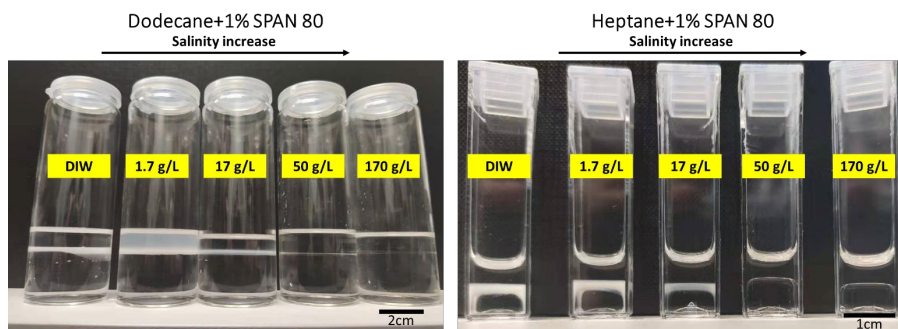
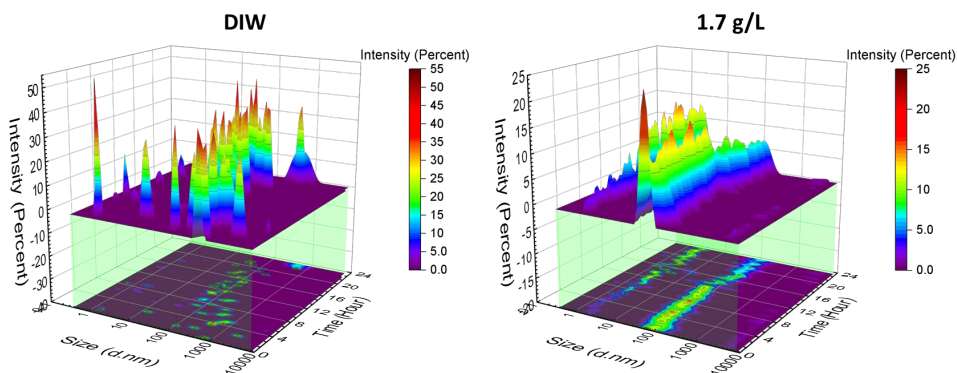


Figure 3-32: Images of spontaneous emulsification for dodecane and heptane after brine-oil contacting 24 hours at room temperature. Note that the dodecane samples are contained in a larger glass bottle (ϕ 3 cm) than the cuvette for heptane. Therefore, the emulsification phenomenon probably is more obvious due to the larger contacting area of brine and oil.

Figure 3-33 shows the 3D plots of the emulsion droplet size versus time for dodecane. In the figures, we can see that the emulsion size distribution changes as the increase in contacting time of brine salinity and dodecane and have variable magnitudes under different salinity conditions. With the increase of salinity, the emulsions perform smaller size, especially in the case of 170 g/L. 50 g/L salinity has an obvious transition of the size intensity from the range of 100 nm to 10 nm after 12 hours. The change of mean size is also plotted in the figure, where mean size is defined as the average value of the peak, weighted by the intensity parameter. 1.7 g/L salinity shows more relatively stable size distribution with a mean size of around 100 nm after 15 hours, while others with over 100 nm of mean size have varying degrees of fluctuation. This trend is consistent with the macro phenomenon in the laboratory bottle and corvettes.



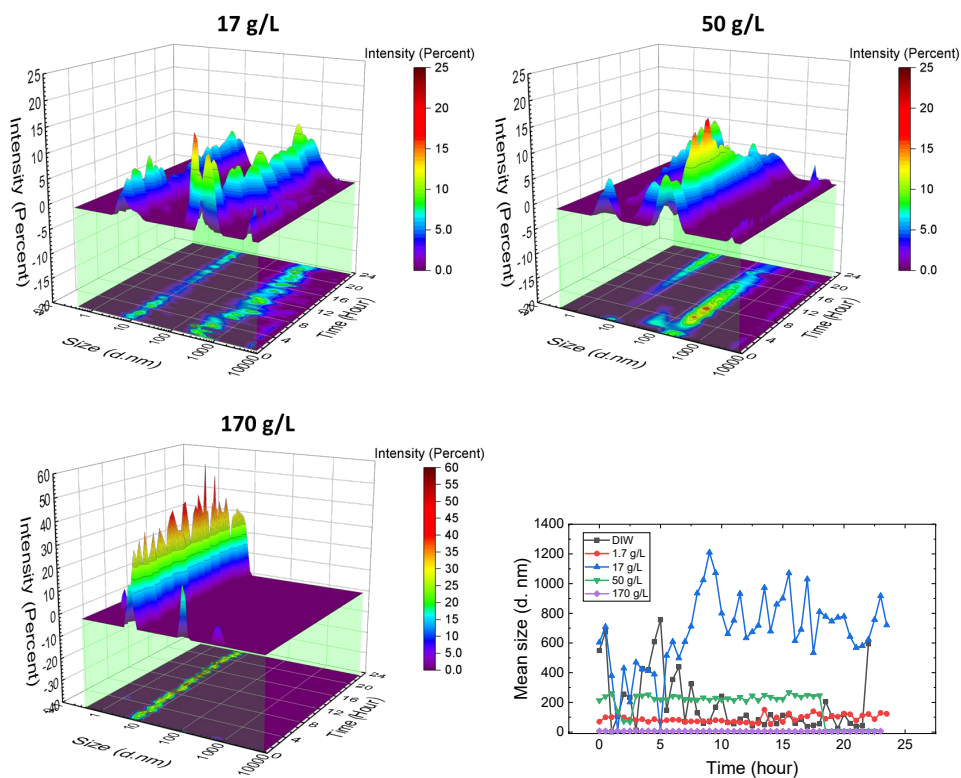


Figure 3-33: Size distribution of emulsions for the case of dodecane+Span80. The images contain the measurements for all five types of brines with a rainbow color bar. The curves are mapped on the top of the image. The measurement of mean size is given for five salinity conditions.

In Figure 3-34, the experiments with heptane illustrate a similar change in emulsion size distribution, where the 1.7 g/L case has the most stable distribution during 24 hours and increasing salinity induces variation in the distribution. From the plotted curves of mean size, DIW and 1.7 g/L both have emulsion swelling. For the samples with 50 and 170 g/L salts, the emulsion is mainly comprised of small-size emulsions (about 10 nm), which indicates a higher salinity reduces the emulsion swelling and inhibits the emulsion aggregation. This phenomenon is consistent with the proposed mechanisms of salinity effect on emulsion generation at the water-oil interface in the literature (Behera, Varade, Ghosh, Paul, & Negi, 2014; Davis et al., 2020). Compared to dodecane, heptane has a better performance on the stability of emulsion generation and swelling in low-salinity environments.

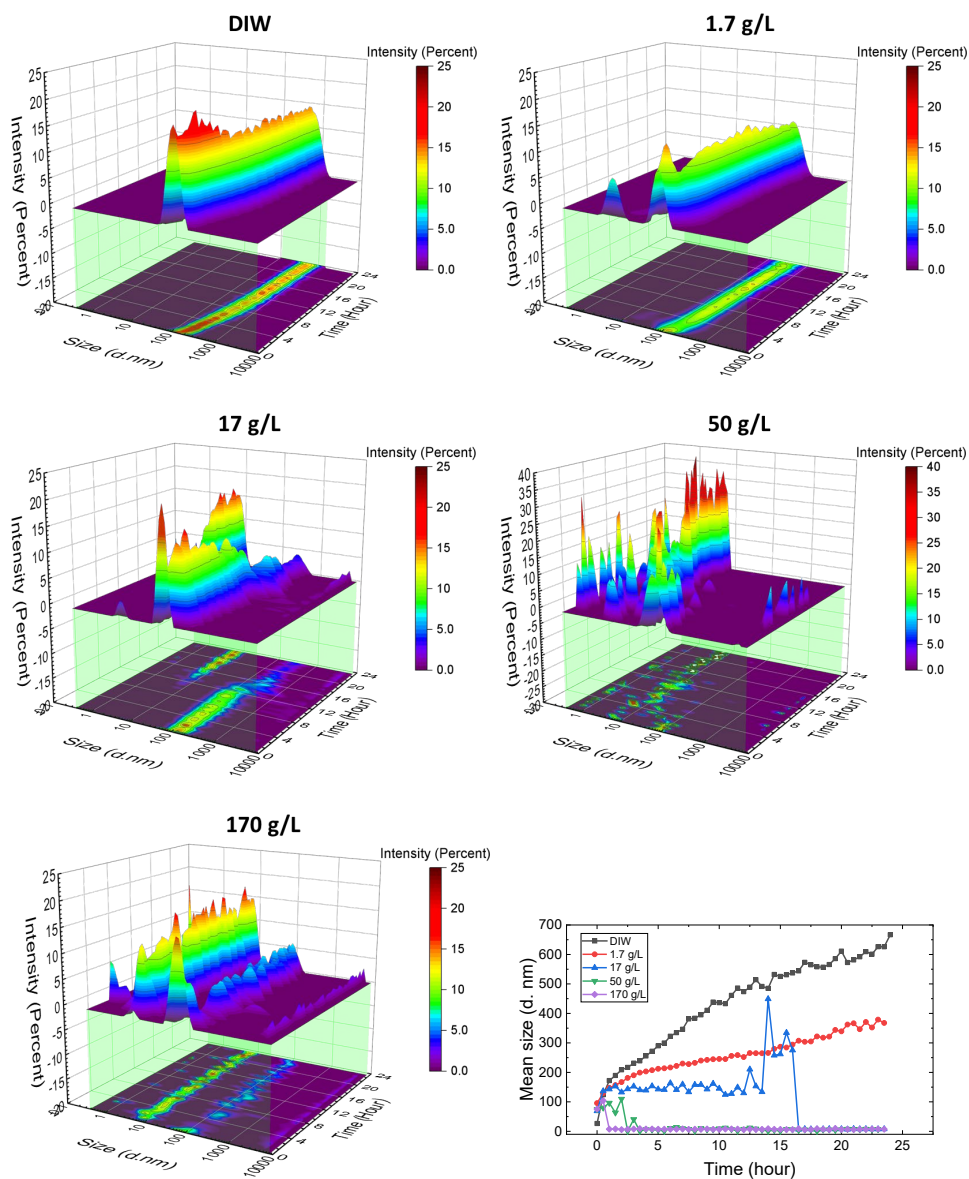


Figure 3-34: Size distribution of emulsions for the case of heptane+Span80. The images contain the measurements for all five types of brines with a rainbow color. The curves are mapped on the top of the image. The measurement of mean size is given for five salinity conditions.

3.4.4 Direct observation of spontaneous emulsification

In this experiment, the purpose is to observe the spontaneous emulsion generation process at the brine-oil interface. Figure 3-35 illustrates the direct observation of the dynamic emulsion generation of a pendant drop of deionized water in the dodecane+1% Span80 solution. The droplet appears darker with time due to emulsion accumulation at the droplet surface. The emulsion layer becomes thicker, and micelles accumulate with time. The micro-emulsion then accumulates and forms protuberance on the surface. After 2 hours, the surface of the droplet is not uniform anymore. Interestingly, the large protruding part will detach from the water droplet due to the unbalance among gravity, surface tension and buoyancy forces. Some emulsion flakes slowly fall from the bottom parts of the droplet and the droplet size subsequently decreases. Some literature gave a similar description and observe the water droplet shrinkage as well (Schmitt, Toor, Denoyel, & Antoni, 2017).

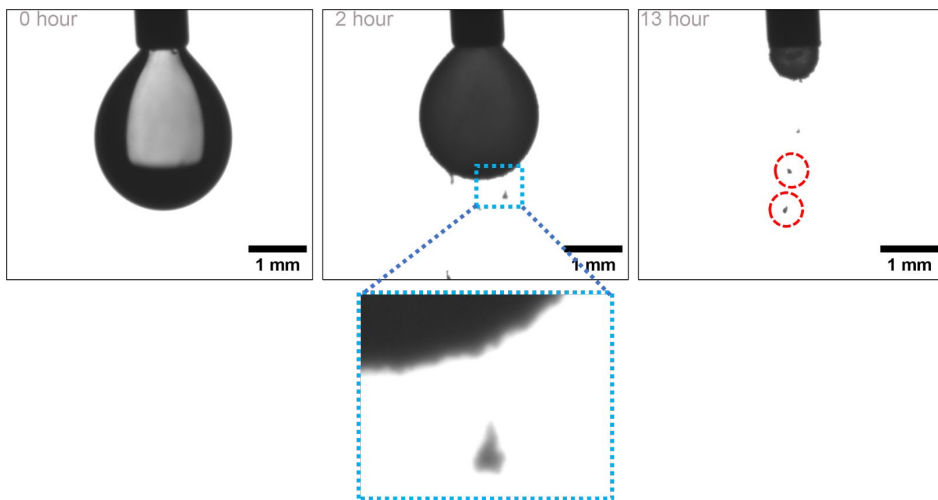


Figure 3-35: Images of dynamic emulsion generation during 13 hours for a pendant drop of denoised water in an environment with Dodecane+1% SPAN 80 solution. One part of emulsion aggregation is observed in the zoomed region of the 2-hour image. Some emulsion flakes are also observed at 13 hours, shown in the red-dashed circles.

To directly observe the salinity effect on the dynamic emulsification, we investigate four kinds of brines in the environments of dodecane and heptane, shown in Figure 3-36 and Figure 3-387. We clearly observe from the images that the increasing salinity induces less emulsion generation at the brine-oil interface,

as we described in the DLS experiments. This trend occurs in both oil cases. 50 g/L brine drop has no visible emulsions around the interface and the size does not have an obvious change. DIW and 1.7 g/L drops have significant shrinkage after several hours. In the case of dodecane, 1.7 g/L drop almost disappears after 5 hours, while DIW drop has the same stage after 13 hours. Meanwhile, the apparent emulsion flakes collapse and detach from the drop surface. 17 g/L drops in both oil environments have the emulsion generation on the interface, but no falling flakes are observed. In the case of heptane, the drops perform a similar phenomenon where DIW and 1.7 g/L have the most notable change after about 4 hours in the drop size and emulsion generation. 50 g/L drop has no changes.

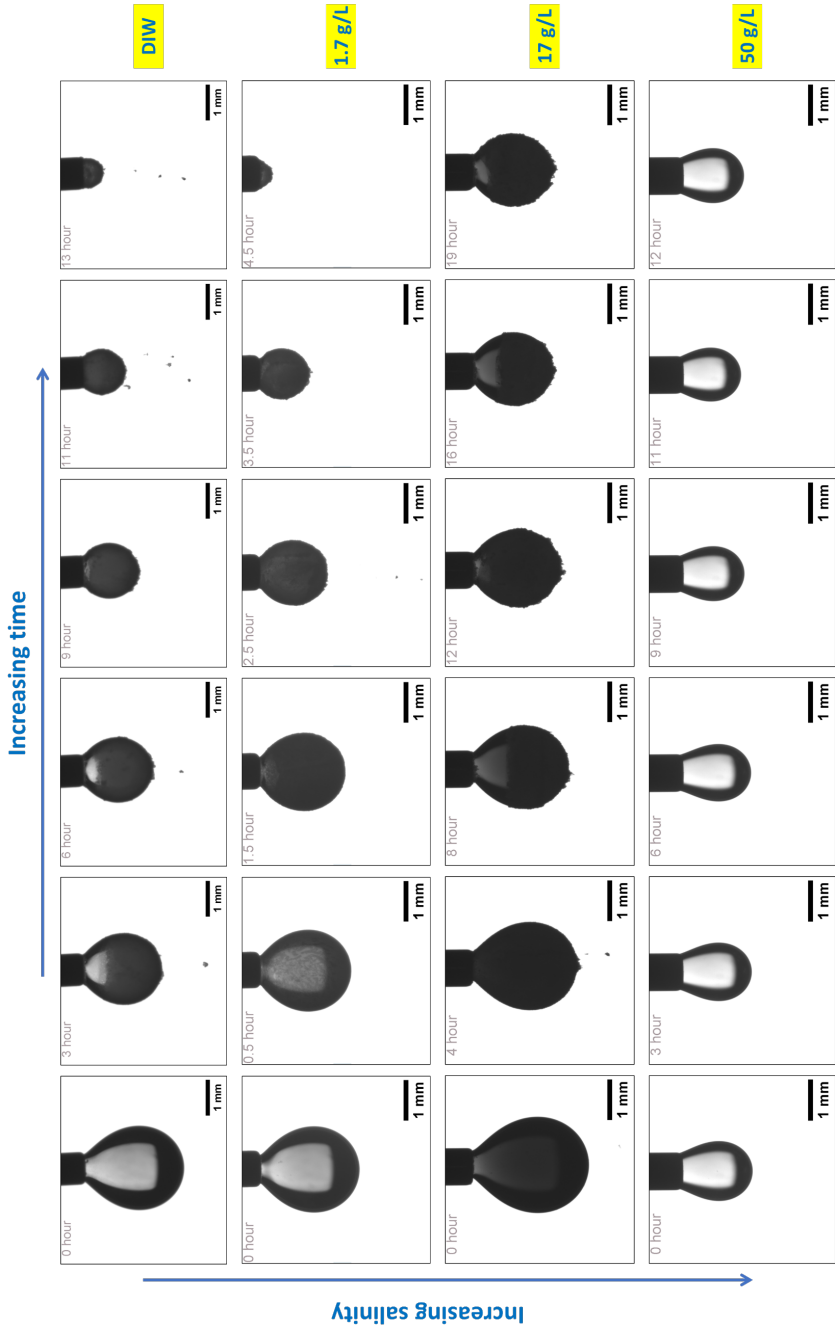


Figure 3-36: Images of salinity effect on spontaneous emulsification with dodecane+1% Span 80 (the white region in images). The salinity increases from top to bottom in the figure and the observation time increases from left to right.

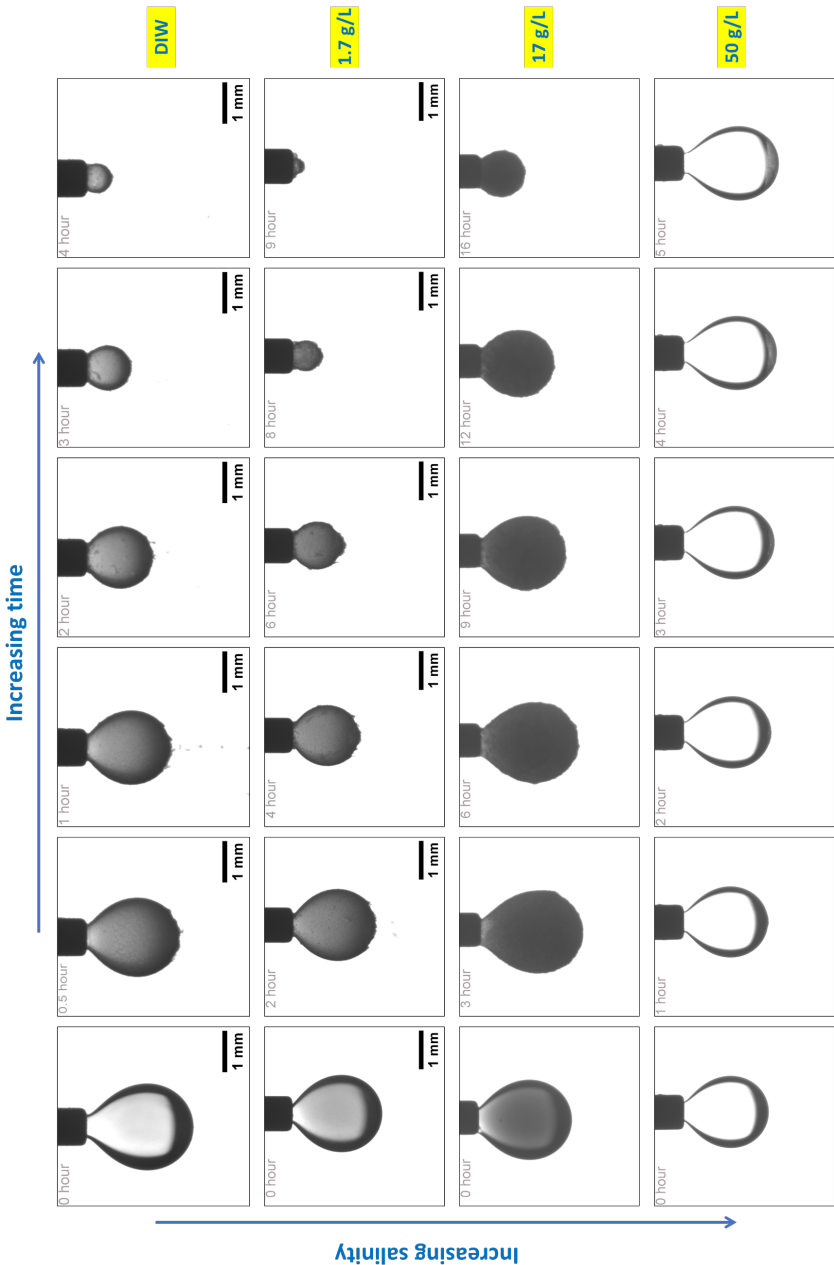


Figure 3-37: Images of salinity effect on spontaneous emulsification with heptane+1% Span 80 (the white region in images). The salinity increases from top to bottom in the figure and the observation time increases from left to right.

By measuring the interfacial tension (IFT) and calculating of emulsification rate for both oils, we are able to evaluate the salinity effect on the brine-water interfacial emulsification. The results are shown in Figure 3-38 and Figure 3-39. The surface tension is measured by the drop analyzer apparatus. The interfacial tensions vary from 3.11 mN/m to 4.59 mN/m for the case of dodecane with various salinity in the beginning. All brine drops have a dramatic decrease IFT within 20 hours of observation, even reaching around 0.14 mN/m for the DIW and 1.7 g/L brines. DIW and 1.7 g/L droplets present higher decreasing rates than that of 17 g/L, while 50 g/L drop initially has a significant decrease and then maintains steady values around 0.8 mN/m after 3.5 hours. This trend is consistent with the observation of the spontaneous emulsification process in Figure 3-36, where the drop shape has no visible change. The case of heptane has a same performance in IFT

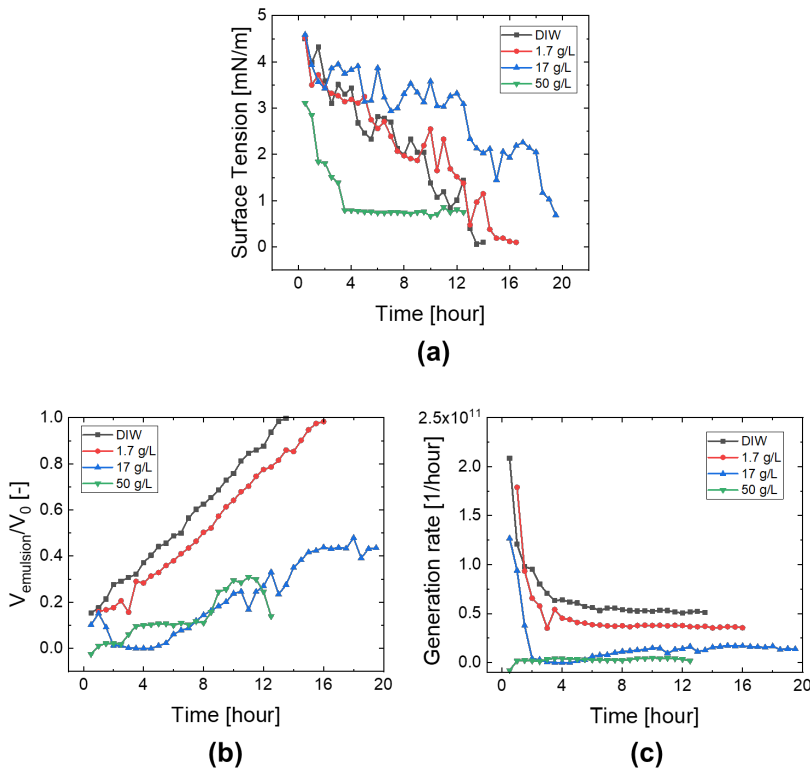


Figure 3-38: measurement of surface tension for brine droplet in dodecane and the estimated values of emulsion generation. (a), measured surface tension for four brine

droplets; (b), ratio of estimated emulsion volume and initial droplet volume; (c), the calculation for the generation rate of emulsion numbers with four brines.

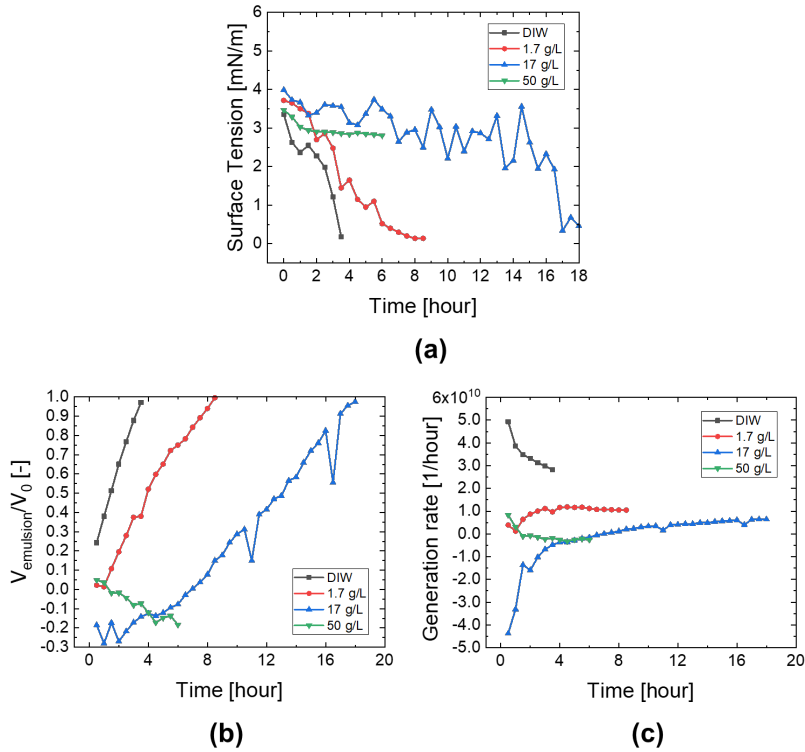


Figure 3-39: measurement of surface tension for brine droplet in heptane and the estimated values of emulsion generation. (a), measured surface tension for four brine droplets; (b), ratio of estimated emulsion volume and initial droplet volume; (c), the calculation for the generation rate of emulsion numbers with four brines.

Furthermore, we attempt to evaluate the emulsion volumes and generation rate according to the mass loss in brine droplets. The shrinkage in the droplet volume (ΔV_{drop}) is assumed to be the volume of the generated emulsions ($V_{emulsion}$). Besides, with the help of DLS measurement, the average diameters of one emulsion for DIW and 1.7 g/L can be given for dodecane and heptane: 150 nm and 250 nm, respectively. When we take the spherical shape into account for the emulsion volume calculation, the dimensionless emulsion volume can be estimated by $V_{emulsion}/V_0$ where V_0 is the initial volume of the brine droplet. The generation rate of emulsion numbers can be calculated by $\frac{\Delta V_{drop}}{\Delta t} \frac{3}{4\pi r^3}$.

In general, the curves of dimensionless emulsion volume depict that DIW and 1.7 g/L have faster increases in emulsion volume than 17 and 50 g/L for both cases of dodecane and heptane. Correspondingly, the results of generation rate also indicate that lower salinity causes more emulsion generation within a unit of time. 50 g/L salinity has almost zero growth in emulsion.

3.5 Conclusion

In summary, this study focused on providing a better understanding of the water transport processes occurring in porous oil reservoirs, which affect oil movement during low-salinity water flooding. The hypothesis of water transport through the oil phase induced by the salinity contrast was expounded, and the oil was dislodged and is thus available for remobilization. To mimic the low-salinity water flooding in an oil reservoir, two series of microscopic experiments were conducted to establish a sandwich-like system of LSW-oil-HSW in hydrophobic microchips. We noted that for both hydrocarbons the HSW areas significantly increased when there was a salinity contrast with the LSW. In contrast, there was no visible change in the reference experiments that HSW and LSW had no salinity difference. The features of water transport were assessed for two pure hydrocarbons at the microscopic scale. Moreover, to advance our insights into the behavior of water molecules in the alkanes, molecular dynamic (MD) simulations were performed with three cases of NaCl concentration difference across an oil film of heptane. We described the trajectory of water diffusion through heptane from low-salinity water to high-salinity water, investigated the statistical results of dynamic net inflow of water molecules into HSW, and determined interfacial tension and the diffusion coefficients of water in heptane for the various salinity systems. Additionally, the influence of salinity on the brine-oil interfacial behavior is investigated through experiments of dynamic light scattering and surface tension. By combining the pore-scale experiments and molecular-scale modelling, we draw the following conclusions.

- Water is capable to transport through the studied alkane phases, i.e., heptane and dodecane, due to a salinity contrast, which causes the expansion of disconnected high-salinity water and displacement of constrained oil.

- Ionic strength and the hydrocarbon chain length both play important roles in water transport. Heptane and dodecane both were found to be diffusive to water and reverse micelles, and this property could be significantly affected by the salinity contrast at two sides of alkanes. A higher salinity contrast of 1.7-170 g/L induces a higher water volumetric flux in heptane and dodecane. 50-170 g/L salinity contrast gives less water flux, even reaching 0 after a certain period.
- Adding SPAN80 in alkanes enhances the water flux by over 100 times, meanwhile eliminating the salinity effect on the water flux. The introduction of surfactant increases the visco-elasticity of the water-oil interface, which is reflected by the significant deformation of swelling HSW bubbles.
- Through conducting MD simulation, we observed water molecules transported through the heptane phase and a higher number of water molecules passed the water-heptane interface driven by ion concentration differences. There was a net flux of water molecules towards the high salinity water. Meanwhile, based on the calculated profiles of ions, almost no ions appear at the oil-water interface and inside the heptane phase.
- By investigating the interfacial tension changes and mean square displacement (MSD) calculations, we conclude that higher salinity leads to a lower diffusion coefficient of water molecules (around 4.48 and 2.98 $\mu\text{m}^2/\text{ms}$ for 5% and 20%, respectively), i.e., slower water movement. Moreover, high salinity reduces the probability of water diffusion through the interface into the oil phase. This leads to lower solubility of water in oil near the oil-HSW interface and thus verifies the experimental result that the direction of net water movement is towards high salinity water.
- The dynamic processes of emulsion generation at the brine-oil interface are captured through DLS and IFT experiments. The salinity effect on the process and interfacial tension are evaluated.
- A hypothesis for explaining water transport through the oil phase is proposed in two scenarios: water diffusion due to chemical potential and

water transport via reverse micelle or micro-emulsions movement towards to HSW-oil interface.

Reference

- Ahmadikhamsi, S., Golfier, F., Oltean, C., Lefèvre, E., & Bahrani, S. A. (2020). Impact of surfactant addition on non-Newtonian fluid behavior during viscous fingering in Hele-Shaw cell. *Physics of Fluids*, 32(1), 012103. doi:10.1063/1.5128589
- Aldousary, S., & Kovscek, A. R. (2019). The diffusion of water through oil contributes to spontaneous emulsification during low salinity waterflooding. *Journal of Petroleum Science and Engineering*, 179, 606-614. doi:<https://doi.org/10.1016/j.petrol.2019.04.041>
- Aminabhavi, T., Patil, V., Aralaguppi, M., & Phayde, H. (1996). Density, viscosity, and refractive index of the binary mixtures of cyclohexane with hexane, heptane, octane, nonane, and decane at (298.15, 303.15, and 308.15) K. *Journal of Chemical & Engineering Data*, 41(3), 521-525.
- Arab, D., Kantzas, A., Torsæter, O., Akarri, S., & Bryant, S. L. (2021). A Crucial Role of the Applied Capillary Pressure in Drainage Displacement. *SPE Journal*, 1-19.
- Ayirala, S. C., Al-Yousef, A. A., Li, Z., & Xu, Z. (2018). Water ion interactions at crude-oil/water interface and their implications for smart waterflooding in carbonates. *SPE Journal*, 23(05), 1817-1832.
- Badizad, M. H., Koleini, M. M., Hartkamp, R., Ayatollahi, S., & Ghazanfari, M. H. (2020). How do ions contribute to brine-hydrophobic hydrocarbon Interfaces? An in silico study. *J Colloid Interface Sci*, 575, 337-346. doi:10.1016/j.jcis.2020.04.060
- Behera, M. R., Varade, S. R., Ghosh, P., Paul, P., & Negi, A. S. (2014). Foaming in micellar solutions: Effects of surfactant, salt, and oil concentrations. *Industrial & Engineering Chemistry Research*, 53(48), 18497-18507.
- Benmekhbi, M., Simon, S., & Sjöblom, J. (2014). Dynamic and rheological properties of span 80 at liquid-liquid interfaces. *Journal of Dispersion Science and Technology*, 35(6), 765-776.
- Berendsen, H., Grigera, J., & Straatsma, T. (1987). The missing term in effective pair potentials. *Journal of Physical Chemistry*, 91(24), 6269-6271.
- Binks, B. P., & Clint, J. H. (2002). Solid wettability from surface energy components: relevance to Pickering emulsions. *Langmuir*, 18(4), 1270-1273.
- Chang, Y., Xiao, S., Ma, R., Wang, X., Zhang, Z., & He, J. (2021). Displacement dynamics of trapped oil in rough channels driven by nanofluids. *Fuel*, 122760.
- Cheng, J., Chen, J.-F., Zhao, M., Luo, Q., Wen, L.-X., & Papadopoulos, K. D. (2007). Transport of ions through the oil phase of W1/O/W2 double emulsions. *Journal of colloid and interface science*, 305(1), 175-182.
- Crestel, E., Kvasničková, A., Santanach-Carreras, E., Bibette, J., & Bremond, N. (2020). Motion of oil in water induced by osmosis in a confined system. *Physical Review Fluids*, 5(10), 104003.
- Davis, C. R., Martinez, C. J., Howarter, J. A., & Erk, K. A. (2020). Diffusion-Controlled Spontaneous Emulsification of Water-Soluble Oils via Micelle Swelling. *Langmuir*, 36(26), 7517-7527.
- Du, Y., Xu, K., Mejia, L., Zhu, P., & Balhoff, M. T. (2019). Microfluidic Investigation of Low-Salinity Effects During Oil Recovery: A No-Clay and Time-Dependent Mechanism. *SPE Journal*.
- Easteal, A. J., Price, W. E., & Woolf, L. A. (1989). Diaphragm cell for high-temperature diffusion measurements. Tracer diffusion coefficients for water to 363 K. *Journal of the Chemical Society, Faraday Transactions 1: Physical Chemistry in Condensed Phases*, 85(5), 1091-1097.
- Guha, I. F., Anand, S., & Varanasi, K. K. (2017). Creating nanoscale emulsions using condensation. *Nature communications*, 8(1), 1-7.

- Heidman, J., Tsonopoulos, C., Brady, C., & Wilson, G. (1985). High - temperature mutual solubilities of hydrocarbons and water. Part II: Ethylbenzene, ethylcyclohexane, and n - octane. *AIChE journal*, 31(3), 376-384.
- Hockney, R. W., & Eastwood, J. W. (2021). *Computer simulation using particles*: crc Press.
- Hynes, J. T., Kapral, R., & Weinberg, M. (1979). Molecular theory of translational diffusion: Microscopic generalization of the normal velocity boundary condition. *The Journal of Chemical Physics*, 70(3), 1456-1466.
- Jorgensen, W. L., Maxwell, D. S., & Tirado-Rives, J. (1996). Development and testing of the OPLS all-atom force field on conformational energetics and properties of organic liquids. *Journal of the American Chemical Society*, 118(45), 11225-11236.
- Joung, I. S., & Cheatham III, T. E. (2008). Determination of alkali and halide monovalent ion parameters for use in explicitly solvated biomolecular simulations. *The Journal of Physical Chemistry B*, 112(30), 9020-9041.
- Koleini, M. M., Mehraban, M. F., & Ayatollahi, S. (2018). Effects of low salinity water on calcite/brine interface: A molecular dynamics simulation study. *Colloids and Surfaces A: Physicochemical and Engineering Aspects*, 537, 61-68. doi:10.1016/j.colsurfa.2017.10.024
- Kopanichuk, I. V., Vedenchuk, E. A., Koneva, A. S., & Vanin, A. A. (2018). Structural properties of Span 80/Tween 80 reverse micelles by molecular dynamics simulations. *The Journal of Physical Chemistry B*, 122(33), 8047-8055.
- Kumar, B. (2012). *Effect of salinity on the interfacial tension of model and crude oil systems*. Graduate Studies,
- Lakshminarayanaiah, N., & White, M. (1969). Water flow through polymeric and nonaqueous liquid membranes. *Journal of Polymer Science Part A - 1: Polymer Chemistry*, 7(8), 2235-2245.
- Li, W., Nan, Y., You, Q., & Jin, Z. (2021). CO₂ solubility in brine in silica nanopores in relation to geological CO₂ sequestration in tight formations: Effect of salinity and pH. *Chemical Engineering Journal*, 411, 127626.
- Li, W., Zheng, X., Dong, Z., Li, C., Wang, W., Yan, Y., & Zhang, J. (2016). Molecular dynamics simulations of CO₂/N₂ separation through two-dimensional graphene oxide membranes. *The Journal of Physical Chemistry C*, 120(45), 26061-26066.
- MacElroy, J., & Boyle, M. (1999). Nonequilibrium molecular dynamics simulation of a model carbon membrane separation of CH₄/H₂ mixtures. *Chemical Engineering Journal*, 74(1-2), 85-97.
- Marrink, S.-J., & Berendsen, H. J. (1994). Simulation of water transport through a lipid membrane. *The Journal of Physical Chemistry*, 98(15), 4155-4168.
- Miller, C. A. (1988). Spontaneous emulsification produced by diffusion—a review. *Colloids and Surfaces*, 29(1), 89-102.
- Mokhtari, R., & Ayatollahi, S. (2019). Dissociation of polar oil components in low salinity water and its impact on crude oil–brine interfacial interactions and physical properties. *Petroleum Science*, 16(2), 328-343.
- Nosé, S. (1984). A molecular dynamics method for simulations in the canonical ensemble. *Molecular physics*, 52(2), 255-268.
- Patterson, J., & Morris, E. (1994). Measurement of absolute water density, 1 C to 40 C. *Metrologia*, 31(4), 277.
- Paul, S., & Chandra, A. (2004). Hydrogen bond dynamics at vapour–water and metal–water interfaces. *Chemical physics letters*, 386(4-6), 218-224.
- Pays, K., Giermanska-Kahn, J., Pouligny, B., Bibette, J., & Leal-Calderon, F. (2002). Double emulsions: how does release occur? *Journal of controlled release*, 79(1-3), 193-205.
- Peltonen, L., Hirvonen, J., & Yliruusi, J. (2001). The behavior of sorbitan surfactants at the water–oil interface: straight-chained hydrocarbons from pentane to dodecane as an oil phase. *Journal of colloid and interface science*, 240(1), 272-276.

- Plimpton, S. (1995). Fast parallel algorithms for short-range molecular dynamics. *Journal of Computational Physics*, 117(1), 1-19.
- Sanahuja-Embuena, V., Lim, S., Górecki, R., Trzaskus, K., Hélix-Nielsen, C., & Shon, H. K. (2021). Enhancing selectivity of novel outer-selective hollow fiber forward osmosis membrane by polymer nanostructures. *Chemical Engineering Journal*, 133634.
- Sandengen, K., Kristoffersen, A., Melhuus, K., & Jøssang, L. O. (2016). Osmosis as mechanism for low-salinity enhanced oil recovery. *SPE Journal*, 21(04), 1,227-221,235.
- Santana-Solano, J., Quezada, C. M., Ozuna-Chacón, S., & Arauz-Lara, J. L. (2012). Spontaneous emulsification at the water/oil interface. *Colloids and Surfaces A: Physicochemical and Engineering Aspects*, 399, 78-82.
- Schatzberg, P. (1963). Solubilities of water in several normal alkanes from C7 to C161. *The Journal of Physical Chemistry*, 67(4), 776-779.
- Schatzberg, P. (1965). *Diffusion of water through hydrocarbon liquids*. Paper presented at the Journal of Polymer Science Part C: Polymer Symposia.
- Schmitt, M., Toor, R., Denoyel, R., & Antoni, M. I. (2017). Spontaneous Microstructure Formation at Water/Paraffin Oil Interfaces. *Langmuir*, 33(49), 14011-14019. doi:10.1021/acs.langmuir.7b02549
- Stukowski, A. (2009). Visualization and analysis of atomistic simulation data with OVITO—the Open Visualization Tool. *Modelling and Simulation in Materials Science and Engineering*, 18(1), 015012.
- Su, J. T., Duncan, P. B., Momaya, A., Jutila, A., & Needham, D. (2010). The effect of hydrogen bonding on the diffusion of water in n-alkanes and n-alcohols measured with a novel single microdroplet method. *The Journal of Chemical Physics*, 132(4), 044506.
- Tsimpanogiannis, I. N., Moulton, O. A., Franco, L. F., Spera, M. B. d. M., Erdős, M., & Economou, I. G. (2019). Self-diffusion coefficient of bulk and confined water: a critical review of classical molecular simulation studies. *Molecular Simulation*, 45(4-5), 425-453.
- Underwood, T. R., & Greenwell, H. C. (2018). The water-alkane interface at various NaCl salt concentrations: a molecular dynamics study of the readily available force fields. *Scientific reports*, 8(1), 1-11.
- Wang, P., Li, W., Du, C., Zheng, X., Sun, X., Yan, Y., & Zhang, J. (2017). CO₂/N₂ separation via multilayer nanoslit graphene oxide membranes: molecular dynamics simulation study. *Computational Materials Science*, 140, 284-289.
- Wang, Z., Fingas, M., & Li, K. (1994). Fractionation of a light crude oil and identification and quantitation of aliphatic, aromatic, and biomarker compounds by GC-FID and GC-MS, part II. *Journal of chromatographic science*, 32(9), 367-382.
- Wen, L., & Papadopoulos, K. D. (2000). Visualization of water transport in W1/O/W2 emulsions. *Colloids and Surfaces A: Physicochemical and Engineering Aspects*, 174(1-2), 159-167.
- Xu, J., Zhang, Y., Chen, H., Wang, P., Xie, Z., Yao, Y., . . . Zhang, J. (2013). Effect of surfactant headgroups on the oil/water interface: An interfacial tension measurement and simulation study. *Journal of Molecular Structure*, 1052, 50-56.
- Yan, L., Aslannejad, H., Hassanizadeh, S. M., & Raoof, A. (2020). Impact of water salinity differential on a crude oil droplet constrained in a capillary: Pore-scale mechanisms. *Fuel*, 274, 117798.
- Yan, Y., Wang, W., Li, W., Loh, K., & Zhang, J. (2017). A graphene-like membrane with an ultrahigh water flux for desalination. *Nanoscale*, 9(47), 18951-18958.
- Zhang, C., Dai, H., Lu, P., Wu, L., Zhou, B., & Yu, C. (2019). Molecular Dynamics Simulation of Distribution and Diffusion Behaviour of Oil–Water Interfaces. *Molecules*, 24(10), 1905.
- Zhao, J., Yao, G., Ramiseti, S. B., Hammond, R. B., & Wen, D. (2018). Molecular dynamics simulation of the salinity effect on the n-decane/water/vapor interfacial equilibrium. *Energy & Fuels*, 32(11), 11080-11092.

Chapter 4

A nano-scale numerical model of ion transport in a thin aqueous film

Published as:

Aseyednezhad, S., Yan, L., Hassanizadeh, S. M., & Raoof, A. (2022). An accurate reduced-dimension numerical model for evolution of electrical potential and ionic concentration distributions in a nano-scale thin aqueous film. *Advances in Water Resources*, 159, 104058.

Abstract

The numerical modelling of ionic diffusive transport through a charged thin film of electrolyte is mathematically and computationally complex due to the strongly coupled hydrodynamics and electrochemical interactions. Generally, simulations are performed by solving the Poisson equation together with the Nernst-Planck flux formula to model electrochemical processes in electro-diffusion problems. One important application of these systems of equations to study the interaction of ionic diffusion and thin film hydrodynamics in petroleum engineering. However, due to the highly nonlinear and coupled equations the computational costs are heavy and very often limited to simulations in two-dimensional geometries. In this article, we have developed an equivalent one-dimensional electro-diffusive transport model based on mathematical averaging of 2D equations to reduce the computational time. Doing so, the computational time is improved substantially and simulation of much larger domain sizes which are required to study and interpret the experimental results is shown to be feasible. We have shown the high accuracy of the developed model by comparing the electric potential and concentration profiles of the developed model against the original 2D simulations. The developed approach reduces the computational effort by over 200 times without losing accuracy.

4.1 Introduction

Poisson-Nernst-Planck (PNP) equations are widely used to describe transport of ions in various applications including chemistry, physics, biology, and engineering (Bazant, Kilic, Storey, & Ajdari, 2009; Eisenberg, 1998; Kurnikova, Coalson, Graf, & Nitzan, 1999; Selberherr, 1984; Suopajarvi, 2015). Poisson equation is used to describe the electrical potential and the Nernst-Planck equation is applied to include the electric double layer effects in the transport of ions through a thin layer of electrolyte. Applying PNP equations in numerical modelling with application to membrane electrochemistry dates back to 1975 in the work of Cohen and Cooley and that of Brumleve and Buck (Brumleve & Buck, 1978; Cohen & Cooley, 1965). Use of PNP equations allows the computation of the space charge density near an interface which may represent a solution/electrode or solution/ion-exchange membrane interface (Uzdenova, Kovalenko, Urtenov, & Nikonenko, 2018). In addition, PNP equations are also known as the drift-diffusion equations and are used for simulating ion diffusion in semiconductor devices (Markowich, 1985; Newman & Thomas-Alyea, 2012). In these systems, the diffusion of ions is affected by the excess chemical potential produced by the mobile ions. Another application of PNP equations is in biological membrane channels (Cardenas, Coalson, & Kurnikova, 2000; Coalson & Kurnikova, 2005; Hollerbach, Chen, Busath, & Eisenberg, 2000), where the underlying mechanisms for ion transport through such channels are studied to understand the cellular activities of the living cells (Eisenman, 1987; Hille, 1978). Moreover, the PNP equations have been applied for solving ion transport in general nano- to macro-scale charged porous media (Mohajeri, Narsilio, Pivonka, & Smith, 2010; Pivonka, Narsilio, Li, Smith, & Gardiner, 2009). For electrically charged nano-porous materials, such as electrodes, the formation of an electrical double layer (EDL) considerably influences the transport and electro-sorption of ions inside the nanopores. This phenomenon leads to changes in pore accessibility (Zhang & Tartakovsky, 2017). Damiani, Yang, Churakov, and Kosakowski developed a reactive transport model based on the PNP to simulate the diffusion of ions through a charged constricted pore. Their work contributed to the understanding of the electrochemical migration of ions caused by changes in electric fields under various chemically reactive conditions such as those related to the swelling of clay minerals. The complex composition of mineral surfaces in geological media, either chemical

heterogeneity or pore property, poses challenges in the accurate description of ionic transport in porous media (Naidu, Bolan, Kookana, & Tiller, 1994; Norde & Lyklema, 1978). In the field of particle transport, Trefalt, Behrens, and Borkovec (2016) discussed the effect of charge regulation in Electrical Double Layer (EDL) on the interaction between colloids and interfaces by using the classical Poisson-Boltzmann theory. Several researchers have proposed theories to explain the impact of interfacial properties on macroscopic transport (Alizadeh, Jin, & Wang, 2019; Liu, Yao, & Shen, 2020). Yet, an accurate simulation of electrochemical processes in the presence of dynamic changes in electrical potential and ionic concentration induced by the alteration of solid charged surfaces and the surrounding electrolyte remains a challenging task.

Considering clayey soil as a notable example of charged porous media, different studies worked on flow, ion and chemical transport, and deformation in these systems (Kirby, 2010). Mahani, Berg, Ilic, Bartels, and Joekar-Niasar (2015) used a model system for sandstone rock consisting of clay minerals deposited at the glass substrate and oil droplets which were attached to clay patches separately. Their study was under the assumption of hydrodynamic equilibrium between the oil phase and the surrounding water. They studied ion diffusion and transport when the system is exposed to two different brine solutions having low and high-salinity values. Later, they studied the DLVO intermolecular forces by considering electrostatic forces and including osmotic pressure to understand the dynamics of disjoining pressure inside a thin film of electrolyte (Joekar-Niasar & Mahani, 2016). They coupled the Nernst-Planck ionic transport and Poisson equations with Navier-Stokes equation in order to describe the disjoining pressure and investigate its impact on the transport of ions within the thin film. They found that the nonlinear behaviour in the pressure field, which is caused by multidirectional and asymmetric ions transport, is strongly affected by the diffusion length and the overlapping of EDL.

While the coupled PNP model provides quantitative prediction of ion transport problem in many areas, it has its own limitations such as neglecting the finite size effect of ion particles and correlation effect (i.e., self-energy) which may become important in very confined channels (Jung, Lu, & Mascagni, 2009).

Concerning model limitations such as ion-ion interactions and steric effects, some recent theoretical modifications have been proposed. For example, Corry, Kuyucak, and Chung (2003) demonstrated that if a specific self-energy term is

included in the NP equation, qualitative improvements could be made in the computational results. Kilic, Bazant, and Ajdari (2007a); (Kilic, Bazant, & Ajdari, 2007b) proposed a simple modification of the widely used PNP equations through including the steric effect due to ion transport. They reported that some limitations confronted in specific applications, such as those related to ionic channels, can be sufficiently improved by adjusting the diffusion coefficients, or by considering additional force terms in the ion flux formula of the NP equation (Zheng & Wei, 2011).

On the other hand, one of the challenges in the application of PNP to model ion transport in electrode and membrane system is the implementation of certain boundary conditions that make models mathematically complex. For example, this is encountered in 2D modelling of ion and water transfer to describe electrochemical processes in membranes (Pismensky et al., 2012) and electrodes in galvanostatic mode (Mareev et al., 2016) on the basis of local electroneutrality. This required applying an integral boundary condition for the electric current density which caused high computational demands. Uzdenova et al. (2018) proposed a 1D model based on PNP equations for the galvanostatic mode. Their model eliminated the need for an additional interface for the time integral calculations. They specified the electric potential gradient as an explicit function of the total current density at the outer edge of the diffusion layer of ion-exchange membrane and solution interface instead of the time derivative of the electric potential gradient at this boundary. Their model eliminated the need for an additional coupling due to the time integral calculations.

Other importance of simplifying the numerical models based on PNP equations is related to the fact that they are computationally very complex. For example, to improve the computational efficiency in the study of ion transport in a multilayer graphene membrane, one approach would be to reduce the dimensionality of the nanochannel. Doing so, the computational cost of the problem without significant loss of accuracy are significantly reduced. Jiang, Wang, Cheng, Li, and Liu (2018) have developed an equivalent one-dimensional ion transport model for the tortuous nano-slit systems embedded in a multi-layered graphene membrane. They concluded that the equivalent 1D model should provide a framework to interpret and rationalize the experimental results of ion transport in the cascading nano-slit systems. It may provide a simple, yet quantitative, model to design 2D

materials-based membranes for various applications, such as energy storage, electrode design, ion separation, water desalination or treatment.

The aim of this study is to enhance the computational efficiency needed to simulate ion transport in charged media. We have first developed a 2D axisymmetric model to investigate the ion transport within a film of water underlying an oil droplet, with negatively charged surfaces on its top and bottom boundaries. The film is initially filled with a high-salinity electrolyte, and then it is exposed on lateral sides to a bulk fluid with lower salinity.

Our 2D model was developed based on the model proposed by Mahani et. al 2016 in which the interaction of ionic diffusion and thin film hydrodynamic was studied. In simulations using the developed 2D model, only very small domain size could be considered as otherwise the very large domain aspect ratio could cause numerical problems. Considering the assumptions of fixed and rigid boundaries and incompressible water phase in the 2D model, there is no net inflow of water into the domain. There could be flow circulation within the domain which is expected to be very small.

In a next step, in order to reduce the complexity and the computational effort, we have derived and developed an averaged, one-dimensional, coupled Poisson-Nernst-Planck model to simulate electro-diffusion in the same system. To do so, we have integrated the governing differential equations along the channel height. This strategy allowed us to solve the equations for a much larger realistic domain size relative to that used in the 2D model. Our results using the 1D model to solve for PNP equations showed exact agreement with the results from the 2D model, however with significantly lower computational time and modelling complexities.

4.2 Theory of Electrical Double Layer

In this section, we will describe the Electrical Double Layer (EDL) and the general form of the equations used in this study to simulate the electric field and ion transport within the channel.

4.2.1 EDL theory

An EDL has a structure of two parallel layers of charges appearing at the surface of a material when exposed to an ionic solution.

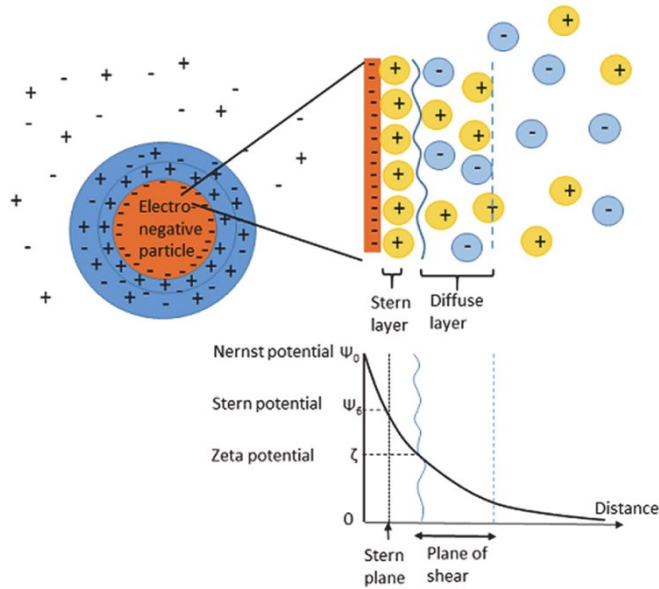


Figure 4-1: Schematic of an electric double layer (EDL) and electrical charge distribution near a negatively charged surface (Kelessidis & Maglione, 2008).

The first layer, called stern layer, consists of either positive or negative ions adsorbed onto the surface due to chemical interactions. The second layer is formed by ions attracted to the surface charge via the coulomb force (shear plane) and free ions moving in the fluid under the influence of electric attraction and thermal motion (diffuse layer). Typically, the electric double layer may be of interest when modelling very thin layers of electrolyte such as that studied here. To model the behaviour of the diffuse double layer, one should solve Nernst-Planck equations for all ions in combination with the Poisson equation for the electrical potential.

4.2.2 Electric field

To simulate the electric field, we use the coupled Poisson-Nernst Plank (PNP) equations. The electro-osmotic flow occurs through the film because electric double-layers are developed at the top and bottom interfaces and overlap with each other. Under these conditions, there is no thermodynamic equilibrium and thus Poisson-Boltzmann equations cannot be used for the simulation of ionic distribution. Instead, the Nernst-Planck equation should be used to find the

distribution of ions within the electric double-layer under dynamic non-equilibrium condition. To model the electrical potential, the Poisson equation is used as:

$$\nabla^2 \Psi = - \rho_e / \epsilon \quad [4.1]$$

where ϵ is the permittivity of the medium and ρ_e is the charge density due to ion concentrations. The latter can be described as:

$$\rho_e = \sum e z_i n_a c_i \quad [4.2]$$

where c_i , represents concentrations of two ions of opposite charge, z_i , n_a and e denote the valence of the ion i (+1/ -1), Avogadro number and elementary charge, respectively.

4.2.3 Ion Transport

To solve for the concentrations, c_i , of two ions in an electrolyte solution, we can use the Nernst-Planck equation. The molar flux of ions, j_i , are described as follow:

$$j_i = c_i V - D_i \nabla c_i - u_{(m,i)} z_i F c_i \nabla \Psi \quad [4.3]$$

where D_i is the diffusion coefficient, V is advective velocity, $u_{m,i}$ is the mobility, F is Faraday's constant, and Ψ is the electrical potential. The conservation of ions in a medium provides $\frac{\partial c_i}{\partial t} + (\nabla \cdot j_i + R_i) = 0$. Assuming no chemical reactions ($R_i = 0$) in the electrolyte, for the two species under equilibrium and dynamic condition we obtain, respectively:

$$\nabla \cdot j_i = 0 \quad [4.4]$$

$$(\partial c_i) / \partial t + \nabla \cdot j_i = 0 \quad [4.5]$$

4.3 1D and 2D numerical modelling

Modelling approach and model configurations

In this study, we assumed that a thin layer of high-salinity electrolyte solution is squeezed between an oil droplet and a clay platelet and is initially under thermodynamically equilibrium condition. Then, we exposed the lateral boundaries of the domain with a solution having lower salinity. This initiates the

diffusion of ions and the evolution of the electric field through the film. Such a thin layer can be conceptualized as a disc with axis-symmetrical properties (Mahani et al., 2015). To simulate electric field and ions transport within this thin layer, we first developed a 2D model. Due to the coupling between highly complex and nonlinear equations, this model had relatively heavy computational costs which limit its usage for larger realistic domain sizes because of the high aspect ratio. This problem together with the dominant flow and transport in the horizontal direction motivates the development an equivalent 1D model to reduce the computational efforts and do the simulation for a larger domain which is comparable to the experiment.

4.3.1 2D model

Initial and boundary conditions in the 2D model

In the following, a 2D simulation domain and schematic overview of the relevant boundary conditions are presented. As shown in Figure 4-2, the 2D system is modelled as axisymmetric geometry with an axial coordinate z and a radial coordinate r , respectively. In order to compare our results with those of Mahani et. al, we considered a similar film size with a radius of 20 nm and a height of 4 nm (i. e., $L = 20\text{ nm}$ and $h = 4\text{ nm}$). On the left boundary of the domain (i.e., the symmetry axis of the cylindrical domain) a no-flux boundary condition was imposed. At the right boundary, being exposed to the low-salinity bulk solution, the electrical potential was set to zero and the concentrations of the ion species, c_p and c_m (mol/m^3), were set to a constant value c_b (i.e., the concentration of low-salinity solution in the bulk region). The top and bottom boundaries represent the interfaces of the electrolyte with oil and clay, respectively, which are negatively charged surfaces and carry constant surface charge density, σ (C/m^2), and a no-flux ($-n \cdot D \nabla c_i = 0$) boundary conditions for Nernst-Planck equation. We specified a space charge density of $\rho_e = e n_a (c_p - c_m)$ (C/m^3) on the entire domain.

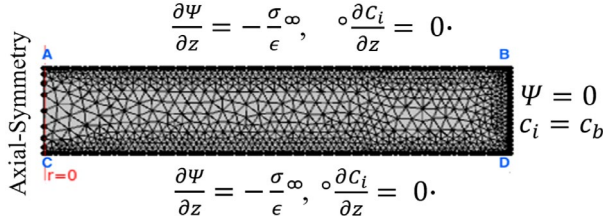


Figure 4-2: The 2D representations of the simulation domain together with the boundary conditions for Poisson and Nernst-Planck Equations. The domain in 2D represents a radial cross-section of 20 nm long with a total height of 4 nm ($L = 20 \text{ nm}$ and $h = 4 \text{ nm}$). The left boundary is axisymmetric, and the right boundary applies a zero electric potential and a fixed concentration of the bulk solution. The top and bottom boundaries represent negatively charged surfaces are the interfaces of electrolytes with oil and clay, respectively, and carrying constant surface charge density and no-mass-flux conditions.

We assumed that initially, the system is in equilibrium with residing high-salinity bulk solution. To solve for the corresponding initial distribution of electrical potential $\Psi(r, z)$ and concentration field, of the cation and the anion $C_i(r, z)$ for our 2D model, we solved Eq. 4-1 and Eq. 4-4, respectively. As the domain is closed with fixed boundaries and water is considered incompressible, the flow into the domain is zero and there is no need to simulate fluid flow.

3.2.2 2D cylindrical form of the governing equations under dynamic conditions

In this section, we provide the governing equations for electrical potential $\Psi(r, z)$ and concentration field of cation and anion $C_i(r, z)$ in a cylindrical coordinate for our 2D model under dynamic conditions. As we exposed the right boundary to the low-salinity bulk solution, the diffusion of ions and evolution of the electric field occurs through the film. In the Poisson equation to calculate the electrical potential $\Psi(r, z)$, Equations 4-1 and 4-2 can be written for axisymmetric conditions as:

$$\frac{\partial^2 \Psi}{\partial z^2} + \frac{1}{r} \frac{\partial}{\partial r} \left(r \frac{\partial \Psi}{\partial r} \right) = - \frac{\sum e N_a z_i c_i}{\epsilon} \quad [4.6]$$

For ions transport under dynamic conditions (and excluding the convection term) Eqs. 5 and 3 provide:

$$\frac{\partial c_i}{\partial t} + \frac{D_i}{k_B T} N_a e z_i \left[\frac{\partial}{\partial z} \left(c_i \frac{\partial \psi}{\partial z} \right) + \frac{1}{r} \frac{\partial}{\partial r} \left(c_i r \frac{\partial \psi}{\partial r} \right) \right] + D_i \left[\frac{\partial^2 c_i}{\partial z^2} + \frac{1}{r} \frac{\partial}{\partial r} \left(r \frac{\partial c_i}{\partial r} \right) \right] = 0 \quad [4.7]$$

4.3.2 1D model

1D domain and boundary conditions

The 1D model has a length of 20 nm long, representing the extent of the electrolyte between oil and clay. In this model, the left boundary is axis-symmetric, and the right boundary applies a zero electric potential and a fixed concentration of bulk solution for Poisson and Nernst-Planck Equations, respectively.

In 1D model, the effect of surface charge density should be taken into account using a source term. We have defined the charge density in the one-dimensional space as

$$\rho_e = \frac{2}{h} \frac{\sigma}{\epsilon} + e n_a (c_p - c_m) \quad [4.8]$$

Derivation of the 1D form of the governing equations in the radial coordinate

In order to derive the 1D equations, we integrate all terms along the height of the film. First, we define the averaged electrical potential $\bar{\Psi}(r)$ and averaged ion concentrations $\bar{C}_i(r)$ as:

$$\bar{\Psi}(r) = \frac{1}{h} \int_0^h \Psi(r, z) dz \quad [4.9]$$

$$\bar{C}_i(r) = \frac{1}{h} \int_0^h C_i(r, z) dz \quad [4.10]$$

Table 4-1 provides the integrated forms of each term in the Poisson and Nernst-Planck equations. For some terms, we have used the top and bottom boundary conditions of the 2D model.

Table 4-1: This table includes the integrated forms of all terms of Poisson and Nernst-Planck equations

Integrated form of each term of Poisson equation	
$\int_0^h \frac{\partial^2 \Psi}{\partial z^2} dz = \left(\frac{\partial \Psi}{\partial z} \right)_h - \left(\frac{\partial \Psi}{\partial z} \right)_0 = -\frac{\sigma}{\epsilon} - \frac{\sigma}{\epsilon} = -2 \frac{\sigma}{\epsilon}$	[4.11]
$\int_0^h \frac{1}{r} \frac{\partial}{\partial r} \left(r \frac{\partial \Psi}{\partial r} \right) dz = \frac{1}{r} \frac{\partial}{\partial r} \left(r \frac{\partial \bar{\Psi} h}{\partial r} \right)$	[4.12]
$-\int_0^h \frac{\sum e N_a z_i c_i}{\epsilon} dz = -\frac{h \sum e N_a z_i \bar{c}_i}{\epsilon}$	[4.13]
Integrated form of each term of Nernst-Planck equation	
$\int_0^h \frac{\partial}{\partial z} \left(c_i \frac{\partial \Psi}{\partial z} \right) dz = \left(c_i \frac{\partial \Psi}{\partial z} \right)_h - \left(c_i \frac{\partial \Psi}{\partial z} \right)_0 = -c_i \frac{\sigma}{\epsilon} - c \frac{\sigma}{\epsilon} = -2 c_i \frac{\sigma}{\epsilon}$	[4.14]
$\int_0^h \frac{1}{r} \frac{\partial}{\partial r} \left(c_i r \frac{\partial \Psi}{\partial r} \right) dz = \frac{1}{r} \frac{\partial}{\partial r} \left(r \int_0^h (\bar{c}_i + \hat{c}_i) \frac{\partial \Psi}{\partial r} dz \right)$ $= \frac{1}{r} \frac{\partial}{\partial r} \left(r \bar{c}_i \int_0^h \frac{\partial \Psi}{\partial r} dz \right) + \frac{1}{r} \frac{\partial}{\partial r} \left(r \int_0^h \hat{c}_i \frac{\partial \Psi}{\partial r} dz \right)$ $= \frac{h}{r} \frac{\partial}{\partial r} \left(r \bar{c}_i \frac{\partial \bar{\Psi}}{\partial r} \right) + \frac{1}{r} \frac{\partial}{\partial r} \left(r \int_0^h \hat{c}_i \frac{\partial \Psi}{\partial r} dz \right)$	[4.15]
$\int_0^h \frac{\partial^2 c_i}{\partial z^2} dz = \left(\frac{\partial c_i}{\partial z} \right)_h - \left(\frac{\partial c_i}{\partial z} \right)_0 = 0$	[4.16]
$\int_0^h \frac{1}{r} \frac{\partial}{\partial r} \left(r \frac{\partial c_i}{\partial r} \right) dz = \frac{1}{r} \frac{\partial}{\partial r} \left(r \frac{\partial}{\partial r} \right) \int_0^h c_i dz = \frac{1}{r} \frac{\partial}{\partial r} \left(r \frac{\partial \bar{c}_i h}{\partial r} \right)$	[4.17]

Based on the information provided in Table 1, the final form of the PNP equations in a one-dimensional space can be written as:

$$\frac{1}{r} \frac{\partial}{\partial r} \left(r \frac{\partial \bar{\Psi} h}{\partial r} \right) - 2 \frac{\sigma}{\epsilon} = \frac{h \sum e N_a z_i \bar{c}_i}{\epsilon} \quad [4.18]$$

$$\frac{\partial \bar{c}_i h}{\partial t} + \frac{D_i N_a e z_i}{k_B T} \left[\frac{1}{r} \frac{\partial}{\partial r} \left(r \bar{c}_i \frac{\partial \bar{\Psi} h}{\partial r} \right) - 2 c_i \frac{\sigma}{\epsilon} \right] + \frac{D_i}{r} \frac{\partial}{\partial r} \left(r \frac{\partial \bar{c}_i h}{\partial r} \right) = 0 \quad [4.19]$$

We first solved these equations for the initial equilibrium condition and the dynamic condition when considering the domain to expose the low-salinity bulk fluid.

4.3.3 Model Parameter values

Parameter values considered for our simulations are given in Table 4-2. In the Nernst-Planck equation, only the migration term and the existence of two ion species (c_p and c_m), with valences 1.0 and -1.0, were included.

Table 4-2: Parameter values used in the simulation

Parameter	Value/Range
Relative solvent permittivity (ϵ_r)	80
Ion Diffusivity (D)	10^{-9} m ² /s
Temperature (T)	298 K
Fluid mass density (ρ)	1000 kg/m ³
Fluid viscosity (μ)	0.001 Pa·s
Domain radius range (L)	20-10000 nm
Domain height (h)	4 nm

To better present the modelling results, some dimensionless variables are used as defined in Table 4-3. Here, λ_D^H , is the Debye length for the system under high-salinity initial condition determined using $\lambda_D^H = \left(\frac{\epsilon k_B T}{e^2 n_a \sum z_i^2 c_b^H} \right)^{0.5}$

Table 4-3: The dimensionless form of some key variables

Dimensionless variable	Formula
Dimensionless radius (r^*)	$\frac{L}{\lambda_D^H}$
Dimensionless height (z^*)	$\frac{h}{\lambda_D^H}$
Dimensionless electric potential (Ψ^*)	$\frac{e\Psi}{k_B T}$
Dimensionless Concentration (c^*)	$\frac{c_i}{c_b^H}$

4.4 Simulation results and discussion

In this section, we provide the results obtained from the numerical simulation of coupled PNP equations. We will first describe the results for electrical potential and ion concentrations under initial equilibrium conditions obtained from our 1D model. Afterwards, we compare the dynamic results of this 1D model with those of the 2D model to verify our model. To show the efficiency of the developed model, the computational time ratio between the 1D model and the 2D model is provided for different domain lengths (including $r = 1000, 5000$, and 10000 nm). The analysis showed that the 1D model can solve the equations 180-220 times faster than the 2D model. After verification, we use the developed efficient model to perform simulation for a much longer domain size ($r = 0.5 \text{ mm}$) which is not feasible to be simulated using the original 2D model due to its computational demands.

4.4.1 Initial equilibrium condition for the 1D model

Initially, the domain is filled with high-salinity bulk solution which is under equilibrium conditions. We performed a simulation for $r^* = 2$ and $z^* = 0.4$ with a constant surface charge density $\sigma = -0.017 \text{ C/m}^2$. Figure 4-3 shows the profile of the electrical potential field along the film radius. It is shown that, moving horizontally away from the centre of the domain ($r^* = 2$), the electrical field becomes weaker. Since the interfaces are negatively charged, the concentration of cation is higher compared to the anion concentration, and by getting closer to the outlet the difference between concentrations becomes smaller and finally at the outlet the ion concentrations reach their bulk value. This behaviour is clear in Figure 4-4a and Figure 4-4b showing the concentration profiles for the anion and cation, respectively.

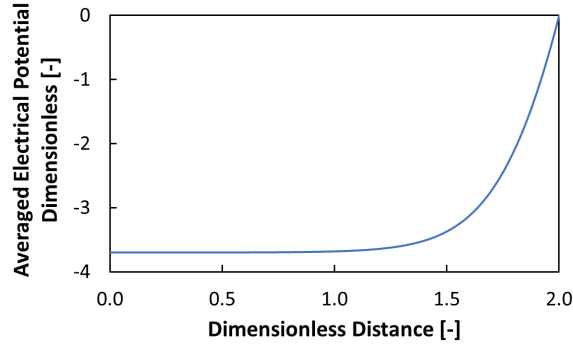


Figure 4-3: Electrical potential. The initial distribution of electrical potential ($r^* = 2$ and $z^* = 0.4$) with the domain filled with high-salinity solution.

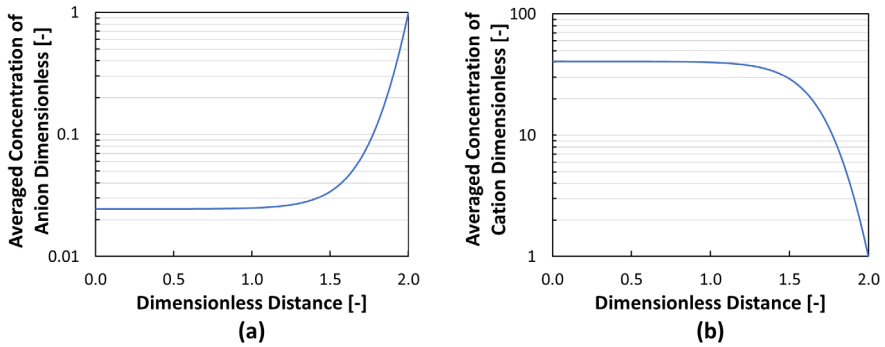


Figure 4-4: Concentration profiles. Initial distribution of concentration along the domain for (a) anion and (b) cation ($r^* = 2$ and $z^* = 0.4$) with the domain filled with high-salinity solution.

4.4.2 1D model verification under dynamic condition

To study the system behaviour under dynamic conditions, we performed simulations by including the unsteady time-dependent terms. To verify the simulation results for electrical potential and ion concentrations, we compared the results with those obtained using the corresponding 2D model (for $r^* = 2$ and $z^* = 0.4$). Figure 4-5 shows this comparison for electrical potential evolution over time in a radial direction for thin film scenarios. The solid line and the

triangular markers show the results that are obtained from 1D and 2D models, respectively. The blue curve shows the results for the first time step and the red curve shows the final, i.e., equilibrium, solution balanced with the low-salinity bulk solution. The simulation run was 10^{-6} seconds, and the graphs are equally distributed between the beginning of the simulation and the end time of the simulation.

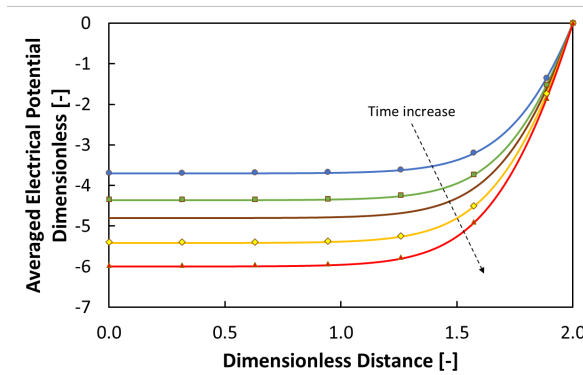


Figure 4-5: Dynamic conditions. Evolution of electric potential in the radial direction ($r^* = 2$ and $z^* = 0.4$). Solid lines represent the results for the 1D and the various markers represent the corresponding results of the 2D models. The blue curve shows the first time step and the red curve shows the final equilibrium under low-salinity bulk solution. The graphs are equally distributed between the beginning of the simulation and the end time of the simulation corresponding to 10^{-6} seconds.

Figure 4-6a and Figure 4-6b show the dynamics of anion and cation concentration for thin film, respectively. Again, the solid lines represent the results obtained from the 1D model and the triangular markers represent those of the 2D models. It is shown that, after we reduce the concentration of the surrounding bulk solution, compared to the high-salinity bulk solution inside the film, the diffusion of ions starts in between the film and the surrounding environment. We considered the ions with similar absolute valence and diffusion coefficient. By comparing the two figures, the outward diffusion rate of cation is lower compared to anion due to the presence of negative electrical charges on the top and bottom boundaries.

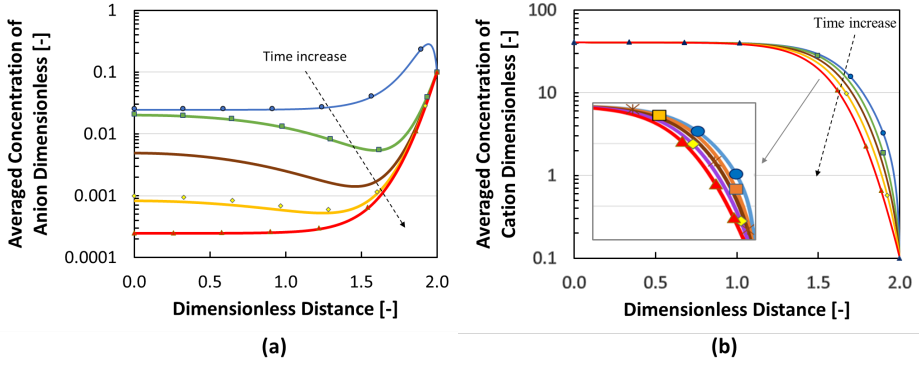


Figure 4-6: dynamic conditions. Evolution of (a) anion and (b) cation concentration profiles in the radial direction (for domain $r^* = 2$ and $z^* = 0.4$). Solid lines represent the results for the 1D and the various markers represent the corresponding results of the 2D models.

Blue curves represent the first time-step after exposing the right boundary to the low-salinity bulk solution and the red curves show the final equilibrium under the low-salinity bulk solution. The graphs are equally distributed between the beginning of the simulation and the end time of the simulation corresponding to 10^{-6} seconds.

The above figures show exact agreements between the results for electrical potential and ions concentration from both models. The 1D model, however, allows reducing the computational time by over 180-220 times without losing accuracy. Figure 4-7 provides the acquired computational benefit using the 1D model for simulations using different film lengths. As demonstrated, the computational benefit becomes much larger for bigger film lengths where the 1D model becomes significantly faster than the 2D model.

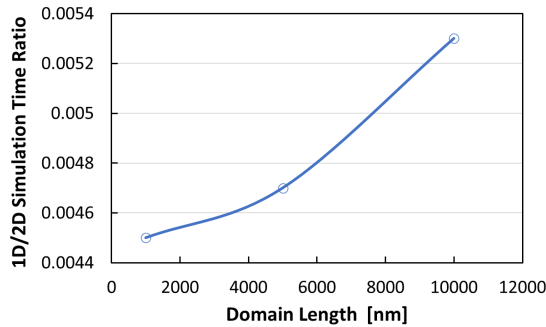


Figure 4-7: Time ratio of 1D over 2D models. to compare how faster the 1D model could solve the simulation giving the same results as those of the 2D model, we plotted the computational time ratio of 1D over the 2D model for different film lengths.

4.4.3 1D Simulation results for a more realistic domain length

We performed simulation using the 1D model for a more realistic domain length, $r = 0.5 \text{ mm}$, i.e., 25000 times larger than simulations used for model verifications which were not possible to simulate using the 2D model due to the high computational cost. The results for the electric potential and the anion and cation concentration profile obtained from the 1D model are provided in Figure 4-8 and Figure 9a-b, respectively. The computational time for this large 1D model was 8 minutes.

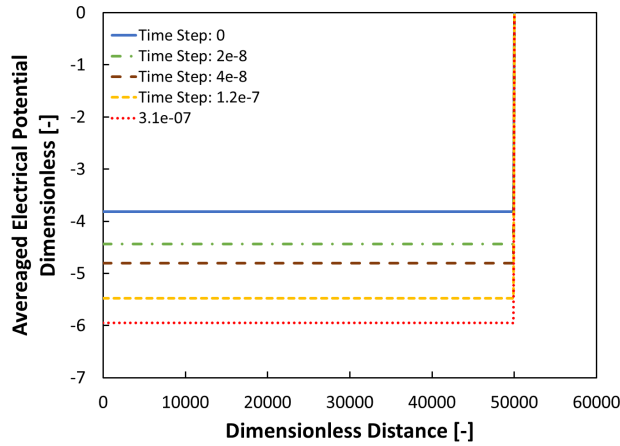


Figure 4-8: Large 1D model. Evolution of electrical potential under dynamic conditions for the film with $r^* = 50000$ and $z^* = 0.4$. The blue curve shows the first time step and the red curve shows the final equilibrium under low-salinity bulk solution.

Figure 4-8 represents the evolution of the electric field along the radial direction for this large 1D model. The blue curve shows initial equilibrium condition under high-salinity bulk solution and the red curve shows the final equilibrium condition under lower salinity bulk solution. The choice of time steps, as shown in the figure legend, was used to better show the evolution of the electrical potential.

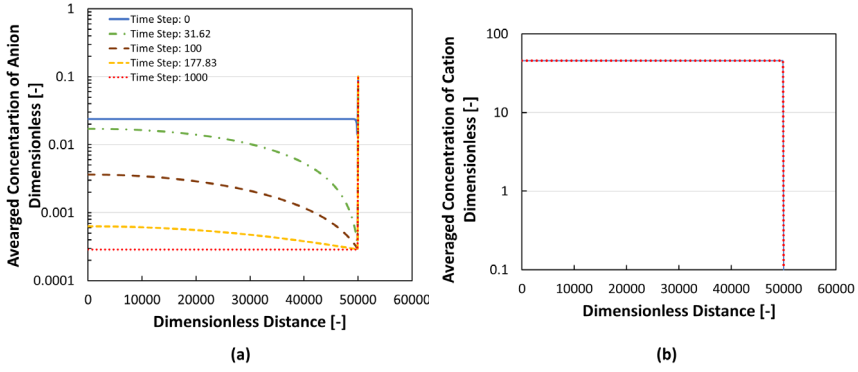


Figure 4-9: Large 1D model. Evolution of (a) anion and (b) cation concentration profiles in radial direction under dynamic condition for the film with $r^* = 50000$ and $z^* = 0.4$. Blue curve shows the first time step and the red curve shows the final equilibrium under low-salinity bulk solution. For cation concentration profiles, all the results overlapping each other due to the presence of negatively electrical charges.

In this large 1D model, the negatively charged system was initially under the thermodynamical equilibrium condition for high-salinity bulk solution. As we exposed the right boundary to the lower salinity solution, this initial equilibrium condition is disturbed, and the diffusion of ions initiates between high-salinity and low-salinity bulk solution. Since a field of the electrical potential gradient is imposed on the concentration gradient (as explained in section 4.3.2) the ionic diffusion becomes more limited and due to the presence of negatively electrical charges the mobility of cations is strongly affected and they mostly remain inside the system. Therefore, as shown in Figure 4-9a, we could see the diffusion of anion over time while Figure 4-9b shows that all the graphs for cation concentration profiles are overlapping each other.

4.5 Conclusion

In this work, we have developed an effective one-dimensional model to simulate electro-diffusion inside a thin layer of electrolyte located between two charged surfaces. This model has been used to simulate the evolution of electrical potential and ion concentrations distribution along the thin film of electrolyte. Simulations showed that because of the negatively charged surfaces the mobility of the cations was severely affected by the electric charges and these ions had lower outward diffusion rate compared to flux of anions. The developed model

could significantly reduce the computational time by a factor of 180-220 compared to simulation using a 2D model. The equivalent 1D model enables solving the nonlinear governing equations for much larger domain lengths providing unique opportunity to simulate experimental results of ion transport in thin films where the very large height to length ratio prevents use of 2D simulations. In future works flow equations can be added to the effective 1D model to investigate the increase of film thickness due to the coupled effects of electroosmotic and water flow over time and detachment of the oil phase from the solid surface in scales comparable with the experimental observations.

References

- Alizadeh, A., Jin, X., & Wang, M. (2019). Pore - scale study of ion transport mechanisms in inhomogeneously charged nanoporous rocks: Impacts of interface properties on macroscopic transport. *Journal of Geophysical Research: Solid Earth*, 124(6), 5387-5407.
- Bazant, M. Z., Kilic, M. S., Storey, B. D., & Ajdari, A. (2009). Towards an understanding of induced-charge electrokinetics at large applied voltages in concentrated solutions. *Advances in colloid and interface science*, 152(1-2), 48-88.
- Brumleve, T. R., & Buck, R. P. (1978). Numerical solution of the Nernst-Planck and Poisson equation system with applications to membrane electrochemistry and solid state physics. *Journal of Electroanalytical Chemistry and Interfacial Electrochemistry*, 90(1), 1-31.
- Cardenas, A. E., Coalson, R. D., & Kurnikova, M. G. (2000). Three-dimensional Poisson-Nernst-Planck theory studies: Influence of membrane electrostatics on gramicidin A channel conductance. *Biophysical Journal*, 79(1), 80-93.
- Coalson, R. D., & Kurnikova, M. G. (2005). Poisson-Nernst-Planck theory approach to the calculation of current through biological ion channels. *IEEE transactions on nanobioscience*, 4(1), 81-93.
- Cohen, H., & Cooley, J. (1965). The numerical solution of the time-dependent Nernst-Planck equations. *Biophysical Journal*, 5(2), 145-162.
- Corry, B., Kuyucak, S., & Chung, S.-H. (2003). Dielectric self-energy in Poisson-Boltzmann and Poisson-Nernst-Planck models of ion channels. *Biophysical Journal*, 84(6), 3594-3606.
- Damiani, L. H., Yang, Y., Churakov, S. V., & Kosakowski, G. *Nernst-Planck Solver (NPS) applied to diffusion of ions through a constricted pore*. Paper presented at the Deliverable nD4. 13 Draft of the 3rd Annual Project Workshop Proceeding.
- Eisenberg, B. (1998). Ionic channels in biological membranes-electrostatic analysis of a natural nanotube. *Contemporary Physics*, 39(6), 447-466.
- Eisenman, G. (1987). An introduction to molecular architecture and permeability of ion channels. *Annual review of biophysics and biophysical chemistry*, 16, 205-226.
- Hille, B. (1978). Ionic channels in excitable membranes. Current problems and biophysical approaches. *Biophysical Journal*, 22(2), 283-294.
- Hollerbach, U., Chen, D. P., Busath, D. D., & Eisenberg, B. (2000). Predicting Function from Structure Using the Poisson- Nernst- Planck Equations: Sodium Current in the Gramicidin A Channel. *Langmuir*, 16(13), 5509-5514.
- Jiang, G., Wang, P., Cheng, C., Li, D., & Liu, J. Z. (2018). An equivalent 1D nanochannel model to describe ion transport in multilayered graphene membranes. *Progress in Natural Science: Materials International*, 28(2), 246-250.
- Joekar-Niasar, V., & Mahani, H. (2016). Nonmonotonic pressure field induced by ionic diffusion in charged thin films. *Industrial & Engineering Chemistry Research*, 55(21), 6227-6235.
- Jung, Y.-W., Lu, B., & Mascagni, M. (2009). A computational study of ion conductance in the KcsA K⁺ channel using a Nernst-Planck model with explicit resident ions. *The Journal of chemical physics*, 131(21), 12B601.
- Kelessidis, V., & Maglione, R. (2008). Yield stress of water-bentonite dispersions. *Colloids and Surfaces A: Physicochemical and Engineering Aspects*, 318(1-3), 217-226.
- Kilic, M. S., Bazant, M. Z., & Ajdari, A. (2007a). Steric effects in the dynamics of electrolytes at large applied voltages. I. Double-layer charging. *Physical Review E*, 75(2), 021502.
- Kilic, M. S., Bazant, M. Z., & Ajdari, A. (2007b). Steric effects in the dynamics of electrolytes at large applied voltages. II. Modified Poisson-Nernst-Planck equations. *Physical Review E*, 75(2), 021503.
- Kirby, B. J. (2010). *Micro-and nanoscale fluid mechanics: transport in microfluidic devices*: Cambridge university press.

- Kurnikova, M. G., Coalson, R. D., Graf, P., & Nitzan, A. (1999). A lattice relaxation algorithm for three-dimensional Poisson-Nernst-Planck theory with application to ion transport through the gramicidin A channel. *Biophysical Journal*, 76(2), 642-656.
- Liu, R., Yao, S., & Shen, Y. (2020). Pore-scale investigation on ion transport and transfer resistance in charged porous media with micro-macro structure. *Journal of Molecular Liquids*, 320, 114481.
- Mahani, H., Berg, S., Ilic, D., Bartels, W.-B., & Joekear-Niasar, V. (2015). Kinetics of low-salinity-flooding effect. *SPE Journal*, 20(01), 8-20.
- Mareev, S., Nichka, V., Butylskii, D. Y., Urtenov, M. K., Pismenskaya, N., Apel, P. Y., & Nikonenko, V. (2016). Chronopotentiometric response of an electrically heterogeneous permselective surface: 3D modeling of transition time and experiment. *The Journal of Physical Chemistry C*, 120(24), 13113-13119.
- Markowich, P. A. (1985). *The stationary semiconductor device equations*: Springer Science & Business Media.
- Mohajeri, A., Narsilio, G. A., Pivonka, P., & Smith, D. W. (2010). Numerical estimation of effective diffusion coefficients for charged porous materials based on micro-scale analyses. *Computers and Geotechnics*, 37(3), 280-287.
- Naidu, R., Bolan, N., Kookana, R. S., & Tiller, K. (1994). Ionic - strength and pH effects on the sorption of cadmium and the surface charge of soils. *European journal of soil science*, 45(4), 419-429.
- Newman, J., & Thomas-Alyea, K. E. (2012). *Electrochemical systems*: John Wiley & Sons.
- Norde, W., & Lyklema, J. (1978). The adsorption of human plasma albumin and bovine pancreas ribonuclease at negatively charged polystyrene surfaces: I. Adsorption isotherms. Effects of charge, ionic strength, and temperature. *Journal of colloid and interface science*, 66(2), 257-265.
- Pismensky, A., Urtenov, M. K., Nikonenko, V., Sistat, P., Pismenskaya, N., & Kovalenko, A. (2012). Model and experimental studies of gravitational convection in an electromembrane cell. *Russian Journal of Electrochemistry*, 48(7), 756-766.
- Pivonka, P., Narsilio, G. A., Li, R., Smith, D. W., & Gardiner, B. (2009). Electrodifusive transport in charged porous media: from the particle-level scale to the macroscopic scale using volume averaging. *Journal of Porous Media*, 12(2).
- Selberherr, S. (1984). *Analysis and simulation of semiconductor devices*: Springer Science & Business Media.
- Suopajärvi, T. (2015). Functionalized nanocelluloses in wastewater treatment applications. *Acta Universitatis Ouluensis C*, 526.
- Trefalt, G., Behrens, S. H., & Borkovec, M. (2016). Charge regulation in the electrical double layer: ion adsorption and surface interactions. *Langmuir*, 32(2), 380-400.
- Uzdenova, A., Kovalenko, A., Urtenov, M., & Nikonenko, V. (2018). 1D mathematical modelling of non-stationary ion transfer in the diffusion layer adjacent to an ion-exchange membrane in galvanostatic mode. *Membranes*, 8(3), 84.
- Zhang, X., & Tartakovsky, D. M. (2017). Effective ion diffusion in charged nanoporous materials. *Journal of The Electrochemical Society*, 164(4), E53.
- Zheng, Q., & Wei, G.-W. (2011). Poisson-boltzmann-nernst-planck model. *The Journal of chemical physics*, 134(19), 194101.

Chapter 5

Wettability effect on pore-filling events for two-phase flow

Abstract

Wettability is a crucial factor for pore-filling events in multiphase flow. If the fluid interface passes an abrupt variation in the cross-section of the porous medium, a sudden redistribution takes place, commonly known as Haines Jump. Different wettabilities of the solid substrate affect the global displacement pattern, the fluid trapping and the hysteretic saturation. Furthermore, the effect of wettability needs to be considered in numerical and analytical models to enable an accurate description of the pressure response during such a pore-filling event.

To better understand the effect of wettability, we conduct a series of wettability modified microfluidic experiments to investigate the drainage and imbibition processes for water-air and water-fluorinert displacement under three injection flow rates. The PDMS micro-model is designed with a depth of 100 μm and with one square pore body of 800 μm in width and length which is connected to 4,000 μm long inlet and outlet channels with a height of 150 μm . The models are rendered with three surface wettabilities of 60°, 95° and 120° static contact angle (measured with the sessile drop method for a water droplet on PDMS in the air). By reversing the flow direction after each pore-filling experiment, also the corresponding drainage or imbibition process was captured. Confocal laser scanning microscopy (CLSM) is applied to recognize the water interface and monitor its movement. With an inserted pressure transducer in the upstreaming plastic tube, the pressure change during the events was continuously measured. The collected pressure curves are compared with existing analytical solutions.

We found for the two cases with contact angles of 95° and 120° similar residual saturation levels of the wetting phase for all imbibition and drainage processes. For the case with a 60° contact angle, the wetting phase can almost fully saturate the pore after imbibition and can be fully displaced by the non-wetting phase after drainage. Besides, we noticed that wettability plays an important role in thin-film generation and the thickness of the film during displacement.

5.1 Introduction

The filling event in porous media inevitably involves capillary filling in the throat and pore-filling in the pore body. The mathematical description of the capillary flow can be traced back to the pioneering work of Lucas (Lucas, 1918) and Washburn (Washburn, 1921) in the early 19th century. By studying the ascension of a liquid in a single capillary, they developed a rising distance (L) versus time (t) relationship from the equation of momentum balance, $L^2 = Dt$, when gravity and acceleration are ignored, where D is the coefficient of percolation (diffusion) related to the diameter of the capillary and the liquid property. This relationship is also referred to as the ‘Lucas-Washburn equation’, which is essentially a balance between the viscous pressure drop and the capillary pressure in the capillary. Through experimental and numerical studies, the Washburn equation has been proved that it would be appropriate for the interpretation of capillary filling rates for most systems of practical interest, even for capillary radii down to $0.3\ \mu\text{m}$ (Fisher & Lark, 1979; Szekely, Neumann, & Chuang, 1971). A significant amount of work has been done by considering the wettability effect (Calvo, Paterson, Chertcoff, Rosen, & Hulin, 1991; Hoffman, 1975; Tanner, 1979), introduced slip length (Dimitrov, Milchev, & Binder, 2007; Schebarchov & Hendy, 2008), the effect of capillary geometry (Legait & Sourieau, 1985; Sorbie, Wu, & McDougall, 1995; Yu & Wardlaw, 1986), and the effects of properties of solid surfaces (Dang-Vu, Hupka, & Drzymala, 2006; Delker, Pengra, & Wong, 1996; Kusumaatmaja, Pooley, Girardo, Pisignano, & Yeomans, 2008; Stukan, Ligneul, Crawshaw, & Boek, 2010). The equation can be widely applied to describe the behavior of fluid displacement (either drainage or imbibition process) for multiphase flow (Firincioglu, Blunt, & Zhou, 1999; Heshmati & Piri, 2014) and to show the connection to the larger (continuum–porous-medium) scale for the use of the bundle-of-tube model (Dahle, Celia, & Hassanizadeh, 2005). However, the naturally porous structure is extremely complicated.

On the basis of 3D porous media, the modified LW equation needs to take the geometrical influences into account for predicting the accurate displacement (Cai et al., 2021). For instance, sudden variation in flow pathways brings out unstable displacement patterns, such as Haines jumps, intermittent behavior and flow stagnation, which cause the transient pressure response or fluid discontinuity (Moura, Måløy, Flekkøy, & Toussaint, 2017; Sun & Santamarina,

2019). Therefore, a detailed characterization of pore-filling behavior provides a better prediction of realistic fluid distribution and physically consistent data for numerical simulation at pore-scale.

Microfluidic device has been extensively applied in porous media research for investigating the fluid behavior for the past several decades. Commonly, the micromodels are quasi-2D due to a 2D pattern design in the X-Y axis and a depth in the Z-axis (Yang, Bondino, Regaieg, & Moncorgé, 2017). Like natural porous media, the variation in flow pathways is ubiquitous in microfluidics, such as inlet/outlet bifurcation and merging structure, capillary valve, complex porous structure with diverging or converging pore spaces (Hagmeyer, Zechnall, & Stelzle, 2014; Olanrewaju, Beaugrand, Yafia, & Juncker, 2018; Papadimitriou, Segerink, van den Berg, & Eijkel, 2018). Similarly, it also causes the sudden pressure change, interface pinning and during fluid-gas and immiscible flow displacements, even in the imbibition process with less phenomenon (Pavuluri et al., 2020; Singh, Jung, Brinkmann, & Seemann, 2019; Zhao et al., 2013). These phenomenon are associated with a balance between an externally imposed force and internal resistance coming from flow and transition zones of pore-throats.

On the other hand, the boundary conditions applied on the whole setup of microfluidic experiment are key points to control the flow pattern and interface behavior. There are two main boundary conditions used for the experiment: constant injection flow rate and constant pressure. Some researchers have proved that the drainage processes under two conditions have distinct pressure signatures and invasion dynamics, in spite of eventually reaching a similar overall morphology (Moura, Måløy, Flekkøy, & Toussaint, 2020). Which boundary condition is better depends on the specific experimental equipment and process.

Accurate investigations on the invasion dynamics give a reliable verification to the elaborate pore-scale numerical models. To simulate two-phase flow and interface motion, several numerical approaches have been proposed in a wide field of research and become popular in recent decades, including Volume of fluid method (Hirt & Nichols, 1981), the level-set method (Dervieux & Thomasset, 1980), phase-field method (Jacqmin, 1999), and Lattice Boltzmann method (LBM) (S. Chen & Doolen, 1998). Volume of fluid methods is used for tracking and locating the free surface based on the description of the volumetric fraction of each phase in grid cells. The main advantages of VOF are its reliability and effectiveness, meaning that it can perform good volume conservation and be

widely applied on any mesh. The limitations of the method are that 2D interface geometry reconstruction is quite difficult, and the simplification of nonlinear terms and the omitted high order terms after discretization can lead to less accurate solutions in some cases (Ménard, Tanguy, & Berlemont, 2007). Level-set method can provide give a sharp fluid-fluid interface and no need for penalization techniques to obtain a discrete solution, but the numerical implementation of interface advection is not mass conservative and it requires high-order numerical schemes (Dianat, Skarysz, & Garmory, 2017). Many researchers have combined the advantages of LS and VOF methods to minimize mass loss through the VOF method and to keep a fine description of the sharp interface through the level set method (Sussman & Puckett, 2000; Yokoi, 2013).

To account for wall-fluid-fluid interactions, an improved Smoothed Particle Hydrodynamic (SPH) method has been developed to track the moving interfaces during two-phase flow (Kunz et al., 2016). It gave well descriptions of interface propagation compared to the experiments of drainage processes in a micro-model. However, although different strategies have been proposed to overcome technical difficulties, they remain quite limited to have a time scale match on flow behavior between experimental and numerical works (Zarikos, Hassanizadeh, van Oosterhout, & van Oordt, 2018). Besides, the unavoidable resistances from the whole system of microfluidic setup bring about extra uncertainty on the experimental results that influence the accuracy of numerical simulation, e.g. shear stress generation from the flow division network (Oh, Lee, Ahn, & Furlani, 2012), hydrodynamic resistance in the connections outside the micromodel (Liu, Ju, Zhang, & Gong, 2019), and pressure fluctuation due to the elastic deformability of the system and the micromodel (N. K. Karadimitriou, 2013). These resistances are barely accounted for the numerical modeling. Therefore, how to precisely characterize the dynamic flow behavior is still challengeable for in pore-scale laboratory work and numerical modeling of multiphase flow.

In this contribution, we fabricated polydimethylsiloxane (PDMS) micromodel with a single pore geometry instead of complex porous networks. The PDMS elastomer is transparent at optical frequencies (240 nm-1100 nm) and facilitates the observation of fluid dynamics through a microscope. The simple pore geometry allows us to accurately control the drainage process for two-phase flow via a quasi-static method. numbers. We performed two drainage processes for two-phase flow, water-air and water-fluorinert under two different injection

velocities. Water is the non-wetting phase for bare PDMS surface, while air and fluorinert act as wetting phases. Detailed information on the experimental methods and micromodel will be provided in Section 5.2. A confocal laser scanning microscope (CLSM) is used to observe the fluid flow and track the interfaces of two phases with a high scanning resolution. To distinguish the water-fluorinert interface, water was dyed with fluorescence to make the water greyish under microscope light and green under 488 nm laser. We present simulations and experiments of drainage processes in a micro-model.

5.2 Analytical solutions of two-phase flow in pore filling

5.2.1 Pressure distribution in a rectangular channel

In microfluidic experiments, many devices encounter sudden diameter changes, such as the diverging and converging pores and throats. Therefore, the interface behavior and local fluid pressure become sensitive and give challenging to match simulation results. To cover most of the situations, we focus on analyzing continuous three phases (two immiscible phases and an air phase) in a microchannel.

The flow in such channels is confined and has a very small Reynolds number (e.g., 10^{-6} -10 (Squires & Quake, 2005)) as the transversal dimensions of the channel are small. Based on the derivation of the Lucas-Washburn equation, we can determine the analytical solutions of the pressure and velocity distributions equation for three-phase flow in an arbitrary cross-section micro-channel.

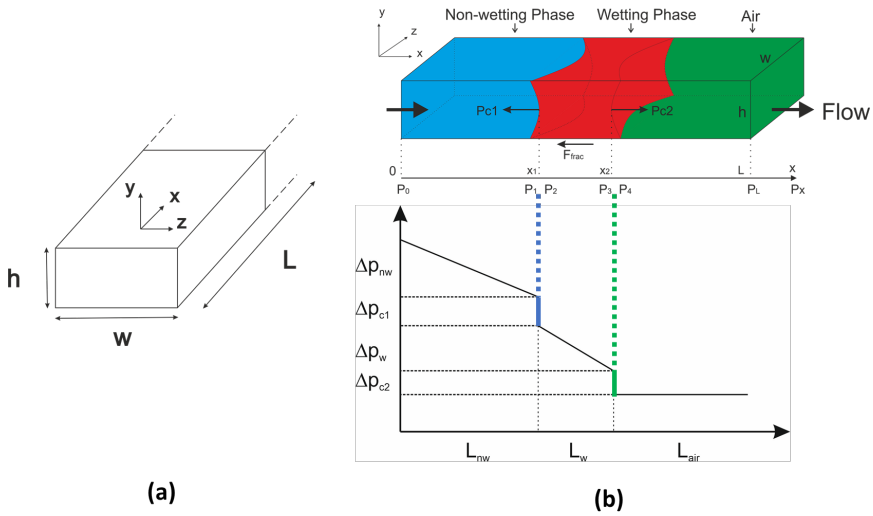


Figure 5-1. schematics of fluid flow in a rectangular channel. (a). the geometry of a rectangular channel. (b). the fluid distributions in the channel, including invading fluid in blue, wetting phase in red and gas in green. Meanwhile, the fluid pressure distribution along the channel during displacement is shown below.

The interface movement rate's theoretical relations, capillary force, and pressure gradient can be obtained when the three phases coexist. The analytical schematic diagram of the pressure at any point in the three phases of water and oil is shown in Figure 5-1. In Figure 5-1b, we present the drainage process, where a non-wetting fluid (blue) displaces the wetting fluids (red) and gas (green) in the rectangular channel. Along the direction of the positive axis, the pressure distribution is shown in the below figure, including the pressure applied on the non-wetting phase to drive the displacement, the capillary pressures at the two interfaces and the neglectable pressure difference in the gas note that here we only show and discuss the drainage process, the imbibition process has the similar behavior, but the flow and pressure directions are converse. The external pressure applied to the system can be controlled by a pressure-supplying device.

In the rectangular channel, the flow in a rectangular channel with length L , width $w \ll L$ and height $h \ll L$, as shown in Figure 5-1a. A constant pressure gradient $G = (p_0 - p_L)/L$ acts along the direction parallel to the motion as a driving source. Neglecting gravity and end effects, the velocity $u(y, z)$ is distributed along x -axis and satisfies the conditions that $u(y, \pm w/2) = 0$ and $u(\pm h/2, z) = 0$. The Navier-Stokes equation reduces to (Stewartson, 1970)

$$\frac{\partial^2 u}{\partial y^2} + \frac{\partial^2 u}{\partial z^2} = -\frac{G}{\mu} \quad [5.1]$$

In terms of a Fourier series, the axial parabolic velocity distribution is analytically solved by (Stone, 2007):

$$u(y, z) = \frac{\Delta p}{2\mu L} \left[\left(\frac{h^2}{4} - y^2 \right) - \sum_{n=0}^{\infty} a_n \cos\left(\frac{\lambda_n y}{h/2}\right) \cosh\left(\frac{\lambda_n z}{h/2}\right) \right] \quad [5.2]$$

Where: $a_n = \frac{h^2(-1)^n}{\lambda_n^3 \cosh(\lambda_n w/h)}$ with the no-slip boundary conditions on $z = \pm w/2$, and $\lambda_n = \frac{(2n+1)\pi}{2}$.

Thereby, the flow rate is given by

$$Q = 4 \int_0^{w/2} \int_0^{h/2} u(y, z) dy dz = \frac{wh^3 \Delta p}{12\mu L} \left[1 - 6 \left(\frac{h}{w} \right) \sum_{n=0}^{\infty} \lambda_n^{-5} \tanh\left(\frac{\lambda_n w}{n}\right) \right] \quad [5.3]$$

As the hyperbolic tangent varies in 0.92~1, the flow rate has a reasonable approximation,

$$Q = \frac{h^3 w \Delta p}{12\mu L} (1 - 0.627\varepsilon) \quad [5.4]$$

The solution has less than 1% error for the case of aspect ratios $\varepsilon = h/w < 0.7$ (Barthès-Biesel, 2012). Consequently, the average velocity u_{avg} in the cross section is defined by

$$u_{avg} = \frac{Q}{hw} = \frac{h^2 \Delta p}{12\mu L} [1 - 0.627\varepsilon] \quad [5.5]$$

The average velocity for each phase can be written as $u_i = \frac{h^2 \Delta p_i}{12\mu_i L_i} [1 - 0.627\varepsilon]$, where $i = nw, w, g$, for the non-wetting fluid, wetting fluids and gas, respectively.

For the cases with $\varepsilon \ll 1$, e.g., the Hele-Shaw cell with a channel of width w , the velocity distribution and approximate flow rate can be given by

$$u(y) = \frac{\Delta p}{2\mu L} \left(\frac{h^2}{4} - y^2 \right) \quad [5.6]$$

and the flux, therefore, is reduced to

$$Q = \frac{wh^3 \Delta p}{12\mu L} \quad [5.7]$$

Apart from the external pressure, the capillary forces F_c act over the circumference of the cross-section of the rectangular channel. We consider the the fluid interface has the contact angles θ_h with the top and bottom walls (here in y direction), and θ_w with side walls (here in the z direction). The Young–Laplace equation yields

$$p_c = 2\gamma \left(\frac{\cos \theta_h}{h} + \frac{\cos \theta_w}{w} \right) \quad [5.8]$$

In the system of three-phase flow, at the interfaces of non-wetting phase/wetting phase and wetting phase/gas, the capillary pressures are described as, $p_{c(nw-w)} = p_1 - p_2$, and $p_{c(w-g)} = p_4 - p_3$, respectively. Note that, the p_1, p_2, p_3, p_4 are presenting the dynamic pressure of the non-wetting phase and wetting phase on the meniscus, as the system is under non-equilibrium conditions (Dahle et al., 2005). The total capillary pressure $\sum p_c$ is the summation of $p_{c(nw-w)} + p_{c(w-g)}$

Thus, the capillary force is given by

$$F_c = whp_c = 2wh\gamma \left(\frac{\cos \theta_h}{h} + \frac{\cos \theta_w}{w} \right) \quad [5.9]$$

Using Newton's viscous law and simple interpolation formulae, the viscous force on the top, bottom and two walls of the rectangular channel is approximately given (Ouali et al., 2013) by

$$F_{visc} = -\frac{12\mu U_{avg} x}{\varepsilon} \lambda \quad \text{for } \varepsilon = 0.0 - 2.0 \quad [5.10]$$

with less than 3% error, where λ is the aspect ratio function defined as $(1 + 0.362374\varepsilon + 1.020980\varepsilon^2)$, and x is the position of the meniscus. For the three-phase flow in a channel, the viscous forces for each phase are presented as, $-\frac{12\mu U_{nw}}{\varepsilon} \lambda(\mu_{nw}(L_{nw} + dx))$, $-\frac{12\mu U_w}{\varepsilon} \lambda\mu_w L_w$, and $-\frac{12\mu U_g}{\varepsilon} \lambda\mu_g L_g$. As the incompressibility and low viscosity of gas, the viscous force of gas is neglected. Meanwhile, with the assumption of incompressible fluids and considering the mass conservation, the average velocities for each phase are equal to the meniscus velocity, shown as $U_{avg} = U_{nw} = U_w = U_m$

Here, by combining Newton's second law of motion, the summation of all forces ($\sum F_{total}$) acting on the fluid under consideration can be illustrated as

$$\begin{aligned}\Sigma F_{total} &= ma = F_{visc} + F_c + \Delta p_e hw \\ &= \Sigma p_c hw + \Delta p_e hw - \frac{12U_m}{\varepsilon} \lambda [\mu_{nw}(L_{nw} + dx) + \mu_w L_w] \quad [5.11]\end{aligned}$$

Where Δp_e is the external pressure imposed on the fluid in the micro-channel. In our case, the syringe pump provides the external driving force to the flow. When the Reynolds number is very small, that is $Re \ll 1$, the viscous forces are much larger than the convective inertia forces. Therefore, the acceleration term a and the viscous stress tensor can be neglected. Correspondingly, the meniscus velocity is processed by solving the equation (5.11),

$$U_m = \frac{h^2(\Sigma p_c + \Delta p_e)}{12\lambda(\mu_{nw}L_{nw} + \mu_w L_w)} \quad [5.12]$$

In microfluidic experiments, the inlet velocity can be easily expressed as saturation through the simple image processing and calculation, $U_{inlet} = U_m = \frac{dA_{nw}}{wdt} = \frac{A_{total}}{w} \frac{dS_{nw}}{dt}$, where A_{total} is the total area of the channel or micromodel, and S_{nw} is the saturation of the non-wetting phase. For our case with a long micro channel and a square pore body, the equation (5.12) is converted into a relationship between saturation and capillary pressure.

$$\frac{dS_{nw}}{dt} = \frac{h^2(\Sigma p_c + \Delta p_e)}{A_{total}12\lambda(\mu_{nw}L_{nw} + \mu_w L_w)} \quad [5.13]$$

Based on the meniscus velocity, we can gain the pressure distribution with approximate solutions for three phases by substituting the equation (5.5), shown as

$$\frac{h^2(p_0 - p_{nw}(x))}{12\mu_{nw}x}(1 - 0.627\varepsilon) = \frac{h^2(\Sigma p_c + \Delta p_e)}{12\lambda(\mu_{nw}L_{nw} + \mu_w L_w)} \quad \text{for } (0 \leq x < L_{nw}) \quad [5.14]$$

$$\frac{h^2(p_3 - p_w(x))}{12\mu_w(x - L_w - L_{nw})}(1 - 0.627\varepsilon) = \frac{h^2(\Sigma p_c + \Delta p_e)}{12\lambda(\mu_{nw}L_{nw} + \mu_w L_w)} \quad \text{for } (L_{nw} \leq x \leq L) \quad [5.15]$$

Note that, the pressure gradient of gas phase in the channel is neglected due to the low Reynolds number, meaning that $p_L = p_4 = p_3 + p_{c(w-g)}$

Therefore, the pressure distribution along the channel at x position inside the non-wetting phase and wetting phase is described as

$$p_{nw}(x) = p_0 - \frac{\mu_{nw}(\sum p_c + \Delta p_e)x}{\lambda(1-0.627\varepsilon)(\mu_{nw}L_{nw} + \mu_w L_w)} \text{ for } (0 \leq x < L_{nw}) \quad [5.16]$$

$$p_w(x) = p_L - p_{c(w-g)} - \frac{\mu_w(\sum p_c + \Delta p_e)(x - L_w - L_{nw})}{\lambda(1-0.627\varepsilon)(\mu_{nw}L_{nw} + \mu_w L_w)} \text{ for } (L_{nw} \leq x \leq L) \quad [5.17]$$

5.2.2 Pressure change at diverging zone

The sudden changes in channel cross-section, either diverging or converging, bring about the pressure barrier for continuous flow that will halt the meniscus of fluid at the edges (Leu & Chang, 2004). The analytical solution for calculating the burst pressure has been presented in other literature (J. M. Chen, Huang, & Lin, 2008; Cho, Kim, Kang, & Kim, 2007).

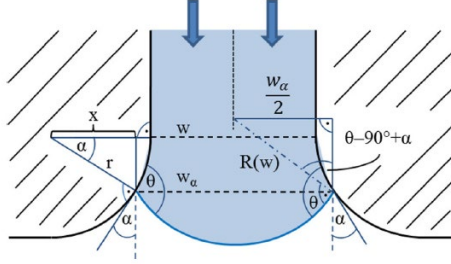


Figure 5-2: schematic of radius change in the diverging zone.

The sudden build-up of capillary pressure at the diverging corners not only happens in the drainage process but also occurs in the process of imbibition of multiphase flow in porous media (Glière & Delattre, 2006; Pavuluri et al., 2019). The radius of curvature of the advancing liquid is then calculated using and shown in Figure 5-2,

$$\kappa = \frac{w_\alpha}{2\sin(\theta - 90^\circ + \alpha)} = \frac{w_\alpha}{-2\cos(\theta + \alpha)} \quad [5.18]$$

The burst pressure inside the liquid to overcome the diverging zone is expressed below with gradual expansions at the corner.

$$\Delta p_{burst} = \max\left(-\gamma\left(\frac{2\cos\theta}{h} + \frac{2\cos(\theta + \alpha)}{w_\alpha}\right)\right), 0 \leq \alpha \leq 90^\circ \quad [5.19]$$

After the fluid overcome the burst pressure, the meniscus starts to move along the diverging walls and the velocity gets accelerated until reaching another pore

region. The change of curvature and capillary pressure can be described below in schematics in Figure 5-3.

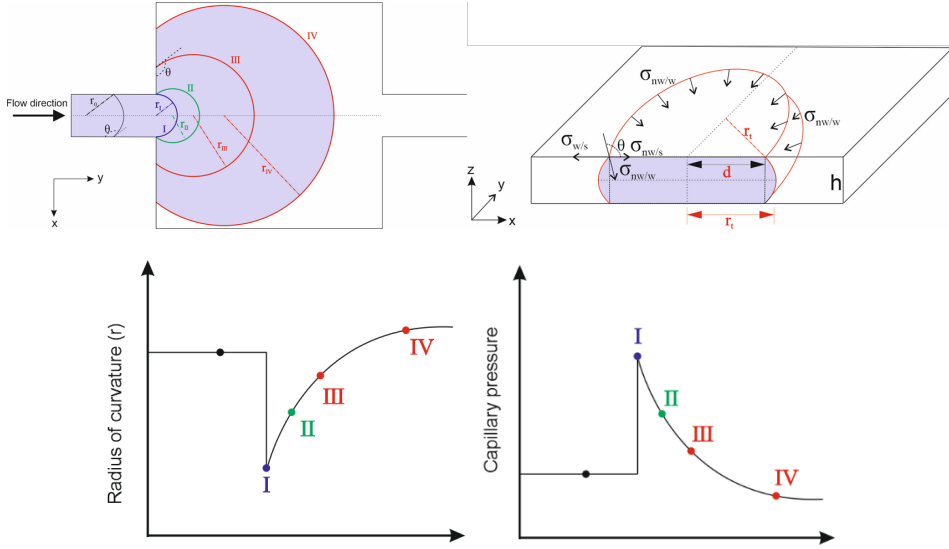


Figure 5-3. schematics of pressure and curvature changes during the diverging zone.

5.3 Experimental set-up and micro-model wettability fabrication

5.3.1 Confocal scanning microscopy setup

We perform a microfluidic experiment to investigate the movement behavior of the two-phase interface. To obtain the movement of the two-phase meniscus, the Nikon A1+ confocal laser scanning microscope (CLSM) is applied for imaging modality through optical sectioning of a sample. The schematic of the whole experimental setup is shown in Figure 5-4. One micro-model is then placed on the piezo-driven stage of the confocal microscope that allows controlling the movements in all three directions. One syringe pump (Harvard Apparatus 1 Pico Plus Elite Programmable Syringe Pump) is used for providing a mean constant injection flow rate and connects the inlet of the micro-model with a 2 mm outer diameter plastic tube. Another utilized plastic tube connects the outlet of the micromodel, and its one side directly touches the indoor atmosphere. Besides, one sensitive fibre-optic micro-transducers is embedded in the plastic tubes in

advance, allowing us to acquire accurate pressure changes in fluids (i.e., water in the inlet plastic tube and air in the outlet plastic tube, respectively). The measurement ranges from 40 Pa up to 40 kPa with a resolution of 40 Pa. The accuracy is 0.6% of the full range. More details of the transducer's structure and monitoring set-up can be found in the other literature (Yan, Aslannejad, Hassanizadeh, & Raoof, 2020; Zarikos et al., 2018).

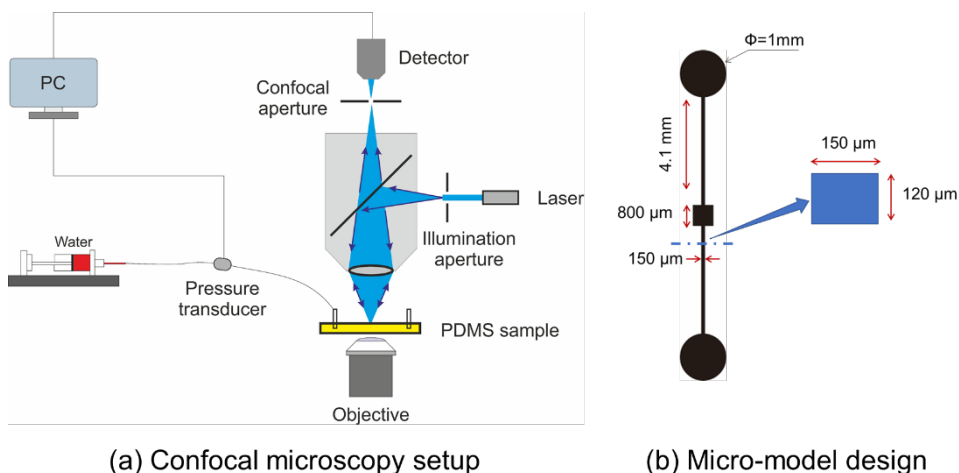


Figure 5-4. schematic of the experimental setup and the details of micromodel.

The microchip is prepared from PDMS (polydimethylsiloxane) by following typical procedures of the soft-lithography technique. More details of a manufacturing process can be extensively found in the other previous literature (Chang-Yen, Eich, & Gale, 2005; N. Karadimitriou et al., 2013; Xia & Whitesides, 1998). We design a mask via AutoCAD drawing and then form the silicon wafer with an inverted microfluidic model. After curing, warming and bonding the PDMS pieces, one micro-model with micro features is fabricated. The micromodel consists of two 4.1 mm (length)×150 μm (width) channels, one 800×800 μm² square pore in the middle. The depth of the whole model is 120 μm. Two reservoirs with a diameter of 2 mm are connecting the two horizontal channels as an inlet and outlet. The entire pore structure and partial channels in the microfluidic model have been investigated by scanning electron microscopy. The amplitude of the roughness can be neglected for our water-fluorinert displacement due to the relatively small surface tension difference between water-PDMS and fluorinert-PDMS (Ismail, Grest, Heine, Stevens, & Tsige, 2009; Zhang & Hassanizadeh, 2017).

Fluorescein sodium salt, purchased from Sigma-Aldrich, is used to dye water as a tracer for fluorescence recovery. Therefore, confocal microscopy is able to observe the part of dyed water with the 488 nm laser. Resonant scanning mirrors are capable of gathering images at 30 frames per second. One fluorescent channel and the camera image are recorded. Images are captured using a 10x microscope objective and the view domain is $1.2 \times 1.2 \text{ mm}^2$ resulting in 512×512 pixel images with a lateral (XY) scan resolution of $2.48 \text{ }\mu\text{m/pixel}$ (covering a horizontal field of view of $\sim 0.65 \text{ mm}$). With fluorescent signal, the dyed water displays green color under microscopy optimization of imaging parameters yields a distinction between water and fluorinert resulting in clear visualization of the two-phase interface. Under the camera image, the fluorinert shows colorless while the dyed water presents in light grey. We have set three injection rates for the syringe pump: 0.01, 0.1 and 0.5 ml/hr. The capillary numbers for water-air displacement are 1×10^{-5} , 1×10^{-4} and 5×10^{-4} .

Table 5-1: List of PDMS experiments for water-air and water-fluorinert displacements.

		Hydrophilic PDMS	Original PDMS	silanized PDMS
	flow rate [ml/h]	$\sim 60^\circ$	$\sim 90^\circ$	$\sim 120^\circ$
Drainage	0,01	x	x	x
Imbibition	0,01	x	x	x
Drainage	0,1	x	x	x
Imbibition	0,1	x	x	x
Drainage	0,5	x	x	x
Imbibition	0,5	x	x	x

5.3.2 Wettability control on PDMS

To achieve wettability fabrication, we combine the physical and chemical approaches in the literature (Trantidou, Elani, Parsons, & Ces, 2017; Zhou, Khodakov, Ellis, & Voelcker, 2012). After the fabrications, PDMS renders to either hydrophilic or hydrophobic surface by gaining the functional chemical groups (such as silanol groups (Si-OH), alcoholic hydroxyls (C-OH), and carboxylic acids (COOH)) on the surface, as shown in Figure 5-5. The hydrophilic micro-model is modified through the oxygen plasma treatment and coating of a layer of Polyvinyl alcohol (PVA) by following the procedures shown

at the top of Figure 5-5. After oxygen plasma exposure, two pieces of PDMS are bonding. The whole oxygen plasma treatment is completed by a 2.6-litre low-cost plasma lab system zepto (plasma cleaner) purchased from Diener electronic GmbH Co. The right amount of oxidation can create enough hydroxyl and carboxyl functional groups on the surface for optimal bonding strength and surface wettability. Here we set the plasma cleaner to 100 W, 10 sccm O₂ flow and 0.65 mbar pressure for 1 min to have strong bonding strength. The bonded PDMS is placed in the oven at 60°C for 30 mins to have permanent adhesive bonding and a $\approx 30^\circ$ contact angle of water. 1 wt% PVA solution is prepared by mixing PVA powder in DI water and stirring it for 24 h at 60 °C and then cooling down for hours until the solution reaches room temperature. Then, we weigh the container with the solution and add water to compensate for the mass loss due to evaporation. Note that the surface wettability will gradually get recovery in one day (Bodas & Khan-Malek, 2007), therefore, the PVA solution needs to be immediately injected into the bonded microchannels using a syringe after plasmas treatment and bonding. After PVA coating, the wettability is maintained with a 60° contact angle of water for at least 20 days (Trantidou et al., 2017). The modified micro-model is stored in the oven overnight.

For having a hydrophobic surface, a silanization method is introduced. As shown in the bottom part of Figure 5-5, the first two steps are the same as the hydrophilicity method, but corona discharge treatment replaces the oxygen plasma treatment. The benefit of using corona discharge is that the activated surface can rapidly recover wettability to 90° contact angle of water by thermally heating it on a hot plate at 120 °C for 20 mins (Pascual, Kerdraon, Rezard, Jullien, & Champougny, 2019). The drawback is the corona discharge can not be easily controlled as a plasma cleaner for reaching a range of hydrophilicity and bonding strength (Lin & Razali, 2019). To avoid the deformation during heating, two glass pieces are tightened with the PDMS pieces. One silanization solution is prepared by mixing trichloro- (1H,1H,2H,2H-perfluorooctyl) silane in ethanol with a volume ratio of 1:10. The mixed solution is injected into the micro-channel for about 5 seconds. Two injection cycles of pure ethanol and DI water are used for flushing out the residual silane solution. The hydrophobic micro-model is dehydrated in the oven at 60°C overnight. Figure 5-5 also gives the images of untreated and treated PDMS samples acquired from the scanning electron microscope (SEM) technique. The zoom-in pictures indicate that after the hydrophilicity treatment some existing cavities along the PDMS channels are

filled with the coating fluids, which reduces the roughness in some extent. The untreated sample and the silanized sample show relatively uniform surfaces. The average roughness of the untreated PDMS microchannel is around 5 μm . Therefore, in our following works, we do not consider the effect of surface roughness on the two-phase flow in the micro-channel and pore-filling events.

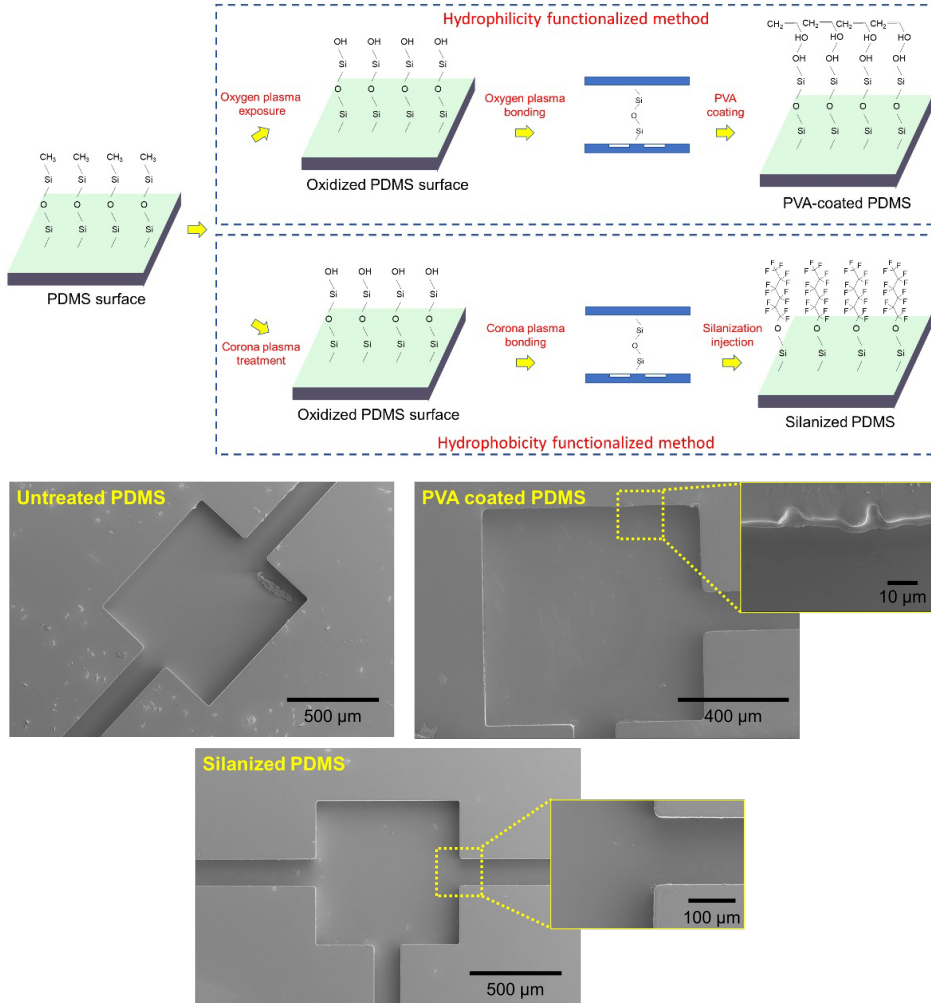


Figure 5-5: Wettability modification for PDMS surface. Top figure is the schematic of modification procedures for hydrophilicity and hydrophobicity methods. Bottom images are the SEM scanning photos for the untreated and treated PDMS samples using PVA and silanization methods.

To evaluate the wettability modification, we measure the contact angle of water droplet in air for three PDMS pieces ($20 \times 20 \times 2$ mm). Front of the sample, a camera is used for taking photos. The duration period of the modified wettability is also investigated for different modification procedures, e.g., plasma+PVA, PVA+plasma+PVA, PVA+plasma, and silanization, shown in Figure 5-6. Notably, in the water environment, fluorinert displays the non-wetting phase to the plasma+PVA coated PDMS surface, while showing the wetting phase to the untreated and silanized samples. It indicates that the hydrophilic modification works well on the surface for the experiments of water-fluorinert displacement.

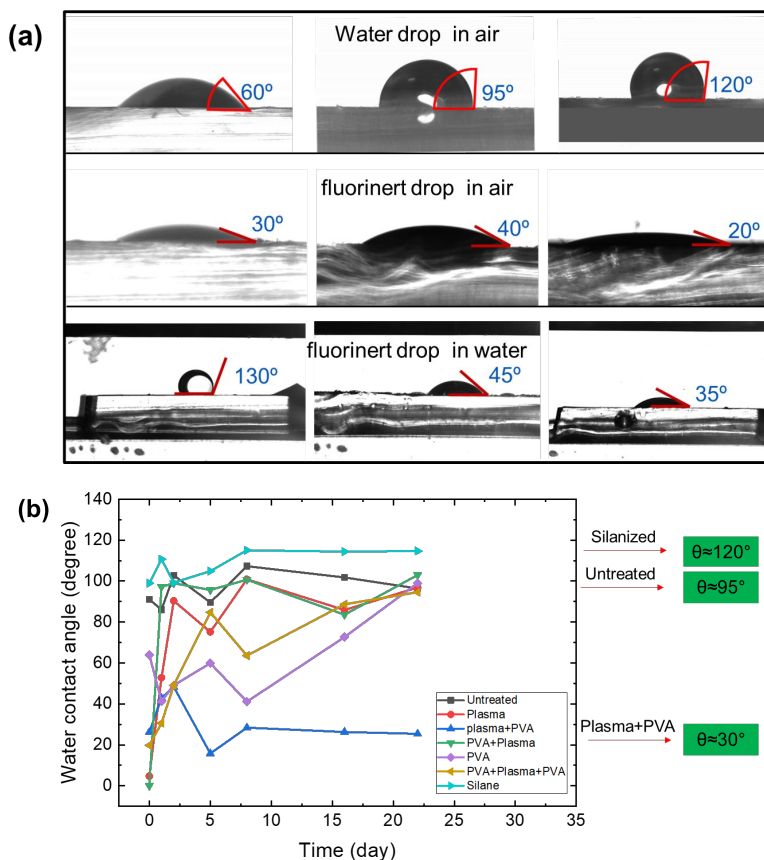


Figure 5-6: Measurements of contact angle for water and fluorinert on PDMS surface. (a), the contact angles for three measurement conditions: water in the air, fluorinert in air, and fluorinert in water; (b), the durability of modified wettability. Three modified PDMS samples (30° , 95° and 120°) can maintain the wettability for 22 days. Note that the plasma+PVA treatment renders the different wettabilities to the samples via various power of plasma treatment. Therefore, the sample marked with a 30° of water contact angle had a

more powerful plasma coating on the surface than that of the one used for the two-phase displacement (60° contact angle).

5.4 Direct numerical simulation of volume of fluid

We perform the numerical modeling of water-air and water-fluorinert displacement using the volume of fluid (VOF) method, which allows us to capture and analyse the fluid-fluid interface behavior in the pore-filling events under various wettability conditions (Takada, Misawa, & Tomiyama, 2005). The model is conducted in the software COMSOL Multiphysics 5.4.

5.4.1 Mass and momentum transport

The Navier-Stokes equations describe the transport of mass and momentum for fluids of constant density. In order to account for capillary effects, it is crucial to include surface tension in the model. Although the micromodel is generally considered as quasi-2D having a small and uniform depth, it is necessary to take into account the effects in z-dimension (Horgue, Augier, Duru, Prat, & Quintard, 2013). With neglecting the gravity force on the flow in the micromodel, the Navier-Stokes equations are given by

$$\rho \frac{\partial \mathbf{u}}{\partial t} + \rho(\mathbf{u} \cdot \nabla) \mathbf{u} = \nabla \cdot \left[-p \mathbf{I} + \mu(\nabla \mathbf{u} + (\nabla \mathbf{u})^T) \right] + \mathbf{F}_{st} \quad [5.20]$$

$$\nabla \cdot \mathbf{u} = 0 \quad [5.21]$$

Where ρ denotes the density (kg/m^3), μ equals the dynamic viscosity ($\text{Pa}\cdot\text{s}$), \mathbf{u} represents the velocity (m/s), p denotes the pressure (Pa), h is the depth of the micro-model, and \mathbf{F}_{st} is the surface tension force acting at the water/air or fluorinert interface.

Due to the quasi-2D dimensional structure of micromodel, the influence of the depth direction is necessary to be taken into account for the simulation in two-dimensional geometry. One of the effects is the viscous resistance induced by the top and bottom surfaces of the micro model. Therefore, considering the velocity in the depth direction, the Navier-Stokes equation is given by adding an extra term of body force (Yin, Zarikos, Karadimitriou, Raoof, & Hassanizadeh, 2019).

$$\rho \frac{\partial \mathbf{u}}{\partial t} + \rho(\mathbf{u} \cdot \nabla) \mathbf{u} = \nabla \cdot \left[-p \mathbf{I} + \mu(\nabla \mathbf{u} + (\nabla \mathbf{u})^T) \right] + \mathbf{F}_{st} - \frac{12\mu}{h^2} \mathbf{u} \quad [5.22]$$

Where h is the depth of the micromodel.

5.4.2 Volume of Fluid (VOF) method

In the solver of COMSOL, by adding an artificial interface compression term, the sharpness of the interface region is obtained. The volume fraction equation is described as

$$\frac{\partial \alpha}{\partial t} + \nabla \cdot (\alpha \mathbf{u}) + \nabla \cdot (\alpha(1-\alpha) \mathbf{u}_c) = 0 \quad [5.23]$$

where compression velocity \mathbf{u}_c is formulated based on maximum velocity magnitude in the interface domain α is the volume fraction field and defined as $0 \ll \alpha \ll 1$ for delineating three regions, wetting phase (1), non-wetting phase (0), and interface (0~1). The density and viscosity of each phase at the interface are described as volume fraction weighted sums, $\rho = \alpha \rho_w + (1 - \alpha) \rho_{nw}$ and $\mu = \alpha \mu_w + (1 - \alpha) \mu_{nw}$, respectively (Gamet, Scala, Roenby, Scheufler, & Pierson, 2020). To calculate the curvature of interface and volume surface tension, the continuum surface force (CSF) model is applied (Brackbill, Kothe, & Zemach, 1992). Therefore, the surface tension force is computed as, $\mathbf{F}_{st} = \sigma \kappa \alpha_i$, where σ is the interfacial tension between wetting phase and non-wetting phase, κ is the curvature and defined as $\kappa = -\nabla \cdot \mathbf{n} = -\nabla \cdot \left(\frac{\nabla \alpha}{\|\nabla \alpha\|} \right)$ where \mathbf{n} is the unit normal vector of the interface. Contact angle θ at the contact line is described by $\mathbf{n} = \mathbf{n}_{wall} \cos \theta + \mathbf{n}_t \sin \theta$, where \mathbf{n}_{wall} is the unit normal directed into the wall, and \mathbf{n}_t lies in the wall and is normal to the contact line between the interface and the wall.

5.4.3 Pore geometry and boundary conditions

Modeling geometry

This pore shape represents one individual part of homogenous microchips used for pore-scale studies, such as the complexity of porous media flow (de Winter et al., 2020) and the pore-filling behavior (Zacharoudiou, Chapman, Boek, & Crawshaw, 2017). The shadow region refers to the throats and pore body. For such simple geometries, it has been shown that 2D simulation is adequate to

capture the complex multiphase flow dynamics (Deng & Cardenas, 2013; Schlüter et al., 2016). Therefore, to save computational time and cost, the geometry is set to a 2D x-axial symmetric shape (Figure 5-7). As our interesting area is the pressure variation in the pore body, the modelling geometry consists of one $100 \times 75 \mu\text{m}^2$ rectangular area as an initial value of one phase, $300 \mu\text{m}$ long inlet channel, $600 \mu\text{m}$ long outlet channel, and an $800 \times 400 \mu\text{m}^2$ rectangular area as pore body. We only investigate the drainage process of water-fluorinert displacement in this modelling.

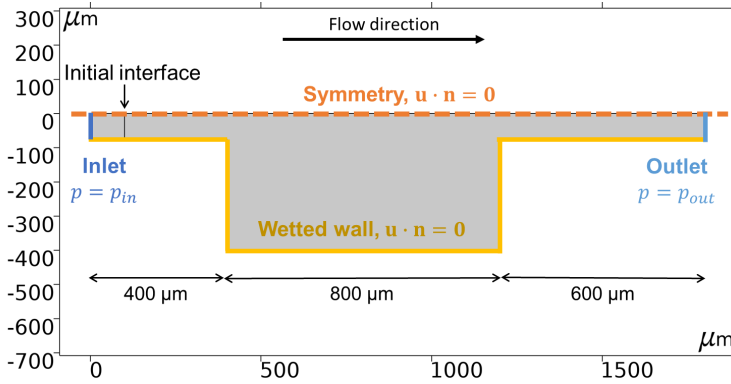


Figure 5-7: 2D model geometry and boundary conditions. The geometry parameters are shown in arrows and values. To save simulation time, the top boundary is set for symmetry. The left part of the initial interface is initially saturated with the water phase, and the other side is saturated with fluorinert. The wall is no-slip and wetting to water with different contact angles.

Initial and boundary conditions

To investigate the wettability effect on the flow behavior, we have set three initial and boundary conditions, e.g., variable inlet and out pressure, and several water contact angles to the wetted wall. Initially, fluorinert is fully saturated in the right part of the initial interface in the geometry, while water fills the other side, shown in Figure 5-8.

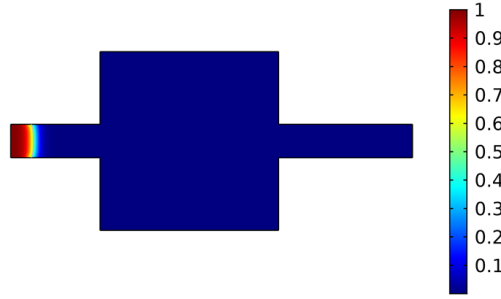


Figure 5-8: The initial status of water-fluorinert displacement. The color bar presents the volume fraction of water from 0 to 1.

The model is given with three different boundary conditions including constant inlet pressure (CIP), constant inlet velocity (CIV), and considering flow resistance (CFR), as listed in Table 5-2. The flow resistance is formulated from the equation (5.12) as $\frac{1}{R_i} = \frac{h^2}{12\lambda(\mu_{nw}L_{nw} + \mu_w L_w)}$, where R_i is the flow resistance and i is the fluid phase, e.g., water, fluorinert and air. For instance, the water flow resistance can be calculated by considering the water phase both in the $\phi \times 1\text{mm}$ circular plastic tube of the experimental setup and in the rectangular microchannel. Given the length of water in the two parts as $L_t = 25\text{cm}$ and $L_c = 5\text{cm}$, the flow resistance used for the simulation is $R_w = \frac{12\lambda\mu_w * L_c}{h_c^2} + \frac{8\lambda\mu_w L_t h_{cw}}{\pi r_t^4}$, where r_t is radius of the plastic tube and h_c is the micro-channel depth.

Although the simulation decreases the water-fluorinert displacement, the flow displacement in the real micro-model experiments involves three phases: water, fluorinert and air. The modeling region presents a part of the whole system of three fluids (water, fluorinert and air) in the real micro-model experiments. Based on the pressure distribution in the three-phase fluids, the inlet pressure for modeling should be the pressure at the water-side of the water-fluorinert interface, while the outlet pressure should be the pressure at the air-side of the fluorinert-air interface. Therefore, the inlet pressure is given as, $p_{inlet} = p_{pump} - U_m R_w$, and the outle pressure is $p_{outlet} = p_{out} + U_m R_f + p_{c(f-a)}$, where p_{pump} is the set pressure for the syringe pump, U_m is the meniscus velocity, and $p_{c(f-a)}$ is the capillary pressure of fluorinert and air, 16 mN/m in our modeling. The interfacial tension between water and fluorinert is 55 mN/m. The dynamic viscosities for water and fluorinert are 1 mPa·s and 4.7 mPa·s.

Table 5-2: List of boundary conditions.

Modeling case	Boundary conditions	Wall wettability (water contact angle)	Water flow resistance (Pa·s/m)
CIP	Inlet: 600, 800, 1000, 1200 [Pa] Outlet: 0 [Pa]	120°	-
CIV	Inlet: 0.02, 0.05 [m/s] Outlet: 0 [Pa]	120°	-
CFR	Inlet : $p_{inlet} = p_{pump} - U_m R_w$ where p_{pump} : 1000 [Pa] Outlet: $p_{outlet} = p_{out} + U_m R_f + p_{c(f-a)}$ where $p_{out}=0$	0,30,60,90,120, 150, 180	8544.8
	Inlet : $p_{inlet} = p_{pump} - U_m R_w$ where p_{pump} : 0500,600,800,1000,1200,1400 [Pa] Outlet: $p_{outlet} = p_{out} + U_m R_f + p_{c(f-a)}$ where $p_{out}=0$	120	8544.8
	Inlet : $p_{inlet} = p_{pump} - U_m R_w$ where p_{pump} : 1000 [Pa] Outlet: $p_{outlet} = p_{out} + U_m R_f + p_{c(f-a)}$ where $p_{out}=0$	120	Range: (0,50000/6,50000)

Moreover, to consider the effect of 3D structure of the micro-model, we have introduced the second curvature of the water-fluorinert interface to calculate the capillary pressure, given as $p_c = \sigma \kappa = \sigma \left(\frac{1}{r_1} + \frac{1}{r_2} \right)$, where r_1, r_2 are the principal interfacial radii. In our case, we assume the second interfacial radii is half of the micro-model depth.

Mesh size selection

Mesh size studies are performed to ensure that the computed profiles and the time evolution of the fluid-fluid interface are grid independent. The unstructured triangular mesh on domains in 2D grid is used for simulations in this study with refined grids near the corners. The process of water flooding through an

fluorinert-saturated pore is applied as a classic and standard example of multiphase flow dynamics for the mesh independency test. This case is applied with the boundary conditions of considering flow resistance (CFR), 1000 Pa of injection pressure and 120° of water contact angle on the walls, which is shortly written as CFR_1000_120 case. We investigate different mesh resolutions with three element numbers: 5232, 8146 and 36706. Time evolution of 2 seconds with a time step of 0.001s is used for calculations. Figure 5-9 shows the pressure distribution in water and fluorinert along the symmetry after the flooding time of 0.01 and 0.2 seconds with applying different mesh resolutions. The results indicate that the pressure distributions are nearly the same, but with some small variations at the interface. There is an anomalously high value in the case of higher mesh resolution. Therefore, considering both computational accuracy and efficiency, the second mesh system with 8146 computational grids is selected for all simulations.

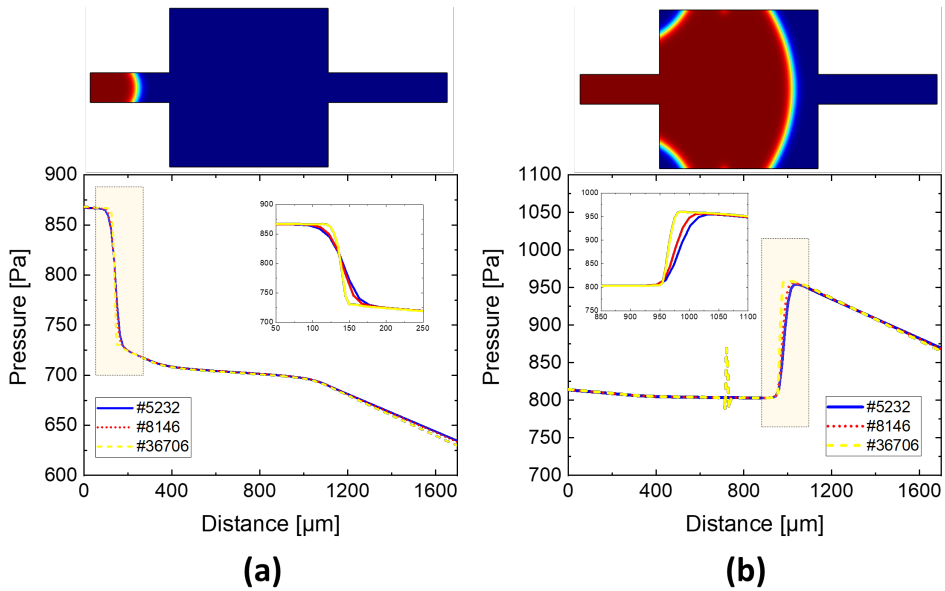


Figure 5-9: Mesh independency study for the CFR_1000_120 case. (a) $t = 0.01$ s; (b) $t = 0.2$ s. The pressure distributions at the water-fluorinert interface (shadowed regions) are plotted and enlarged in the smaller figures.

5.5 Experimental results and discussion

5.5.1 Description of displacement and validation of analytical solution

To fully understand the pore-filling event, we need to figure out the exact pressure change during the pore filling and synchronize it with the recorded data from the pressure sensor. Figure 5-10a describes five phases of the process for the water-air displacement in the whole micro-model, including filling inlet reservoir, flow in the rectangular micro-channel, pinning region, pore-filling behavior and flow in the outlet channel. Correspondingly, we analyse the recorded pressure data for gaining a better understanding of the displacement shown in Figure 5-10b. With fluid filling the inlet reservoir, the meniscus stops at the front region of the inlet and the pressure keeps increasing until overcome the entry pressure channel, p_{ch} , which can be calculated by the critical pressure in channel flow (Zacharoudiou et al., 2017). The accumulated pressure drives the meniscus movement and accelerates the velocity, see the shadow region in Figure 5-10c. Meanwhile, based on the image processing, the measured velocity and meniscus position can be plotted and validated with the calculated values. The pressure fluctuation in channel flow is displayed in shadow region 2 in Figure 5-10b, which can be matched with the analytical pressure (yellow line) for a flow in the rectangular channel given in Section 2.1. When the meniscus encounters a diverging zone, e.g., the right-angle corner of a pore, the pinning behavior occurs, and the capillary pressure has a corresponding change. Figure 5-10d reflects clear changes in the meniscus movement and the fitted radius. Figure 5-10e has an enlarged window of recorded pressure and meniscus radius. In the pinning region, since the velocity of the meniscus decreases, the pressure increases for almost 10 seconds until reaching the burst pressure. The radius has a matching drop at the pinning point and a significant rise when the meniscus moves along the walls of the pore body. The pressure and radius behavior are consistent with the description in Section 5.2.2.

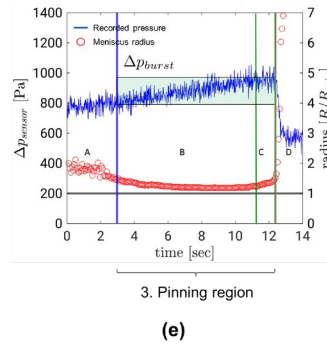
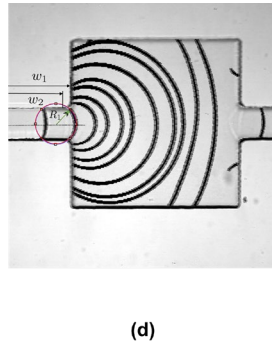
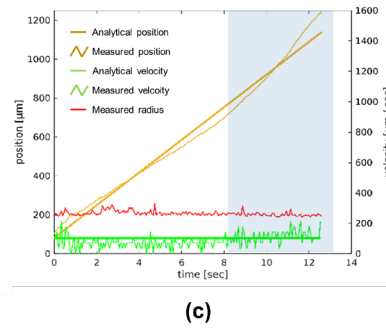
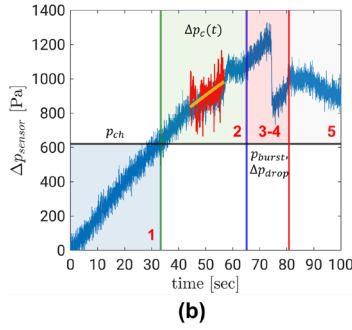
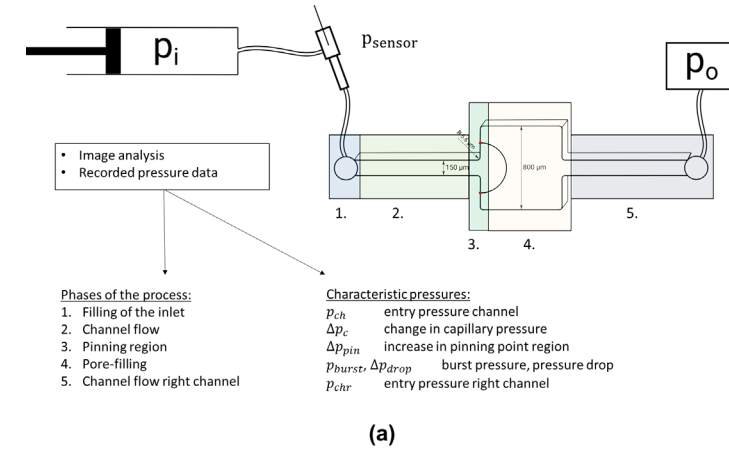


Figure 5-10: Description of the water-air displacement in the micro-model. (a) shows the schematic of five regions during the displacement; (b) shows the recorded pressure in the process. The changes related to the five phases are separated into different colorful regions. Part of pressure is marked in red and validated with the analytical solution; (c) gives the measured and calculated meniscus position and velocity, and the radius fitted from the images; (d) gives the meniscus shapes during the pore filling; (e) shows the enlarged view of recorded pressure and meniscus radius.

5.5.2 Water-air displacement

Under three injection velocities, the pressure has different performance due to the various meniscus curvature for three wettability conditions, as shown in Figure 5-11. For the hydrophilic cases, low velocity has an opposite trend to the higher velocities since water performs as a wetting phase, but a non-wetting phase for the higher velocity cases. For the hydrophobic cases, the pressure data shows a dramatic increase with the increase in velocity, especially in the case of 120 Q1-Q3. It indicates that the hydrophobic surface requires a longer time for pressure accumulation to overcome the higher entry capillary pressure. In other words, the meniscus renders a larger curvature for gaining a higher flow driving force.

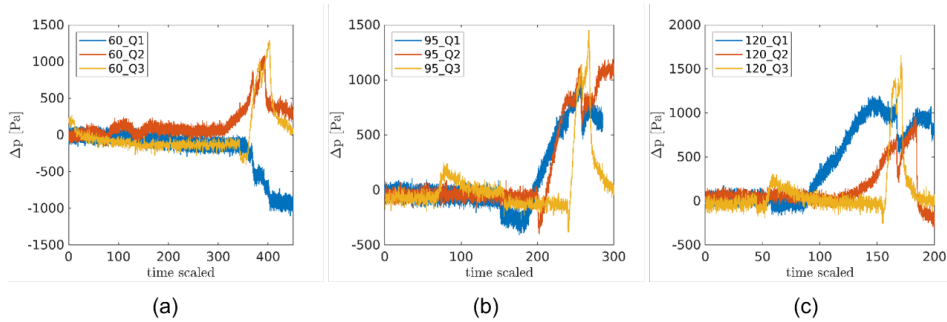


Figure 5-11: Recorded pressure data with three injection velocities for three wettability.

Influence of wettability and velocity on interface behavior in the single pore-filling

Through imaging and data processing, we are able to obtain the water-air meniscus movement under three wettability and injection flow rate conditions. Figure 5-12 presents the tracking interface in the event of non-wetting phase pore-filling under three wettability conditions with Q1 injection flow rate. The curve is the water-air meniscus and tracked with a 1/30 frequency and the intensity reflects the meniscus stagnant time. For all wettabilities, the meniscus renders a slow movement in the pinning point region until the cumulated fluid pressure overcomes the burst pressure. Interestingly, with the help of hydrophilic treatment, the meniscus initially displays a concave shape in the micro-channel from the view of flow direction, while it changes to the convex shape and maintains the non-wetting behaviour until touching the horizontal side walls. This phenomenon will be reflected in the pressure plot as well in the later discussion.

No air phase remains in the pore. The other two cases with the hydrophobic wettabilities do not give the water film generation and the reverse behavior of interface in the pinning zone. The meniscus can grow to the maximum radius and be cut into several sections by the horizontal walls. The main interface displaces air in the pore body until reaching the vertical walls at the outlet throat zone. Therefore, air (acting as a wetting phase) is trapped in the four corners of the pore. Figure 5-13 gives the water saturation during pore-filling for three wettability conditions. Clearly, with the Q1 injection flow rate, the hydrophilic model performs full water saturation of the pore space, but the hydrophobic model owns less saturation. Higher velocity induces a low water saturation under all wettability conditions and weakens the wettability effect for the hydrophobic cases (see Figure 5-13 Q3 plots).

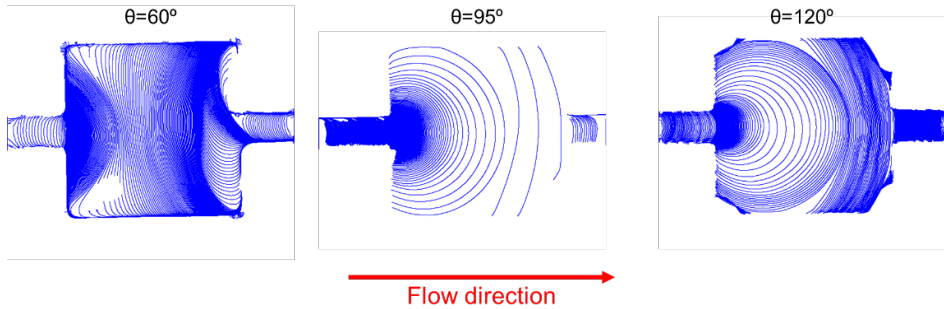


Figure 5-12. Interface tracking during pore-filling behavior for three wettability conditions with Q1 injection flow rate.

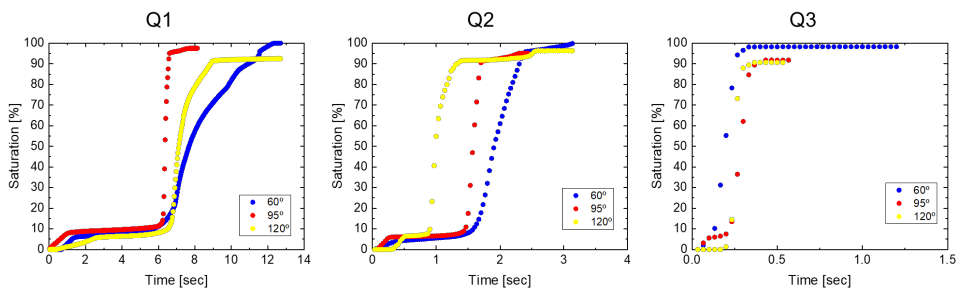


Figure 5-13: Saturation of water during pore filling for three injection velocities under three wettability conditions.

Pressure variation and meniscus curvature change

Now, we focus on the description of interface behavior in the pore filling under different conditions, see Figure 5-14. In general, the pressure (red curve) and radius (blue circles) are consistent with each other. When the meniscus moves at the pinning region, the pressure becomes the maximum and the radius reaches the minimum. This trend matches the theory of two-phase flow in a rectangular channel and the diverging zone in Section 2. Note that in this figure we only give the radius plots in the pore body, which do not include the data for the flow in the outlet channel. Notably, in the case of 60_Q1, the radius has a significant change at the pinning point where the value becomes an infinite positive value and then shifts to infinite negative due to the sudden change of meniscus shape. This trend is consistent with a numerical observation of the capillary barrier zones in which capillary forces accompany viscous forces to resist spontaneous imbibition (Pavuluri et al., 2020). We notice that wettability has a significant influence on the meniscus shape and stability. As the hydrophobicity increases, the dimensionless radius, r/r_0 , displays stable with lower values for the flow in microchannels. The magnitude difference becomes slight between flow in the channel and the pinning region, e.g., in the case of Q2, $\Delta r_{60} \approx 7 > \Delta r_{95 \text{ and } 120} \approx 3$. Therefore, the capillary pressure has a corresponding response and the variation becomes smaller.

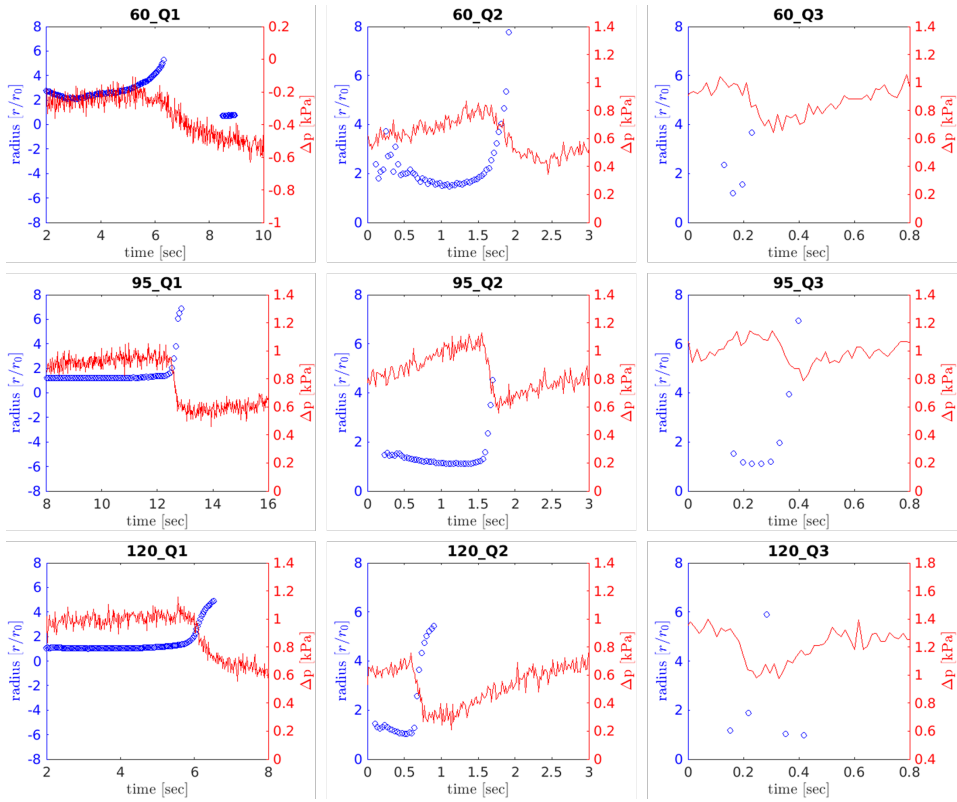


Figure 5-14: Pressure and radius data in pore-filling events. The red curve presents the pressure data, and the blue circle presents the radius. r_0 is half width of micro-channel. With the increase in injection flow rate, the numbers of acquired pressure and image data decrease and appear scattered in the figures.

To obtain more details, the enlarged radius data at the pinning region are plotted and compared in Figure 5-15. Similarly, wettability plays a role in the curvature change at the diverging corner. For the cases of 95 and 120 contact angles, the radius has a similar trend and can reach the minimum value of half-width of the inlet microchannel, while it doesn't occur in the case of 60 contact angles. Another phenomenon is that a higher velocity (Q3) eliminates the wettability influence on the radius change. Figure 5-15c shows that the radiuses among three wettability conditions display a very close curve variation. Interestingly, the flow behavior in the micro model with intermediate wettability has consistent performance and is not affected by the velocity, while other models do not show the same behavior, see Figure 5-15e.

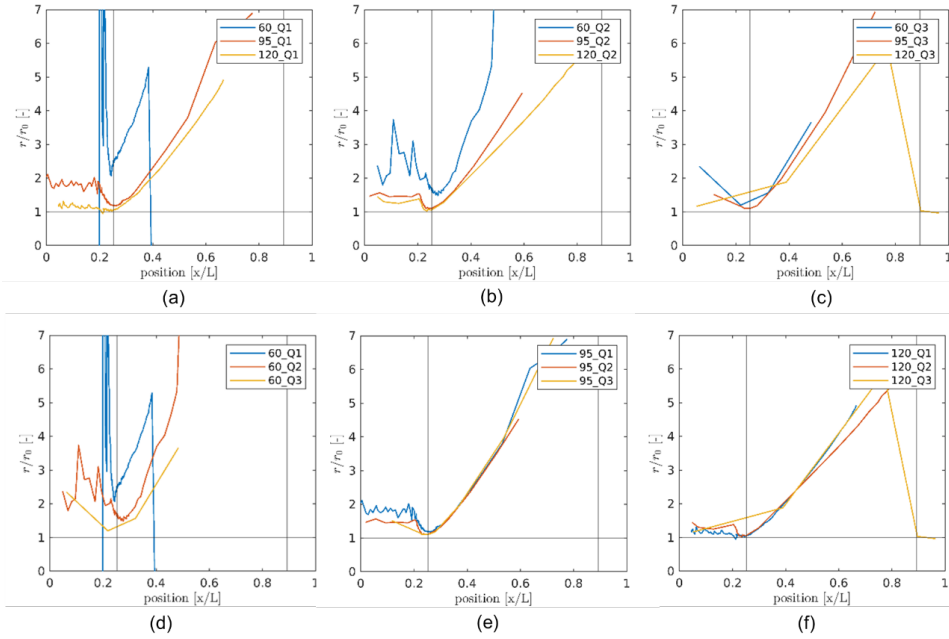


Figure 5-15: The relationship between meniscus radius and position for three wettabilities and injection velocities. The dimensionless pinning point position is indicated by the ratio of the meniscus pixel position in a horizontal direction (x) to the length of interested domain (L), shown with a vertical line in the figures. The dimensionless radius ($\frac{r}{r_0} = 1$) is indicated by the ratio of measured radius of the meniscus (r) to the half width of the micro-channel (r_0), shown with a horizontal line along the y-axis.

5.5.3 Water-fluorinert displacement

To achieve the water displacing fluorinert, we first saturate the micromodel with fluorinert. Due to the natural adhesive property of PDMS to fluorinert, the micromodel occurs the spontaneous imbibition when contacting the fluorinert phase. Afterwards, water is injected into the saturated model. Figure 5-16 illustrates the wettability influence on the interface movement under the same injection flow rate. The water-fluorinert displacement gives a similar behavior in general. The main difference is the case of 60 contact angle, where the water acts as a non-wetting phase. The experiments of static fluorinert droplets show that the plasma-PVA treated PDMS is wetting to fluorinert in the air but wetting to water in the container with water. Figure 5-16b shows the spontaneous imbibition during fluorinert saturation of the micro model, which causes the corner flow of

fluorinert along the solid surface. During the piston-like displacement in the channel, due to almost 5 times larger of the dynamic viscosity of fluorinert than that of water at 25°, water displays a non-wetting phase to the hydrophilized PDMS. The displacing contact angle is about 125° of water-PDMS.

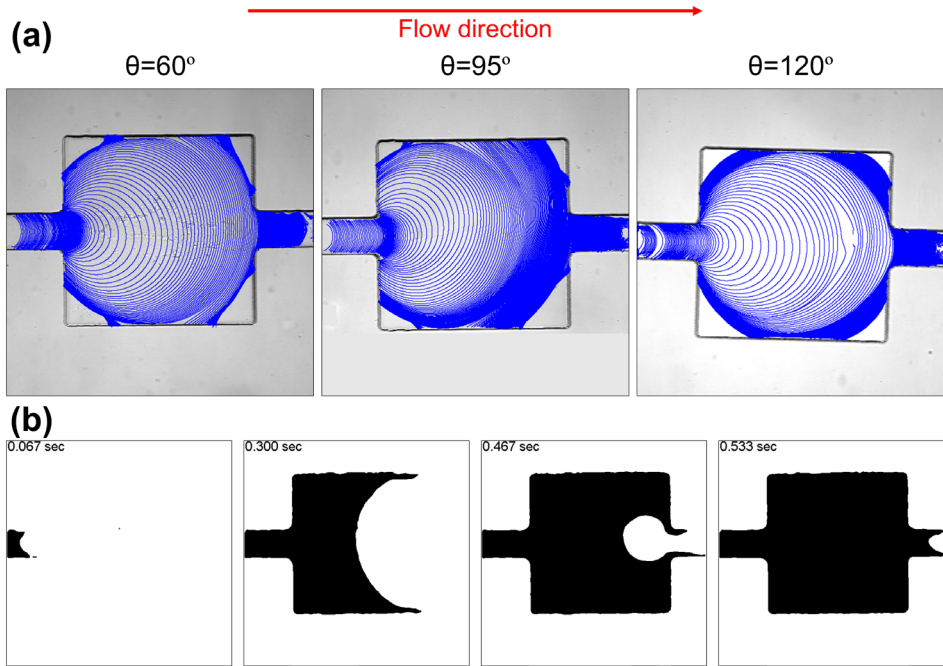


Figure 5-16: Interface detection during pore-filling behavior. (a) shows the interface detection for three wettability conditions with Q1 injection flow rate. The grey and black outlines are the shapes of the micromodel. (b) shows the process of fluorinert spontaneous imbibition. Black is the fluorinert phase.

The saturation of water for three injection rates is plotted in Figure 5-17, as well as the wettability effect. Figure 5-17a displays that the higher injection flow rate, the lower water saturation is. Wettability also plays a crucial role in the final water saturation. Although the water-wet PDMS micro-model presents non-wetting to water in the water-fluorinert displacement, the water saturation is still higher than the untreated and silanized micro-model. However, this effect becomes weakened for the highest injection flow rate. Furthermore, we compare the functions between final water saturation and capillary number for both water-air displacement and water-fluorinert displacement under three wettability conditions, as shown in Figure 5-17b. In general, water-air displacement induces

a larger final water saturation than that in water-fluorinert displacement for three wettability conditions. The water saturation decreases with the increase in the capillary number, and the decreasing rate slightly slows down when the flow rate changes from Q2 to Q3 for both displacements.

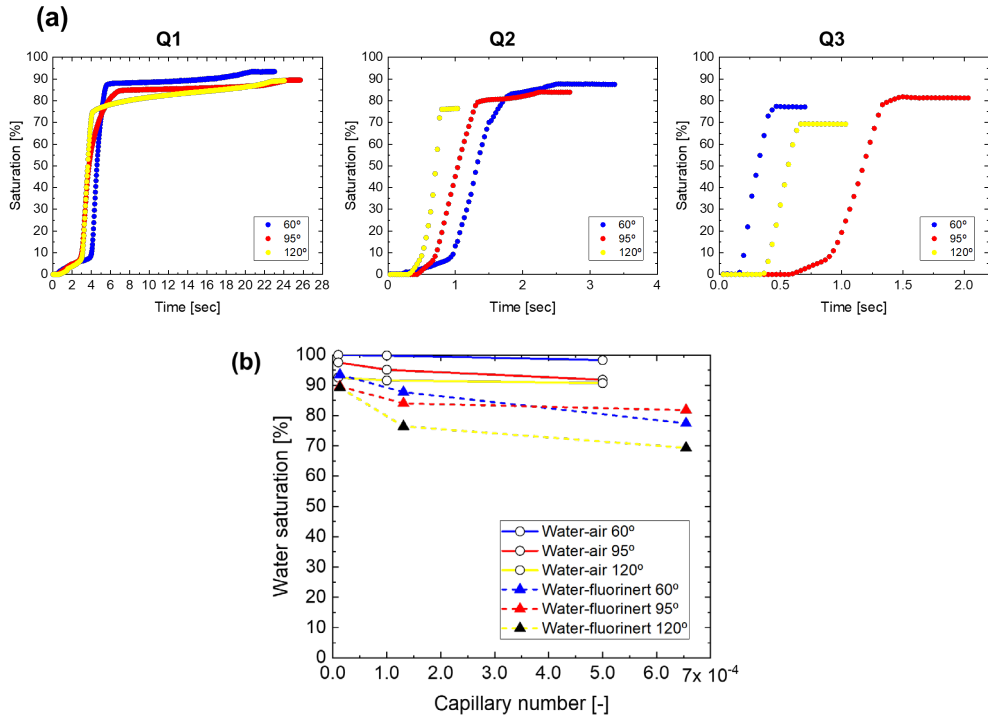


Figure 5-17: Saturation of water during water-fluorinert displacement. (a), water saturation for three injection flow rates under three wettability conditions; (b), the function of final water saturation and capillary number for water-air and water-fluorinert displacement.

According to the pressure monitoring and interface radius measurement, the water-fluorinert displacement in the pore filling process is captured. The tendency of the plotted curves is similar to that in the water-air displacement, as shown in Figure 5-18. The measured radius from images matches the changes in the recorded pressure data, where the burst pressure reflects the smallest radius of the water-fluorinert interface and the pressure rapidly decreases as the interface overcomes the pinning region. Interestingly, the amplitude of pressure curve variation becomes less remarkable with high flow rate than the experiments in low flow rate, $\Delta p_{Q3} > \Delta p_{Q2} > \Delta p_{Q1}$.

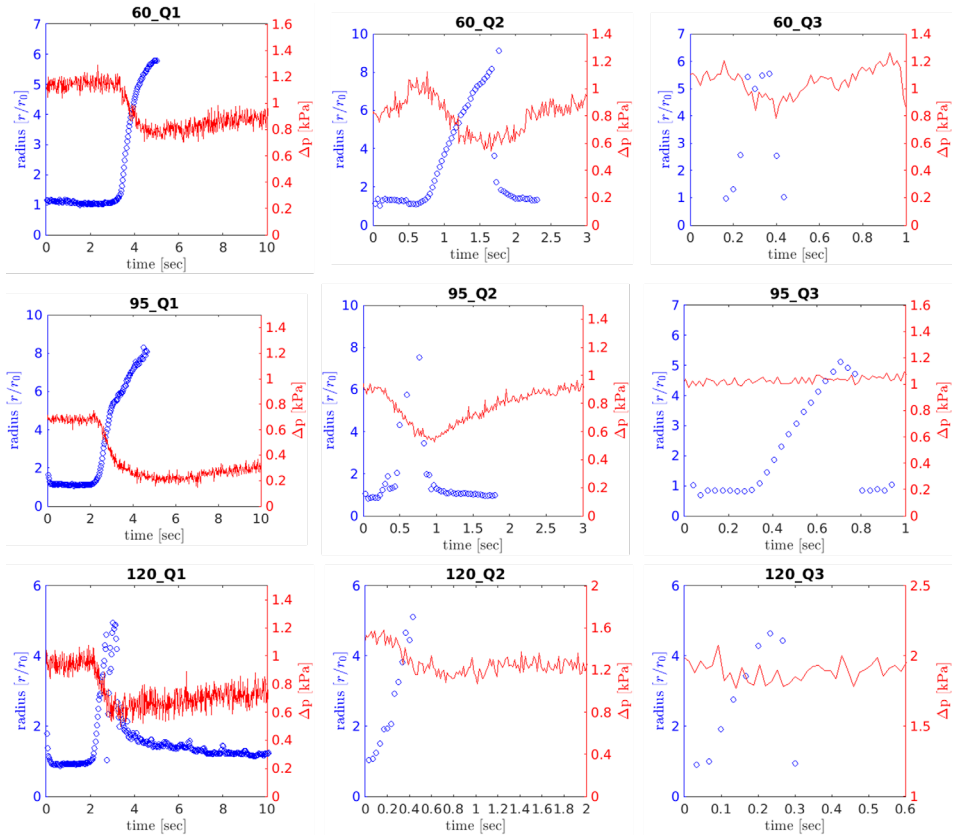


Figure 5-18. Pressure and radius data in pore-filling events for water-fluorinert displacement. The red curve presents the pressure data, and the blue circle presents the radius. r_0 is half width of micro-channel. With the increase in injection flow rate, the numbers of acquired pressure and image data decrease and appear scatted in the figures.

The direct relationship between the interface radii and position is given in Figure 5-19 for the pore-filling process. The curves reflect that both wettability and flow rate have impacts on the meniscus movement in the pinning region. PVA-treated micromodel has the most stable and less variation of the dimensionless radius in the pinning region for three flow rates. However, a higher degree of hydrophobicity causes more variations at the pinning point.

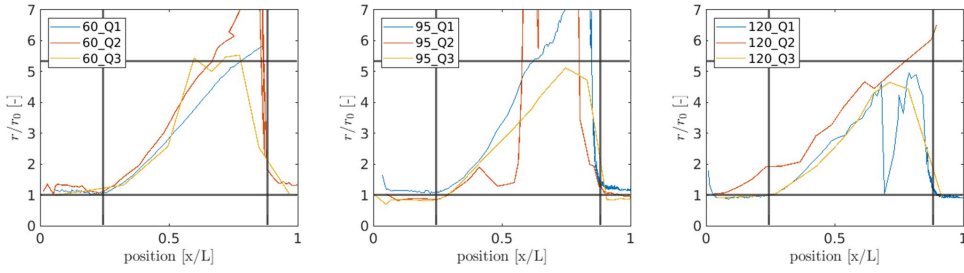


Figure 5-19: The relationship between meniscus radius and position for three wettabilities and injection flow rates. The dimensionless position is indicated by the ratio of the meniscus pixel position in a horizontal direction (x) to the length of interested domain (L), shown with two vertical lines in the figures where one is for the pinning position and another is for the maximum position of the meniscus in the pore body. The dimensionless radius is indicated by the ratio of measured radius of the meniscus (r) to the half width of the micro-channel (r_0), shown with two horizontal lines along the y-axis where one is for the minimum value ($\frac{r}{r_0} = 1$) and another is for the maximum value in pore body.

To compare the pore-filling process for both fluid displacements, the function of flux versus injection time is shown in Figure 5-20. Both displacements have the initial decrease in the flux of invading water phase when the meniscus reaches the pinning region, then have a sudden increase in the flux due to the decreasing capillary pressure in the diverging zone. However, under the same wettability and flow rate, e.g., 60_Q1, the water-air flooding exhibits a longer pinning period for defeating the burst pressure than the water-fluorinert experiments. The highest flow rate eliminates the event because of the non-remarkable fluctuation in the pressure as shown in Figure 5-18. Interestingly, by comparing the time difference in the two flux peaks between two displacements that indicates the occurrence of overcoming burst pressure, it is clear to see that Q1 has much larger values than the other two flow rates. Besides, the untreated PDMS model under Q1 flow rate performs the longest time difference, which indicates that the water-air interface needs the longest time to beat the burst region than the water-fluorinert interface.

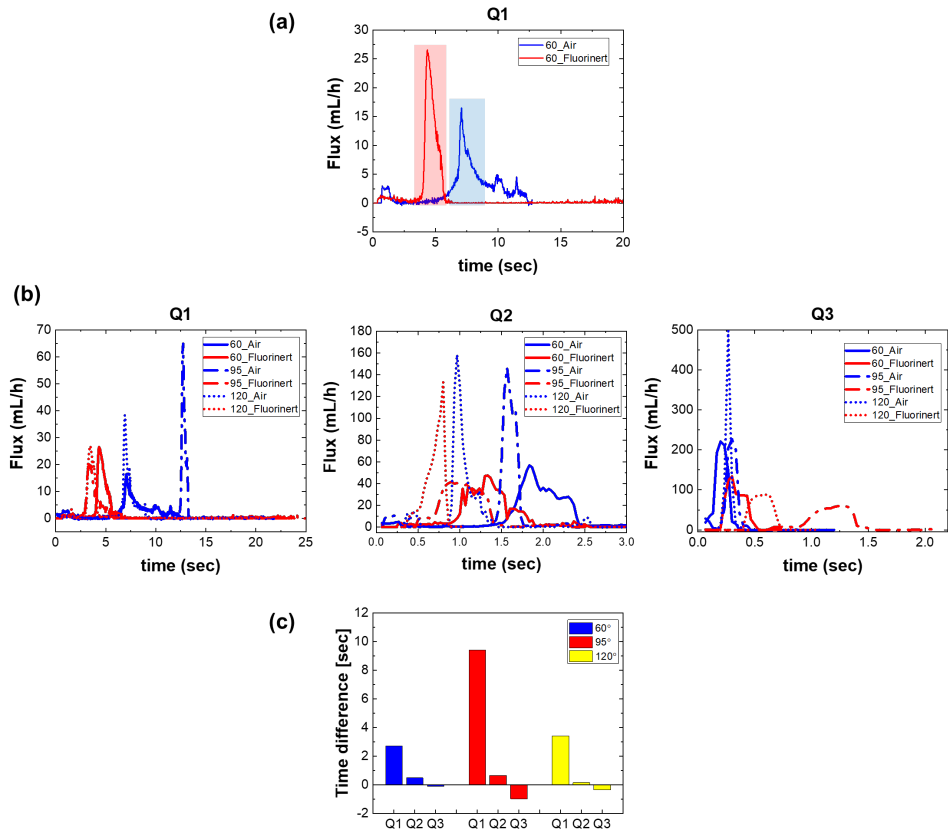


Figure 5-20: The function of flux and injection time. (a), one example to explain the difference between two fluid displacements under the same wettability condition and injection flow rate. Blue and red lines present the water-air displacement and water-fluorinert displacement, respectively. The shadowed regions indicate the suddenly appearing flux peaks induced by the breakthrough of invading phase in the pinning region for both displacements; (b), plots for all cases with three injection flow rates; (c), statistics of the time difference in two peaks for the displacements. A positive value means the pinning period in water-air flooding is longer than that in water-fluorinert flooding, and vice versa. The x-axis gives three flow rates.

5.6 Simulation result

5.6.1 Comparison of the various boundary conditions

We have run the simulations by giving three main boundary conditions, including constant inlet pressure (CIP), constant velocity (CIV) and considering flow resistance (CFR) on the inlet and outlet pressure.

Figure 5-21 gives the distribution of two fluid phases under three boundary conditions. In general, the constant inlet pressure induces either stops the meniscus at the pinning point with a low inlet pressure (e.g., 400 Pa) or overshoot the interface through the pore body with a high value (e.g., 1000 Pa). With a constant inlet velocity, although the meniscus won't stop at the pinning point, the meniscus has a constant moving speed, which is obviously not realistic.

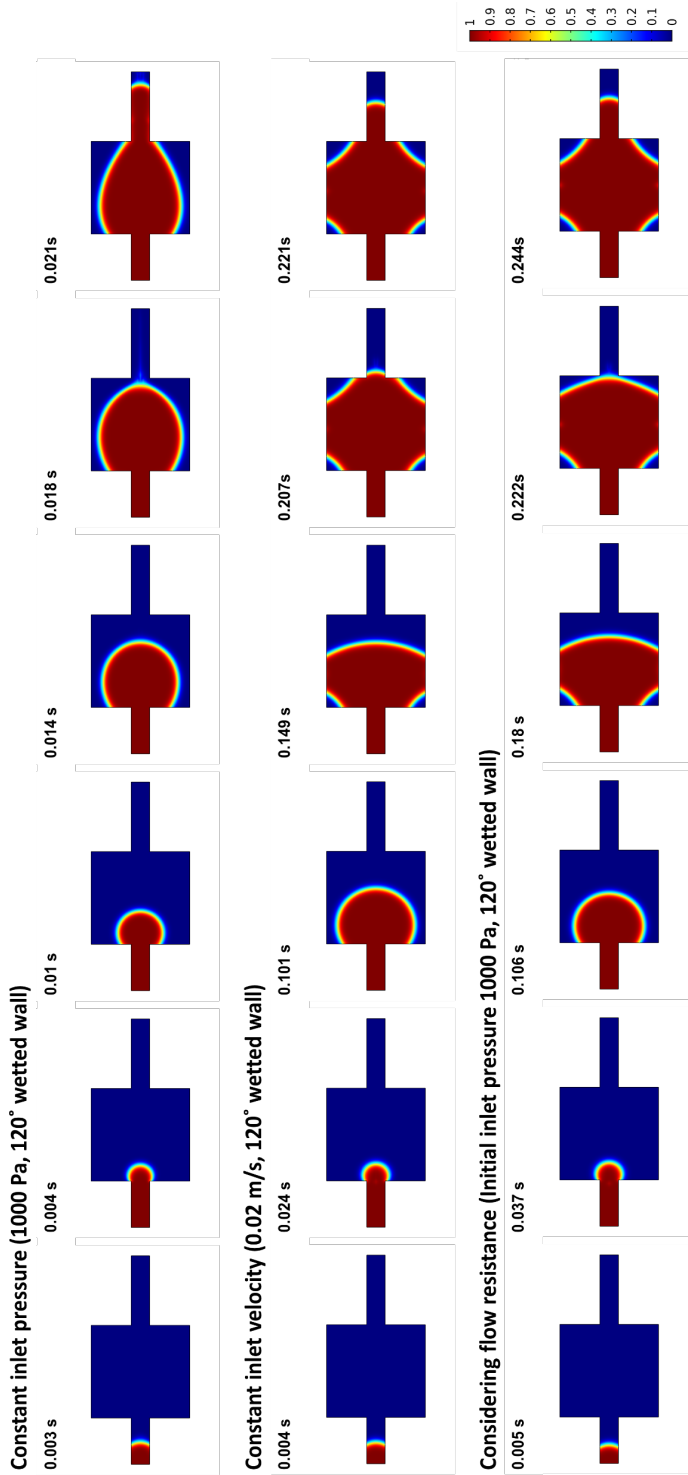


Figure 5-21: Interface behavior under different boundary conditions. From top to bottom, the conditions include the constant pressure, constant velocity and one case of considering the specific flow resistance.

Figure 5-22 show the constant inlet velocity induces a constant meniscus velocity and linear increase of water saturation. Although constant pressure can have variations in the volume flux and water saturation, the tendency has less consistency with the experimental data than it considering flow resistance. Therefore, we select the third type of boundary condition to conduct the following modeling and discussion on the wettability effect on the two-phase displacement.

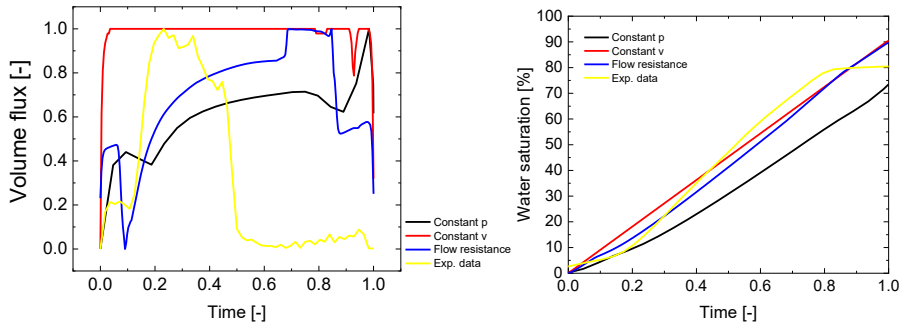


Figure 5-22: The function of normalized time versus normalized volume flux and saturation.

5.6.2 Wettability effect on meniscus behavior in pore filling

To investigate the wettability effect, the simulations with seven wettability conditions on the geometry walls are conducted. All simulations have the same inlet and out pressure situations, but the wetted wall is different in water contact angle: 0, 30, 60, 90, 120, 150, 180, named in the sequence of CFR_1000_0 to CFR_1000_150. All displacement profiles in pore filling are shown in Figure 5-23. The figures indicate that wettability plays an important role in the phase distributions. One notable thing is that in the experiments, due to the higher density and viscosity of fluorinert, the PVA-treated micromodel displays non-wetting to water in the displacement. Therefore, the phase distribution in the water-wet conditions (0, 30, and 60 water contact angle) shows different behavior with experiments.

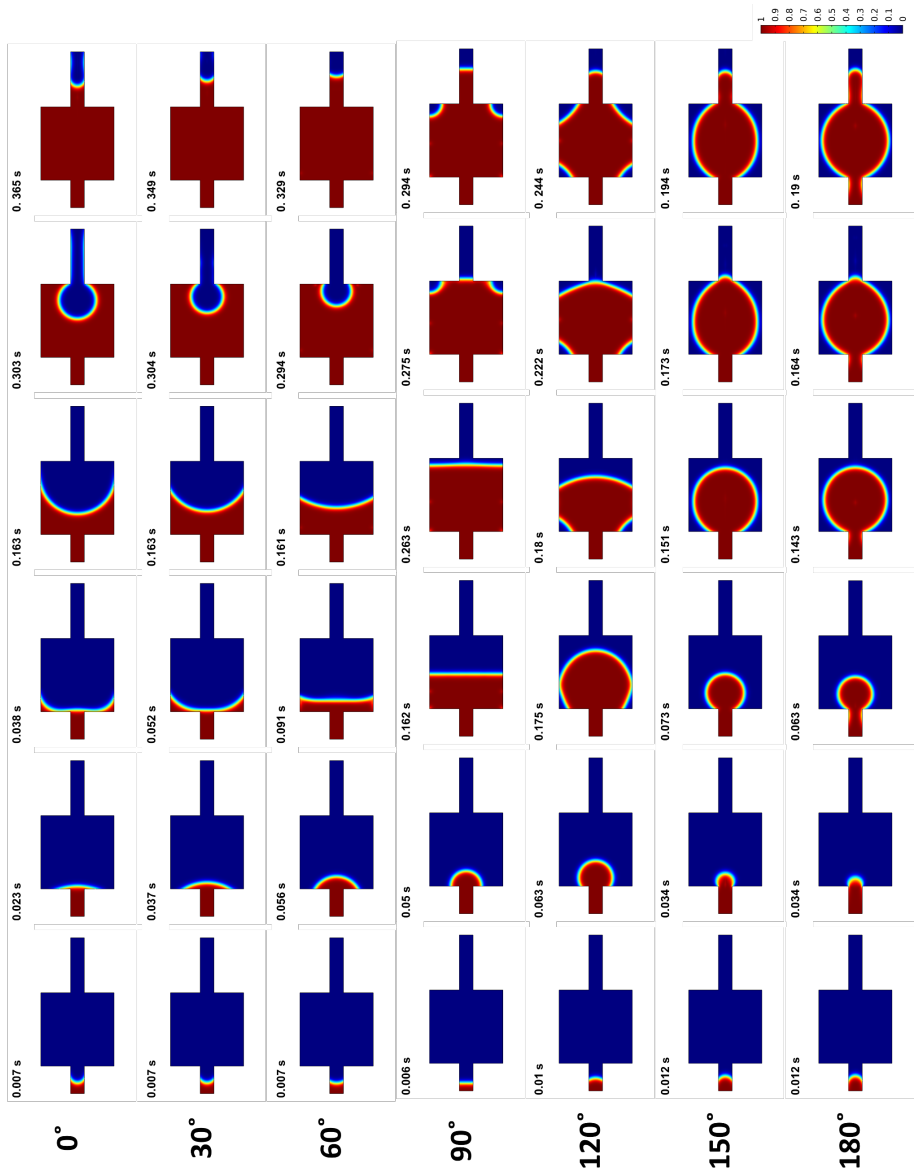


Figure 5-23: Comparison of water-fluorinert interfacial behavior in pore-filling events under various wettability conditions.

However, the water-air displacement in the water-wet micromodel gives a similar displacement to the modeling figures of water-fluorinert displacement. From water-wet to fluorinert-wet models, the interface gives the corresponding shapes and changes in the pinning region. For instance, the 0, 30 and 60 contact angles

cause the conversion of the meniscus in the region from concave to convex, where the capillary pressure has relative fluctuations. Figure 5-24 shows the capillary pressure for all wettability cases in simulation. When the meniscus encounters every corner of the pore body, the capillary pressure changes with the interface curvature, which induces fluctuations in the total pressure applied to the fluids.

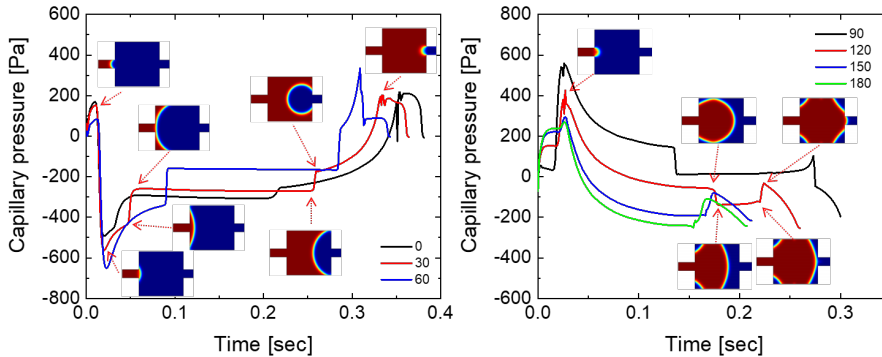


Figure 5-24: Capillary pressure under various wettability conditions. The left picture is the computational results for water-wet conditions, and the right picture is the results for fluorinert-wet conditions. The images represent the key turning points of capillary pressure curves for the cases of 30 and 120 contact angles. The capillary pressure is calculated by $p_{nw} - p_w$, where p_{nw} is the non-wetting phase and p_w is the wetting phase.

Figure 5-25 gives the variation of water saturation for various cases. These curves clearly show the breakthrough time in each case. The rising portion of the water saturation curves represents the displacement period when the invading water phase principally enters the pore body. The figure also shows that wettability plays an important role in the final saturation. The high hydrophobicity leads to a lower water saturation, which is consistent with the experimental observation.

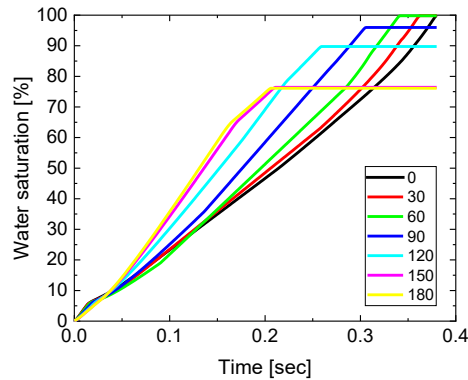


Figure 5-25: Water saturation profile in the numerical simulations with various wetting conditions.

The comparison of phase distributions between the experiment and simulation is shown in Figure 5-26. We have compared three cases of various wetting situations in experiments: 60°, 95°, and 120°. Note that the displacing (advancing) contact angle is larger than the static contact angle. For the cases of 95° and 120°, the displacing contact angles are around 130° and 150°. Therefore, the comparison for the two cases is used the modeling results of 120° and 150° cases. As the fluorinert film along the PVA-treated (60° static water contact angle) model, the experiment of water-fluorinert displacement does not show a water-wetting meniscus. Thus, we use the experimental results of water-air displacement in the PVA-treated model to conduct the comparison. In general, the simulations of interface behavior have good consistency with the experimental observations. Notably, in the case of 60°, the modeling captures the irregular shape of the two-phase interface when the meniscus touches the horizontal wall of the pore. This variation is captured in the experiment as well.

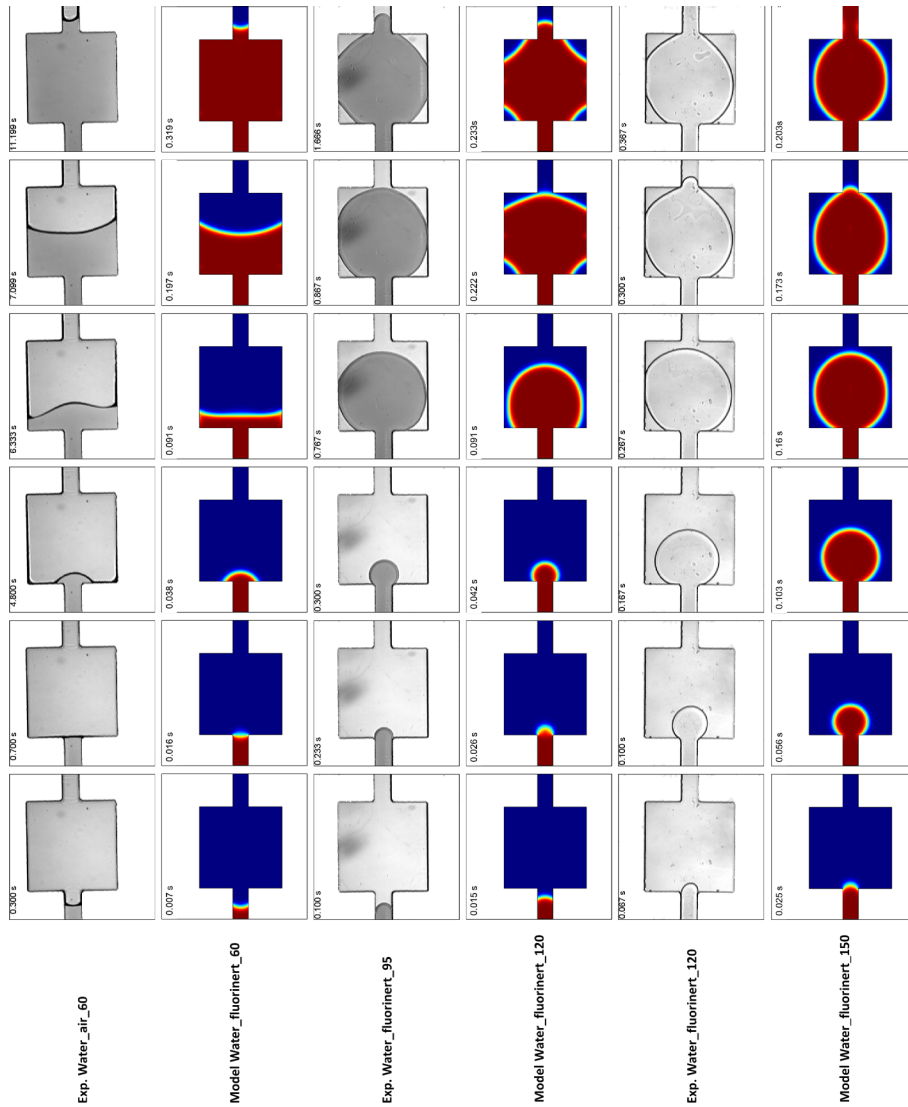


Figure 5-26: Comparison of phase distribution during pore filling for different wettability situations. In the experimental images, the water is the invading phase shown in darker grey, while the other phases, e.g., air and fluorinert, are transparent. In the modeling images of fluid volume fraction, the water is shown in red, and the fluorinert is in blue.

Figure 5-27 gives the pressure difference between the inlet and outlet of model, $p_{in} - p_{out}$. The experimental data are plotted in the figure. Although the initial injection pressure is different from the simulation, the modelling results have a similar variation to the experimental data. As water-wet models have the shape

reversion of the meniscus, the pressure has more fluctuations when the meniscus meets the horizontal walls of the pore. And the total magnitude of pressure (998.9 Pa for the 60° case) is larger than the non-water-wet models (658.4 Pa for the 90° case), which indicates that the wetting substrate causes higher pressure change.

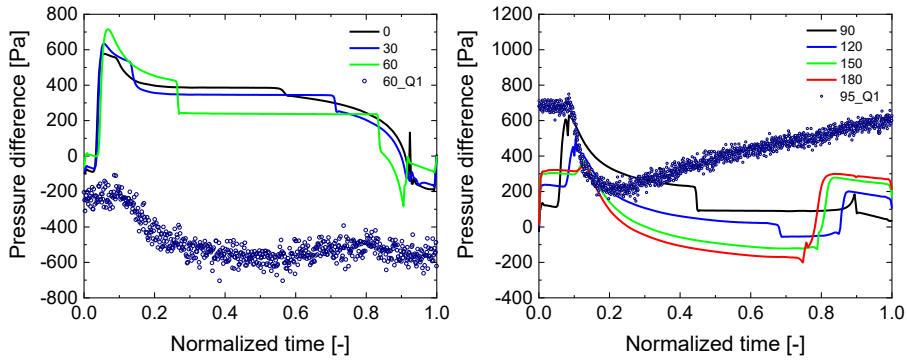


Figure 5-27: Pressure difference in the pore filling with various wetting walls. The experimental data are plotted with blue circles, including the cases of water-air displacement 60_Q1 and water-fluorinert displacement 95_Q1. As the water-air displacement with a relatively low flow rate, the displacement is similar to spontaneous imbibition and the pressure difference is initially negative.

5.7 Future work

5.7.1 Further analysis of the dynamic contact angle

During displacements, we observe that either in the microchannel or in the pinning region there is a hysteresis of contact angle in the meniscus movement depending on the substrate wettability and flow rate. The hysteresis of the contact angle is different from the static contact angle and the advancing contact angle in the droplet measurement. Figure 5-28 presents the dynamic contact angle in the water-air displacement in the micro-channel and pore-filling event. All of three wetting conditions have the hysteresis phenomenon. For instance, the original PDMS has an averaged dynamic contact angle of around 110°. The water-wet PDMS gives an angle around 75° and silanized micromodel has the angle around 145°. In the pinning region, the meniscus stops movement but the contact angle of air is decreasing. When the meniscus starts to move along the vertical walls of the pore, the contact angle increase again until almost reaching to the dynamic contact angle in the channel.

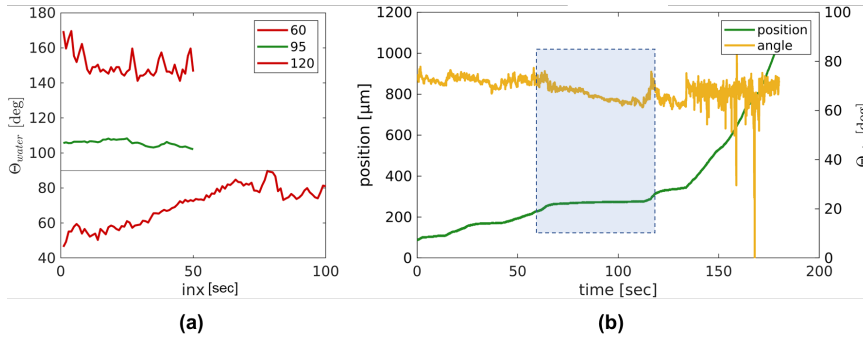


Figure 5-28: The displacing contact angle in the micro-channel and pore filling for the water-air displacement. (a), the water contact angles for three wetting conditions under the Q1 flow rate, where the top red curve is for the 120 case and the bottom curve is for the 60 case. (b), the comparison of meniscus position and the change of air contact angle for the 95_Q1 case. The pinning region is shown in the shadow domain.

We have analyzed the advancing process for two-phase flow in the previous sections, however, the receding process after pore-filling events, e.g., air and fluorinert displacing water back from the outlet reservoir to the inlet reservoir of the micromodel. Furthermore, we have conducted experiments on water displacing crude oil with various wetting conditions. The images have been collected, but the massive works on the data post-processing need to be continued and finished in the near future. Figure 5-29 gives an example of the receding process for water-air displacement and water-crude oil displacement under 95° wettability and Q1 receding flow rate. The air drainage process shows that the trapped air bubbles around the pore corners are not burst due to the thin film of water between the invading air and trapped air bubbles. The water drainage process in the crude-oil saturated model presents an obvious different interface behavior from the water-fluorinert drainage. As the thick film of crude oil (25 μm) is absorbed on the micromodel surface, the water acts non-wetting phase and the shape of the meniscus is like an ellipse in the pinning region. Besides, the property of non-Newtonian crude oil leads to the discontinuous water phase (water-oil emulsions) after the water-oil interface passing through the pore body.

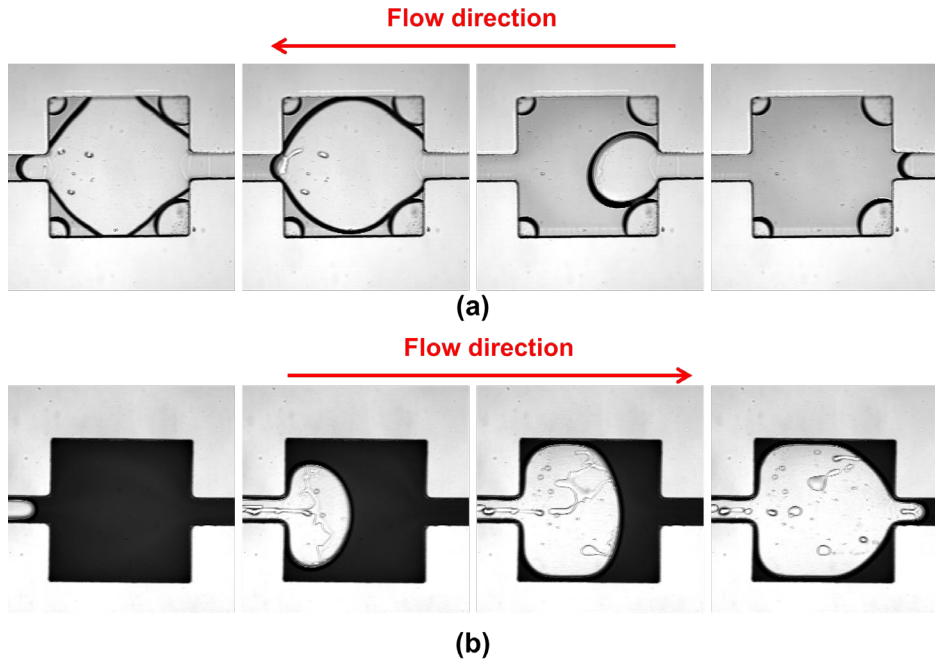


Figure 5-29: Images of water-air receding process and water-crude oil advancing process. (a), air drainage process. The grey phase in the pore is water; (b), the water-crude oil drainage process. The crude oil is black while the water (not dyed) is transparent.

5.7.2 Wettability effect in a complex porous media

The wettability effect in a single pore filling is investigated, but the substrate conditions and geometry are too simple compared to the real rock with a complex porous media. Therefore, based on the single pore geometry, a fracture is added to one side of the porous domain and two models are designed to study two types of spontaneous imbibition co-and counter-current, shown in Figure 5-30. The future work is focused on the wettability control on the PDMS surface to gain a super hydrophilic condition in a long term, e.g., 10° water contact angle, then investigate the interface behavior during the spontaneous imbibition with various wetting conditions.

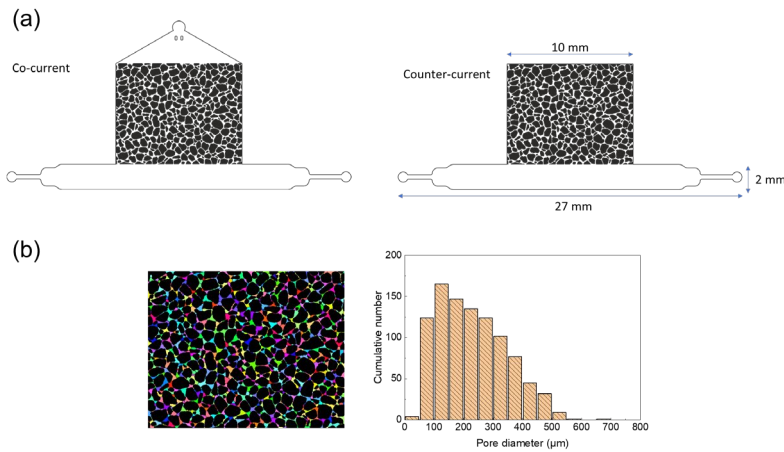


Figure 5-30: Design for experiments of co- and counter-current spontaneous imbibition. (a), mask design for the two micro-models; (b), segmentation of pore spaces in the porous domain and the pore size distribution.

5.8 Conclusion

Wettability is a crucial factor for pore-filling events in multiphase flow. Naturally, pore spaces have various sizes and often contain the sudden transient zone. Therefore, the investigation of the wettability effect on the flow behavior in the pore filling process is important to predict the fluid pressure. In our work, we have reviewed the analytical solution of pressure distribution in a two-phase flow in a rectangular channel and combined it with the calculation for the pressure variation in the capillary barrier zone. We conduct a series of microfluidic experiments for water-air displacement with three injection velocities (Q1, Q2 and Q3) under three wettability conditions (60°, 95° and 120°). Through image and pressure data processing, we are able to systematically figure out the details of meniscus behavior in the whole experimental process and the influence of wettability. Hereby, we conclude the following points.

- A comprehensive analytical solution is given for predicting the pressure change during a single square pore filling. The theory is validated with the experimental pressure data and meniscus behavior at the pinning region of the pore.

- Wettability plays a crucial role in the pressure accumulation for driving flow in rectangular micro-channel and meniscus movement at the pinning region. The hydrophobic surface (95° and 120° of water contact angle) requires a longer time for pressure accumulation to overcome the higher entry capillary pressure.
- Injection flow rate impacts the meniscus behavior as well. With Q1 injection flow rate, the hydrophilic model performs full water saturation in the pore but the hydrophobic model owns less saturation. Higher velocity induces a low water saturation for all wettability conditions and weakens the wettability effect for the hydrophobic cases.
- As the hydrophobicity increases, the meniscus radius stays more stable with lower values for the flow in micro-channels. The magnitude difference becomes slight between flow in channel and in the pinning region. Correspondingly, the capillary pressure has a response and the variation becomes smaller.
- A higher velocity (Q3) eliminates the wettability influence on the radius change in the channel and pinning region. Furthermore, intermediate wettability has consistent performance on the meniscus curvature and is not affected by the velocity.
- CFD numerical modeling has consistent results of interface behavior and pressure changes with the experiments.

References

- Barthès-Biesel, D. (2012). *Microhydrodynamics and complex fluids*: CRC Press.
- Bodas, D., & Khan-Malek, C. (2007). Hydrophilization and hydrophobic recovery of PDMS by oxygen plasma and chemical treatment—An SEM investigation. *Sensors and actuators B: chemical*, 123(1), 368-373.
- Brackbill, J. U., Kothe, D. B., & Zemach, C. (1992). A continuum method for modeling surface tension. *Journal of Computational Physics*, 100(2), 335-354.
- Cai, J., Jin, T., Kou, J., Zou, S., Xiao, J., & Meng, Q. (2021). Lucas–washburn equation-based modeling of capillary-driven flow in porous systems. *Langmuir*, 37(5), 1623-1636.
- Calvo, A., Paterson, I., Chertcoff, R., Rosen, M., & Hulin, J. (1991). Dynamic capillary pressure variations in diphasic flows through glass capillaries. *Journal of colloid and interface science*, 141(2), 384-394.
- Chang-Yen, D. A., Eich, R. K., & Gale, B. K. (2005). A monolithic PDMS waveguide system fabricated using soft-lithography techniques. *Journal of lightwave technology*, 23(6), 2088.
- Chen, J. M., Huang, P.-C., & Lin, M.-G. (2008). Analysis and experiment of capillary valves for microfluidics on a rotating disk. *Microfluidics and Nanofluidics*, 4(5), 427-437.
- Chen, S., & Doolen, G. D. (1998). Lattice Boltzmann method for fluid flows. *Annual Review of Fluid Mechanics*, 30(1), 329-364.
- Cho, H., Kim, H.-Y., Kang, J. Y., & Kim, T. S. (2007). How the capillary burst microvalve works. *Journal of colloid and interface science*, 306(2), 379-385.
- Dahle, H. K., Celia, M. A., & Hassanizadeh, S. M. (2005). Bundle-of-tubes model for calculating dynamic effects in the capillary-pressure-saturation relationship. *Transport in Porous Media*, 58(1), 5-22.
- Dang-Vu, T., Hupka, J., & Drzymala, J. (2006). Impact of roughness on hydrophobicity of particles measured by the Washburn method. *Physicochemical Problems of Mineral Processing*, 40, 45-52.
- de Winter, D., Weishaupt, K., Scheller, S., Frey, S., Raoof, A., Hassanizadeh, S., & Helmig, R. (2020). The Complexity of Porous Media Flow Characterized in a Microfluidic Model Based on Confocal Laser Scanning Microscopy and Micro-PIV. *Transport in Porous Media*, 1-25.
- Delker, T., Pengra, D. B., & Wong, P.-z. (1996). Interface pinning and the dynamics of capillary rise in porous media. *Physical review letters*, 76(16), 2902.
- Deng, W., & Cardenas, M. B. (2013). Dynamics and dislodgment from pore constrictions of a trapped nonwetting droplet stimulated by seismic waves. *Water Resources Research*, 49(7), 4206-4218.
- Dervieux, A., & Thomasset, F. (1980). A finite element method for the simulation of a Rayleigh-Taylor instability. In *Approximation methods for Navier-Stokes problems* (pp. 145-158): Springer.
- Dianat, M., Skarysz, M., & Garmory, A. (2017). A Coupled Level Set and Volume of Fluid method for automotive exterior water management applications. *International Journal of Multiphase Flow*, 91, 19-38.
- Dimitrov, D., Milchev, A., & Binder, K. (2007). Capillary rise in nanopores: molecular dynamics evidence for the Lucas-Washburn equation. *Physical review letters*, 99(5), 054501.
- Firincioglu, T., Blunt, M. J., & Zhou, D. (1999). Three-phase flow and wettability effects in triangular capillaries. *Colloids and Surfaces A: Physicochemical and Engineering Aspects*, 155(2-3), 259-276.
- Fisher, L. R., & Lark, P. D. (1979). An experimental study of the Washburn equation for liquid flow in very fine capillaries. *Journal of colloid and interface science*, 69(3), 486-492.

- Gamet, L., Scala, M., Roenby, J., Scheufler, H., & Pierson, J.-L. (2020). Validation of volume-of-fluid OpenFOAM® isoAdvector solvers using single bubble benchmarks. *Computers & Fluids*, 213, 104722.
- Glière, A., & Delattre, C. (2006). Modeling and fabrication of capillary stop valves for planar microfluidic systems. *Sensors and Actuators A: Physical*, 130, 601-608.
- Hagmeyer, B., Zechnall, F., & Stelzle, M. (2014). Towards plug and play filling of microfluidic devices by utilizing networks of capillary stop valves. *Biomicrofluidics*, 8(5), 056501.
- Heshmati, M., & Piri, M. (2014). Experimental investigation of dynamic contact angle and capillary rise in tubes with circular and noncircular cross sections. *Langmuir*, 30(47), 14151-14162.
- Hirt, C. W., & Nichols, B. D. (1981). Volume of fluid (VOF) method for the dynamics of free boundaries. *Journal of Computational Physics*, 39(1), 201-225.
- Hoffman, R. L. (1975). A study of the advancing interface. I. Interface shape in liquid—gas systems. *Journal of colloid and interface science*, 50(2), 228-241.
- Horgue, P., Augier, F., Duru, P., Prat, M., & Quintard, M. (2013). Experimental and numerical study of two-phase flows in arrays of cylinders. *Chemical Engineering Science*, 102, 335-345.
- Ismail, A. E., Grest, G. S., Heine, D. R., Stevens, M. J., & Tsige, M. (2009). Interfacial structure and dynamics of siloxane Systems: PDMS– Vapor and PDMS– Water. *Macromolecules*, 42(8), 3186-3194.
- Jacqmin, D. (1999). Calculation of two-phase Navier–Stokes flows using phase-field modeling. *Journal of Computational Physics*, 155(1), 96-127.
- Karadimitriou, N., Musterd, M., Kleingeld, P., Kreutzer, M., Hassanizadeh, S., & Joekar - Niasar, V. (2013). On the fabrication of PDMS micromodels by rapid prototyping, and their use in two - phase flow studies. *Water Resources Research*, 49(4), 2056-2067.
- Karadimitriou, N. K. (2013). *Two-phase flow experimental studies in micro-models*. UU Department of Earth Sciences,
- Kunz, P., Zarihos, I., Karadimitriou, N., Huber, M., Nieken, U., & Hassanizadeh, S. (2016). Study of multi-phase flow in porous media: comparison of SPH simulations with micro-model experiments. *Transport in Porous Media*, 114(2), 581-600.
- Kusumaatmaja, H., Pooley, C., Girardo, S., Pisignano, D., & Yeomans, J. (2008). Capillary filling in patterned channels. *Physical Review E*, 77(6), 067301.
- Legait, B., & Sourieau, P. (1985). Effect of geometry on advancing contact angles in fine capillaries. *Journal of colloid and interface science*, 107(1), 14-20.
- Leu, T.-S., & Chang, P.-Y. (2004). Pressure barrier of capillary stop valves in micro sample separators. *Sensors and Actuators A: Physical*, 115(2-3), 508-515.
- Lin, W.-C., & Razali, N. A. M. (2019). Temporary wettability tuning of PCL/PDMS micro pattern using the plasma treatments. *Materials*, 12(4), 644.
- Liu, J., Ju, Y., Zhang, Y., & Gong, W. (2019). Preferential paths of air-water two-phase flow in porous structures with special consideration of channel thickness effects. *Scientific Reports*, 9(1), 1-13.
- Lucas, R. (1918). Rate of capillary ascension of liquids. *Kolloid Z*, 23(15), 15-22.
- Ménard, T., Tanguy, S., & Berlemont, A. (2007). Coupling level set/VOF/ghost fluid methods: Validation and application to 3D simulation of the primary break-up of a liquid jet. *International Journal of Multiphase Flow*, 33(5), 510-524.
- Moura, M., Måløy, K. J., Flekkøy, E. G., & Toussaint, R. (2017). Verification of a dynamic scaling for the pair correlation function during the slow drainage of a porous medium. *Physical review letters*, 119(15), 154503.
- Moura, M., Måløy, K. J., Flekkøy, E. G., & Toussaint, R. (2020). Intermittent dynamics of slow drainage experiments in porous media: Characterization under different boundary conditions. *Frontiers in Physics*, 7, 217.
- Oh, K. W., Lee, K., Ahn, B., & Furlani, E. P. (2012). Design of pressure-driven microfluidic networks using electric circuit analogy. *Lab on a Chip*, 12(3), 515-545.

- Olanrewaju, A., Beaugrand, M., Yafia, M., & Juncker, D. (2018). Capillary microfluidics in microchannels: from microfluidic networks to capillary circuits. *Lab on a Chip*, 18(16), 2323-2347.
- Ouali, F. F., McHale, G., Javed, H., Trabi, C., Shirtcliffe, N. J., & Newton, M. I. (2013). Wetting considerations in capillary rise and imbibition in closed square tubes and open rectangular cross-section channels. *Microfluidics and Nanofluidics*, 15(3), 309-326.
- Papadimitriou, V., Segerink, L., van den Berg, A., & Eijkel, J. C. (2018). 3D capillary stop valves for versatile patterning inside microfluidic chips. *Analytica chimica acta*, 1000, 232-238.
- Pascual, M., Kerdraon, M., Rezard, Q., Jullien, M.-C., & Champougny, L. (2019). Wettability patterning in microfluidic devices using thermally-enhanced hydrophobic recovery of PDMS. *Soft Matter*, 15(45), 9253-9260.
- Pavuluri, S., Maes, J., Yang, J., Regaieg, M., Moncorgé, A., & Doster, F. (2019). Towards pore network modelling of spontaneous imbibition: contact angle dependent invasion patterns and the occurrence of dynamic capillary barriers. *Computational Geosciences*, 1-19.
- Pavuluri, S., Maes, J., Yang, J., Regaieg, M., Moncorgé, A., & Doster, F. (2020). Towards pore network modelling of spontaneous imbibition: contact angle dependent invasion patterns and the occurrence of dynamic capillary barriers. *Computational Geosciences*, 24(2), 951-969.
- Schebarchov, D., & Hendy, S. (2008). Dynamics of capillary absorption of droplets by carbon nanotubes. *Physical Review E*, 78(4), 046309.
- Schlüter, S., Berg, S., Rücker, M., Armstrong, R., Vogel, H. J., Hilfer, R., & Wildenschild, D. (2016). Pore - scale displacement mechanisms as a source of hysteresis for two - phase flow in porous media. *Water Resources Research*, 52(3), 2194-2205.
- Singh, K., Jung, M., Brinkmann, M., & Seemann, R. (2019). Capillary-dominated fluid displacement in porous media. *Annual Review of Fluid Mechanics*, 51, 429-449.
- Sorbie, K., Wu, Y., & McDougall, S. (1995). The extended Washburn equation and its application to the oil/water pore doublet problem. *Journal of colloid and interface science*, 174(2), 289-301.
- Squires, T. M., & Quake, S. R. (2005). Microfluidics: Fluid physics at the nanoliter scale. *Reviews of modern physics*, 77(3), 977.
- Stewartson, K. (1970). Modern Fluid Dynamics, Volume 1: Incompressible Flow. By N. Curle and HJ Davies. Pp. xiv, 290. Paperback 32s. 6d. Cloth 65s. 1968.(D. van Nostrand.). *The Mathematical Gazette*, 54(387), 102-103.
- Stone, H. A. (2007). Introduction to fluid dynamics for microfluidic flows. In *CMOS biotechnology* (pp. 5-30): Springer.
- Stukan, M. R., Ligneul, P., Crawshaw, J. P., & Boek, E. S. (2010). Spontaneous imbibition in nanopores of different roughness and wettability. *Langmuir*, 26(16), 13342-13352.
- Sun, Z., & Santamarina, J. C. (2019). Haines jumps: Pore scale mechanisms. *Physical Review E*, 100(2), 023115.
- Sussman, M., & Puckett, E. G. (2000). A coupled level set and volume-of-fluid method for computing 3D and axisymmetric incompressible two-phase flows. *Journal of Computational Physics*, 162(2), 301-337.
- Szekely, J., Neumann, A., & Chuang, Y. (1971). The rate of capillary penetration and the applicability of the Washburn equation. *Journal of colloid and interface science*, 35(2), 273-278.
- Takada, N., Misawa, M., & Tomiyama, A. (2005). *A phase-field method for interface-tracking simulation of two-phase flows*. Paper presented at the Fluids Engineering Division Summer Meeting.
- Tanner, L. (1979). The spreading of silicone oil drops on horizontal surfaces. *Journal of Physics D: Applied Physics*, 12(9), 1473.
- Trantidou, T., Elani, Y., Parsons, E., & Ces, O. (2017). Hydrophilic surface modification of PDMS for droplet microfluidics using a simple, quick, and robust method via PVA deposition. *Microsystems & nanoengineering*, 3(1), 1-9.

- Washburn, E. W. (1921). The dynamics of capillary flow. *Physical review*, 17(3), 273.
- Xia, Y., & Whitesides, G. M. (1998). Soft lithography. *Annual review of materials science*, 28(1), 153-184.
- Yan, L., Aslannejad, H., Hassanizadeh, S. M., & Raoof, A. (2020). Impact of water salinity differential on a crude oil droplet constrained in a capillary: Pore-scale mechanisms. *Fuel*, 274, 117798.
- Yang, J., Bondino, I., Regaieg, M., & Moncorgé, A. (2017). Pore to pore validation of pore network modelling against micromodel experiment results. *Computational Geosciences*, 21(5), 849-862.
- Yin, X., Zarikos, I., Karadimitriou, N., Raoof, A., & Hassanizadeh, S. (2019). Direct simulations of two-phase flow experiments of different geometry complexities using Volume-of-Fluid (VOF) method. *Chemical Engineering Science*, 195, 820-827.
- Yokoi, K. (2013). A practical numerical framework for free surface flows based on CLSVOF method, multi-moment methods and density-scaled CSF model: Numerical simulations of droplet splashing. *Journal of Computational Physics*, 232(1), 252-271.
- Yu, L., & Wardlaw, N. C. (1986). The influence of wettability and critical pore-throat size ratio on snap-off. *Journal of colloid and interface science*, 109(2), 461-472.
- Zacharoudiou, I., Chapman, E. M., Boek, E. S., & Crawshaw, J. P. (2017). Pore-filling events in single junction micro-models with corresponding lattice Boltzmann simulations. *Journal of Fluid Mechanics*, 824, 550-573.
- Zarikos, I., Hassanizadeh, S., van Oosterhout, L., & van Oordt, W. (2018). Manufacturing a micro-model with integrated fibre optic pressure sensors. *Transport in Porous Media*, 122(1), 221-234.
- Zhang, Q., & Hassanizadeh, S. M. (2017). The role of interfacial tension in colloid retention and remobilization during two-phase flow in a polydimethylsiloxane micro-model. *Chemical Engineering Science*, 168, 437-443.
- Zhao, B., MacMinn, C. W., Szulczewski, M. L., Neufeld, J. A., Huppert, H. E., & Juanes, R. (2013). Interface pinning of immiscible gravity-exchange flows in porous media. *Physical Review E*, 87(2), 023015.
- Zhou, J., Khodakov, D. A., Ellis, A. V., & Voelcker, N. H. (2012). Surface modification for PDMS - based microfluidic devices. *Electrophoresis*, 33(1), 89-104.

Chapter 6

Summary and Conclusion

Summary and Conclusion

Many challenging issues involving two-phase flow in porous media are encountered in low-salinity water flooding technique. During the invasion of low-salinity water the ionic strength in the bulk phase varies from high to low, which causes alteration of the water-oil interfacial properties - e.g., interfacial tension and wettability changes. In addition to the oil that is displaced during water flooding, there is some oil that is constrained between water and grains and can be remobilized by the low-salinity effects. As many as ten controlling mechanisms have been proposed to explain the low-salinity effects. Osmosis and water-in-oil emulsification are among these mechanisms. However, our knowledge of these processes is limited. In particular, the water transport in oil and its associated time scales are not well understood.

In this thesis, we report on a series of microfluidic experiments to explore the low-salinity effects. Sequential injections of high-salinity water (HSW), pure or surfactant-laden synthetic oils, and low-salinity water (LSW) are performed to obtain a fluid distribution where oil is sandwiched between disconnected HSW water and the connected LSW phase. A $2,797.16 \times 2,238.39 \mu\text{m}^2$ area is continuously observed over 70 hours using a high-resolution microscope. Based on our observations, two scenarios for explaining water transport through the oil phase are proposed: water diffusion in response to the chemical potential and water transport via reverse micelle or micro-emulsions movement. Additionally, the influence of salinity on the brine-oil interfacial behavior is investigated through experiments of dynamic light scattering and exploring changes in surface tension. To investigate the effect of salinity on water transport in heptane, molecular dynamic (MD) simulations are conducted by considering three different concentrations in the high-salinity water region found in microfluidic experiments.

Another common mechanism is wettability alteration due to the double layer expansion, where one macro-scale phenomenon is generation of an aqueous thin film and its expansion between oil and solid surface. The numerical modelling of ionic diffusive transport through a charged thin film of electrolyte is mathematically and computationally complex due to the strongly coupled hydrodynamics and electrochemical interactions. Generally, simulations are

performed by solving the Poisson equation together with the Nernst-Planck flux formula to simulate electrochemical processes in electro-diffusion problems. However, because of highly nonlinear and coupled equations, the computational costs are heavy and very often limited to simulations in two-dimensional geometries. Therefore, in this thesis, in order to reduce the computational time, an equivalent one-dimensional electro-diffusive transport model is developed based on averaging of 2D equations. This model has been used to simulate the evolution of electrical potential and ion concentration distribution along the thin film of electrolyte.

Given the complexity of the minerals, the formation rock often attains various wettability ranging from water-wet to the oil-wet. Wettability plays a crucial role in two-phase displacement patterns. When the two-phase meniscus crosses a pore throat an abrupt variation in fluid redistribution can occur – i.e., the commonly known Haines Jump. To better understand the effect of wettability, we conduct a series of wettability-modified microfluidic experiments to investigate the drainage and imbibition processes for water-air and water-fluorinert displacement under three injection flow rates. The PDMS micro model is designed with a depth of 100 μm containing one square-shape pore body of 800 μm in width and length, which is connected to 4,000 μm long inlet and outlet channels with a height of 150 μm . The models are rendered with three surface wettabilities of 60°, 95° and 120° static contact angles. Confocal laser scanning microscopy (CLSM) is employed to image the water interface and monitor its movement. With a pressure transducer inserted in the upstreaming plastic tube, the pressure change during the events was continuously measured. The collected pressure curves are compared with existing analytical solutions. Furthermore, direct numerical modeling of water-fluorinert displacement is conducted with various boundary conditions to investigate the wettability effect. Instead of using constant inlet pressure or velocity, flow resistance is considered in the simulation for having more comparable results of pressure and interface behavior to the experimental data in the single pore-filling event.

The main conclusions of each chapter are described as follows.

- **Chapter 2:** We directly observed that oil globules can be remobilized by salinity differential in a microcapillary. The contact angle measurement of low/high-salinity water has been done by using a 2D reconstruction of the water-oil interface that was obtained using confocal laser scanning

microscopy. We noticed that LSW and HSW both have the potential of making the surface more water-wet, even if in the cases with hydrophilic coated capillary. However, LSW renders the solid surface more water-wet than HSW. We found that the pressure difference between high/low-salinity water phases around the constrained oil globule reached a plateau with a maximum value of 1.65 kPa during a period of 24 days. The change in the pressure difference is consistent with the change of contact angle and oil movement.

- **Chapter 3:** The fundamental theory of water transport through oil phase is described. Two scenarios for explaining the transport are proposed: water diffusion due to chemical potential gradient and water transport via reverse micelle or micro-emulsions movement towards to HSW-oil interface. Through a series of microfluidic experiments, we directly capture that the salinity contrast over oil films can cause water transport through the oil. Water is capable to pass through the selected alkane phases (heptane and dodecane) with and without adding a surfactant. This caused the expansion of trapped high-salinity water and oil mobilization. Ionic strength and the hydrocarbon chain length both play important roles in water transport. Heptane and dodecane both are found to be diffusive to water and reverse micelles, and this property could be significantly affected by the salinity contrast at the two sides of alkanes. A higher salinity contrast of 1.7-170 g/L induces a higher water volumetric flux through heptane and dodecane. We found that 50-170 g/L salinity contrast gives less water flux, even reaching 0 after a certain period. Adding SPAN80 surfactant to alkanes enhances the water flux by more than 100 times, but eliminates the salinity effect on the water flux. The presence of surfactant increases the visco-elasticity of the water-oil interface. Furthermore, the dynamic process of emulsion generation at the brine-oil interface are captured through DLS and IFT experiments. The salinity effect on the process and interfacial tension are evaluated.

Through conducting MD simulation, we observed water molecules transported through the heptane phase and a higher number of water molecules passed the water-heptane interface driven by ion concentration differences. There was a net flux of water molecules towards the high salinity water. Meanwhile, based on the calculated profiles of ions,

almost no ions appeared at the oil-water interface and inside the heptane phase. By investigating the interfacial tension changes and mean square displacement (MSD) calculations, we conclude that higher salinity leads to a lower diffusion coefficient of water molecules (around 4.48 and 2.98 $\mu\text{m}^2/\text{ms}$ for 5% and 20%, respectively), i.e., slower water movement. Moreover, high salinity reduces the probability of water diffusion through the interface into the oil phase. This leads to the lower solubility of water in oil near the oil-HSW interface and thus verifies the experimental result that the direction of net water movement is towards high salinity water.

- **Chapter 4:** We have developed an effective one-dimensional model to simulate electro-diffusion inside a thin layer of electrolyte sandwiched between two charged surfaces. This model has been used to simulate the evolution of electrical potential and ion concentration distribution along a thin film of electrolyte. Simulations showed that because of the negatively charged surfaces, the mobility of the cations was severely affected by the electric charges and these ions had a lower outward diffusion rate compared to the flux of anions. The developed 1-D model could significantly reduce the computational time by a factor of 180-220 compared to simulation using a 2D model. The equivalent 1D model enables solving the nonlinear governing equations for much larger domain lengths providing a unique opportunity to simulate experimental results of ion transport in thin films where the very large height-to-length ratio prevents the use of 2D simulations. In future works, flow equations can be added to the effective 1D model to investigate the increase of film thickness due to the coupled effects of electroosmotic and water flow over time and detachment of the oil phase from the solid surface in scales comparable with the experimental observations.
- **Chapter 5:** The wettability effect on two-phase flow is investigated in this chapter. We have reviewed the analytical solution of pressure distribution in a two-phase flow in a rectangular channel and combined it with the calculation for the pressure variation in the capillary barrier zone. By conducting the PDMS microfluidic experiments, the pore filling event in a single square pore has been studied for two-phase displacement under three injection flow rates (Q_1 , Q_2 and Q_3) and three wettability

conditions (contact angles of 60° , 95° and 120°). Wettability plays a crucial role in the pressure variation for driving flow in the rectangular micro-channel and meniscus movement at the pinning region. The hydrophobic surfaces (95° and 120° contact angles) require a longer time for pressure accumulation to overcome the higher entry capillary pressure. Injection flow rate impacts the meniscus behavior as well. With Q1 injection flow rate, the hydrophilic model reaches full water saturation in the pore but the hydrophobic model remains at lower saturation. Higher velocity induces a low water saturation for all wettability conditions and weakens the wettability effect for the hydrophobic cases. As the hydrophobicity increases, the meniscus radius stays more stable with lower values for the flow in microchannels. The magnitude difference becomes slight between flow in the channel and in the pinning region. Correspondingly, the capillary pressure has a response and the variation becomes smaller. Direct simulation of the water-fluorinert displacement using Volume-of-fluid method gives a detailed description of interface behavior during pore filling and provides consistent results of capillary pressure changes with the experimental data.

Samenvatting en Conclusie

Veel uitdagende problemen met betrekking tot tweefasige stroming in poreuze media worden aangetroffen bij wateroverstromingstechnieken met een laag zoutgehalte. Tijdens de invasie van water met een laag zoutgehalte varieert de ionsterkte in de bulkfase van hoog naar laag, wat een verandering van de water-olie-grensvlakeigenschappen veroorzaakt - b.v. grensvlakspanning en bevochtigbaarheid verandert. Naast de olie die wordt verdrongen tijdens overstromingen, is er enige olie die wordt vastgehouden tussen water en granen en kan worden geremobiliseerd door de effecten van een laag zoutgehalte. Er zijn maar liefst tien controlemechanismen voorgesteld om de effecten van een laag zoutgehalte te verklaren. Osmose en water-in-olie emulgering behoren tot deze mechanismen. Onze kennis van deze processen is echter beperkt. Met name het watertransport in olie en de bijbehorende tijdschalen zijn niet goed begrepen.

In dit proefschrift rapporteren we over een reeks microfluidische experimenten om de effecten van een laag zoutgehalte te onderzoeken. Opeenvolgende injecties van water met een hoog zoutgehalte (HSW), zuivere of met oppervlakactieve stoffen beladen synthetische oliën, en water met een laag zoutgehalte (LSW) worden uitgevoerd om een vloeistofverdeling te verkrijgen waarbij de olie wordt ingeklemd tussen losgekoppeld HSW-water en de aangesloten LSW-fase. Een gebied van $2.797,16 \times 2.238,39 \mu\text{m}^2$ wordt gedurende 70 uur continu geobserveerd met behulp van een microscoop met hoge resolutie. Op basis van onze waarnemingen worden twee scenario's voorgesteld voor het verklaren van watertransport door de oliefase: waterdiffusie als reactie op het chemische potentieel en watertransport via omgekeerde micel- of micro-emulsiesbeweging. Daarnaast wordt de invloed van het zoutgehalte op het pek-olie grensvlakgedrag onderzocht door middel van experimenten met dynamische lichtverstrooiing en het onderzoeken van veranderingen in oppervlaktespanning. Om het effect van het zoutgehalte op het watertransport in heptaan te onderzoeken, worden moleculaire dynamische (MD) simulaties uitgevoerd door drie verschillende concentraties in het water met een hoog zoutgehalte te beschouwen die worden gevonden in microfluidische experimenten.

Een ander veel voorkomend mechanisme is de wijziging van de bevochtigbaarheid als gevolg van de uitzetting van de dubbele laag, waarbij een fenomeen op macroschaal het genereren van een waterige dunne film en de

uitzetting ervan tussen olie en vast oppervlak is. De numerieke modellering van ionisch diffuus transport door een geladen dunne film van elektrolyt is wiskundig en rekenkundig complex vanwege de sterk gekoppelde hydrodynamica en elektrochemische interacties. Over het algemeen worden simulaties uitgevoerd door de Poisson-vergelijking samen met de Nernst-Planck-fluxformule op te lossen om elektrochemische processen in elektrodiffusieproblemen te simuleren. Vanwege zeer niet-lineaire en gekoppelde vergelijkingen zijn de rekenkosten echter zwaar en vaak beperkt tot simulaties in tweedimensionale geometrieën. Daarom is in dit proefschrift, om de rekentijd te verminderen, een equivalent eendimensionaal elektro-diffuus transportmodel ontwikkeld op basis van het middelen van 2D-vergelijkingen. Dit model is gebruikt om de evolutie van de elektrische potentiaal en de verdeling van de ionenconcentratie langs de dunne film van elektrolyt te simuleren.

Gezien de complexiteit van de mineralen, bereikt het formatiegesteente vaak verschillende bevochtigbaarheid, variërend van water-nat tot olie-nat. Bevochtigbaarheid speelt een cruciale rol in tweefasige verplaatsingspatronen. Wanneer de tweefasige meniscus een porie-keel kruist, kan er een abrupte variatie in de herverdeling van vocht optreden, d.w.z. de algemeen bekende Haines-sprong. Om het effect van bevochtigbaarheid beter te begrijpen, voeren we een reeks bevochtigings-gemodificeerde microfluidische experimenten uit om de drainage- en imbibitieprocessen voor water-lucht- en water-fluorinert-verplaatsing onder drie injectiestroomsnelheden te onderzoeken. Het PDMS-micromodel is ontworpen met een diepte van 100 μm en bevat één vierkant porieliichaam van 800 μm breed en lang, dat is verbonden met 4.000 μm lange in- en uitlaatkanalen met een hoogte van 150 μm . De modellen zijn weergegeven met drie oppervlaktebevochtigingen van 60°, 95° en 120° statische contacthoeken. Confocale laser scanning microscopie (CLSM) wordt gebruikt om de waterinterface in beeld te brengen en de beweging ervan te volgen. Met een drukopnemer in de bovenstroomse kunststof buis werd de drukverandering tijdens de gebeurtenissen continu gemeten. De verzamelde drukcurven worden vergeleken met bestaande analytische oplossingen. Verder wordt directe numerieke modellering van water-fluorinert verplaatsing uitgevoerd met verschillende randvoorwaarden om het bevochtigingseffect te onderzoeken. In plaats van constante inlaatdruk of -snelheid te gebruiken, wordt in de simulatie rekening gehouden met stromingsweerstand om resultaten van druk en

grensvlakgedrag beter vergelijkbaar te maken met de experimentele gegevens in de gebeurtenis met één porievulling.

De belangrijkste conclusies van elk hoofdstuk worden als volgt beschreven.

- **Hoofdstuk 2:** We hebben direct waargenomen dat oliebolletjes geremobiliseerd kunnen worden door een verschil in zoutgehalte in een microcapillair. De contacthoekmeting van water met een laag/hog zoutgehalte is gedaan met behulp van een 2D-reconstructie van de water-olie-interface die is verkregen met behulp van confocale laserscanningmicroscopie. We hebben gemerkt dat LSW en HSW beide het potentieel hebben om het oppervlak meer waternat te maken, zelfs in de gevallen met hydrofiel gecoat capillair. LSW maakt het vaste oppervlak echter meer waternat dan HSW. We ontdekten dat het drukverschil tussen de waterfasen met een hoog/laag zoutgehalte rond de ingeperkte oliebol een plateau bereikte met een maximale waarde van 1,65 kPa gedurende een periode van 24 dagen. De verandering in het drukverschil is consistent met de verandering van contacthoek en oliebeweging.
- **Hoofdstuk 3:** De fundamentele theorie van het watertransport door de oliefase wordt beschreven. Er worden twee scenario's voorgesteld om het transport te verklaren: waterdiffusie als gevolg van chemische potentiaalgradiënt en watertransport via omgekeerde micel- of micro-emulsiesbeweging naar het HSW-olie-interface. Door middel van een reeks microfluidische experimenten, leggen we direct vast dat het zoutgehaltecontrast over oliefilms watertransport door de olie kan veroorzaken. Water kan door de geselecteerde alkaanfasen (heptaan en dodecaan) gaan met en zonder toevoeging van een oppervlakteactieve stof. Dit veroorzaakte de expansie van ingesloten water met een hoog zoutgehalte en mobilisatie van olie. Ionische sterkte en de lengte van de koolwaterstofketen spelen beide een belangrijke rol bij het watertransport. Heptaan en dodecaan blijken beide diffuus te zijn voor water en micellen om te keren, en deze eigenschap kan aanzienlijk worden beïnvloed door het zoutcontrast aan de twee zijden van alkanen. Een hoger zoutgehaltecontrast van 1,7-170 g/L induceert een hogere watervolumestroom door heptaan en dodecaan. We ontdekten dat een zoutgehalte van 50-170 g/L contrast minder waterflux geeft en zelfs na

een bepaalde periode 0 bereikt. Het toevoegen van oppervlakteactieve SPAN80 aan alkanen verhoogt de waterstroom met meer dan 100 keer, maar elimineert het zoutgehalte op de waterstroom. De aanwezigheid van oppervlakteactieve stoffen verhoogt de visco-elasticiteit van het water-olie-grensvlak. Bovendien wordt het dynamische proces van emulsiegeneratie bij de pekel-olie-interface vastgelegd door middel van DLS- en IFT-experimenten. Het effect van het zoutgehalte op het proces en de grensvlakspanning worden geëvalueerd.

Door MD-simulatie uit te voeren, observeerden we watermoleculen die door de heptaanfase werden getransporteerd en een groter aantal watermoleculen passeerde het water-heptaan-interface aangedreven door ionenconcentratieverschillen. Er was een netto stroom van watermoleculen naar het water met een hoog zoutgehalte. Ondertussen verschenen, op basis van de berekende profielen van ionen, bijna geen ionen aan het olie-watergrensvlak en in de heptaanfase. Door de veranderingen in de grensvlakspanning en de berekeningen van de gemiddelde kwadratische verplaatsing (MSD) te onderzoeken, concluderen we dat een hoger zoutgehalte leidt tot een lagere diffusiecoëfficiënt van watermoleculen (ongeveer 4,48 en 2,98 m²/ms voor respectievelijk 5% en 20%), d.w.z. langzamer water beweging. Bovendien vermindert een hoog zoutgehalte de kans op waterdiffusie door het grensvlak naar de oliefase. Dit leidt tot de lagere oplosbaarheid van water in olie nabij het olie-HSW-grensvlak en verifieert zo het experimentele resultaat dat de richting van de netto waterbeweging in de richting van water met een hoog zoutgehalte is.

- **Hoofdstuk 4:** We hebben een effectief eendimensionaal model ontwikkeld om elektrodiffusie in een dunne laag elektrolyt tussen twee geladen oppervlakken te simuleren. Dit model is gebruikt om de evolutie van de elektrische potentiaal en de verdeling van de ionenconcentratie langs een dunne laag elektrolyt te simuleren. Simulaties toonden aan dat vanwege de negatief geladen oppervlakken de mobiliteit van de kationen ernstig werd beïnvloed door de elektrische ladingen en dat deze ionen een lagere diffusiesnelheid hadden vergeleken met de stroom van anionen. Het ontwikkelde 1D-model zou de rekentijd met een factor 180-220 aanzienlijk kunnen verminderen in vergelijking met simulatie met

een 2D-model. Het equivalente 1D-model maakt het mogelijk om de niet-lineaire heersende vergelijkingen voor veel grotere domeinlengtes op te lossen, wat een unieke kans biedt om experimentele resultaten van ionentransport in dunne films te simuleren waar de zeer grote hoogte-tot-lengteverhouding het gebruik van 2D-simulaties verhindert. In toekomstige werken kunnen stroomvergelijkingen worden toegevoegd aan het effectieve 1D-model om de toename van de filmdikte te onderzoeken als gevolg van de gekoppelde effecten van elektro-osmotische en waterstroom in de tijd en loslating van de oliefase van het vaste oppervlak op schalen die vergelijkbaar zijn met de experimentele waarnemingen.

- **Hoofdstuk 5:** Het bevochtigingseffect op tweefasenstroming wordt in dit hoofdstuk onderzocht. We hebben de analytische oplossing van drukverdeling in een tweefasenstroom in een rechthoekig kanaal beoordeeld en gecombineerd met de berekening voor de drukvariatie in de capillaire barrièrezone. Door de PDMS-microfluidische experimenten uit te voeren, is de porievijlingsgebeurtenis in een enkele vierkante porie bestudeerd voor tweefasige verplaatsing onder drie injectiestroomsnelheden (Q_1 , Q_2 en Q_3) en drie bevochtigbaarheidsomstandigheden (contacthoeken van 60° , 95° en 120°). Bevochtigbaarheid speelt een cruciale rol in de drukvariatie voor het aansturen van de stroming in het rechthoekige microkanaal en meniscusbeweging in het pinninggebied. De hydrofobe oppervlakken (contacthoeken van 95° en 120°) hebben een langere tijd nodig voor drukaccumulatie om de hogere capillaire ingangsdruk te overwinnen. De stroomsnelheid van de injectie heeft ook invloed op het meniscusgedrag. Met de Q_1 -injectiestroomsnelheid bereikt het hydrofiele model volledige waterverzadiging in de porie, maar het hydrofobe model blijft op een lagere verzadiging. Hogere snelheid induceert een lage waterverzadiging voor alle bevochtigingscondities en verzwakt het bevochtigingseffect voor de hydrofobe gevallen. Naarmate de hydrofobiciteit toeneemt, blijft de meniscusradius stabiel met lagere waarden voor de stroming in microkanalen. Het grootteverschil wordt klein tussen stroming in het kanaal en in het pinninggebied. Dienovereenkomstig reageert de capillaire druk en wordt de variatie kleiner. Directe simulatie van de water-fluorinert-verplaatsing met behulp van de vloeistofvolume-

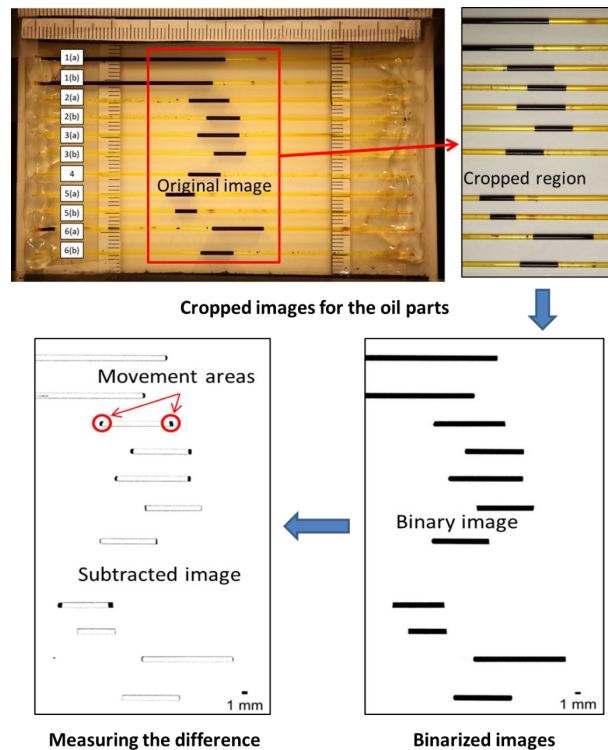
methode geeft een gedetailleerde beschrijving van het interfacegedrag tijdens het vullen van de poriën en biedt consistente resultaten van capillaire drukveranderingen met de experimentele gegevens.

Appendix A

Impact of water salinity differential on a crude oil droplet constrained in a capillary: Pore-scale mechanisms

Data and image processing in Chapter 1

This material is for explaining the method mentioned in section 2.4 of Chapter 1. In order to quantify the oil phase movement, we processed the camera images using ImageJ software. The main steps of image processing are: cropping oil parts of images, making binary images, subtracting the oil areas with a wand tool, and then measuring the length difference of the front and end of oil globules from the beginning to the end of the experiment.



Appendix A- 1 Main steps of image processing. (a) Cropping oil parts of the original images acquired from a CMOS camera. (b) Making binary images. (c) Subtracting the oil areas with wand tool, and measuring the length difference of the front and end of oil globules.

Appendix B

Fundamental study of water transport through oil phase

Data and image processing in Chapter 3

B.1. Images of experiment No.2 with n-heptane and 50 g/L LSW

We continuously monitored the observed domain of the No.2 experiment, see Figure B-1, for about 70 hours. In the figure, the bulk phase (50 g/L of low-salinity water) is seen in purplish. The whitish regions are the grains along with the trapped 170 g/L HSW. Brown areas are the heptane phase confined between low-salinity water and grain or high-salinity water. The dashed square is the zone that we select and study in detail; there we have the system of LSW/oil/HSW.

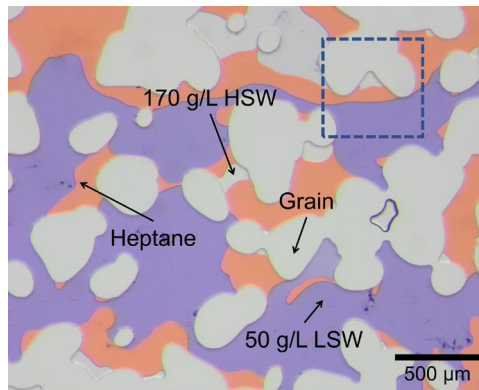


Figure B-1: The observed domain in experiment No.2. The blue dashed squares are the selected regions for quantifying the HSW area change.

We present the four pictures for presenting the area change in HSW of the selected region, see Figure B-2. It is obvious to see that the HSW area didn't have a significant swelling during 70 hours of monitoring. The HSW area grew by 20.66%, which was much less than the measured area change with a higher salinity differential, meaning that the salt ions play an important role to prevent water diffusion through the heptane phase.

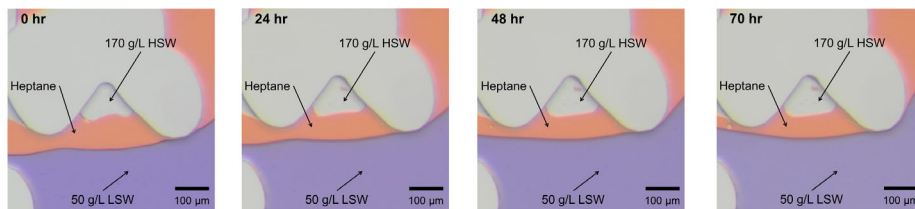


Figure B-2: Images of the selected region at four different moments from 0 to 70 hours. The purplish area represents 50 g/L LSW as the bulk phase. Heptane is shown in brown, and 170 g/L HSW is confined by heptane and solid surfaces.

The changes in the heptane area and HSW are over 70 hours of monitoring are shown in Figure B-3a. The measurements indicated that the HSW area had a slight swelling, reaching a plateau after about 30 hours, and eventually increased by 20.7% after 70 hours, while oil region area remained relatively constant. The increase in HSW area was much less than in experiment No.1. The results of water mass flux at six moments are shown in Figure B-3b. The trend presented that in the first 24 hours, water mass flux in heptane decreased rapidly by 51.8%, but after 36 hours it levelled off. Correspondingly, concentration differences of water at two water-alkane interfaces (presented in Figure B-3c) showed a dramatic drop and then gradually decreased. The inset figure shows the non-linear relationship between water solubility change and HSW area change as well.

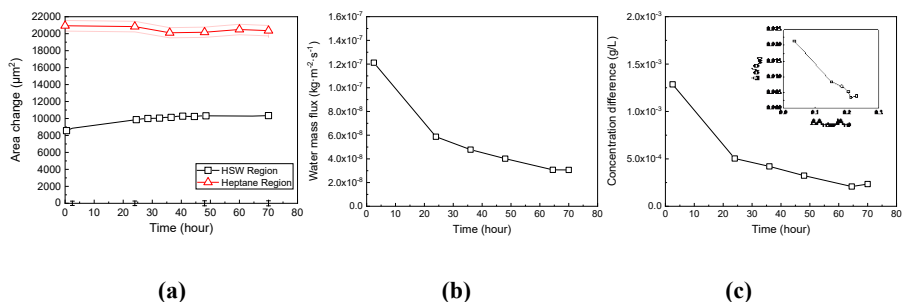


Figure B-3: Results of observations of heptane and HSW, for the case of LSW having a salt concentration of 50 g/L. (a) This figure shows the area changes of heptane and HSW for 70 hours. The measurement error is indicated in the shadow band. (b) This figure shows the water mass flux as a function of time. (c) This figure shows the change in water concentration difference between the LSW-heptane interface and the HSW-heptane interface. The inset presents a relationship between water concentration change and HSW area change.

B.2. Images of experiment No.3 with n-heptane and no salinity differential

A reference experiment was conducted to verify no effect of low salinity on the water diffusion in alkane phases. The images of one LSW/heptane/LSW system are presented in Figure B-4. No obvious change in trapped LSW areas is found.

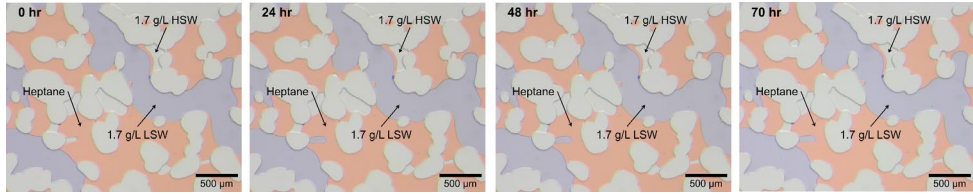


Figure B-4. Images of the observed domain at four different moments from 0 to 70 hours.

B.3. Images of experiment No.5 with n-dodecane and 50 g/L LSW

The experiment with 50 g/L LSW was conducted as well, to investigate the effect of salt concentration difference. The observed domain is shown in Figure B-5. In the figure, the bulk phase (50 g/L of low-salinity water) is seen in purplish. The whitish regions are the grains along with the trapped 170 g/L HSW. Brown areas are the dodecane phase confined between low-salinity water and grain or high-salinity water. The dashed square is the zone that we select and study in detail; there we have the system of LSW/oil/HSW.

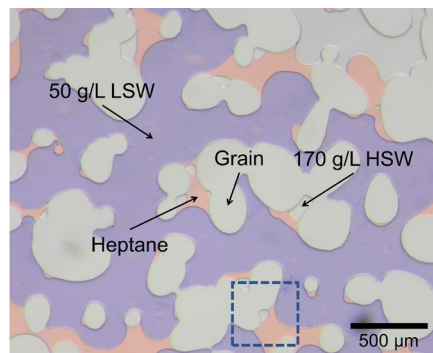


Figure B-5: The observed domain in experiment No.2. The blue dashed squares are the selected regions for quantifying the HSW area change.

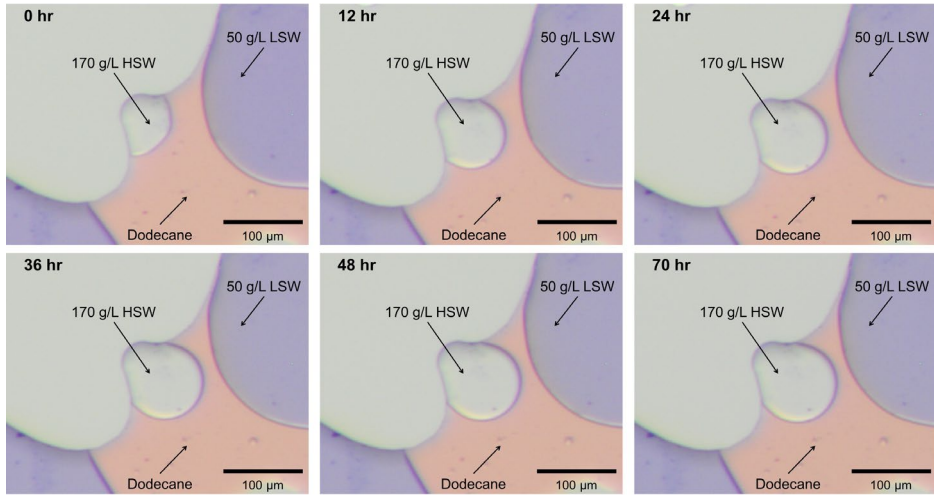


Figure B-6: Images of selected regions at six different moments from 0 to 70 hours. The bluish area presents 50 g/L LSW as the bulk phase. Dodecane is shown in brown, and 170 g/L HSW is confined by dodecane and solid surfaces.

The images of the selected region at six different moments from 0 to 70 hours are presented in Figure B-6. The HSW area increased by 82.7% after 70 hours of observation.

B.4. Images of experiment No.6 with n-dodecane and no salinity differential

A reference experiment was conducted to verify no effect of low salinity on the water diffusion in alkane phases. The images of one LSW/dodecane/LSW system are presented in Figure B-7. No obvious change in trapped LSW areas is found.

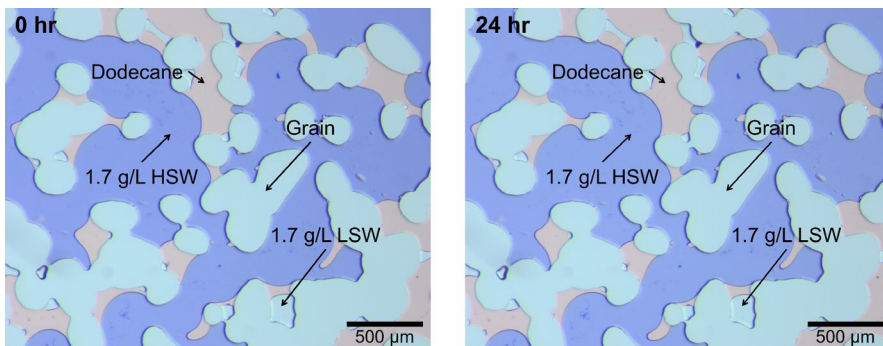


Figure B-7: Images of the observed domain at two different moments from 0 to 24 hours.

B.5. Images of experiment No.8 with n-heptane+1%SPAN80 and 50 g/L LSW

Two images of experiment No.8 at 0 and 46 hours are presented below. The analyzed region is marked with a dashed blue square. The HSW area increases 174.51% during 46 hours.

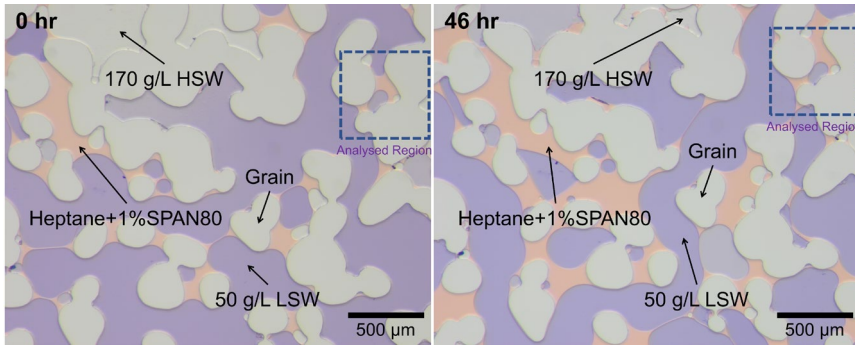


Figure B-8: The observed domain in experiment No.8. The blue dashed squares are the selected region for quantifying the HSW area change.

The changes in the HSW area during 46 hours are shown below with four moments.

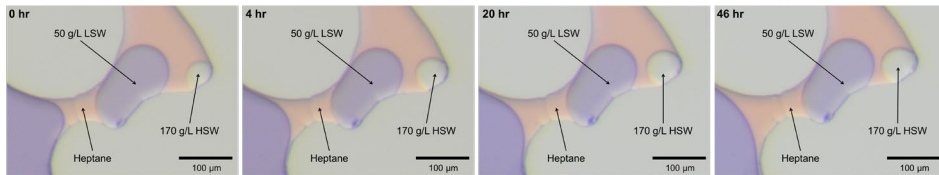


Figure B- 9: Images of the analyzed region at six different moments from 0 to 46 hours. The bluish area presents 50 g/L LSW as the bulk phase. Heptane+1%SPAN80 is shown in brown, and 170 g/L HSW is confined by heptane and solid surfaces.

B.6. Images of experiment No.11 with n-dodecane+1%SPAN80 and 50 g/L LSW

Two images of experiment No.11 at 0 and 48 hours are presented below. The analyzed region is marked with a dashed blue square. The HSW area increases 38.44% during the observation period.

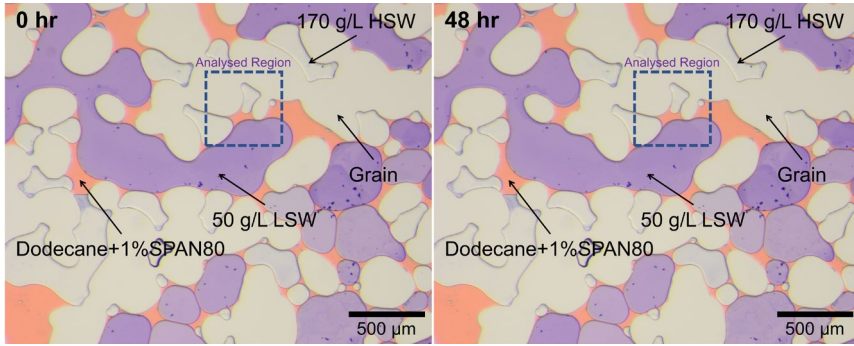


Figure B-10: The observed domain in experiment No.11. The blue dashed squares are the selected region for quantifying the HSW area change.

The changes in the HSW area during 48 hours are shown below with four moments.

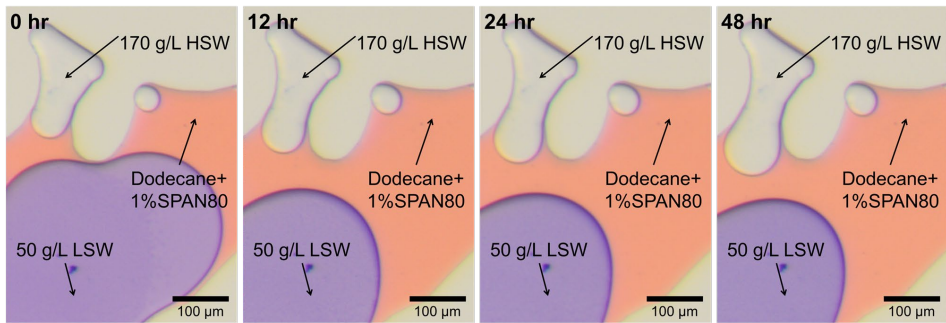
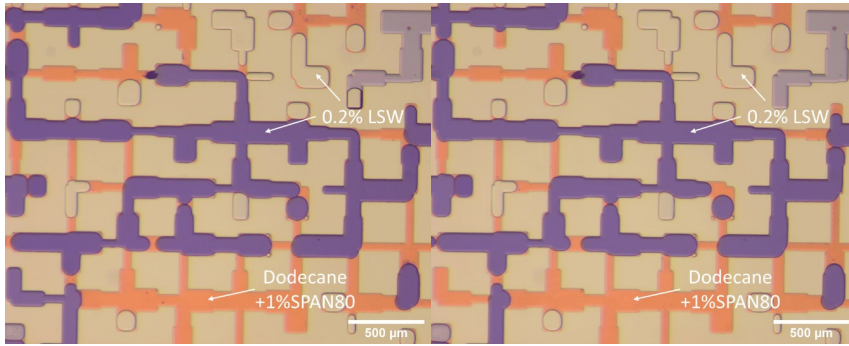


Figure B-11: Images of the analyzed region at six different moments from 0 to 46 hours. The bluish area presents 50 g/L LSW as the bulk phase. Dodecane+1%SPAN80 is shown in brown, and 170 g/L HSW is confined by dodecane and solid surfaces.

B.7. Images of experiment No.12 with no salinity differential

The reference experiment (i.e., 1% SPAN 80+dodecane and LSW only) showed no significant changes in the trapped LSW after even 68 hours of monitoring; see Figure B-12. This microchip has another randomly generated pore structure, but it doesn't affect the formation of the isolated system and the observation of the oil-brine interface.



(a) After 1 hour

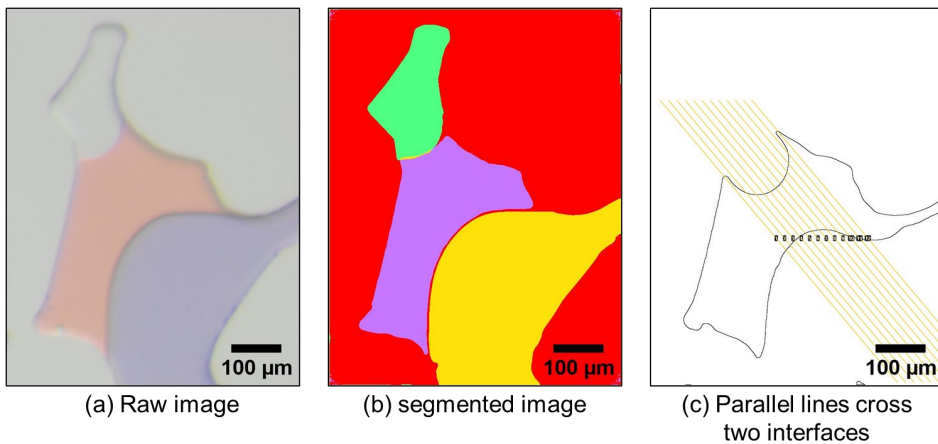
(b) After 68 hours

Figure B-12: The reference experiment: images of the LSW/dodecane+1% SPAN80/LSW system after 1 hour (a) and 68 hours (b).

The unmarked areas are the substrates representing solid grains. This reference test gives a clear indication that the salinity contrast is the only factor to causes trapped HSW expansion, regardless of whether a surfactant is present or not.

B.8. Imaging and data processing method

We gain the raw images from the microscope imaging software. To acquire the area change and the interface movement, we have conducted the post-imaging and data processing for each experiment. Here, we give the example for experiment No.1 with pure heptane and focus on the analysis in Region 1 with a single cluster of HSW-oil-LSW.



(a) Raw image

(b) segmented image

(c) Parallel lines cross two interfaces

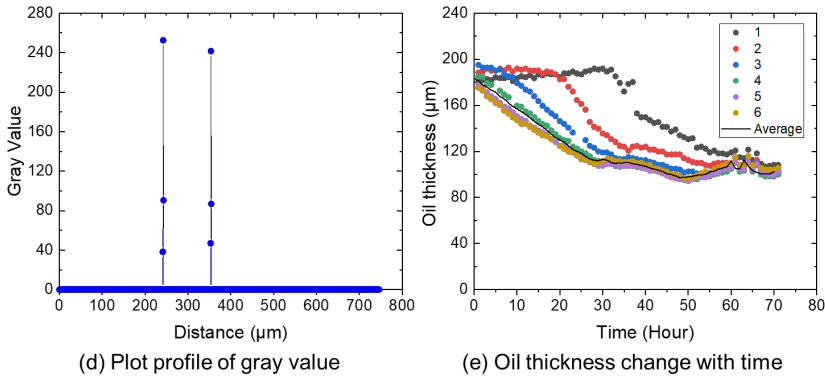


Figure B-13. Imaging and data processing method.

We have segmented the three fluids (HSW, oil and LSW) and grain in the raw image, as shown in Figure B-13(a-b). With the segmented image, the areas of HSW and oil can be measured. In addition, the increasing length for LSW-oil and HSW-oil interfaces are calculated with the increase in the perimeters of HSW and oil regions. To evaluate the variation in the oil thickness, we first find the edges of oil phase and then make parallel lines across the oil phase, as shown in Figure B-13c. By building a Marco code in ImageJ, the gray value (0-255) along the parallel lines are plotted in the stack of images. Therefore, the oil thickness for one parallel line is acquired by subtracting the two distances with the maximum gray values. Later, all oil thicknesses for each line can be measured and plotted in Figure B-13e. Note that here we only plot the oil thickness for 6 lines and the average value used for later calculation. We use the same method to obtain the area change, interface lengths, oil thickness for each phase. The Marco code for measuring the oil thickness is listed below:

```
//generate the parallel line in a selected rectangular;
getSelectionBounds( x, y, w, h );
for ( i=0; i<w; i += 20 ) {
    makeLine( x+i, y-100, x+i, y+h-1 );
    p = getProfile();
    //roiManager("Select", i);
    roiManager("Add");
    t = "";
```

```
        for (k=0; k<p.length; k++) {
            t += "" + k + "\t" + p[k] + "\n";
        }
        //File.saveString( t, dir + "x" + i + ".txt" );
    }

    roiManager("Show All");
    //rotate the parallel line to a specific angle;
    num = 100; // number of lines you want drawn
    for ( j=0; j < num; j++) {
        roiManager("Select", j);
        run("Rotate...", " angle=55");
        //getSelectionCoordinates(xpos,ypos);
        //makeLine(xpos,ypos);
        roiManager("Update");
    }

    roiManager("Show All");
    //plot stack profile data for one selected line;
    macro "Stack profile Data" {
        if (!(selectionType()==0 || selectionType==5 || selectionType==6))
            exit("Line or Rectangle Selection Required");
        setBatchMode(true);
        run("Plot Profile");
        Plot.getValues(x, y);
        run("Clear Results");
        for (i=0; i<x.length; i++)
            setResult("x", i, x[i]);
        close();
        n = nSlices;
        for (slice=1; slice<=n; slice++) {
            showProgress(slice, n);
```



```

setSlice(slice);

profile = getProfile();

sliceLabel = toString(slice);

sliceData = split(getMetadata("Label"), "\n");

if (sliceData.length>0) {

    line0 = sliceData[0];

    if (lengthOf(sliceLabel) > 0)

sliceLabel = sliceLabel+ " (" + line0 + ")";

}

for (i=0; i<profile.length; i++)

    setResult(sliceLabel, i, profile[i]);

}

setBatchMode(false);

updateResults;

}

```

B.9. Detailed non-bonded interactomic interaction parameters

Table SI-1

Table B-1: Force field parameters for the systems

Atom types	ϵ , Kcal/mol	δ , Å	q, e
table	0.0660	3.1700	-0.1800
C (heptane, -CH ₂ -)	0.0660	3.1700	-0.1200
H (heptane, C-H)	0.0300	2.1700	0.0600
O (water)	0.1554	3.1655	-0.8200
H (water)	0.0000	0.0000	0.4100
Na ⁺	0.3526	2.1600	1.0000
Cl ⁻	0.0128	4.8305	-1.0000
C (graphene)	0.1480	3.6170	0.0000

B.10. The dynamic number of diffusion water molecules across the oil phase in the three model systems during simulations

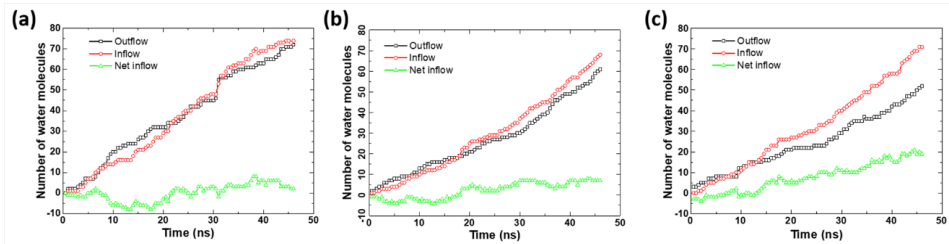


Figure B-14: The dynamic number of diffusion water molecules across the oil phase from pure water phase into the solution phase in the three model systems. From (a) to (c) are the systems of 0%-0%, 0%-5%, and 0%-20% salinity, respectively.

B.11. The dynamic number of diffusion water molecules

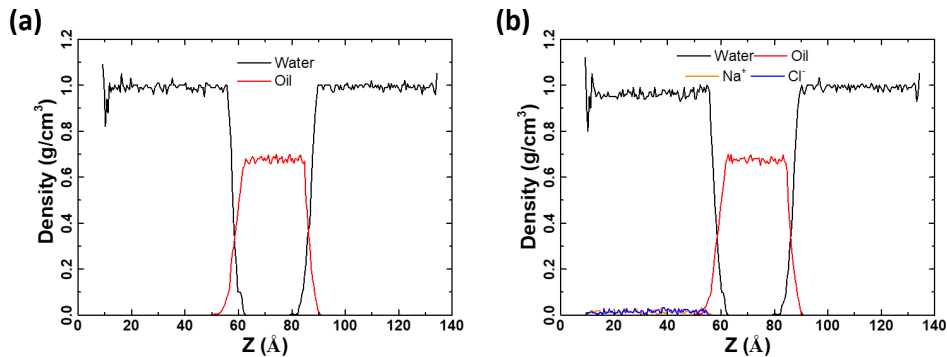


Figure B-15: Density profiles of different molecular components in systems with 0%-0% salinity (a) and with 0%-5% salinity (b).

B.12. The modeling and calculation of interfacial tension

A heptane/salinity water system (Figure B-16a) was specifically built for study the effect of salinity on the interfacial tension. During simulation, all the parameters between molecules were the same as those used in the other simulations in this work. The system was equilibrated first for 5 ns under NPT ensemble, and followed by another 5 ns equilibration under the NVT ensemble. For calculating the interfacial tension, a further 4 ns simulation under the NVT

ensemble was carried out, with the interfacial tension in the system constantly monitored during the simulation, as the results shown in Figure B-16b.

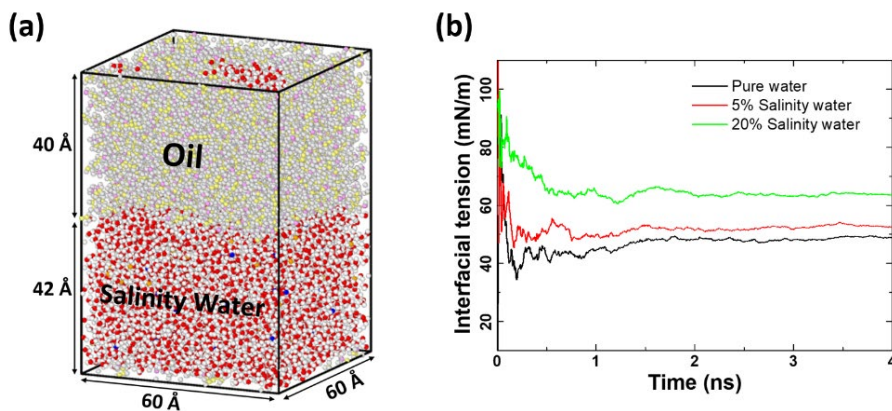


Figure B-16: Calculation of interfacial tension in the system. (a) A representative of the systems used for calculating the interfacial tension; (b) The results of the interfacial tension in each system with a solution of varied salinity.

Acknowledgements

First and foremost I am extremely grateful to my supervisors, Prof. dr. Ruud Schotting, Prof. dr. ir. Majid Hassanizadeh and Dr. Amir Raoof for their invaluable advice, continuous support, and patience during my PhD study. Their immense knowledge and plentiful experience have encouraged me all the time in my academic research and daily life. When I joined the Environmental hydrogeology group at Utrecht University in 2018 as a PhD candidate, I realized this is a remarkable turning point in my career. At the beginning of PhD project, I acquired a fundamental understanding of flow and transport in geological porous materials from the master's courses as a teaching assistant. Those courses, taught by Ruud, Majid, Rien van Genuchten, Veerle Cnudde, and Amir, inspired my interest in the world of porous media.

I firstly met with Amir in his office and expressed my interest to pursue this PhD degree in the earth sciences. Although I was not knowledgeable about the project, he kindly encouraged me and guided me on how to gain a deep understanding of microfluidics and find the key research questions. He supported me a lot in the laboratory and numerical modelling works and spent plenty of time on my daily supervision. Without his support, I can not finish this project. Ruud helped me generously, both in life and academically. I often reported to him on the progress of my project, and he had given me many impressive suggestions and corrected the errors in math. I also enjoyed a lot and was surprised by his outstanding teaching in his course, Principles of groundwater flow and Water in geoprocess, which enlightened my curiosity to dig into the flow and transport in the porous media. He tried his best and paid plenty of effort into solving my financial issue. Thank you for helping me to go through the tough time, Ruud. Majid guided me to complete the first publication and kept supervising me on the following research. When I doubted my research output and had no confidence in the first publication, Majid encouraged me to bravely take the first step. I still remember what he said to me in 2019. The main words were, “Don't be afraid of making mistakes and don't worry about not being perfect, just do it and be innovative”. He always accurately pointed out the errors in my works and generously shared his broad knowledge of the porous media. With his help and generous ideas, I was able to continue my work and got the opportunity to finish the short research stay in Norway.

I would like to thank Enno de Vries for all his help in the lab and many discussions in our office. He taught me how to fabricate the PDMS micromodels and provided all the tricks to avoid mistakes in the experiments. We spent a lot of time to discuss on image acquisition and processing. Thanks for the kind suggestions. I would also like to thank Vahid Nikpeyman for the kind words to encourage my work and for the discussion on the ongoing projects. We had a wonderful time in the office. Thanks to Qianjing Tang for his help in performing the experiments in the lab. We often had brainstorming to improve the experiments and many discussions on the results. I would express my gratitude to Ioannis Zarikos, Mahin Bagheri and Giovanni Dammers for the kind support in the lab and for teaching me to correctly conduct the experiments. Thanks to Sona Aseyednezhad who was one of my co-supervised master students for contributing to my work. I appreciate the help from Annuska Exel, our group secretary, during my PhD. She always actively supported me to solve problems in my work.

Thanks to the former and current colleagues in the Environmental hydrogeology group whom I met over my PhD years. Thanks to Chaozhong Qin and Luwen Zhuang for their kind concern and wonderful discussions on my research, especially in the first two years of my PhD. Thanks to Hamed Aslannejad, Matthijs de Winter Suzanne Faber, Alraune Zech, Willem-Bart Bartels, Johan van Leeuwen, Gillian Schout, Amir Hossein Tavangarrad, Tuong Hoang, Xiaoguang Yin, Mandana Samari Kermani, Alejandra Reyes-Amézaga and Ellie Buena.

I would like to thank my friends outside Utrecht University. Thanks to Rien van Genuchten and Betty May for their kind concerns about my life and research. Thanks to Fernanda Oliveira Hoerlle and William Godoy from Universidade Federal do Rio de Janeiro. We had many discussions about our collaborations on the research and core flooding experiments. Thanks to Dr. Carl Fredrik Berg and Mohammad Hossein Golestan from Norwegian University of Science and Technology for kindly having me during the two-month research stay. That was an amazing winter in 2020 in Trondheim. Thanks to Wenyu Zhou who was my co-supervised master student for his contribution to my work. We had a happy time in the lab of NTNU and fruitful results from the microfluidic experiments. Thanks to Johannes Müller and Cynthia Michalkowski for the collaboration in

the PDMS experiments. We had a wonderful time in our lab and impressive talks on the image and data processing.

I would also like to thank my partner, Zheng Ying, who supported me and helped me to overcome the tough periods. Many thanks to my great friends, Madhuri Prabhakar and Martin, Dom Weinberg and Sarah Oxley, Zhu Zhang, Yuntao Ji, Xin Jin, Miao Zhang, for their support in my daily life and work.

Last but definitely not least, I would like to express my gratitude to my family I am very thankful to my parents, Shengping Yan and Chunzhi Yang, for their encouragement and support. Thanks to my sister Lina Yan, my niece Jincan Xu and other relatives. Without their tremendous understanding and encouragement over the past few years, it would be impossible for me to complete my PhD.

Lifei Yan

August 2022

Curriculum Vitae

Lifei Yan was born on the 24th of January 1988 in Xingtai, Hebei, China. He grew up in Baxian town until moving to Renqiu city in 1997. In 2006, he started his Petroleum Engineering bachelor at China University of Petroleum (Beijing) and obtained his bachelor's degree in 2010. He then moved to Panjin, Liaoning, and began his professional career as a geologist and engineer for the Geological Research Institute of Changcheng drilling company of CNPC. For almost 3-year working, he carried out research and practice of geology-engineering integration in the exploration and development of oil fields, such as tight sandstone natural gas of Sulige reservoir, SAGD heavy oil in Liaohe, and development design for the heavy oil field in Canada.

In February 2013, he started his master study in Petroleum and Natural Gas Engineering at China University of Petroleum (Beijing) and obtained his master's degree in 2015. During the master period, he completed an internship at the Drilling Research Institute of CNPC, Beijing, for about 2 years. From 2015 to 2016, he formally joined the institute as a junior scientific researcher. He conducted research in geological analysis, geomechanics modeling and engineering field practice for unconventional oil and gas fields, such as coalbed methane in Shanxi, shale gas in Sichuan, and gas storage in salt caverns in Xinjiang. He participated in two National Science and Technology Major Projects from 2013-2016: Coalbed methane gas development; Underground natural gas storage in the salt cavern. He also helped to establish a geo-energy laboratory in the institute and completed the lab management.

From Oct. 2016 to Jan. 2018, he performed a short period of research in geomechanics modeling at the University of Groningen. In Jan. 2018, he then joined the Environmental Hydrogeology group at Utrecht University as a PhD candidate. The PhD project focused on the interface behavior in two-phase flow: impacts of salinity and wettability at the nano to micro scales. From Oct. to Dec. 2020, he conducted a research visit to Norwegian University of Science and Technology, Trondheim, Norway, and finished the collaboration with PoreLab on multiphase flow and transport in porous media. During the PhD period, he assisted several bachelor's and master's courses in Earth Sciences and supervised 2 master's thesis in geo-energy.

List of Publications

Chapter 1: prepared for submission; Literature review of osmosis and emulsification mechanisms for low-salinity water flooding.

Chapter 2: Yan, Lifei, Hamed Aslannejad, S. Majid Hassanizadeh, and Amir Raoof. "Impact of water salinity differential on a crude oil droplet constrained in a capillary: Pore-scale mechanisms." *Fuel* 274 (2020): 117798.

Chapter 3: Yan, L., Chang, Y., Hassanizadeh, S. M., Xiao, S., Raoof, A., Berg, C. F., & He, J. (2022). A quantitative study of salinity effect on water diffusion in n-alkane phases: From pore-scale experiments to molecular dynamic simulation. *Fuel*, 324, 124716.

Prepared for submission; Direct evidence of salinity differential effect on water transport in oil: pore-scale mechanisms

Chapter 4: Aseyednezhad, S., Yan, L., Hassanizadeh, S. M., & Raoof, A. (2022). An accurate reduced-dimension numerical model for evolution of electrical potential and ionic concentration distributions in a nano-scale thin aqueous film. *Advances in Water Resources*, 159, 104058.

Chapter 5: prepared for submission; Wettability effect on pore-filling events for two-phase flow.

Prepared for submission; Direct simulations of pore filling behavior in a single square pore for two-phase flow.